Force-based Engineering of Gradients

Chunching Li

Submitted in Accordance with the Requirements for
the Degree of Doctor of Philosophy and the Diploma of Imperial College

The Department of Materials
Imperial College London

2019

Declaration of Originality

I, Chunching Li, declare that the scientific content contained within this thesis was prepared, acquired, and analysed by myself at Imperial College London unless otherwise stated. Contributors of all collaborative efforts are noted in the text.

There are chapters in this thesis derived from peer-reviewed journal articles.

Chapter 3 is derived from the peer-reviewed article: "Glycosylated superparamagnetic nanoparticle gradients for osteochondral tissue engineering", which was published in Biomaterials (vol.176, 2018). This project was led by Chunching Li. The study was designed by Chunching Li with the supervision of Dr. James P.K. Armstrong. In this research, Dr. Isaac J. Pence performed Raman spectroscopy experiments and assisted with the statistical analysis. Dr. Worrapong Kit-Anan, Dr. Jennifer L. Puetzer and Dr. Axel C. Moore assisted with mechanical characterisation. Dr. Ioanna Mylonaki assisted in modelling of growth factor release.

Chapter 4 is derived from the peer-reviewed article: "Buoyancy-driven Gradients for Biomaterial Fabrication and Tissue Engineering", which was published in Advanced Materials (1900291, 2019). The project was led by Chunching Li. Chunching Li conceived the project and carried out the majority of experimental work. Dr. Isaac J. Pence performed all Raman spectroscopy experiments, Dr. Axel C. Moore performed all mechanical characterisation, Dr. Yiyang Lin assisted on the material modification and synthesis, and Charles W. Winter assisted with extracellular vesicle production. Dr. Vincent Leonardo assisted in producing the fluorescent cell line used to generate extracellular vesicles. Dr. Yunqing Zhu for advice in polymer experiments.

Acknowledgement

"It is good to have an end to journey toward; but it is the journey that matters, in the end."

Ernest Hemingway

Thank you all for being part of the journey -

Molly Stevens, James Armstrong, Taiwan TUSA PhD Scholarship

Adrian Najer, Amanda You, Arianna Ferrini, Axel Moore, Camille Marijon, Charlie Winter, Charlotte Lee-Reeves, Chia-Chen Hsu, Coline Jumeaux, Colleen Loynachan, Conor Horgan, Håkon Høgset, Ioanna Mylonaki, Isaac Pence, Jean-Philippe St-Pierre, Jelle Penders, Jennifer Puetzer, Jonathan Wojciechowski, Leah Frenette, Liliang Ouyang, Lucia Massi, Marco Sorbona, Maria João Cruz, Michael Potter, Michael Thomas, Michele Becce, Qu Chen, Sahana Gopal, Shweta Agarwal, Spencer William, Stacey Skaalure, Thomas Whittaker, Timothy Keane, Valeria Nele, Vincent Leonardo, Worrapong Kit-Anan, Ye Wang, Yiyang Lin, Yunlei Xianyu, Zhang Shaodong

And also, those who I cherish the most

Abstract

"Simplicity is the Ultimate Sophistication", Leonardo Da Vinci

Tissue engineering research has opened a new chapter in modern medicine since it emerged as a mainstream research field in the early 90s. Until now, however, effective strategies to fully emulate the complexity of natural tissue remain elusive. One of the key features in the development of complex tissue structures is the presence of morphogen gradients during development. In nature, from squid beaks to human teeth, gradients are preserved in many structures after evolution. In a living organism, gradients play an essential role in defining the physiological function. The formation of these gradients is often largely dictated by an anisotropic distribution of different morphogens present during development. The spatial difference in concentration of different morphogens results a spatial variance in cell signalling, patterning the development of tissue and leading to the formation of heterogeneous structure.

Although these principles of development are well-established, the overwhelming majority of *in vitro* engineering strategies use uniform scaffolds and spatially invariant growth factor delivery to produce homogeneous tissue constructs. It is clear that more sophisticated fabrication processes are required to replicate the native complexity and fulfil the functional requirements of tissue grafts. A few material strategies have been developed that can heterogeneously deliver biological or mechanical cues; however, most of them are limited by complex fabrication procedures or restricted compatibility with different material systems.

By establishing signaling factor gradients within tissue engineering scaffolds, the formation of heterogeneous tissue interfaces can be achieved. This thesis will demonstrate two gradient casting strategies to emulate physiological gradients, exploiting magnetism and buoyancy to distribute growth factors. These strategies are shown to be capable of establishing gradients in different materials, and are used to engineer osteochondral tissue. The strategies proposed in this research are designed to be widely applicable and easy to reproduce. It is hoped that these strategies may be adapted and tailored for wider use by the tissue engineering field, allowing development of complex, functional tissue by mimicking the processes used by nature.

Table of Contents

List of Tables

List of Figures

List of Abbreviations

ALP	Alkaline phosphatase
BCA	Bicinchoninic acid
BMP	Bone morphogenetic protein
BMPR1A	The bone morphogenetic protein receptor, type 1A
COL10	Collagen type X
COL2	Collagen type II
CTGF	Connective tissue growth factor
DAPI	4',6-diamidino-2-phenylindole
DKK1	Dickkopf-related protein 1
DMEM	Dulbecco's modified eagle's medium
DMMB	Dimethylmethylene blue
DNA	Deoxyribonucleic acid
ECM	Extracellular matrix
EDC	1-ethyl-3-(3-dimethylaminopropyl) carbodiimide
EGF	Epidermal growth factor
ELISA	Enzyme-linked immunosorbent assay
EVs	Extracellular vesicles
FGFs	Fibroblast growth factors
FITC	Fluorescein isothiocyanate
FRZB	Frizzled related protein
GAG	Glycosaminoglycan
GDF10	Growth differentiation factor 10
GelMA	Gelatin-methacyloyl
GMP	Good manufacturing practice
GPI	Glycosyl phosphatidylinositol
GTP	Guanosine triphosphate
HAP	Hydroxyapatite
HepMA	Heparin-methacyloyl
Hh	Hedgehog
hMSCs	Human mesenchymal stem cells
HS	Heparan sulphate
HSPGs	Heparan sulphate proteoglycans
ICP-OES	Inductively coupled plasma optical emission spectroscopy
IHH	Indian hedgehog
ITS	Insulin-transferrin-selenium
LAP	Latency-associated peptide
MAPK	Mitogen-activated protein kinase
MMP13	Matrix metallopeptidase 13
MRI	Magnetic resonance imaging
MSCs	Mesenchymal stem cells
MTf	Membrane-bound-transferrin-like protein
NF-kB	Nuclear factor kappa-light-chain-enhancer of activated B cells
NHS	N-hydroxysuccinimide
NMR	Nuclear magnetic resonance
NPs	Nanoparticles
NTA	Nanoparticle tracking analysis
PBS	Phosphate buffered saline
PCL	Poly(caprolactone)
PDGF	Platelet derived growth factor
PLGA	Poly(lactic-co-glycolic acid)
POPC	1-palmitoyl-2-oleoyl-sn-glycero-3-phosphocholine
PTHrP	Parathyroid hormone-related protein
PVA	Poly(vinyl alcohol)
PBS	Phosphate buffered saline
PCL	Poly(caprolactone)
PDGF	Platelet derived growth factor
PLGA	Poly(lactic-co-glycolic acid)
POPC	1-palmitoyl-2-oleoyl-sn-glycero-3-phosphocholine
PTHrP	Parathyroid hormone-related protein
PVA	Poly(vinyl alcohol)

qPCR	Quantitative real-time reverse-transcription polymerase chain reaction
Ran	Ras-related nuclear protein
RFP	Red fluorescent protein
RNA	Ribonucleic acid
ROS	Reactive oxygen species
RUNX2	Runt-related transcription factor 2
SDF-1	Systemic stromal-derived factor-1
siRNA	Small interfering RNA
SPION	Superparamagnetic iron oxide nanoparticles
SQUID	Superconducting quantum interference device
TEM	Transmission electron microscopy
TGF-β	Transforming growth factor-β
VEGF	Vascular endothelial growth factor
Wnt	Wnt ligand
β−TCP	β-tricalcium phosphate
ρ	Density

Scope of the Thesis

Spatial gradients are a pervasive feature of biology, with conserved functional roles in tissue development and physiology. In this thesis, various gradients in nature will be overviewed, and engineering approaches to emulate them will be investigated.

Chapter I: Introduction and Literature Review

The chapter will introduce the literature closely related to the study. This will include (1) the process and the mechanism of gradient formation, (2) the current approaches of recreating gradients and (3) the gradient features of osteochondral tissue, which is also the engineering target of the study.

Chapter III: SPIONs-derived Gradient in Osteochondral Tissue Engineering

This chapter will introduce a novel gradient fabrication technology utilising superparamagnetic nanoparticles (SPIONs) and an external magnetic field. It is then demonstrated how the proposed platform could be applied in osteochondral tissue engineering, and the engineered osteochondral tissues will be assessed in detail.

Chapter IV: Buoyancy-driven Gradients Fabrication

This chapter will introduce a versatile gradient fabrication technology utilising buoyancy force. Several applications (*e.g.,* stiffness gradient, composition gradient) of the technology will be demonstrated. I will then discuss how the proposed fabrication approach could be applied in osteochondral tissue engineering, and the engineered tissues will be assessed in detail.

Chapter V: Conclusions

This chapter will summarise results from Chapter I to Chapter IV, and the possible impacts of the study to the field of complex tissue engineering.

Chapter I: Introduction and Literature Review

1.1 Past, Present and the Future of Tissue Engineering

The emergence of tissue engineering

The dysfunction or failure of tissue due to disease, injury, wear or ageing is devastating for an individual and also brings an enormous burden in health care [1]. There were few effective remedies until 1954 when Joseph Murray performed the very first tissue transplantation between twins, and two unrelated individuals five years later [2, 3]. Many lives have been saved through transplantation although the gap between the demand and availability of tissues and organs is huge. Tissue engineering is a highly interdisciplinary field where the principles of medicine, biology, and engineering are augmented. Published in 1981, the earliest tissue engineering study by Bell and colleagues demonstrated the successful graft of skin-equivalent constructs consisting collagen matrix and autologous fibroblasts onto patients with extensive burn injuries [4]. After years of research, the hallmark review of the field was published in 1993 by Langer and Vacanti [1]. In the review, the concepts of tissue engineering were defined and its potential was summarised. The concept of tissue engineering has also made popular through the vivid image of auriculosaurus, a human-ear-bearing mouse [5].

From oversimplified to sophisticated: recreating gradients

Since the emergence of tissue engineering, research has aimed to generate functional tissue or organs to restore, replace, or improve the function of damaged tissue [1]. In general, a tissue engineering design comprises cells residing in a biomaterials scaffold which is usually intended to provide space for cell proliferation and differentiation. There are also material-free tissue engineering designs in which high-density cells form the engineered tissue. In addition to cells and biomaterials, bioactive signals are an indispensable factor. In a robust tissue engineering design, an appropriate signal should guide the cells to differentiate or maintain their phenotype. While growth factors were the main signal used in early research designs, various motifs including nucleic acids, small molecules, peptides, and macromolecules have now all been used as bioactive signals.

In the early stages of tissue engineering research, most designs were oversimplified. For example, the most conventional bioactive signal delivery strategy is to homogeneously deliver soluble signalling molecules to a homogeneous scaffold system. But this kind of homogeneous strategy could only create homogeneous tissue constructs without any complex architecture. Thus far, a homogeneous construct has only successfully translated into the clinic for simple tissue targets (*e.g.* skin and cornea) that don't require a complex structure. For tissue bearing a more complex structure to support the physiological function, homogeneous designs are usually insufficient. Indeed, while a successful tissue engineering design should aim to allow the construct to emulate the physiological function of the target tissue, an oversimplified design incapable of creating precise native structure could not provide the physiological function of heterogeneous tissue.

Recently, there has been a trend toward developing more biomimetic and sophisticated tissue engineering strategies. These strategies aim to generate functional vascular networks, utilise extracellular matrix (ECM) components for signal delivery, and fabricate scaffolds with appropriate tissue geometry [6, 7]. In this thesis, the aim is to recreate gradients, a sophisticated character in living organisms. Gradients play an essential role in guiding the function of a wide range of tissues. During development, gradients play a major role in defining the character of heterogeneous tissue by spatially regulating the morphology, behaviour, and differentiation of un-polarised cells [8-14]. While oversimplified strategies usually fail to produce tissue with heterogeneous architecture, tissue engineers have recently tried to emulate physiological gradients with more sophisticated strategies. For all the different gradient casting technologies, the goal is to reproduce gradients features in order to investigate, study, or manipulate cell behaviour [15].

In this chapter, the historical context and basic concepts of tissue engineering are briefly summarised. The main focus of the thesis is the character and formation mechanisms of physiological gradients and the engineering approaches to emulate them. In the next section, physiological gradients will be discussed.

1.2 Physiological Gradients

Over recent years, advances in developmental biology have shown that various gradients can spatially and temporally regulate cell behaviour including homeostasis, proliferation, migration, and differentiation. Aside from regulating cell metabolism and tissue formation, gradient cues can also participate in the cascade of inflammation, wound healing, and disease progress [9, 16].

Cells are exposed to complex biochemical and biophysical gradients in their surrounding milieu [17, 18]. These gradients are often necessary for heterogeneous tissue development since these gradients often carry essential spatial information for polarised developmental processes. During development, from the zygote single-cell stage to a fully developed individual, both biophysical and biochemical gradients could play roles at different spatial scales.

In the following sections, both physical and biochemical gradients will be introduced, with the main focus on biochemical gradients since their recreation was the main focus of the current research.

1.2.1 Biophysical Gradients

Biophysical gradients are defined as the continuous change of physical properties within a tissue. These properties include porosity, topology, rigidity, extracellular tension, and electrostatic potential [16, 19]. Physical gradients contribute to tissue development, in which the presence of a physical gradient can alter the differentiation outcome. During tissue development, undifferentiated cells are subjected to the biophysical stimulus from their residing ECM. For example, stiffness and elasticity modulus of the ECM can have a subtle effect on cell morphology and metabolism [18]. In the context of tissue engineering based on stem cells, a biophysical stimulus is even more important due to its effect on the differentiation fate of stem cells. Different reports have shown that stem cells exhibit lineage-specific differentiation when the stiffness of the culture substrate matched the corresponding native tissue. For example, depending on the elasticity of the matrix, mesenchymal stem cells

(MSCs) could differentiate into neurogenic, myogenic or osteogenic cell lineages [20]. It is hypothesised that the biophysical properties of the substrate regulate the differentiation outcome through the changes of cell shape and the creation of cytoskeletal tension [21]. However, most of the studies investigating stem cell response to substrate stiffness were carried out in a static setting, while the physical properties are actually spatially and temporally varied in tissues. For instance, spatial stiffness gradient is present at the osteochondral interface while the temporal stiffness gradient is present during epicardial tissue development [22]. Consequently, the stem cells response should be investigated using the model system with temporal and spatial biophysical gradient.

Several studies have investigated the effect of the biophysical gradient and the differentiation outcome. A study carried out by Tse *et al.*, demonstrated the importance of this dynamic gradient by culturing MSCs on top of the polyacrylamide substrate possessing stiffness gradient. In the report, it was shown that durotaxis (*i.e.,* directed migration in response to stiffness gradient) was triggered when a physiological relevant stiffness gradient was present. In the same study, in addition to cell migration, a differentiation tendency toward the myogenic lineage was also observed. Interestingly, these alterations were not observed in the substrate without stiffness variation, suggesting that the physical gradient is a crucial regulator of MSC behaviour [23]. Aside from the stiffness gradient, other biophysical characters such as porosity gradient could also affect tissue development. A study carried out by Di Luca *et al.*, demonstrated that a 3D-printed scaffold with porosity gradient (from 500 μm to 1100 μm) could have a profound effect on the differentiation fate of residing hMSCs. In the study, by mimicking the porosity gradient between the cancellous bone and the cortical bone interface, it was found the osteogenic differentiation and mineralisation (*e.g.,* alkaline phosphatase activity) were positively correlated with pore dimensions [24]. Undoubtedly, the physical gradient stimulus contributed to the tissue development, and in some cases also sculpted the final biophysical gradient of the developed tissue.

In addition to the important role in tissue development, physical gradients can also be found in mature heterogeneous tissues such as cartilage and tendon [25]. In these tissues, physical gradients are derived from the heterogeneous composition and complex architecture. Concurrently, the derived physical gradients contribute to the physiological function of these tissues. The mechanical gradient found between tendon and bone was found to play a critically important role in the smooth transmission and distribution of compressive loads through tissue interfaces [26, 27]. Similarly, the stiffness gradient found at the osteochondral interface also supported the necessary physiological function of joints [28].

In summary, biophysical gradients participate in the tissue development and contribute to the physiological function of the final developed heterogeneous tissue, and are altogether an important subset of gradients in the biological system. Although beyond the scope of this thesis, other examples for the biophysical gradients include the mineral density gradient found in the tooth [29], the gradient of collagen fibre orientation across the heart ventricular wall [30], and even the hydration gradient found across the stratum corneum layer of skin [31].

1.2.2 Biochemical Gradients

While biochemical gradients could imply to several gradients, the focus in this thesis is morphogen gradients. Morphogens are substances that trigger distinct cellular responses in a dose dependent manner. Morphogens such as chemokines and growth factors often provide positional information, which is interpreted by cells to give rise to spatial patterns. These spatial patterns can consist of cytoplasmic proteins within a cell or, in most circumstances, the secreted proteins that make up extracellular gradient across a field of cells [8]. Various morphogen gradients exist since the early stage of embryo development, and these morphogen gradients orchestrate the formation of heterogeneous tissue.

This research focuses mainly on biochemical gradients at tissue-scale, although it should be noted that there are different levels of gradients. In the following sections, gradient examples at different scales including intracellular gradients, tissue gradients and systemic gradients will be summarised. Importantly, the mechanism of gradient establishment and logic of gradients interpretation will be introduced.

Intracellular Gradients

The intracellular gradient of morphogen emerges at the very beginning stage of the life and participates in essential cell metabolism processes such as mitosis. The establishment of the intracellular gradient is thought to arise by diffusion from a point source of a morphogen. Here, two examples of intracellular gradients are given.

(A) Gradients in the embryo

Gradients play an essential role since the embryonic stage of life. For example, within the single-cell *Drosophila* embryo, bicoid gradient is present. While different genes are transcribed at different levels based on the concentration of bicoid, the gradient of bicoid regulates embryonic development [8]. In a *Drosophila* embryo, bicoid protein forms a gradient across the anterior-posterior axis that patterns the head and thorax during embryo development. It was initially hypothesised that this gradient was established *via* the diffusion of bicoid protein from a point source. However, recent studies have shown that the diffusion rate of the protein is much slower than the observed dynamic of gradient formation. Alternatively, it is now proposed that the protein gradient is derived from the diffused bicoid RNA gradient.

(B) Gradients during mitosis

The gradient also plays a crucial role during the mitosis process. Intracellular gradients use intrinsic diffusion and self-feedback loops to establish stable regions of activity within the cytosol during the mitosis process [32]. During mitosis, mitotic gradients regulate several events along the mitotic spindle. Among all events, the Ran-GTP gradient and its nuclear transport receptors cascades and cargos have been greatly investigated. The concentration of Ran-GTP could provide the positional signal while it decreases away from the chromosome [16, 32]. This activity difference induced by the RAN-GTP gradient then triggers the spatial microtubule nucleation, which occurs within the region close to the chromosome, while the spindles form around. Accordingly, the RAN-GTP gradient is essential for self-organisation of microtubules into a bipolar spindle for successful mitosis [33].

Tissue Gradients

While the intracellular gradient is crucial in a single cell, extracellular gradients dominate the later stages of embryonic and tissue development. The extracellular gradient formation mechanism is challenging to investigate due to the difficulty of detecting soluble protein in low concentrations. In recent years, the breakthrough in fluorescence tagging and imaging techniques enables the real-time tracking of morphogen gradient in unfixed tissues [8]. While simple diffusion from a point source acts as the primary mechanism for intracellular gradient establishment, it is usually rare for a simple diffusion event to be the main mechanism behind extracellular gradient establishment [34].

In most cases, aside from diffusion, other factors also participate in the formation of the extracellular gradient. For instance, the strong affinity between secreted morphogens and their receptors constrains the free diffusion, and hence influences the final gradient pattern [8]. In addition to this interaction, receptors that participate in the process either stabilise motif on the cell surface or target them for endocytosis and the following lysosomal degradation. Proteins on the cell surface or in the extracellular matrix could also participate in the gradient formation process by either hindering or enhancing morphogen transportation [35, 36].

Because different morphogens have their distinct biophysical and biochemical properties, the gradient formation cannot be fully explained *via* a single mechanism. Based on the comprehensive review by Christian, aside from simple diffusion, four main gradient formation mechanisms can be summarised [8]. Interestingly, most of these gradient formation mechanisms are closely related to the interaction between morphogens and other molecules in extracellular space. It should also be noted that a single morphogen might utilise different binding partners to promote the diffusion. Similarly, a binding partner may simultaneously participate in the transportation of several morphogens [8]. Here, the main mechanisms of gradient formation are summarised.

(A) HSPGs mediated gradient formation

Heparan sulphate proteoglycans (HSPGs) comprise a protein core to which glycosaminoglycan (GAG) chains and heparan sulphate (HS) are attached. There are three major classes of HSPGs: glypicans, syndecans and perlecans [8]. HSPGs have been investigated for their critical role in the transportation of several developmental morphogens including Hedgehogs (Hh), Wnt ligands (Wnts), fibroblast growth factors (FGFs), and bone morphogenetic proteins (BMPs) [37].

While the importance of HSPGs in establishing morphogen gradients has been well recognised, the mechanism by which they do so remains elusive. In general, it is hypothesised that HSPGs help the establishment of the gradient by promoting the stability of morphogen once bound. This then affords them time to diffuse away from the source prior to its degradation or aggregation [38]. Through the help of HSPGs, the morphogen could also be moving down its concentration gradient by being passively displaced from GAG chains closer to the source to more distal cells. Alternatively, a mechanism was discovered to allow the "jumping" of HSPG-bound morphogen between cells. In this "jumping" event, the protein linker (glycosyl phosphatidylinositol, GPI) between the cell membrane and the HSPGs-morphogen complex was released by the help of phospholipase or directly transferred between the plasma membrane to the adjacent cells [39].

(B) Lipid mediated gradient formation

Lipid-containing vehicles assist in the transportation of some classes of morphogens required by lipids post-translational modification. Classes of the morphogens such as Wnts require lipid modification for being active [40]. However, lipid-modified proteins must acquire a soluble form in order to travel by diffusion.

One strategy to become water soluble is by folding the lipid moiety in the core while hydrophilic residues expose outside [41]. To become water soluble, another proposed solution is to transport lipid-modified morphogen within a class of vesicles consisted of the membrane bilayer. This class of vesicles, called extracellular vesicles, are then released during exocytosis and start to diffuse to the distal cells [42]. Another class of particles known as lipoproteins have also been shown to assist the morphogen gradient formation. In this case, morphogen proteins co-fractionate with lipoprotein particles, and the reduction in lipoprotein levels causes a loss of long-range but not short-range gradient signalling. In a study carried out by Panakova *et al.*, it was found that within the *Drosophila* larvae with a reduced lipoprotein production, the Hedgehog protein could only deposit at its site of secretion, and a proper morphogen gradient was unable to be established. Consequently, embryonic development was impaired [43].

(C) Transcytosis mediated gradient formation

More recent data shows that transcytosis – consecutive rounds of exocytosis and endocytosis – operates as a mechanism to generate a robust and stable gradient in the development of *Drosophila's* wing disc [44]. This mechanism also has the advantages of tackling the difficulties that come with some insoluble proteins (*e.g.*, lipid-modified protein) being unable to freely diffuse within the extracellular matrix.

(D) Cytonemes mediated gradient formation

A more sophisticated way for morphogen gradient formation is *via* the assistance of cytonemes. Cytonemes are thin actin-based filopodial channels that bridge multiple cells. After formation, these channels let membranes from non-adjacent cells link into close apposition with morphogen secreting cells [8]. Two possible mechanisms for gradient formation are hypothesised. First, the morphogens are released from signal sending cells and then bind to the receptors located on the filopodial channels. This binding then triggers the second messenger to travel along the cytoneme to reach the distally located targets. The signal decays during transportation, and hence generates a gradient of activity. Second, instead of the transportation of the second messenger, the morphogen-receptor complexes are transported to the cell body of the distal cells.

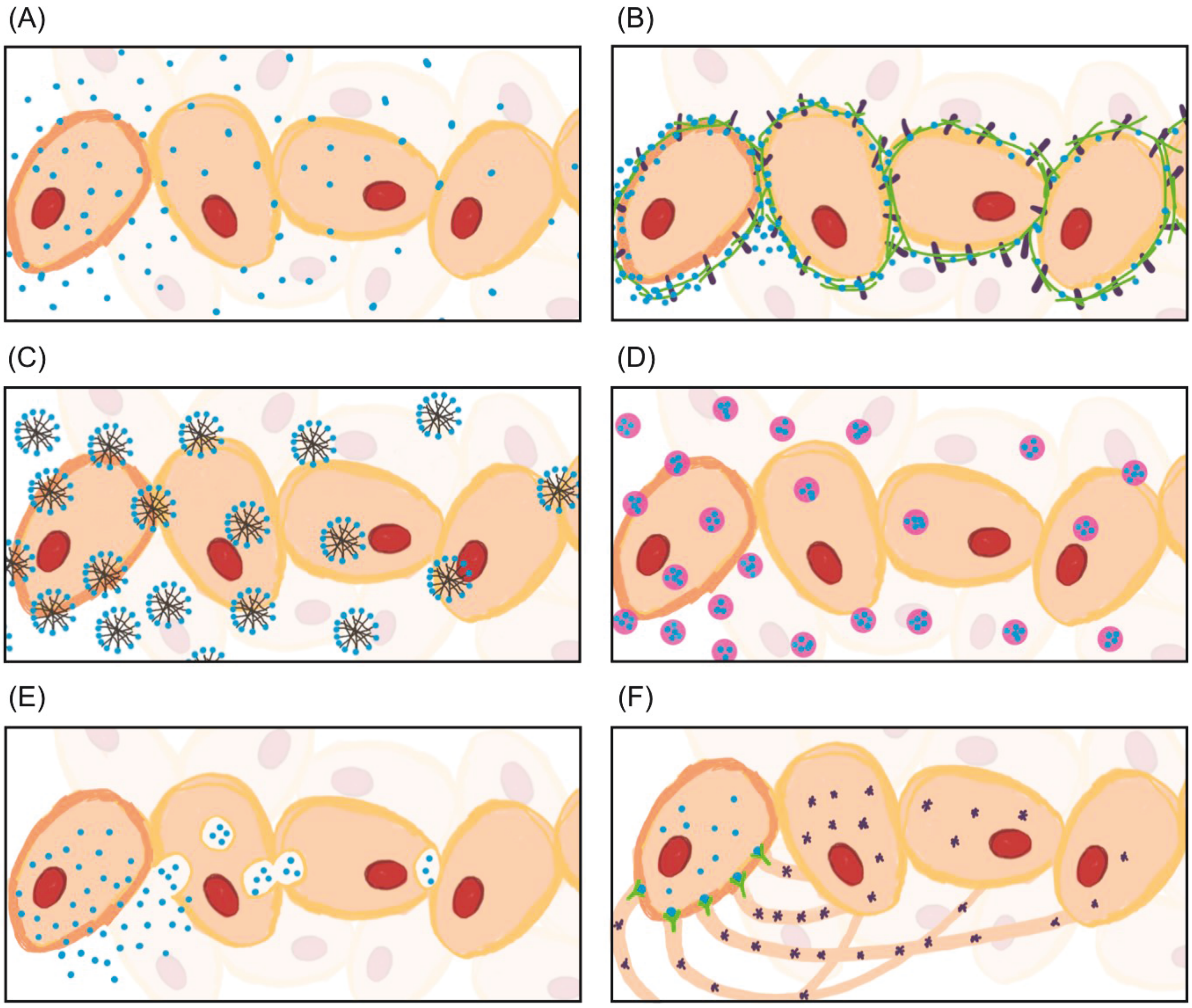

Figure 1.1 Different morphogen gradient formation mechanisms

The gradient of the morphogen (light blue) could be formed by (A) a free diffusion or (B) intermediate by interactions with HSPGs (HSPGs on the surface of cells in green). (C) Lipid-linked morphogens could become water-soluble by forming micellar-like structure in which lipids are folded inside. (D) Alternatively, they could be transported by encapsulated within extracellular vesicles or lipoprotein particles (in purple). (E) The morphogen gradient could also be derived from the mechanism of transcytosis. Through this mechanism, even a more hydrophobic morphogen could be actively transported between cells. (F) In the mechanism of cytonemes, morphogens bind to the receptors (in light green) and activate second messengers (in dark purple), which can then traffic to the distal cells. Reproduced from Christian et al. [8].

Systemic Gradients

Besides the morphogen gradients present during heterogeneous tissue development, gradients are also found across different tissues and organs of a developed individual. Several systemic gradients can be found *in vivo*. Chemotaxis is a classic example of systemic biochemical gradients in which cells migrate along the concentration gradient of chemoattractants [45]. Examples of chemotaxis include the migration of leukocytes toward inflammation site, movement of fibroblasts during wound healing, and the process by which axons find their synaptic partners. In each case, the gradient of chemoattractant activates spatially polarised cellular signals, and eventually induces the cell movement toward the area with the highest chemoattractant concentration. The systemic gradient could also be applied in the context of tissue engineering; for example, systemic stromal-derived factor-1 (SDF-1) gradient could be used to direct bone marrow stem cell movement *in vivo* [46].

1.3 Biochemical Gradients and Development

Biophysical gradients could be determined quantitively. For example, elastic modulus of rat myocardium can be measured using an atomic force microscope [47], and compression modulus of cartilage can be measured using a universal testing machine [48]. For biochemical gradients, quantifying morphogen concentration *in vivo*, however, is not straightforward. In most studies focusing on physiological gradients characterisation, imaging technique such as fluorescence *in-situ* hybridization (FISH) or confocal microscopy combined with genetically encoded fluorescent probe was used [49, 50]. In these approaches, only the relative rather than the absolute concentration of a specific morphogen (or its downstream signalling protein) can be visualised. Moreover, most of the *in vivo* imaging techniques are based on model organisms such as *Danio rerio* and *Drosophila* [51, 52]. Biochemical gradients play a crucial role in development process. Intracellular morphogen gradients have pronounced roles in embryonic development, extracellular gradients become more important after the single-cell stage. In this section, the relationship between gradients and tissue development will be reviewed.

During the tissue development process, the initial naïve cells transform from homogenous into heterogeneous cell populations and form the organised arrangement. The patterning of mammalian tissues is governed by morphogen gradients including hedgehog (Hh), transforming growth factor-β (TGF-βs), fibroblast growth factors (FGFs), bone morphogenetic proteins (BMPs), and Wnt ligands (Wnts) [53]. The extracellular gradient of a morphogen signal is often established from an initially localised protein and followed by the complex gradient formation process in which the protein is spatially redistributed. Since different levels of morphogen concentration bring the variance in cell signalling and different differentiation fates, morphogen gradients across the field could support the formation of organised tissues [8, 13, 26].

However, the formation of extracellular morphogen gradient is only the beginning. To develop heterogeneously, cells within the gradient field must interpret the morphogen gradient and ultimately translate this information into qualitatively distinct gene responses [8]. In other words, the interpretation of the morphogen gradient is the essence of the development of multicellular organisms. In this section, the generalised rules will be summarised [10].

Role of morphogen concentration

The first general rule for the gradient interpretation is that morphogen governs the target genes in a dose-dependent manner [8]. Morphogen concentration in the extracellular matrix space is often found to be directly proportional to the activity of the downstream transcription factors. In some class of morphogen, it is shown that the individual cell response toward the morphogen gradient is based on the absolute number of occupied morphogen receptors on the cell surface. For instance, Dyson *et al*. demonstrated that *Xenopus* blastula cells could sense the number of occupied activin (a morphogen) receptor, with the absolute number of occupied receptors rather than the ratio of occupied to unoccupied receptors activating the morphogen-regulated genes [54].

In some cases, the response triggered by different morphogen concentration scales exponentially rather than linearly, with small morphogen concentration changes becoming non-negligible. In vertebrates, a 2 to 3 fold difference in Sonic hedgehog morphogen concentration is sufficient to trigger 25 to 50 fold difference in response, which could lead the cell into a different fate [55].

These rules are not exhaustive in more complicated systems. Some class of morphogen receptor complex can trigger multiple intracellular signal transduction routes. In this circumstance, ligand could only be used to determine a qualitative change rather than predict an exact level for any single transcription factor [8].

Memory of cells

The extracellular gradients are usually transient and dissipate over time. However, the cells in the field continuously perceive the morphogen gradient, with spatial information becoming internalised into a cell’s memory even without the presence of extracellular morphogen gradient. In a study carried out by Jullien *et al.*, it was shown that the cell memory could be attributed to the prolonged residence of a signalling complex in the endo-lysosomal pathway. Specifically, this "memory" can last till the morphogen-receptor complex is transferred to lysosomes, in which the degradation of the signal will take place [56].

Number of thresholds

To meet the definition of being a morphogen, a graded signal must be able to lead the generation of at least two distinct gene expression profiles. In other words, a low concentration can lead to one profile and a high concentration can lead to another (in this instance, the graded signal leads to the generation of 2 distinct cell types, so the threshold value is 2). While the empirical observation has typically demonstrated between 3 to 7 thresholds, theoretical analysis has revealed the possibility that the gradient can lead to up to 30 thresholds [10]. There is always more than one component in the system, that is, when cells interpret the gradient of a specific motif, additional signals from other factors are believed to also contribute to some of the threshold response. Whether an independent morphogen could also produce the same number of the observed threshold is difficult to resolve experimentally.

Logic of interpretation

After perceiving the morphogen gradient, the level of a downstream transcription effector in the cell is determined. Although the gene response to transcription factor concentration remains to be fully resolved, three basic rules are thought to apply:

(1) In principle, low-affinity binding sites on promoter will only be occupied when the concentration of the related morphogen is high. In contrast, for high-affinity binding sites, they will be occupied throughout the field of the gradient.
(2) Cell response is based on both positive and negative inputs provided by transcription factors triggered by a morphogen gradient.
(3) The gene activated by a morphogen gradient could later affect the overall response. For example, a positive feedback circuit could be created.

Apart from these general rules, it should also be noted that in most of the tissue development process, there are usually more than one overlapping morphogen gradient. With inputs from all the signal gradients, the cells can then generate sophisticated feedback circuits and the possible secondary overlapping gradients of transcription factor eventually leads to the development of heterogeneous tissues.

1.4 Engineering Gradients

As previous sections summarised, both physical and biochemical gradients play an essential role during cell differentiation and hence shape a tissue's final heterogenous architecture (*e.g.*, bone and cartilage interface [14]) and spatial polarisation (*e.g.*, ventral and dorsal side of central nervous system [13]). To produce a more biomimetic tissue, one must consider the numerous gradients present in native tissue, including transitions in biochemical composition (*e.g.*, extracellular matrix, soluble growth factors) and physical environment (*e.g.*, stiffness, topography). Despite the important role of gradients, most of the *in vitro* engineering strategies use uniform scaffolds and homogeneous growth factor delivery to produce homogeneous tissue constructs. However, these homogeneous constructs are often functionally inferior and fail to recreate the complexity of heterogeneous structure in natural tissue. Accordingly, intensive effort has been invested in designing materials with well-defined gradients.

It is clear that more sophisticated fabrication processes are required to replicate the native complexity. Strategies that seek to engineer tissues *in vitro* must strive to recreate these natural gradients in order to produce fully functional grafts or physiologically-relevant models. In the following sections, biochemical and physical gradients fabrication approaches are discussed.

1.4.1 Gradient Fabrication Strategies

Layering and sequential deposition

To fabricate spatially patterned constructs, one of the most common methods is to sequentially combine or deposit layers of materials on top of another. As a result, gradients such as biochemical composition or mechanical property could be fabricated. While the principle itself is straightforward, it can be transformed and combined with other technologies. Here, several approaches utilising this principle will be introduced.

A. Combining layers

Various approaches have been applied to create layered constructs. Among all these approaches, the most intuitive approach is to combine distinct layers together with an adhesive. For instance, biphasic osteochondral scaffolds composed of PLGA/PGA layer and calcium phosphate substrate were prepared by combining two layers with a small amount of solvent [57]. Constructs possessing distinct layers can also be fabricated without the use of an adhesive with several other approaches. For example, with the "iterative layering freeze-drying" process, additional layers of material could be attached to a porous base material by a fabrication protocol having more than a single lyophilisation process. Specifically, the new layer of liquid material was added on top of the hydrated lyophilised porous base prior to the sequential lyophilisation process [58]. In addition to sequential freeze-drying process, to combine layers of materials, controlled polymerisation chemistry could also be used. Nguyen *et al.* demonstrated a sequential polymerisation platform in which layer by layer stacking of materials was achieved by repeatedly triggering the polymerisation process after each layer of monomer materials was added on the previously polymerised layer [59].

Creating gradient constructs by directly combining different layers is a straightforward and facile strategy. Gradients of various materials could be cast using this strategy with suitable chemistry. However, one of the concerns of these multilayered scaffolds is the risk of delamination, which is due to layered constructs consistng of material layers with different properties. Consequently, the mechanical properties mismatch at the interface between adjacent layers will lead to delamination. To prevent disintegration of the construct, a buffer region with a finer transition of the material's property could be cast between the layers possessing the properties mismatch [60]. Since the strategy is to combine distinct layers of material, the other limitation of the strategy is that it can only produce a discrete, step-wise transition rather than a continuous gradient. This makes the strategy unsuitable for applications trying to emulate physiological gradients, which are usually a continuous transition in nature.

B. Deposition and 3D printing

Under a similar rationale, sequential deposition of the extruded fibre could also create constructs with spatial patterns. In 2004, Woodfield *et al.* demonstrated a computer-controlled extrusion platform capable of creating a 3D spatial pattern. By varying the composition of materials and geometry of the fibril deposition, both porosity and composition gradient could be patterned within the constructs [61].

With the advancement of 3D printing in tissue engineering, the concept of sequential deposition has also been applied. By designing the appropriate structure, pore size gradient could be fabricated using the technology. For example, the porosity gradients of cartilage tissue engineering scaffolds can be fabricated [62]. Other physical character gradients such as stiffness gradients could also be achieved by changing printing parameters through varying fibre thickness or crosslinking degree (*e.g.,* by altering the intensity of the UV in stereolithography) [63]. In addition to physical gradients, 3D printing has also been used to generate biochemical gradient. When using an inkjet 3D printing system, the formation of biochemical gradients could be achieved by combining more than one ink tank. In a recent study by Liu *et al.*, up to 7 different bioinks were connected using capillaries system into a single print head. By controlling pressure applied to these capillaries, a desired formula mixture of bioinks could be printed and gradient patterns be created [64].

Although providing a highly spatial control, fibre extrusion and 3D printing are still only capable of creating discrete rather than continuous gradients. The "printability" of 3D printed material should also be considered; while printability is closely related to viscosity and surface tension (especially in ink-jet, hydrogel-based bio-printers), many materials in hydrogel applications are actually unable to be printed without further modification of the material and extensive optimisation of the printing protocol [65].

C. Gradient maker

Through using the commercially available "gradient maker", high control over compositional changes can be established in both 2D and 3D constructs. Using sequential deposition, two or more different liquid materials are kept in separate reservoirs, with their outflows combined into a jointed outlet which then injects the mixed material into a mould. By controlling different outflow rates from two or more reservoirs during the course of casting and the vertical movement of the mould, the gradient of biomolecule concentration can be produced along the z-axis [66].

A mechanical gradient can be cast using the gradient maker. Nemir *et al.* have demonstrated that by using a two photo-initiator doped poly(ethylene glycol) diacrylate of different molecular weight, a gradient of injected materials can be locked into place by crosslinking with UV light [67]. In addition to physical gradients, biochemical gradients can also be achieved by the incorporation of an extra intermediate. By encapsulating in or absorbing on carriers such as PLGA microspheres, the gradient maker can be used to create growth factor or ECM gradients [68, 69].

With the gradient maker, centimetre range gradients can be generated in a reasonable period of time. However, given that the structure of the final construct is defined by a simple deposition of injected materials, it is difficult to create constructs with a complex structure.

D. Electrospinning

Besides 3D printing and the gradient maker, the concept of sequential deposition could also be combined with other platforms such as electrospinning [70]. Electrospinning is a facile and economic technique that uses electrostatic forces to generate fibrils with a dimension ranging from nanometres to microns. To create composition gradients, an electrospinning platform equipped with more than one material reservoirs can be used. Several studies have demonstrated the capability of electrospinning in gradient casting. By sequentially altering material inlet between reservoirs loaded with different materials, a fibril mesh with composition gradient can be deposited on a movable collector [71, 72]. Aside from biochemical gradients, electrospinning could be used to generate heterogeneous fibril architecture. Using a sequential electrospinning process, McCullen *et al.* fabricated a trilaminar scaffold in which both the materials concentration and collecting condition for fibril were varied to create constructs with heterogeneous fibril architecture [73].

While being the most commonly used approach to create fibril structures, the electrospinning process could not easily produce thick mesh substrates with gradients in the millimetre range. This is due to the surface charge build up during the electrospinning process. It has been shown that the charge builds up at the collected mesh and can hinder the further growth of fibril mesh thickness [74].

Diffusion

Molecular diffusion from the source in the space is a thermodynamically favourable process. Using this basic phenomenon, continuous gradients can be fabricated. Dodla and Bellamkonda placed an agarose hydrogel between two different medium reservoirs with one of them containing laminin-1; a gradient of laminin-1 concentration within the agarose hydrogel between two reservoirs was subsequently created [75]. By applying the scaffold to a reservoir of different geometry, different gradient patterns could be created after the diffusion process. For example, when dipping part of the scaffold into a soaked paper reservoir, a longitudinal portion gradient was created. Alternatively, when the reservoirs were applied around the scaffold, proteins diffused from the lateral walls of the scaffolds and resulted in a radial gradient pattern [76].

Aside from being used as the gradient cargo itself, the diffused molecule could be used to create other gradient features. A facile protocol using gas diffusion was used by Yang *et al.* to generate polydopamine gradients on the substrate [77]. Specifically, by tilting and immersing the substrate into a reaction solution (*i.e.*, increasing distance between solution/air interface and the substrate along the longitudinal axis), an oxygen concentration gradient along the longitudinal axis of the substrate surface was established due to a different distance for oxygen diffusion. This oxygen gradient at the substrate eventually led to a different rate of polymerisation and hence the fabrication of a longitudinal gradient of polydopamine on the substrate.

In contrast to step-wise gradients created by layering and deposition, this simple and classic approach can create a continuous gradient. However, the scale of the created gradient is often limited in micron-metre range. Approaches relying on diffusion are also time-consuming. Since crosslinking of the hydrogel is required to preserve the established gradient, the long duration of gradient formation *via* cell-laden hydrogel tissue engineering will be a major issue due to the prolonged exposure of cells under fabrication [78].

Adsorption and dipping/filling

Aside from diffusion, the adsorption of molecules to the substrate could also be used to create gradients with the control of the immersion time of cargo and substrate. One of the first examples of this strategy was reported in 2008 by Phillips *et al.* [79]. In the report, gradients of different molecules were precisely coated in a spatial control manner using a motorised dip coater. By controlling the dipping time and speed, a gradient of poly-lysine was formed on the collagen scaffold. This mechanism is commonly employed to control the density and thickness of the coating in industrial applications. The same principle is applied in a similar method proposed by Shi *et al.* whereby a homemade "filling" device was built to deposit protein molecules to the electrospun fibre matrix. By vertically placing the matrix in the tank and filling it with a protein solution at controlled speed, the different level of matrix was immersed in reaction solution for different durations [80].

This simple and straightforward approach can create a continuous gradient. Unlike the micro-metre range gradient in a diffusion-based strategy, the platform could also prepare centimetre range gradient in a reasonable period of time. However, since an effective adsorption is needed to create gradients, a proper chemistry modification on the surface is needed to facilitate the binding of cargos [79].

Convection

Aside from diffusion and absorption, other natural phenomena could also be used to create gradients. Du *et al.* have demonstrated a fluid convection-based approach to create various gradients within a fluid channel. Using a fluidic shear-driven stretching process known as convection, the particle in the centre of the channel moves faster than the particle closer to the channel's wall, with a gradient forming in the laterally averaged concentration profile. In the same study, it was also found that the difference between the moving rates of particles at the centre and periphery was proportional to the maximum channel velocity, which meant that a different gradient pattern could be established by varying the flow velocity [81]. Convection could produce centimetre range gradients of small molecules, microspheres, cells and materials in a much shorter time frame than diffusion. However, the process requires a fluid channel and pump system.

In addition to convection arising from the flow within the fluidic channel, the convection process of a different mechanism has also been used to create gradients. Canadas *et al.* demonstrated an approach using temperature difference to generate convection for microparticles gradients. Two hydrogel precursors at different temperatures were prepared, with one of them was premixed with microparticles. By subsequently injecting two precursors into a mould, a convection flow was established between the two materials due to temperature difference. This process resulted in the redistribution of the materials and microparticles, with the microparticle gradient then preserved by triggering the gelation of the materials [82]. While there is no need for a fluidic system using this approach, it is more complicated to control the established gradient pattern.

Microfluidic device

Aside from inducing fluid convection, a microfluidic device can also be used as a mixing platform to create gradient patterns. Specifically, geometric expansion or a tree-like structure of the channel layout could lead to several outlets (usually more than 10) from a limited number of initial inlets (usually less than 3). The technology could be used to create physical gradients. Zaari *et al*. created stiffness gradients with a tree-like microfluidic channel from polyacrylamide tanks with 2 different levels of crosslinker doping [83]. Aside from simply creating materials gradients, the technology could also produce patterns of cell gradients. Mahadik *et al.* included cells within the microfluidic channel and created hydrogels with opposing gradients of two different cell populations [84].

To pattern gradients with this approach, a strategy to preserve the gradient is crucial or the gradient will disappear after the source of the flow is switched off. Accordingly, a material that reacts to gelation trigger is favoured [83]. Importantly, in order to be a strategy that utilises mixing, the created hydrogel could possess continuous gradients as opposed to discrete, step-wise gradients.

Centrifugation

Physical forces can also be used to create gradients. Oh *et al.* have proposed an approach that creates gradients *via* centrifugal force. In this centrifugal force driven platform, polycaprolactone (PCL) fibrils were incorporated within a cold thermosensitive Pluronic F127 hydrogel at its liquid state. The PCL fibrils/Pluronic F127 mixture solution was then filled into cylinder mould and centrifuged. During the centrifugation, the PCL fibrils were redistributed along the cylindrical axis due to the gradual increment of the centrifugal force and formed a density gradient. The final mixture solution with a PCL fibril gradient was then heated above the melting temperature of PCL to bond the PCL fibrils in contact. Finally, the Pluronic F127 was removed by washing the construct extensively in cold water [85].

Using this approach, both the porosity and the surface area gradient can be fabricated. The generated PCL fibrils gradient is also highly correlated with its surface area. By modifying the surface chemistry of the created fibril network, biochemical gradient could be created in parallel by conjugating cargo on the surface of the fibril network [86]. Indeed, the strategy provides a facile approach to generate polymer gradients, although it requires an intermediate fibril carrier and cannot easily generate gradients between components with a similar density.

Photopolymerisation / photopatterning

Light is a useful tool in gradient fabrication. For materials that can be ultraviolet crosslinked, graded UV exposure across the hydrogel prepolymers could generate hydrogels with stiffness gradients. To achieve the graded exposure of UV, different approaches can be used. For example, a movable photo-mask can be applied to control the UV exposure time across the hydrogel [70, 87]. Alternatively, a fixed photomask printed with a greyscale gradient could also be used to shield the UV light in a graded manner [23]. In addition to stiffness gradients, light can further be used to create biochemical gradients. In a system where the cargo can conjugate to the substrate under UV exposure by sliding a photomask over a substrate due to a different UV exposure time, protein gradients can be prepared [88]. Aside from creating continuous gradients, a photoreactive hydrogel system could also be combined with a high-resolution confocal laser to create precise spatial patterns [89]. While the approach could create both centimetre range gradients and micro-metre range spatial patterns, it usually requires that materials used in the system to possess certain chemical functional groups, or that a photo-initiator is incorporated into the final system.

Freezing protocol

During the fabrication process, different environmental parameters such as temperature could be used to create gradients. Vlierberghe *et al.* have demonstrated that pore size gradients can be achieved by tuning the cooling temperature gradient during the cryogenic process prior to lyophilisation. In the study, a customised cooling device was assembled to establish a temperature gradient between the top and bottom of the mould during the freezing step. It was found that a higher temperature gradient across two-ends of the mould could facilitate the pore size gradient along the long axis of the scaffold [90].

In some occasions, when material could respond to temperature through phase transformation, a cooling protocol with temperature fluctuation can be used. Oh *et al.* showed that a stiffness gradient can be produced on polyvinyl alcohol (PVA) hydrogel by using a gradual freezing-thawing protocol. In brief, the aqueous solution of PVA was added into a cylinder mould with its bottom in contact using a liquid nitrogen tank, and the PVA solution was gradually frozen from bottom to top. After the solution was fully frozen, it was allowed to thaw completely. After 10 freeze/thaw cycles, a higher crystallisation degree of PVA at the bottom could support a higher stiffness modulus and form the stiffness gradient [91]. However, it should be noted that rather than creating biochemical gradients, the approach is mostly used for physical gradients fabrication.

1.4.2 Criteria for Ideal Gradient Fabrication Strategies

Both biochemical and physical gradients are crucial in defining the morphology, behaviour and differentiation of cells. In the previous section, several approaches for gradient fabrication were reviewed. While each approach has its own merits and disadvantages, the criteria for ideal gradient fabrication strategies in the context of tissue engineering are now summarised.

A. Facile methodologies for gradient preservation

An ideal gradient fabrication technology must allow the patterned gradient to be preserved after the removal of the gradient driven force (*e.g.,* the flow in microfluidic-based approach or centrifugal force in centrifugation approach). In general, the main principle of the stabilisation is to crosslink, polymerise or solidify the materials carrying the decorated gradients [70]. To design a proper stabilising approach, the material used in the system must be considered carefully. For example, the gelation of a thermosensitive hydrogel such as agarose or photoresponsive hydrogel such as gelatin-methacyloyl (GelMA) can be triggered after the gradient is established *via* temperature change and UV exposure, respectively [92, 93].

In a gradient platform generating cargo gradient, in addition to the crosslinking of the substrate, the immobilisation of the entrapped cargo is also essential. Depending on the application, the cargo of interest could either be temporally or persistently bound to the scaffold. Strategies such as covalently binding the cargos with the substrate or physically entrapping the cargos within the hydrogel network are commonly used [92, 93]. Indeed, a facile approach for gradients stabilisation is one of the most crucial steps of all the introduced gradient fabrication strategies.

B. Spatial resolution and design flexibility of the patterned gradient

An ideal fabrication process should provide a certain level of spatial resolution. The resolution of the gradient in a microsphere-based gradient maker is restricted to the radius of the microsphere used in the design. By contrast, the photo-patterning approach based on the confocal system could support a higher resolution of the gradient pattern. It should also be noted that many of the introduced technologies based on layering and sequential deposition (*e.g.*, combining layers and 3D printing) could only support the formation of "discrete gradient", *i.e.*, the gradient is not continuous but rather has a step-wise transition. However, in certain *in vivo* applications, a continuous gradient is more favourable. Under this condition, technologies supporting the formation of the continuous gradient should be used. Diffusion, dipping/filling, or microfluidic systems are capable of creating continuous gradients.

In addition to gradient resolution, design flexibility is another criterion for defining an ideal gradient fabrication technology. In strategies such as 3D printing, a more complicated gradient pattern (*e.g.*, overlapping gradients in different resolution, non-linear or radial gradient) can be fabricated. However, the design flexibility is more constrained in approach such as centrifugation, dipping/filling or convection, in which only a longitudinal gradient can be easily generated.

C. Minimum requirements in production facilities

For being widely applicable, an ideal fabrication technology should have a minimum requirement in terms of a specialised apparatus. While many of the mentioned systems could produce gradients, most of them require a specialised or customised apparatus such as a 3D printer, confocal laser system, or microfluidic device. For both translation applications and academic research, a strategy requires a specialised platform could limit the spreading of the technology. In this sense, a fabrication technology using common lab equipment could be adopted more easily, *e.g.,* gradient fabrication approaches using a centrifuge or a UV-lamp/photomask.

An ideal gradient fabrication platform should also be user-friendly. The fabrication protocol should be easy to reproduce and be able to tolerate parameter changes. While strategies such as dipping and combining layers have an intuitive fabrication protocol, some strategies such as 3D printing and photopatterning have a rather complicated fabrication protocol and often require users to have specific training or expertise. Lastly, gradient fabrication strategies that are equipment-free are favoured. For example, gradient casting uses molecule diffusion from a point source or chemical reaction associated with an oxygen concentration gradient.

D. Applicability across different materials and cargos

While some of the introduced technologies can be tailored to apply to different gradient engineering schemes, most of them are restricted to certain parameters such as physical characters of the substrate materials. This is particularly an issue for complex fabrication procedures. When it comes to different material systems, these fabrication procedures often have constrained compatibility. For example, in 3D printing, the printability of the material greatly limits the material choice, and in photo-polymerisation approach, a photoresponsive material is required. An ideal technology should also support the formation of a wide range of cargo gradients (*e.g.*, growth factors, peptides, vectors, *etc.*). For instance, while the dipping/filling approach solely relies on electrostatic absorption, alternative approaches need to be considered for loading cargos with a neutral charge. Indeed, the compatibility of substrate materials needs to be considered while the fabrication process is sensitive to certain materials characters.

E. Potential in high-throughput and standardised production

To ensure translational applications, an ideal fabrication strategy should be scalable, high-throughput, and have standardised fabrication protocol. In industry, standardisations are the best practice, and technology must achieve good standardisation for being valuable. 3D printing technology, which has been widely applied in the industry, ensures a highly standardised and reproducible fabrication protocol. Aside from a standardised protocol, an ideal fabrication process should also be high-throughput. Strategies such as dipping and filling could allow for rapid production while a strategy solely relying on diffusion could greatly limit production throughput.

For translational applications, biocompatibility is another important criterion to be considered. An ideal strategy should allow for cells to be encapsulated during the fabrication process. However, this is not the case for strategies with a harsh fabrication protocol (*e.g.*, low temperature, high voltage, cytotoxic free radical byproducts or solvent use). In order to ensure a technology for successful translation, a well-rounded production protocol needs to be developed with consideration of multiple aspects.

1.5 Osteochondral Tissue

There remains an urgent and unmet need for a simple and versatile gradient casting method that can be universally applied to different biomaterial and tissue engineering protocols. The aim of this research is to develop versatile gradient casting platforms and use these platforms to engineer heterogeneous tissue. To investigate the translational potential of developed platforms, osteochondral tissue was engineered.

Creating robust osteochondral constructs for osteochondral lesions repair remains as one of the challenges in the field of tissue engineering. In this section, the development and properties of the osteochondral tissue will be introduced. Importantly, the gradient characters of the tissue will be illustrated. After reviewing the development and physiology of osteochondral tissue, related literature regarding tissue engineering design will be summarised.

1.5.1 Development of Osteochondral Tissue

Existing as a complex interface between bone and cartilage, osteochondral tissue is a gradient tissue located at the end of long bones [57]. Two types of osteochondral interface, articular cartilage (the hyaline cartilage that locate at the end of long bones) and growth plate cartilage (the hyaline cartilage that locate within the metaphysis), have been extensively studied [94]. Both articular and growth plate cartilage have their own distinct structural characters and have their functional roles *in vivo*. In this section, the morphogen gradient present during the development process and the various gradient features in the developed osteochondral tissue will be summarised.

The development of osteochondral tissue at long bones is depicted in Figure 1.2. Articular and growth plate osteochondral tissue are both derived from the same origin. During development, cartilage formation is one of the earliest morphogenetic events of the embryonic mesoderm. The development of the osteochondral tissue starts with chondrogenic differentiation of MSCs. This process involves the mesenchymal condensation, chondrocyte differentiation and maturation. Depending on its spatial location, mature chondrocytes could undergo terminal differentiation and become hypertrophic chondrocytes. Following the hypertrophy, endochondral ossification process could take place. During the endochondral ossification process, the chondrocytes undergo apoptosis and the extracellular space around the apoptotic chondrocytes is invaded by blood vessels, osteoblasts and osteoclasts. Eventually, these invaded cells remodel remnants of the cartilage matrix into bone tissue [95, 96].

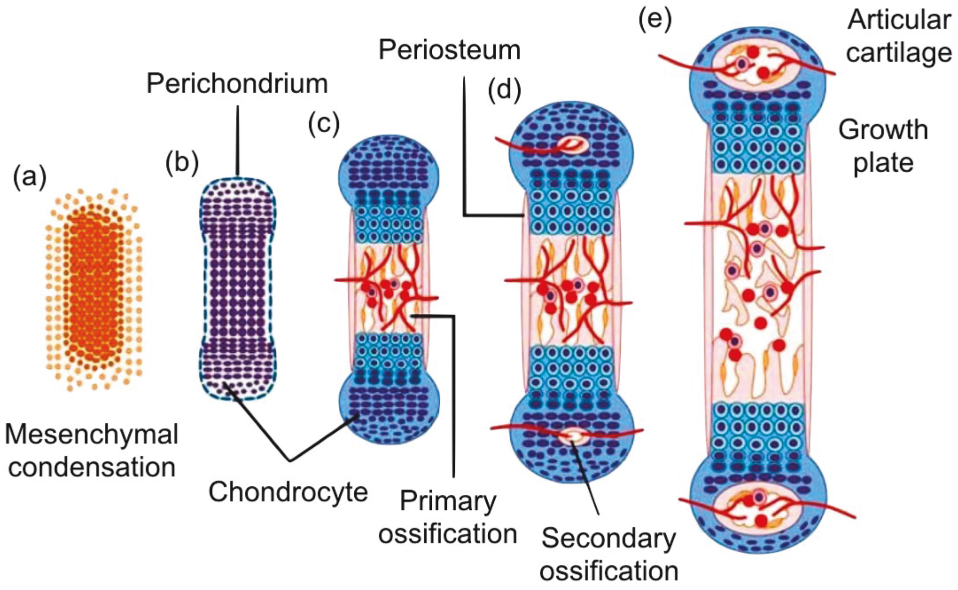

Figure 1.2 Development of osteochondral tissue

(a) Both articular cartilage and growth plate cartilage are derived from the initial condensation of osteochondroprogenitors. Within this condensed structure, cells undergo the chondrogenesis process and become primordial cartilage. (b) This primordial cartilage is an avascular cartilaginous template surrounded by the perichondrium. At the centre of the primordial cartilage, the chondrocytes undergo hypertrophy, and the ossification process takes place. (c) During the ossification process, hypertrophic chondrocytes undergo apoptosis and the matrix is calcified and invaded by microvessels. This place of the initial ossification at the diaphysis is called the primary ossification centre. (d) As the development process continues, vessels invade the epiphyses and form the secondary ossification centre. (e) After birth, the growth plate within the epiphyseal region contributes to long bone growth, while articular cartilage provides resilience and smooth movement to the joint. Modified from Usami et al. [94].

Various key molecular factors govern different stages of osteochondral development, with the process of chondrogenesis regulated *via* several factors (*e.g.*, fibroblast growth factors (FGFs), transforming growth factor β (TGF-β) superfamily, and wingless-type (Wnt) proteins) operating in concert with various transcription factors (*e.g.*, SOX9, RUNX2, and Twist1) [97]. Together with local ECM, cocktails of growth factors orchestrate the onset of differentiation at different stages of the process which eventually leads to different chondrocyte phenotypes. A general summary of main growth factors and transcription factors are shown in Figure 1.3 [96, 98]; for a more thorough overview of growth factors in different development stages, please refer to the review by Demoor *et al*.

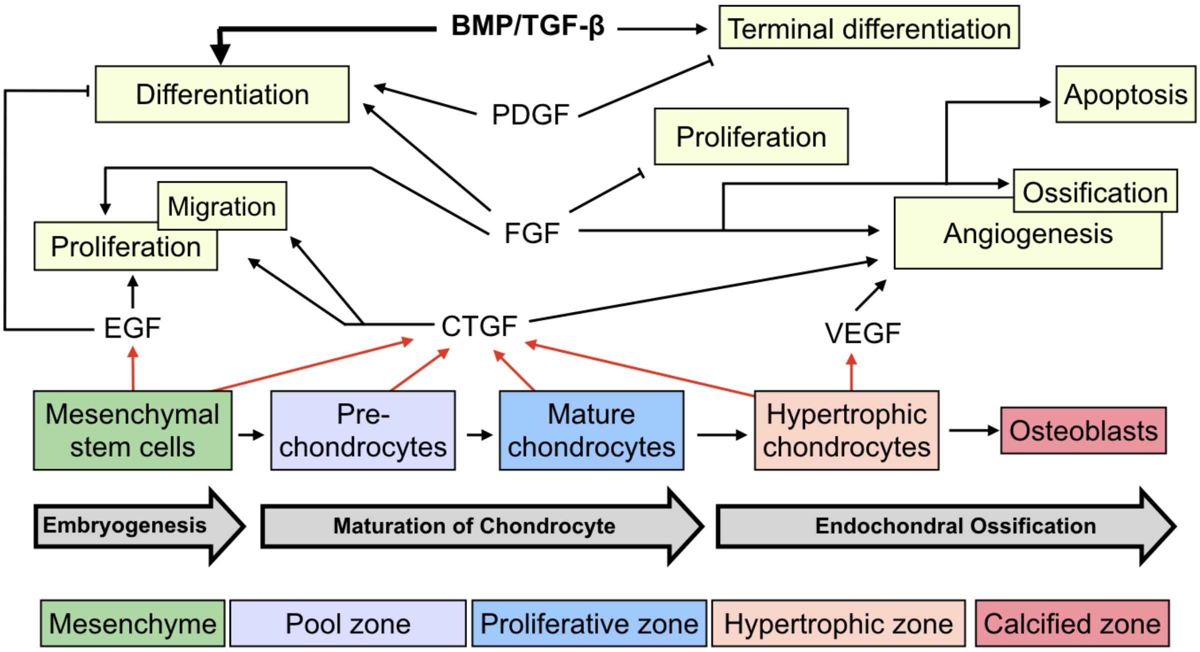

Figure 1.3 Overview of distinct roles of growth factors at different stages/location during osteochondral tissue development

The progression of cell phenotype is both spatial and temporal-dependent. Temporally, cell phenotype progress along the development process from mesenchymal condensation, chondrogenesis, hypertrophy to endochondral ossification. Spatially, chondrocytes at different zones are subjected to different morphogen cocktails, and hence the different cell profile is induced. Recently, it has been shown that hypertrophic chondrocytes can survive the endochondral ossification process and become osteoblasts [99]. Bone morphogenetic protein (BMP), transforming growth factor beta (TGF-β), fibroblast growth factor (FGF), vascular endothelial growth factor (VEGF), platelet derived growth factor (PDGF) and connective tissue growth factor (CTGF). Reproduced from Demoor et al. [98].

The development of the osteochondral tissue is a lengthy process which continues after birth. During the postnatal period, the long bones undergo axial directional growth and remodelling. During this time, the articular cartilage act as the "surface growth plate" that is responsible for the growth of the underlying epiphyseal bone [100]. During this growth, the thickness of articular cartilage decreases due to the rate of endochondral ossification in the deep layer is faster than appositional growth. In addition to the surface growth plate, the epiphyseal growth plate governs the growth of the metaphyseal and diaphyseal bone. The growing of the long bones only ceases after the puberty. Toward the end of puberty, the growth plate cartilage undergoes epiphyseal fusion and becomes part of the epiphyseal line [14, 101]. At this stage, a mature osteochondral tissue at the end of the long bone is fully developed.

Structurally, both osteochondral interfaces have distinct zones during development. Growth plate cartilage exists before long bones are fully developed. Growth plate cartilage locates in the metaphysis of the long bone. From epiphyseal side (end of the long bone) to diaphysial side (middle of the lone bone), growth plate cartilage can be categorised into: (1) the resting zone (2) the proliferative zone, (3) pre-hypertrophic zone, and (4) hypertrophic zones (Figure 1.4 A). In developed articular cartilage, from cartilage surface to bone, it can be categorised into (1) the superficial zone, (2) the middle (transitional) zone, (3) the deep (radial) zone, and (4) the calcified zone. There is no clear margin between these zones with the exception of the tide mark that appears as a clear margin between the deep zone and the calcified zone. Beneath the calcified zone, subchondral bone bridges the cartilage to the long bone [96] (Figure 1.4 B).

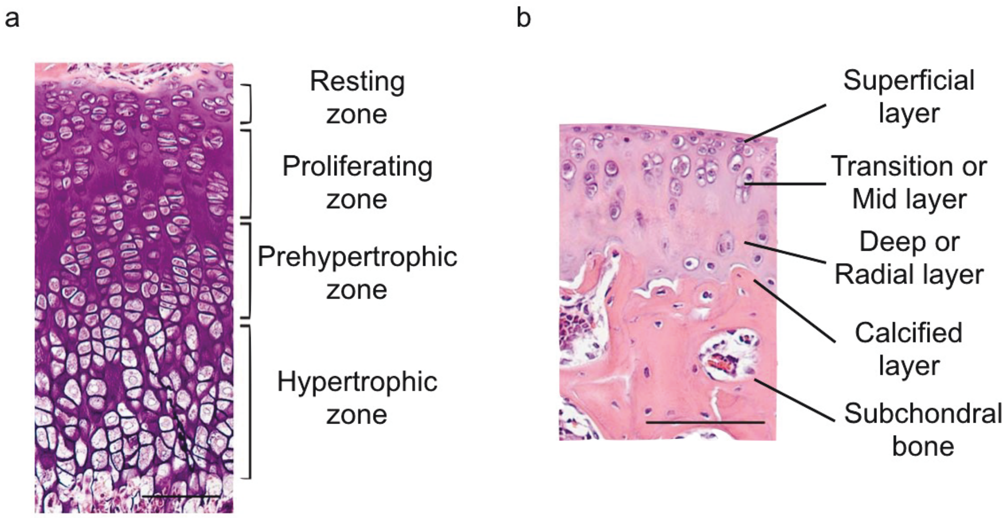

Figure 1.4 Distinct zones of osteochondral tissue

Prior to the full development of the osteochondral tissue at long bones, both articular and growth plate cartilage are present. (a) Growth plate could be categorised into several morphologically distinct zones: resting zone, proliferating zone, pre-hypertrophic zone, and hypertrophic zone. (b) In the developed articular cartilage, superficial layer, transition or mid layer, deep or radial layer, and calcified layer could be categorised. Scale bars = 100 µm. Modified from Usami et al. [94].

1.5.2 Morphogen Gradients During Osteochondral Development

From the initial condensation through to postnatal development, numbers of morphogen gradients participate in the development of osteochondral tissue. Several axial morphogen gradients, which distribute along the direction from subchondral bone to cartilage surface, are believed to be crucial for the formation of osteochondral tissue. While different extracellular matrix components are secreted along axial morphogen gradients, the secreted extracellular matrix could further participate the formation process by acting as a reservoir of growth factor [17]. In this section, morphogen gradients during osteochondral tissue development will be introduced.

Morphogen gradients are present at the growth plate cartilage. Within the growth plate cartilage, cells at different zones are subjected to spatial and temporal changes of several morphogen gradients (Figure 1.5). These local differences of morphogen concentration produce a spatial variance in cell signalling, which can lead to distinct cell phenotypes across the tissue (*e.g.,* osteoblasts, hypertrophic chondrocytes, and chondrocyte). Here, two groups of gradient morphogens regulating (1) cell proliferation and terminal differentiation, and (2) hypertrophy of the chondrocytes will be introduced.

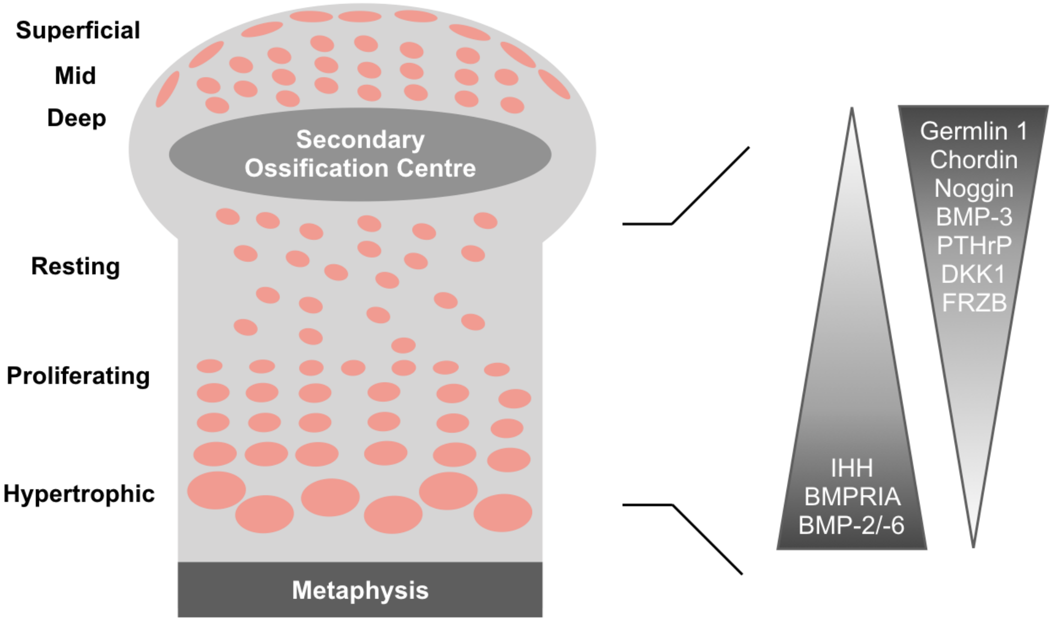

Figure 1.5 Various growth factor gradients during development

Schematic of multiple gradients within the developing growth plate cartilage within an osteochondral tissue. The chondrocytes at different zones subjected to various morphogen gradients. Modified from Di Luca et al. [28].

(A) Cell proliferation and terminal differentiation

Different morphogen gradients often crosstalk with each other, *e.g.,* the indian hedgehog (Ihh) and parathyroid hormone-related protein (PTHrP) gradient. At the growth plate, the Ihh/PTHrP gradients regulate the proliferation and differentiation of chondrocytes within. While only the chondrocytes at perichondrial region (the outmost periphery region at the surface of cartilage) secrete the PTHrP, the PTHrP gradient is formed across the surface to the deeper extracellular matrix of the osteochondral tissue. The presence of the PTHrP gradient not only stimulates the chondrocytes in the surface to proliferate but also prevents chondrocytes from undergoing hypertrophy. As a result, the chondrocytes at the articular cartilage surface are generally small when compared to deep zone hypertrophic chondrocytes [102].

Ihh is a crucial factor governing chondrocyte hypertrophy since the presence of PTHrP could delay the secretion of Ihh. The crosstalk between PTHrP and Ihh only emerge in the deeper region where the PTHrP concentration is sufficiently low. In this region, the residing chondrocytes stop proliferating and start to secrete Ihh, with the accumulated Ihh within the matrix then triggering the hypertrophy process of the chondrocytes in the deeper zone. Accordingly, when the PTHrP gradient is formed, the Ihh is only produced at the region where it is sufficiently distant to the surface of the articular cartilage [102]. While the Ihh diffuses to the articular surface from the deep zone, it can also stimulate PTHrP production from the chondrocytes within the perichondria region. In other words, a feedback mechanism plays an important role in regulating the PTHrP/Ihh gradients (Figure 1.6).

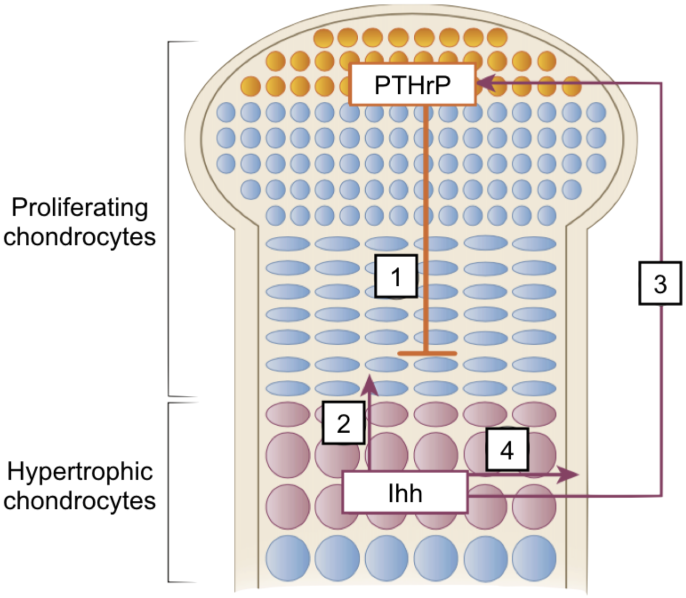

Figure 1.6 Gradients of PTHrP and Ihh

The mechanism of PTHrP-Ihh negative feedback loop. (1) PTHrP is specifically secreted by the chondrocytes within the perichondrial region. The PTHrP binds to the receptors on proliferating chondrocytes to maintain the proliferation. PTHrP also inhibits the production of Ihh. When the concentration of PTHrP is sufficiently low within the ECM, Ihh is produced. (2) Ihh also facilitates the proliferation of the chondrocytes that are close to the hypertrophic zone, and (3) stimulates the production of PTHrP in the perichondria region through an uncertain mechanism. (4) Importantly, Ihh facilitates chondrocytes in the hypertrophic zone to convert into osteoblasts. Modified from Kronenberg et al. [102].

(B) Hypertrophy of chondrocytes

Aside from the proliferation process regulated by the gradients of Ihh and PTHrP, other crucial bone development events such as endochondral ossification are also regulated by morphogen gradients. Endochondral ossification is regulated by various gradients of BMPs within the growth plate. Among different members of the BMPs, BMP-2 and BMP-6 are more abundantly produced in hypertrophic chondrocytes. Accordingly, the gradients of BMP-2 and BMP-6 are found in the osteochondral tissue, in which the concentration of BMP-2 and BMP-6 are lower when closer to the surface. While the BMP-2 and BMP-6 gradients facilitate the completion of the bone formation process in the deeper zones, the BMP activity is finely regulated through various antagonists in order to maintain the correct spatial development.

For example, in a recent report, it is shown that although BMP-2 and BMP-6 are more abundant in the hypertrophic zone at the growth plate, the BMPs signalling was higher in proliferative zone due to the higher expression of inhibitory Smad-7 in the hypertrophic zone [14] (Figure 1.7). At the resting zone, on the other hand, the antagonist of BMPs including BMP-3, gremlin, noggin, and chordin are found to be more abundant in the resting zone compared to the hypertrophic zone within the growth plate [57, 103]. The gradient of BMP-2 and BMP-6 are also found in the articular cartilage. While several BMP agonists are more abundant in the superficial zone, the antagonists are found mainly in the deep zone [14] (Figure 1.7). This contrasts to most of the tissue engineering applications in which BMP-2 is often used as the trigger for osteogenic differentiation rather than for maintaining the chondrocyte morphology [104].

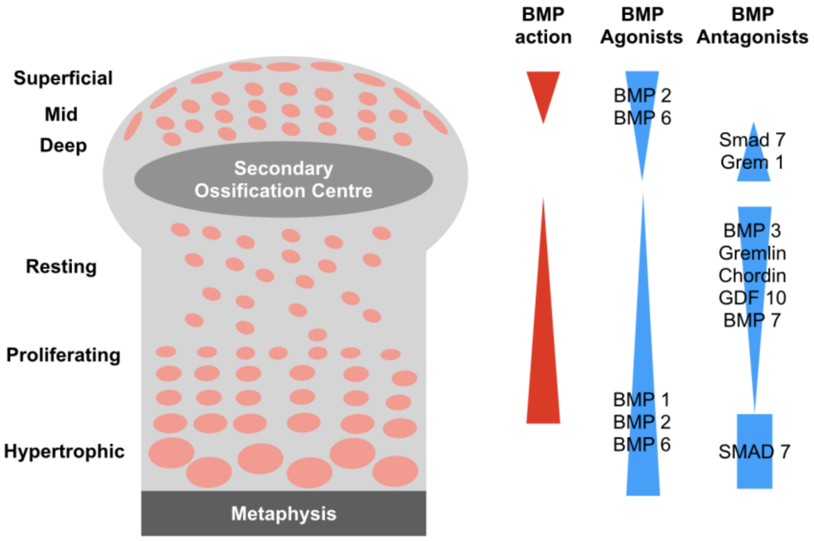

Figure 1.7 Gradients of BMPs in growth plate and articular cartilage

Various BMPs gradients and their antagonists within the developing osteochondral tissue. The action of BMP is a result of the dynamic balance between BMP agonists and antagonists. Modified from Garrison et al. [14].

Several other factors participate in the osteochondral tissue development together with the aforementioned BMPs gradient. Among all the factors, TGF-βs and Wnts signalling pathways have been intensely investigated. The crosstalk between these pathways and morphogen gradients shape the final architecture of the tissue. Within the matrix containing gradients of several cytokines, whether the chondrocytes mature into a hypertrophic state depends on the dynamic crosstalk between BMPs, Wnts and TGF-β. These growth factors could lead to the regulation of transcription factors including RUNX2, SOX9, and Twist1 [97]. While TGF-β could enhance the chondrocyte marker through SOX9, the BMP could induce the expression of hypertrophic protein through RUNX2, which results in expression of collagen type X and alkaline phosphatase (Figure 1.8). Aside from these pathways, the hypertrophic state of the chondrocyte is also finely tuned *via* Wnt antagonists including Gremlin1, Dkk-1, and Secreted frizzled-related protein. These proteins act as natural brakes for the hypertrophic process and are found to be more abundant in the superficial zone [105]. There are also other factors such as FGFs participating in the development process. Although the exact mechanism of FGFs in this process is still under investigation, it is proposed that FGF-2 could up-regulate SOX9 and subsequently enhance chondrogenesis process through the interaction with Wnt pathway [106].

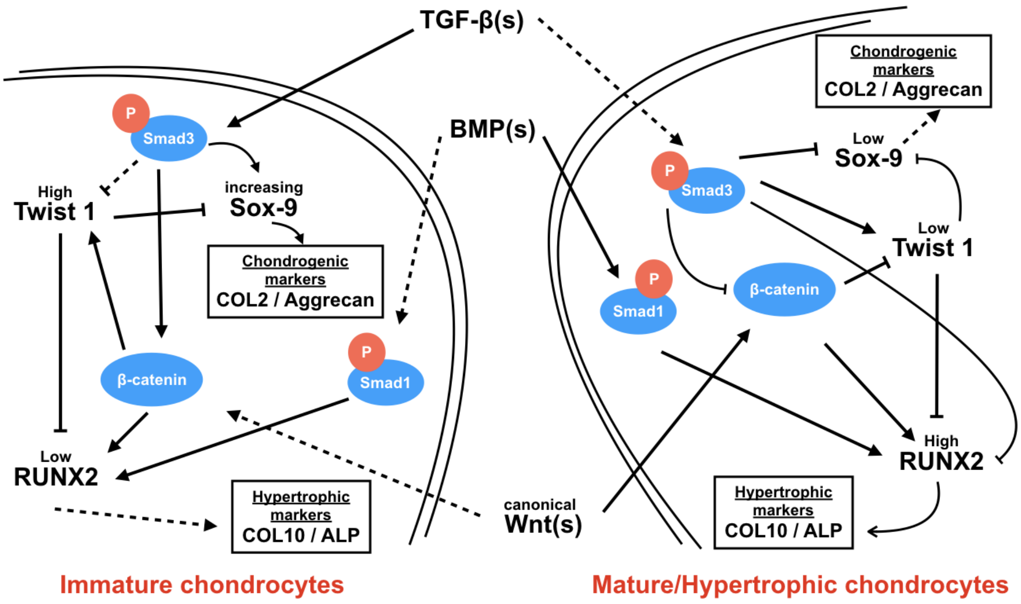

Figure 1.8 Interplay between TGF and BMP

Interaction between TGF-βs, BMPs and Wnts during osteochondral tissue development. All the three factors could regulate the dynamics and crosstalk of RUNX2, SOX9, and Twist1. While SOX9 could trigger chondrogenesis, RUNX2 could trigger osteogenesis, The figure is reproduced from Cleary et al. [97].

In conclusion, for osteochondral tissue including both articular cartilage and growth plate cartilage, the formation of gradient tissue interface is largely dictated by various morphogen gradients present during embryological development and preadolescent growth. In the next section, the structure and composition gradient of developed articular cartilage tissue will be introduced.

1.5.3 Gradients in Osteochondral Tissue

Osteochondral tissue (Figure 1.9) has a depth of approximately 3 mm in human adults. It could be categorised into cartilage (90%), calcified cartilage (5%), and the subchondral bone (5%) [57, 107]. Beginning with initial morphogen gradients, distinct cell types are derived and eventually shape this heterogeneous tissue to possess (1) composition gradients, (2) heterogeneous cell distribution and morphology, and (3) functional gradients [57, 108-111].

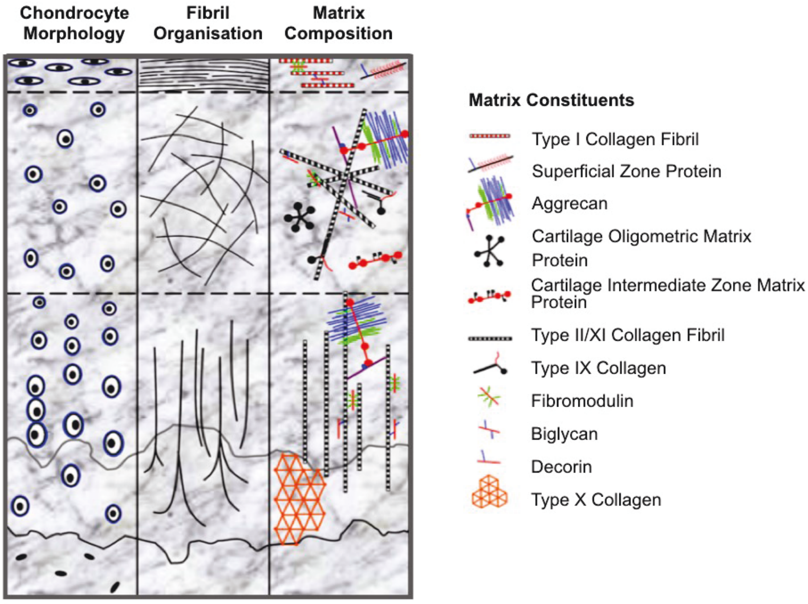

Figure 1.9 Various gradients of osteochondral tissue

Various gradients could be found within the osteochondral tissue. These gradients include cell morphology, cell distribution, fibril organisation, and ECM compositions. Modified from Di Bella et al. [112].

Cell Distribution and Morphology

The chondrocyte is the only cell type within the cartilage region of an osteochondral tissue and accounts for approximately 2% of total cartilage tissue volume [108, 113]. Although there is only a single cell type in cartilage, the density, size, distribution, and morphology of chondrocytes are distinct across different zones of osteochondral tissue [108].

(A) Heterogeneous distribution/cell morphology

The morphology of chondrocytes varies across different cartilage zones. The superficial zone of cartilage is in contact with synovial fluid and accounts for approximately 10-20% of the thickness of articular cartilage [113]. In the superficial zone, the chondrocytes are flat and aligned in parallel to the cartilage surface. The zone beneath the superficial zone is the transitional zone (or mid-zone), which accounts for approximately 40-60% of the articular cartilage thickness. In contrast to the flattened morphology found in the superficial zone, the chondrocytes in this region are more rounded [113]. Beneath the transitional zone, the radial zone (or deep zone) constitutes around 30-40% of the articular cartilage thickness.

Chondrocytes in this region are either rounded or ellipsoid, and are organised in vertical columns oriented perpendicular the surface of the articular cartilage [113]. Beneath these three zones, a wavy margin that separates unmineralised and mineralised ECM can be found. This margin, also known as the tidemark, distinguishes calcified cartilage from the radial zone and is a key feature of osteochondral tissue. The calcified cartilage acts as a transitional region between articular cartilage and subchondral bone [113]. The chondrocytes in this zone have a hypertrophic phenotype, and a cell volume that can be up to 20 times greater than chondrocytes in other zones.

Beneath the calcified cartilage, there is the subchondral bone. Two types of bone, cortical bone, and trabecular bone, can be found in osteochondral tissue [108]. Cortical bone is directly beneath the articular cartilage, while trabecular bone is beneath the cortical bone. Unlike cartilage, there are several cell populations that reside in the bone tissue. Among these different cell populations, osteoblasts synthesise bone ECM, osteoclasts are responsible for bone resorption, and osteocytes regulate bone metabolism between osteoblasts and osteoclasts [114].

Osteochondral tissue also has other characteristic gradient features. For instance, the chondrocyte density varies across the different cartilage zones. A study performed on human femoral condyles showed that the superficial zone has the highest cell density (24,000 ± 8,000 cells mm^{-3}), and the density is lower in the transitional zone (10,000 ± 1,000 cells mm^{-3}) and in the radial zone (8,000 ± 2,000 cells mm^{-3}) [115]. A separate study showed that the number of chondrocytes per chondron increases from the articular surface to the radial zone, and the density of chondrons is lower in the deep zone compared to the density near the surface [116].

(B) Origin of the anisotropic cell architecture

Most of these depth-dependent features are less pronounced, or completely absent, at birth. In other words, osteochondral tissue is much more homogeneous before the tissue is fully developed. Different hypotheses have been used to explain the formation mechanism behind the heterogeneous development of osteochondral tissue. For example, studies carried out by Hunziker *et al.* have provided a possible mechanism for the formation of heterogeneous cell distribution and the formation of chondrocyte columns within the radial zone [100].

In their study investigating articular cartilage development, the authors found that new cartilage is formed during postnatal development. Specifically, they observed a stem cell pool present near the surface of articular cartilage. During postnatal development, the stem cells within the pool possess bidirectional mitotic activity. The proliferation of stem cells in the horizontal direction (*i.e.* relative to the cartilage surface) provides new stem cells that replenish the cell pool for chondrogenic differentiation and support the lateral growth of the cartilage. In the longitudinal direction (*i.e.*, the same direction as the axis of the long bone), the proliferation feeds chondrocytes into the transitional and radial zone of the cartilage and supports the axial direction growth of articular cartilage.

The chondrocytes columns also emerge during early postnatal development. At this stage, it is found that the epiphysis bone enlarges in the longitudinal, radial and lateral direction to develop irregular complicated hemispherical structures. As this shaping process approaches completion and the rate of lateral growth of the epiphyseal bone declines, the articular cartilage then begins to grow in the axial direction. At this stage, organised cell columns start to emerge. In short, the lateral and radial growth of the cartilage is more pronounced in the earlier stage of postnatal growth and is less active in the later stage, and this leads to the formation of the chondrocyte columns within the radial zone. This study also showed that the thickness of the articular cartilage decreases during the postnatal development. In other words, the cartilage is resorbed during development. Moreover, it was found that the border of the tide mark is not connected at birth and is only fully developed toward the end of the development. These findings shed light on the development of structural gradients in osteochondral tissue. In particular, these findings suggest that the development of osteochondral is a dynamic process that evolves from the processes of tissue resorption and neoformation [100].

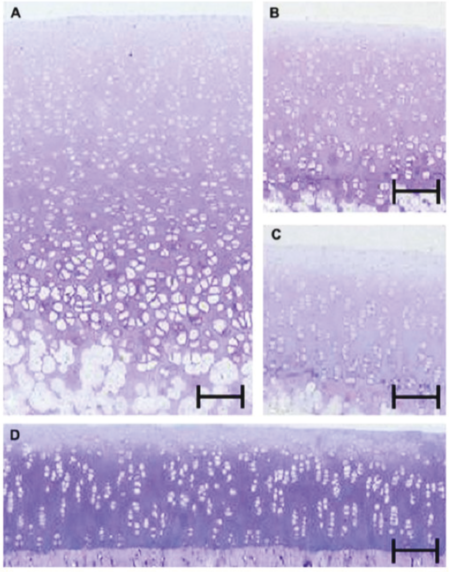

Figure 1.10 Formation of the heterogeneous cell distribution

The cell distribution evolved from an initial homogeneous organisation to a highly heterogeneous organisation during development. Cell morphology and distribution within articular cartilage tissue derived from the medial femoral condyle of rabbits after birth at (A) 1 month, (B) 2 months, (C) 3 months, and (D) 8 months. Scale bars: A = 220 μm; B, C, and D = 110 μm. Derived from Hunziker et al. [100].

Composition Gradients

In bulk, fluids including water and electrolytes account for approximately 60-80% of the total wet weight of cartilage and 10% of the wet weight of bone [108]. However, as mentioned previously, various subtypes of chondrocytes and bone-lineage cells shape the gradient tissue composition *via* the production and remodelling of different ECM components. In this section, different ECM gradients will be summarised.

(A) Collagen subtypes and fibril transition

Collagen is the most abundant ECM component in osteochondral tissue. The type of collagen and the architecture of the collagen fibrils differs from the superficial zone to the subchondral bone. The superficial zone contains the highest density of fine collagen fibres in osteochondral tissue, which can be up to 86% of the dry mass [108]. The diameter of collagen fibres in this zone is around 30-35 nm and is oriented in the direction parallel to the cartilage surface. This fibril orientation provides the superficial zone with a high tensile and shear strength [117]. While collagen type II is distributed across the entire cartilage tissue, the outermost layer of the superficial zone comprises only types I and III collagen [118].

Toward the transitional zone, collagen type II dominates the composition of collagen fibres, and the fibril diameter increases. However, the proportion of collagen among total ECM decreases to 67% of the dry mass of cartilage. There is no predominant fibril orientation in the transitional zone, however, deeper in the radial zone, the collagen fibrils are oriented perpendicular to the articular cartilage surface. The collagen fibrils in this region are also the largest, with a diameter of approximately 40-80 nm [108].

Beneath the radial zone, the calcified cartilage region contains collagen type X, which is secreted by hypertrophic chondrocytes. The direction of collagen fibrils does not play a significant role in this region, with the mineral presence dominating the mechanical properties in this zone [57]. Finally, in the subchondral bone, most of the fibrils are type I collagen.

It should be noted that these fibrils are initially arranged homogeneously at birth and it is tissue remodelling during postnatal growth that results in the organization of collagen fibrils [100]. Aside from the main collagen types (type I, type II and type X), other types of collagen are also be found within osteochondral tissue. For instance, collagen type VI and IX are the main collagen type found around the chondrons within the cartilage. These collagen proteins are only present in close proximity to the chondrocytes, and decrease to a negligible level in the cartilage matrix [57]. In addition to type VI and type IX collagen, collagen type III and type XI also present in the cartilage matrix and help to stabilise the collagen type II fibril network [113].

(B) Glycosaminoglycans and water

Proteoglycan is the second most abundant (20-25%) ECM within the cartilage tissue. The most abundant proteoglycan in cartilage is the large chondroitin sulphate proteoglycan, aggrecan. [119]. Other proteoglycans, such as decorin, fibromodulin, limuan, biglycan, and epiphycan are expressed during chondrogenesis and are present in developed cartilage [119]. Glycosaminoglycan consists of a repeating disaccharide and is the main structure of the proteoglycan. For instance, aggrecan can be assembled from up to 50 glycosaminoglycan monomers with a protein core. Because of its highly negative charge, proteoglycans can bind water and maintain the osmotic resistance necessary for cartilage to resist compressive loads [119].

The content of collagen, proteoglycan, and water varies from the articular cartilage surface to the deeper regions. Using Fourier transform infrared imaging and Raman spectroscopy mapping it was found that water and collagen is more abundant near the surface of the cartilage while proteoglycan is more abundant in the deep zone [120, 121]. (Figure 1.11). The composition of glycosaminoglycan also changes across the osteochondral tissue. For instance, aggrecan can be substituted with a variety of chondroitin sulphate isomers (*e.g.*, chondroitin-4-sulphate, chondritic-6-sulphate), and keratin sulphate. In a study carried out by Archer *et al.*, it was found that glycosaminoglycan composition changes throughout the tissue. Specifically, the ratio of chondroitin-6-sulphate over chondronitin-4-sulphate increases toward the surface, and the keratan sulphate amount increases toward the subchondral bone [122].

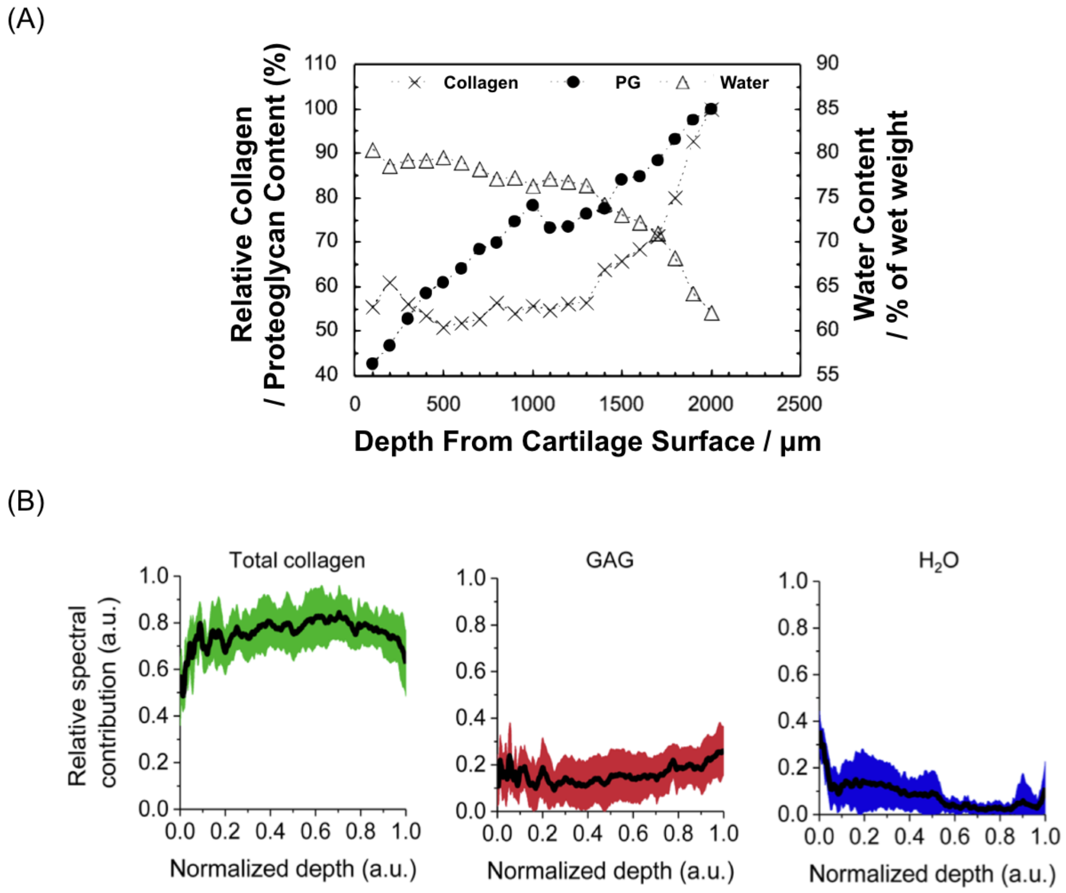

Figure 1.11 Gradients of collagen, proteoglycan, and water

The spatial distribution of collagen, proteoglycan (PG), and water in osteochondral tissue. (A) The water content at different depths was assessed by measuring the wet and dry mass of the tissue. Fourier transform infrared imaging (FTIRI) was used to determine the spatial distribution of collagen and proteoglycan. Reproduced from Saarakkala et al. [121]. (B) The relative content of water, proteoglycan, and collagen at different depths was found in a similar manner by Raman spectroscopy. Reproduced from Bergholt et al. [120].

(C) Mineral

There is no mineral found above the tidemark of osteochondral tissue, however, hydroxyapatite is present beneath the tidemark. The hydroxyapatite found within osteochondral tissue is crystalline particles derived from the deposits of calcium and phosphate. They are usually found in the shape of a plate, with lengths of between 20-50 nm, widths of approximately 15 nm, and a thickness of around 5 nm [108, 123]. The dry weight percentage of hydroxyapatite is 65 ± 2% in calcified cartilage, which is significantly less than that found in subchondral bone (86 ± 3%) [124].

Mechanical Gradients

Osteochondral tissue exhibits nonlinear mechanical profiles due to the composition and structure of the ECM. The compressive modulus of cartilage and subchondral bone is in the order of 0.5-0.8 MPa and 0.8-3.8 GPa, respectively [57]. A study carried out by Gao *et al.*, demonstrated that the compressive modulus of cartilage increases in a depth-dependent manner, and the measured modulus is related to the applied stress rate, in which higher stress rates increase the measured modulus [48]. These mechanical properties are closely related to the ECM composition of osteochondral tissue. Based on several studies in the past, proteoglycans are considered to be responsible for the equilibrium compressive stiffness of cartilage because of its ability to hold osmotic pressure [125]. On the other hand, it is believed that the collagen fibril network contributes to the instantaneous compressive modulus and the tensile response of cartilage tissue. As a result, the content ratio between type II collagen and proteoglycans defines different mechanical properties to the tissue. It is hypothesized that the higher proteoglycan content in the deep zones of cartilage contributes to the increasing compressive modulus [57, 108]. Mechanical properties are also related to the relative direction between the applied force and the fibril orientation. For instance, on the cartilage surface, different tensile moduli can be measured depending on the direction of the applied force. When stress was applied parallel to the direction of the fibril, a higher modulus was observed [108]. Similarly, higher equilibrium compressive modulus are measured when forces are applied parallel to the articular surface [126].

Due to the presence of mineral crystals, the stiffness of the calcified cartilage and subchondral bone is much higher than the cartilage. Recently, the development of advanced techniques (*e.g.*, spherical tipped diamond indenters for nanoindentation, quantitative backscattered electron imaging for mineral density), higher resolution measurements can be carried out in order to discover the relationship between mineral content and mechanical properties. In a recent study carried out by Ferguson *et al.*, the mineral and mechanical properties were resolved in a high spatial resolution at the interface between subchondral bone and calcified cartilage. While subchondral bone might be expected to possess higher stiffness than the cartilage zones, this study revealed that the mean compressive moduli of calcified cartilage and subchondral bone were extremely similar. Moreover, in the same study, some hyper-mineralised regions within calcified cartilage were found to be twice as stiff as the neighbouring subchondral bone [127].

1.6 Current Treatments for Osteochondral Lesions

The graded architecture of osteochondral tissue provides this interface with high load-bearing capacity, however, the tissue can still develop defects after acute trauma or long-term wear. Cartilage lesions are very common in the clinic; in a study carried out in 2005, it was shown that more than 250,000 cartilage repair procedures are carried out annually in the U.S. [128]. In another study reviewing more than 25,000 knee arthroscopies, 60% of cases revealed the presence of articular lesions [129]. Osteoarthritis, a systemic and late-stage disease, is the main disease target for the osteochondral tissue engineering field, however, there are other diseases associated with osteochondral lesions. For instance, osteochondritis dissecans is a disease characterised by the separation of osteochondral fragments from the joint surface and affects a predominately young demographic experiencing joint trauma [130, 131]. The regeneration of osteochondral defects is limited due to the avascular nature of cartilage. In fact, the initial defects can develop into more severe diseases, such as osteoarthritis [132].

Conventional treatment options

Late stage osteoarthritis usually requires total joint replacement, however, for the mild lesions, the main treatment options are chondroplasty (~77%) and microfracture (~22%) [128]. Chondroplasty involves the removal of debris and the flap on the cartilage surface, with smoothing of the remaining cartilage but no induced regeneration. This procedure is only suitable for patients with minor lesions and only provides short-term outcomes. Microfracture is a procedure that involves the induction of bleeding by puncturing through to the underlying bone. This results in the migration of multipoint marrow cells, and the subsequent differentiation and formation of cartilage tissue. However, this process usually leads to the formation of fibrocartilaginous tissue with inferior mechanical quality that will deteriorate in the long term [133].

Autografts and allografts can provide alternative treatment options. For instance, mosaicplasty is a surgical technique in which lesions are filled by cylindrical plugs harvested from neighbouring healthy osteochondral tissue [134]. The technique can provide better outcomes than microfracture, however, it is limited to small lesions and can result in donor site morbidity.

Osteochondral allografts are an attractive option for the treatment of full-thickness defects, however, this approach is limited by supply and has the risk of disease transmission [110].

Osteochondral Tissue Engineering

Osteochondral tissue engineering provides a potential treatment option by seeding chondrocytes, osteoblasts or stem cells within degradable scaffolds in order to engineer constructs that can fill the defect site. The autologous chondrocyte implantation (ACI) procedure, which has been carried out since 1995 [135], is the first cartilage tissue engineering approach used in the clinic. In this procedure, autologous chondrocytes are extracted from cartilage tissue and expanded *in vitro* and then implanted as a cell suspension sealed by a sutured periosteal flap. As a procedure using chondrocyte as cell source, it was expected that high quality hyaline cartilage could be formed. However, the outcomes of ACI have been inconsistent. A 10 year follow-up study showed that the failure rate of ACI could be up to 25% [136]. These failures have been attributed to procedural inconsistencies, de-differentiation of the chondrocytes during culture expansion, and poor retention of the implanted cells. New generations of the ACI procedure include the use of scaffolds, which are seeded with expanded cells prior to the surgery.

In addition to chondrocytes harvested from the healthy cartilage, mesenchymal stem cells can also be expanded and differentiated to generate cartilage tissue. Accordingly, outcome of differentiation triggered by growth factors and small molecule have been extensively studied [137-139]. In addition to soluble factors, different biomaterials, including natural derived and synthetic polymer have also been investigated [140].

Apart from developing a system that supports chondrocytes phenotype or chondrogenic differentiation, recently, more and more strategies are focusing on how to recreate the graded nature of osteochondral tissue. For example, in contrast to a single homogeneous layer, bi-phasic or tri-phasic scaffolds mimicking different zonal compositions are prepared [141]. Structural, cellular, compositional, and mechanical gradients have also been created using a wide range of engineering approaches [108].

Current Osteochondral Tissue Engineering Products

In recent years, several cartilage-specific products have been launched or undergone clinical trials. Two main categories are currently under investigation: acellular biomaterials plugs, such as Agili-C®, TruFit-CB® and CaRes®, and cellularised tissue grafts, including NeoCart®, MACI and Chondrosphere®. While acellular plugs can be supplied as off-the-shelf products, cellularised tissue grafts require additional cell culture procedures.

Most of these products have a homogeneous structure (*e.g.,* MACI, Chondrosphere®), which are poorly suited for the regeneration of full-thickness cartilage defects. There are only a limited number of products for osteochondral replacement with heterogenous structure. The summary table of these products can be found in Table 1.1. It should also be noted that all these products are multi-layered scaffolds, requiring adhesives to combine the different layers [57], and are all acellular osteochondral plugs that can be delivered directly to the defect site. For instance, ChondroMimetic® is delivered after punctures are created on the subchondral bone plate. These scaffolds can retain the bone-marrow-derived stem cells from the blood released *in-situ*. Most of these products are still in clinical trials, apart from TruFit-CB®, which was recalled from the market by the FDA after reports of swelling, pain, and implant failure.

Table 1.1 Summary table of osteochondral products with zonal characters

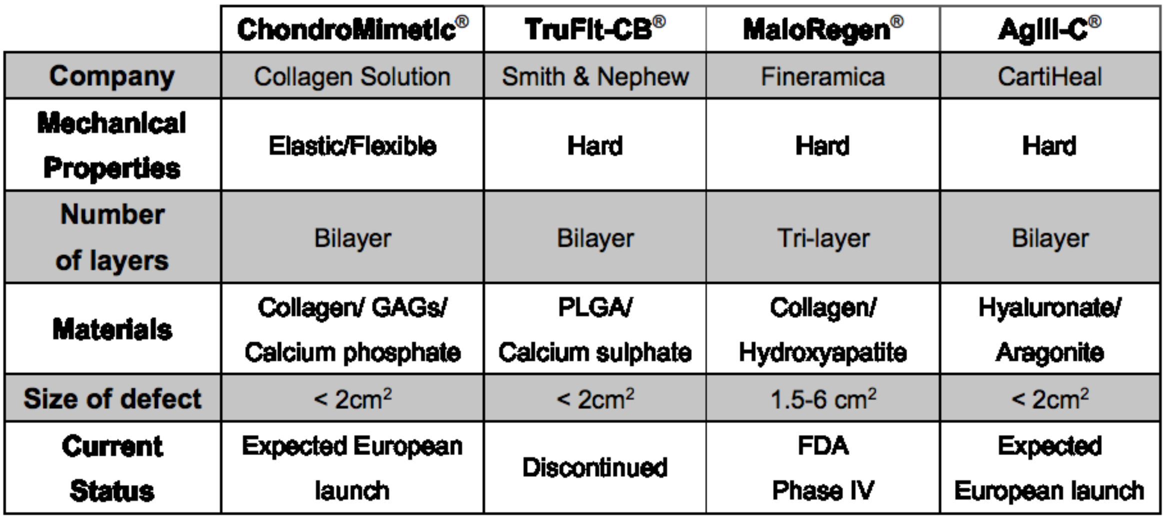

	ChondroMimetic®	**TruFit-CB®**	**MaloRegen®**	**Agili-C®**
Company	Collagen Solution	Smith & Nephew	Fineramica	CartiHeal
Mechanical Properties	**Elastic/Flexible**	**Hard**	**Hard**	**Hard**
Number of layers	Bilayer	Bilayer	Tri-layer	Bilayer
Materials	**Collagen/ GAGs/ Calcium phosphate**	**PLGA/ Calcium sulphate**	**Collagen/ Hydroxyapatite**	**Hyaluronate/ Aragonite**
Size of defect	< 2cm^2	< 2cm^2	1.5-6 cm^2	< 2cm^2
Current Status	**Expected European launch**	**Discontinued**	**FDA Phase IV**	**Expected European launch**

1.7 Osteochondral Tissue Engineering in the Thesis

Osteochondral tissue engineering provides an alternative and promising therapeutic option for patients with osteochondral lesions. In this research, two gradient-casting technologies were developed and used for osteochondral tissue engineering. This section will summarise three main components used in this study: the cell source (hMSCs), differentiation signals (BMP-2/TGF-β3), and delivery intermediate (heparin).

1.7.1 Cell Source: hMSCs

The selection of the cell source is crucial for any tissue engineering design. The ideal cell source should maintain, or differentiate into, the desired phenotype and enable the engineered constructs to possess the required physiological function [142]. To generate osteochondral constructs, one could use primary cells harvested from bone and cartilage (*i.e.*, osteoblasts/chondrocytes). However, the use of primary cells requires harvesting from healthy tissue, moreover, the *in vitro* expansion of cells can result in loss of cell phenotype [143]. An alternative approach is to use stem cells that are capable of differentiating into both lineages. Stem cells possess two key features: (1) the ability of self-renewal under certain environmental conditions and (2) the ability to differentiate into multiple cell lineages [144]. For osteochondral tissue engineering, possible stem cell sources include embryonic stem cells (ESCs), adult stem cells and induced pluripotent stem cells (iPSC). While human ESCs and iPSCs have been shown to be able to promote cartilage and bone repair, there are ethical concerns related to the ESCs source and potential safety concerns of teratoma formation of iPSCs [145].

On the other hand, MSCs offer a potentially autologous source of cells that can differentiate into cells of stromal lineage, such as chondrocytes, osteoblasts, myoblasts, and tenocytes [146]. MSCs can be isolated from a variety of tissues, including bone marrow, synovium, adipose tissue, and connective tissues [147]. MSCs from different tissues are known to have different differentiation tendencies. For instance, it has been shown that adipose-derived MSCs exhibit a lower potential for chondrogenesis; bone-marrow-derived MSCs derive chondrocytes with a greater tendency to undergo hypertrophy; synovial-derived MSCs exhibit a lower propensity to hypertrophy [144, 147, 148]. It should also be noted that even when

MSCs are derived from a single tissue source, there is a high degree of heterogeneity. MSCs are usually a mixture of different cell subpopulations with their own distinct cell marker signatures. For instance, it has been shown that CD271$^+$ synovial-derived MSCs and CD$_{105}^+$ or ROR2$^+$ (receptor tyrosine kinase-like orphan receptor 2) bone-marrow-derived MSCs exhibit an enhanced capacity for cartilage formation [144, 149]. Because of the heterogeneity of MSCs, research investigating the differentiation capability of each sub-populations is important. One clear advantage of using autologous MSCs is that they are relatively abundant, accessible and can be further expanded *in vitro* [109]. In terms of safety and translational potential, there is evidence showing that MSCs possess immunosuppressive properties and do not induce tumour development [150, 151]. These properties make MSCs an attractive option for clinical tissue engineering applications.

1.7.2 Differentiation Signal: BMP-2 / TGF-β

When using stem cells in tissue engineering applications, appropriate differentiation signals are needed. These signals can include biochemical and non-biochemical cues. For this study, differentiation signals capable of orchestrating osteogenic and chondrogenic differentiation of hMSCs are used. Specifically, we selected TGF-β3 and BMP-2 to trigger chondrogenic and osteogenic differentiation of MSCs, respectively [152, 153].

TGF-β superfamily and chondrogenesis

The transforming growth factor-β (TGF-β) superfamily comprises the BMP subfamily (BMPs and growth and differentiation factors, GDFs) and the TGF-β subfamily (TGF-β 1-3, Activin, Nodals, myostatin). Among all these factors, TGF-β is the most commonly applied growth factor in the field of cartilage tissue engineering [154]. TGF-β is a 25 kDa dimer comprising two identical chains of 112 amino acids [155]. TGF-β is secreted as a latent protein (LTGF-β) and stored in the ECM. The latent TGF-β only becomes active when it is released from the latency-associated peptide (LAP) [156]. There are three isoforms for the dimer (TGF-βs; TGF-β1, -β2 and -β3), with a similar structure of 60–70% identical amino acid sequence. Among three isoforms, TGF-β1 and TGF-β3 are often used for cartilage tissue engineering. Studies have shown that TGF-β3 possesses a higher chondrogenic potential [156, 157].

TGF-βs regulate every stage of cartilage development, including condensation, proliferation, maintenance of phenotype, and terminal differentiation. Mutations in TGF-βs or their receptors can cause severe musculoskeletal malfunction and diseases [152, 153]. TGF-β signalling is initiated through the membrane-bound TGF-β heteromeric receptors (Type I and Type II). After binding of TGF-β, the serine/threonine kinase domain of type II receptor phosphorylates the recruited type I receptor. The phosphorylation of Type I receptor subsequently activates the intracellular effector, TGF-β-specific Smads, *via* phosphorylation. The activated Smads translocate to the nucleus and bind to Smad-binding elements on DNA sequences together with other gene-regulatory proteins, such as SOX9 [158]. Cartilage-related genes, including proliferation, differentiation, and ECM metabolism, are then modulated. Beside the Smads-mediated pathway, TGF-β also activates other signalling cascades, such as the mitogen-activated protein kinase (MAPK) mediated pathway [156]. TGF-βs are extremely important regulators for chondrocyte development, and all three TGF-βs are involved in the condensation process in early chondrogenesis. In fact, *in vitro* supplementation of TGF-βs have been widely used to initiate chondrogenesis. TGF-βs are also important in maintaining chondrocyte homeostasis. In developed cartilage tissue, TGF-βs prevent terminal hypertrophic differentiation of chondrocytes, and it has been shown that TGF-β3 can inhibit the terminal hypertrophic differentiation of cultured MSCs [152].

BMP-2 and osteogenesis

The mammalian skeleton is established *via* two distinct processes: intramembranous ossification and endochondral ossification [153]. In intramembranous process, direct differentiation of osteoblasts from mesenchymal stem cells is modulated by the expression of RUNX2 and osterix. This process produces the flat bones in the body. Endochondral ossification involves the cartilage mould being replaced by bone. Endochondral ossification contributes to most bone formation processes in the body, including long bones [159]. While several different factors participate in endochondral bone formation, it has been shown that BMPs have significant capability in facilitating this process [160]. In several murine models, BMPs knockouts have been shown to lead to skeletal patterning defects and newborn death [153]. BMPs play important roles during mesenchyme condensation. It has been shown that supplementation of BMP-2 *in vitro* can trigger chondrogenic differentiation of hMSCs [161].

BMPs are dimeric molecules which can be classified into 4 distinct subfamilies based on their function and sequence. Among the discovered 14 BMPs, BMP-2, BMP-4, and BMP-7 are shown to have the highest osteogenic potential, while some BMPs contributed to other processes such as cartilage development (BMP-8 and BMP-9) [159]. Similar to TGF-β, BMP signalling is initiated *via* the binding of ligands to membrane-bound receptors. After binding of BMPs to homomeric type II receptors, the homomeric type I receptor becomes phosphorylated. This further induces Smad-dependent signalling, an interaction that is implicated in nearly every stage of osteogenesis. In Smad-dependent signalling, Smad-4 complexes with phosphorylated Smads (Smad-1, Smad-5, or Smad-8) and co-translocates into the cell nuclei. Together with transcription factors, such as RUNX2, osteogenic genes are regulated. It should be noted that besides Smad-dependent signalling, MAPK also participates in the regulation of the osteogenic differentiation [153].

Due to the widely recognised effect in skeletal development, BMPs have been investigated for therapeutic potential. For instance, the osteogenic capability of BMP-2 has been widely studied and is currently the only FDA-approved osteoinductive growth factor. In a human fracture healing study, BMP-2 was found to have a dose-dependent effect on bone tissue formation [162]. The current FDA-approved concentration of BMP-2 is 1.5 mg mL^{-1}. In addition to the concentration of BMP-2, the time frame for BMP-2 supplement is also important for both *in vitro* and *in vivo* applications. For instance, instead of long-term supplementation of BMP-2, it was demonstrated that 6 d exposure of BMP-2 was sufficient to induce osteogenic differentiation of MSCs [104].

Interplay between TGF-β and BMPs

The antagonistic mechanism between TGF-β and BMP signalling can be found in several tissues [161]. Since both TGF-βs and BMPs pathways closely regulate the development process for osteochondral tissue, crosstalk between two factors are particularly important. Understanding how BMPs and TGF-βs interact is crucial for our osteochondral tissue engineering design. For example, TGF-β has have a synergic effect with BMPs during osteochondral development. During the early stages of chondrogenesis, the TGF-β could promote BMP-initiated chondrogenesis and ECM production. This has been shown in an *ex-vivo* bovine synovial set-up in which TGF-β was delivered to enhance the BMP-2 triggered chondrogenesis [163]. A similar result was observed in a study with chondrogenic ATDC5 cell lines. In this study, TGF-β signalling was shown to enhance BMP signalling, however, in the same study, it was also found that BMP-2 could significantly reduce the level of TGF-β signalling [161]. These studies indicate that TGF-β promotes BMP signaling during early chondrogenesis.

However, TGF-β has been shown to inhibit the effect of BMP-2 during the later stages of osteochondral development. In a study using an ATDC5 cell line, it was found that TGF-βs could down-regulate BMP signalling and thus chondrocyte hypertrophy. This process was found to be mediated *via* a transcription corepressor, SnoN. In another study, Smad-3 deficient mice with impaired TGF-βs signalling have been shown to possess an increase expression of collagen type X and other maturation markers [164]. These results suggest that TGF-βs can inhibit BMP-2 signalling, prevent calcification and catabolic gene expression and hence retain chondrocytes in a quiescent state [152, 165]. In the context of tissue engineering, however, it was found that co-delivery of TGF-βs with BMPs could enhance bone formation. For instance, it has been demonstrated that bone formation was observed after the transplantation of bone marrow-derived MSCs together with BMP-2 and TGF-β3 in SCID mice. Similarly, a higher degree of BMP-2 induced ectopic bone formation was observed in a study in which TGF-β1 was co-delivered [166, 167]. It should be noted that dynamic crosstalk is also involved with other types of machinery (*e.g.*, Wnt, Hedgehog or FGF) [153]. Given that studies in the field were conducted with different biomaterials (natural derived polymers and synthetic polymers) and culture conditions (static, dynamic, 2D, and 3D), appropriate optimisation is necessary in the present study.

1.7.3 Growth Factor Sequestration Using Heparin

General delivery strategy

It is essential to have a robust strategy for growth factors delivery since the bioactivity of the delivered growth factor could alter the differentiation outcome. In the heterogeneous tissue engineering, as long as the diffusion kinetic across the construct is considered, universally deliver the bioactive signal is the most intuitive approach. Until now, supplementing media with cytokines, growth factors, and other small molecule is the most common strategy to deliver bioactive signal. However, in biologic systems, these bioactive factors are usually connected to and closely interact with extracellular matrix. *In vivo*, release and activation of growth factors are regulated by extracellular matrix. Accordingly, co-presentation of growth factor with other extracellular matrix components could have different levels of activation compared with soluble administration of growth factor [168]. For instance, delivery of BMP-2/ fibronectin complex could enhance the downstream pathway activation compared with soluble BMP-2 [169]. To engineer heterogeneous tissue, the spatial and temporal control of the growth factor delivery are equally important.

In general, to decorate tissue engineering scaffolds with bioactive factors, physical encapsulation, absorption or covalently immobilisation approaches can be used [170]. In the physical encapsulation approach, fabrication methods such as solvent casting, freeze drying, or particulate leaching can sequester growth factors within the scaffold. In some applications, a carrier system such as liposomes or microspheres could be introduced. Aside from encapsulation, other physical interactions such as electrostatic interactions have also been used. It is important to minimise the exposure of bioactive factors to harsh conditions such as solvents and high temperature in these approaches. Chemical immobilisation approaches can also be used to decorate bioactive signals. Specifically, cargos of interest could be covalent bounded to the matrix. Different conjugation approaches using active esters (*e.g.*, EDC/NHS), click chemistry (*e.g.*, alkyne-azide or thiol-ene), and other chemistry have been extensively studied [171, 172]. To effectively decorate functional signals, the specificity of the coupling site should be considered since the bioactivity of the molecule may be lost during the immobilisation process.

For both physical and chemical strategies, the fabrication process should minimise the cargo denaturation and maintain the accessible binding site of the cargo. To support the differentiation process, a system with a desirable releasing profile is more favourable.

Utilising heparin for signal delivery

Both the development of tissue and organs are subjected to the molecular and physical information encoded within the extracellular matrix [173]. In nature, besides structural support, extracellular matrix regulates specific genes and a variety of signalling pathways together with growth factors. For example, in the early stage of development, the morphogen gradient is established with the presence of some critical extracellular matrix components. Among all the components in extracellular matrix, proteoglycans, which comprise both glycosaminoglycans and their core protein, are important.

It is recognised that negatively charged glycosaminoglycans act as a reservoir of the growth factors. Several growth factors such as FGFs and VEGFs can effectively bind to heparin [17]. Besides the role as a growth factor reservoir, glycosaminoglycans can also interact with cell signal receptors together with growth factor ligands and contribute to morphogen gradient formation during the development [174].

As mentioned in previous sections, strategies without a direct conjugation could avoid denaturation of the protein cargo. For instance, electrostatic interaction was used to non-covalently sequester protein cargos. While negatively charged glycosaminoglycans such as heparin could bind the proteins bearing a net positive charge, recently, there is an increasing number of applications using glycosaminoglycans to deliver growth factors [69].

Given that heparin has been extensively used as a BMP-2 reservoir in several tissue engineering applications, in this thesis, a heparin-based biomimetic design is used to deliver BMP-2 in a spatially controlled manner. In the past, BMP-2 has been employed together with heparin in scaffolds and applied as a controlled release platform [175, 176]. The abundant sulphate and carboxylate groups of heparin not only enable crosslinking chemistry with other materials but also give heparin unique characters to mediate its electrostatic interactions with proteins. Interaction between heparin and BMP-2 is more than electrostatic. In a docking simulation study carried out by Gandhi and Mancera, non-protonated histidines of BMP-2 were identified as participating in the heparin/BMP-2 interaction. Moreover, there are different heparin binding sites for different BMPs [177]. In the presence of heparin, the loaded protein can be protected so the half-life could be extended. The half-life of BMP-2 in culture media is prolonged by 20-fold in conjunction with the use of heparin [175].

1.8 Conclusion

There have been a lot of advancements within the field of tissue engineering since its emergence in the early 90s. With nearly 30 years of research, a growing number of commercial products are in the market, with many promising clinical trials ongoing [173, 178]. However, there is still a huge gap between homogenous tissue engineering constructs and heterogeneous natural tissue. To produce a more robust tissue replacement, more sophisticated strategies are needed. It can be summarised from previous sections that the gradient nature of morphogen distribution is crucial in guiding and the formation of heterogeneous tissues [8]. Gradients within the extracellular environment of tissue should be considered in tissue engineering design [173].

In this chapter, fundamental concepts regarding gradients have been introduced. This chapter covers mechanisms of gradient formation and rationale of gradient interpretation. In order to have a better understanding of the landscape of gradient casting technology, different strategies have been introduced. Moreover, the criteria for an ideal fabrication process have been proposed.

The essence of the research in this thesis is to develop technologies capable in patterning bioactive signal gradients in the context of heterogeneous tissue engineering. Among all the potential tissue targets, osteochondral tissue is selected due to its unmet clinical need, and because it is a suitable tissue model to verify the proposed technologies. In the last part of this chapter, the gradient nature of the osteochondral tissue has been summarised. In the following chapters, two morphogen gradient casting platforms will be introduced. As suggested in section 1.4, Criteria for Ideal Gradient Fabrication Strategies, these strategies were developed to be versatile and applicable to different materials systems and applications.

Chapter II: Materials and Methods

2.1 Magnetically-formed Gradients

2.1.1 Gradient Constructs Fabrication and FEMM Modelling

Magnetic Field Alignment and Simulation

Finite element magnetic modelling (FEMM, D. C. Meeker, Finite Element Method Magnetics, Version 4.2) was used to characterise the magnetic field based on the dimensions and physical properties of the cylindrical N42 magnet (eMagnets, UK) used throughout the study (ø = 20 mm, height = 20 mm, HcB = 915 kA/m or 11500 Oe, provided by the manufacturer).

Gradient Formation

All gradients were formed in a customised mould composed of two glass slides and a cut 2 mm silicone spacer (final well dimensions = 13 × 5 × 2 mm). 30 µL of solution containing 20 nm SPIONs or hydrogel precursor containing SPIONs were dispensed into the mould, followed by 60 µL of the same components minus the SPIONs. The magnetic field was subsequently applied from approximately 2 mm above the mould to redistribute the SPIONs into a gradient. To image the gradient formation process, gradients were formed in deionised water using a layer of 0.5 mg mL^{-1} SPIONs. To test the limitation in the diameter of SPIONs used in the gradient formation set-up, same process was carried out by using 5, 50 and 200 nm of the SPIONs.

To examine the gradient forming capability in different hydrogels, a layer of 0.5 mg mL^{-1} SPIONs was used. After the formation of the gradient, the hydrogel precursor was gelled and the constructs were imaged using an Axio Observer inverted widefield microscope (Zeiss, Germany). Type VII-A Agarose (Sigma Aldrich, UK) was dissolved by heating the solution to boil at 1 wt% in PBS and gelled at room temperature. Cold Geltrex (Thermo Fisher, USA) on ice was used undiluted and gelled at 37°C. Gellum gum (Sigma Aldrich, UK) was used at 0.75% in water and crosslinked by the addition of an equal volume of 0.06 wt% solution of calcium chloride. 5 5 wt% Gelatin (Sigma Aldrich, UK) in PBS was prepared at 40°C and gelled at 4°C.

1 wt% agarose was used to test the influence of viscosity on pattern formation, with the

gradient forming process carried out in a temperature-controlled water bath (27, 30, 37°C) and the resulting gels imaged using a desktop scanner. The viscosity of the agarose solutions at these temperatures was measured by rheological creep tests performed at 2Pa stress over 5 min using an AR2000ex rheometer (TA Instruments, USA) equipped with a temperature-controlled stage.

2.1.2 Glycosylated SPION Synthesis and Characterisation

Glycosylated SPION Synthesis

A 0.9 mL solution of 1.5 mg mL^{-1} of heparin (Sigma Aldrich, UK) was prepared in pH 5.4 4-morpholineethanesulfonic acid buffer (MES, Thermo Fisher, USA), and mixed for 15 min with 5 mg of *N*-(3-dimethylaminopropyl)-*N'*-ethylcarbodiimide hydrochloride (EDC, Sigma Aldrich, UK) and 1 mg of *N*-hydroxysuccinimide (NHS, Sigma Aldrich, UK). 0.1 mL of 5 mg mL^{-1} amine-functionalised 20 nm SPIONs (SHA- 20, Ocean NanoTech, USA) were then added and mixed for 24 h at room temperature. After the conjugation, the product was dialysed against 5 L of phosphate-buffered saline (PBS, Thermo Fisher, USA) for 3 d with two daily buffer changes to ensure complete removal of unconjugated heparin. The conjugated SPIONs were then concentrated to 2 mg mL^{-1} using 100 kDa cut-off Amicon ultra-centrifugal filter unit (Merck Millipore, USA).

Glycosylated SPION Characterization

Zeta potential and hydrodynamic diameter measurements were performed using a Zetasizer Zen 3600 (Malvern Instruments, UK), with samples in pH 7 deionised water at a concentration of 40 µg mL^{-1}. Heparin quantification was performed using dimethylmethylene blue (DMMB, Sigma Aldrich, UK), with standards ranging between 0 and 25 µg mL^{-1} and an unconjugated SPION reference. The absorbance was measured at 525 nm using a SpectraMax M5 microplate reader (Molecular Devices, USA). The sulphated glycosaminoglycan content was normalised to the nanoparticle number, which was measured using a Nanosight (Ns300, Malvern Instruments, UK) equipped with Nanoparticle Tracking Analysis 3.0 software. Magnetic analysis was performed using a SQUID magnetometer (MPMS-7, Quantum Design, UK) on 1.5 mg mL^{-1} samples. These values were normalised by iron content, which was measured by digesting the nanoparticles in 2 N nitric acid (Sigma Aldrich, UK) at 40°C for 24 h to ensure complete digestion and analysing samples using inductively coupled plasma optical emission spectrometry (ICAP 6300 Duo, Thermo Fisher, USA).

The protein loading capacity of the glycosylated SPIONs was assessed by mixing avidin (Thermo Fisher, USA) with glycosylated and unconjugated SPIONs at room temperature for 10 min, and then centrifuging the sample at 20,817 g for 100 min. The concentration of avidin was detected using a Micro BCA™ Protein Assay Kit (Thermo Fisher, USA) following the manufacturer's protocol, using avidin standards between 0 and 20 µg mL^{-1}. The loading capacity was determined by subtracting the initial loading mass of avidin with the mass of avidin detected in the supernatant.

The Distribution of Protein Loaded Glycosylated SPIONs

To visualise the distribution of loaded protein, 10^{11} glycosylated SPIONs were first loaded with 300 ng of fluorescein-labelled avidin (Thermo Fisher, USA) prior to gradient formation. Fluorescent images were then acquired with an Axio Observer inverted widefield microscope (Zeiss, Germany). Intensity plots were produced using FIJI software. Specifically, a region of interest (ROI) without the boundary of the hydrogel was selected on the acquired fluorescent image, and the plot profile function was used to generate an intensity profile across the hydrogel.

2.2 Buoyancy-driven Gradient Fabrication

2.2.1 Materials Preparation

Synthesis of Agarose Conjugated with Rhodamine B

Rhodamine-labelled agarose was prepared following a method described in the literature [179]. In brief, 50 mg of type VII agarose was dissolved in 5 mL of anhydrous dimethyl sulfoxide at 70°C. 50 mg of sodium hydrogen carbonate, 20 μL of dibutyltin dilaurate and 20 mg rhodamine B isothiocyanate was added to this solution. The mixture was stirred at 70°C for 16 h, then diluted in 50 mL deionised water and precipitated in 100% ethanol. The sample was then vacuum dried and stored at -20°C.

Synthesis of GelMA

GelMA was synthesised following a method described in the literature [180]. In brief, methacrylic acid was added dropwise to a 10% (w/v) solution of gelatin in deionised water (0.6 g of methacrylic acid per 1.0 g of gelatin). After 3 h of reaction, the solution was diluted with deionised water and dialysis was performed with 12-14 kDa membrane (Spectrum Laboratories) against deionised water at 40°C for 7 d. The sample was then lyophilised and stored at -20°C.

Synthesis of HepMA

HepMA was synthesised following a method described in the literature [181]. In brief, methacrylic acid was added dropwise to a 2% (w/v) solution of heparin in deionised water (5.0 g of methacrylic acid per 1.0 g of heparin). The pH was adjusted to 8.5 using 5 M NaOH and stirred overnight at room temperature. The solution was precipitated in 100% ethanol and then dialysis was performed with 1 kDa membrane (Spectrum Laboratories) against deionised water at room temperature for 7 d. The sample was then lyophilised and stored at -20°C.

To investigate if the modified heparin could form covalent bonds with GelMA, release kinetics of heparin and HepMA from GelMA were measured. Specifically, 200 μg mL^{-1} solutions of heparin or HepMA were mixed with equivalent volume of solution containing 20% (w/v) GelMA and 5 mg mL^{-1} Irgacure 2959. The resulting solutions were cast into 100 µL hydrogels using UV irradiation (365 nm, 6 mW cm^{-2}, 5 min). The hydrogels were incubated for 28 d with 500 µL PBS supplemented with 0.02% (w/v) sodium azide (pH 7.4) at 37°C. 250 µL of PBS was removed at intervals and frozen at -20°C, with 250 µL of fresh PBS added to the hydrogel to ensure sink conditions were respected at all times. The concentration of released heparin or HepMA was quantified and measured using a dimethylmethylene blue colorimetric assay, in which heparin and HepMA powder were used as standard solution separately. The assay was carried out following a method described in the literature [182]. In brief, 10 µL of sample or heparin standard was mixed with 90 µL of DMMB assay buffer (16 mg DMMB in 1 L water containing 3.04 g glycine, 2.37 g NaCl and 9.5 mL 0.1 M HCl), with the absorbance measured at 530 nm using a SpectraMax M5 plate reader.

Synthesis of Gold Nanoparticles

79 mg of $HAuCl_4 \cdot 3H_2O$ was dissolved in in 185 mL of deionised water and then added to a 250 mL round-bottom flask and refluxed in an oil bath. The solution was stirred gently while 10 mL of 2% (w/v) trisodium citrate dihydrate was rapidly injected. After 5 min of fast stirring, the flask was removed from the oil bath and allowed to cool to room temperature. The nanoparticles were stored at 4°C.

Preparation of Liposomes Labelled with Rhodamine B

2.5 mg of 1-palmitoyl-2-oleoyl-*sn*-glycero-3-phosphocholine (POPC) and 0.025 mg of Lissamine™ rhodamine B 1,2-dihexadecanoyl-*sn*-glycero-3-phosphoethanolamine triethylammonium salt (rhodamine-DHPE) in chloroform were added to a glass vial and the solvent removed by nitrogen flow. The resulting lipid film was hydrated with 0.5 mL of water, vortexed for 30 s and then extruded through a 50 nm polycarbonate membrane using an Avanti Mini Extruder (Avanti Polar Lipids).

Preparation of Exosomes Labelled with RFP

MDA-MB-231 cells expressing LAMP-RFP were cultured until confluent in high glucose Dulbecco's modified Eagle's medium (Thermo Fisher Scientific) supplemented with 10% (v/v) foetal bovine serum (Gibco) and 1% (v/v) penicillin-streptomycin (Thermo Fisher Scientific). The cells were then cultured in the same medium, but without serum, for 3 d. The resulting conditioned media was clarified through a 0.45 µm filter and concentrated to a final volume of 500 µL using Amicon 100 kDa MWCO filters. The concentrated conditioned media was separated into 1 mL fractions by size exclusion chromatography using a Sepharose CL-2B matrix. Extracellular vesicles were eluted in fractions 8-10, and stored at -80°C.

2.2.2 Fabrication of Gradients

Unless stated otherwise, all chemicals used were from Sigma Aldrich. To create the gradient constructs, the denser liquid was added to a mold as a base layer. An electronic dispenser (Multipette® E3/E3x, Eppendorf) was used to inject the lighter liquid at a defined flow rate, with the injection outlet maintained at the initial liquid-air interface. Injection rates were measured manually. Immediately after injection, the dispenser was removed, and the gradients were preserved by gelation or polymerisation. Two moulds were used in this report: a cuboid mould (5 × 15 × 3 mm) and a cylindrical mould (∅ = 5 mm, h = 15 mm). Polymer gradients were characterised using Raman spectroscopic mapping. Briefly, a confocal Raman microspectroscopy system (WITec alpha 300R+) was used to raster map the entire surface of the gradient construct and obtain spectra comprising compositional information at 50 µm steps [183, 184]. The resulting data was analysed *via* peak ratio to reveal the location and relative concentration of the construct polymers. Stiffness gradients were characterised using spherical indentation mapping. Briefly, a 3 mm diameter stainless steel sphere was indented along the gradient in 0.5 mm steps, and the contact modulus of each indent was characterised by a modified Hertzian solution to account for substrate effects [185]. All other gradients were characterised by imaging the constructs using a wide field microscope, converting the images to 16-bit and then using the plot profile function in Image J. For full details of the fabrication and characterisation of each gradient system, see the following table for fabrication parameters:

Table 2.1 Fabrication Parameters

Gradient Applications	Injection Phase Components	Base Layer Components	Injection Rate / µL s^{-1}		Polymerization or Gelation Parameters
			Sharp Transition	Gradient Transition	
Agarose-RhoB Gradient	1% (w/v) Rhodamine B conjugated agarose	1% (w/v) agarose, 5% (w/v) sucrose	-	17	Thermal setting 4 °C, 10 min
Polymer Gradient	Lauryl methacrylate, 2% (v/v) PEG dimethacrylate, 4 mg mL^{-1} 2,2-dimethoxy-2-phenylacetophenone	*N*,*N*-dimethylacrylamide, 2% (v/v) PEG dimethacrylate 2.75 mg mL^{-1} Irgacure 2959	3	20	UV irradiation 365 nm, 6 mW cm^{-2}, 20 min
Stiffness Gradient	1.0% (w/v) Gelzan, 0.03% (w/v) $CaCl_2$	1.5% (w/v) Gelzan, 0.03% (w/v) $CaCl_2$, 5.0% (w/v) sucrose	5	20	Thermal setting 4 °C, 10 min
Gold NPs Gradient	1.0% (w/v) type VII agarose, gold nanoparticle solution (OD_{530} = 2.04)	1.0% (w/v) type VII agarose, 5.0% (w/v) sucrose	5	20	Thermal setting 4 °C, 10 min
Liposomes Gradient	1.0% (w/v) type VII agarose, 5 mg/mL Rhodamine B-liposome	1.0% (w/v) type VII agarose, 5.0% (w/v) sucrose	3	17	Thermal setting 4 °C, 10 min
Extracellular Vesicles Gradient	1.0% (w/v) type VII agarose, 2 x 10^{12} RFP-EVs / mL	1.0% (w/v) type VII agarose, 5.0% (w/v) sucrose	3	17	Thermal setting 4 °C, 10 min
Macromolecule (Dextran) Gradeint	1.0% (w/v) type VII agarose, 0.5 mg/mL 200 kDa FITC-Dextran	1.0% (w/v) type VII agarose, 5.0% (w/v) sucrose	3	17	Thermal setting 4 °C, 10 min
Protein (Avidin) Gradeint	5.0% (w/v) GelMA, 1 mg mL^{-1} HepMA, 50 µg mL^{-1} Texas Red® avidin	5.0% (w/v) GelMA, 5% (w/v) Ficoll	3	17	Thermal setting 4 °C, 10 min *

**The hydrogel was imaged cold to prevent fluorescence loss from UV exposure.*

2.2.3 Gradient Constructs Characterisations

Characterisation of Rhodamine-Agarose and Sucrose Gradients

An agarose-rhodamine gradient was generated using sucrose (see the previous section) and the resulting hydrogel was equally dissected into 4 transverse sections. These sections were heated above the melting temperature of agarose, along with 1 mL of water to prevent gelation upon cooling. After the samples were cooled to room temperature and the agarose completely dissolved, the fluorescence intensity was measured using a microplate reader at an excitation of 543 nm and an emission of 580 nm. An identical experiment was performed using agarose instead of rhodamine-agarose (see the previous section) with the dissolved sections measured using a sucrose assay kit (Abcam), following the manufacturer's protocol. In brief, the sucrose in the sample was converted into glucose using invertase and then measured using the reagent and enzyme provided in the kit. The absorbance at 570 nm was measured using a SpectraMax M5 plate reader.

Characterisation of Polymer Gradients

Raman spectroscopic mapping was performed using a confocal Raman microscope (alpha300R+, WITec) equipped with a 532 nm laser and either a × 10/0.25 NA or × 20/0.4 NA objective lens (EC Epiplan, Zeiss). Scattered light was coupled to the spectrometer through a 100 µm fibre, which further served as the confocal pinhole. The 600 lines per mm grating spectrograph (UHTS 300, WITec) and thermoelectrically-cooled back-illuminated CCD camera (Newton DU970N-BV-353, Andor), which yielded a spectral resolution of ~10 cm^{-1} (defined at full-width-at-half-maximum of mercury argon emission lines), were used to record spectra with 37 mW laser power focused through the objective to the sample. Full cross-sectional images were recorded with a 50 × 50 µm step-size were acquired with 0.5 s integration time for the polymer sample (x 10/0.25 NA objective, imaged through glass slides to control the sample interface). Since two polymers, *N,N*-dimethylacrylamide and lauryl methacrylate, possess different Raman signals on their CH_2 and CH_3 stretching features, the acquired Raman scattering signal was analysed based on the ratio of CH_2 and CH_3 stretching features to determine the profiles of polymer gradients.

Characterisation of Stiffness Gradients

Stiffness gradients were characterised using Hertzian indentation to determine the bulk contact modulus. To prevent slippage during indentation, samples were adhered to the bottom of 35 mm diameter tissue culture dish using a thin layer of Loctite 406 (Loctite). 50 µl of PBS was added to the free surface of the hydrogels. A 3 mm diameter stainless steel ball bearing was indented and retracted at 0.5 volts s^{-1} (~1.4 mm s^{-1}) with a 0 s dwell time to a target displacement of 1 mm. Indentations were performed on a TA Electroforce 3200 test frame with a 250 g tension-compression load cell. Samples were indented every 0.5 mm along their gradient coordinate in order to map the local mechanical properties. Raw indentation (force-displacement) files were post processed in MatLab® to quantify the contact modulus as a function of position. Briefly, the analysis code detected contact between the probe and sample, accounted for substrate effects, and fitted the data [181, 185]. The approach indentation data were fitted to Hertz's solution for contact between a sphere and an elastic half-space [186].

Contact was determined through a piecewise fit to the force-displacement data. Using this method, we assume that prior to contact (x<xc); where ΔF is the change in force and Δx is the change in displacement. For x>xc, we assume; where E' is the effective contact modulus, R' is the effective radius of curvature, and δ is the indentation depth. Under the assumptions that the sample was flat (infinite radius of curvature) and that the stainless-steel probe was infinitely stiff compared to the sample being indented, then E' is the contact modulus of the sample and R' is the radius of curvature of the indenter (1.5 mm) [186]. However, to account for the finite thickness of these samples, a substrate correction model was necessary to properly quantify the contact modulus [181, 185].

2.3 Cell Culture and Tissue Engineering Methods

2.3.1 Stem Cell Culture and Differentiation

hMSCs from three donors (Lonza, Switzerland) were expanded using Mesenchymal Stem Cell Growth Medium (MSCGMTM, Lonza, Switzerland) in sterile culture at 37°C/5% CO_2. The culture medium was changed every 2-3 d, and hMSCs cultured up to passage 5. Differentiation was induced after encapsulating the hMSCs into agarose hydrogels at a cell density of 9×10^6 hMSCs mL^{-1}. Osteogenic differentiation was triggered using high glucose Dulbecco's Modified Eagles Medium with pyruvate supplement (HG_DMEM 31966021, Thermo Fisher, UK) together with 10% (v/v) fetal bovine serum (FBS, Thermo Fisher, USA), 100 nM dexamethasone (Sigma Aldrich, UK), 50 µg mL^{-1} *L*-ascorbic acid 2-phosphate sesquimagnesium salt (L- ascorbic acid, Sigma Aldrich, UK) and 10 mM β-glycerophosphate (Sigma Aldrich, UK). Chondrogenic differentiation was triggered using HG_DMEM supplemented with 1 × ITS^+ (BD, USA), 100 nM dexamethasone, 50 µg mL^{-1} *L*-ascorbic acid, 50 µg mL^{-1} *L*-proline (Sigma Aldrich, UK) and 10 ng mL^{-1} TGF-β3 (R&D System, USA). Osteochondral differentiation was triggered using HG_DMEM supplemented with 1 × ITS^+, 100 nM dexamethasone, 50 µg mL^{-1} L-ascorbic acid, 50 µg mL^{-1} *L*-proline, 2 mM β-glycerophosphate and 10 ng mL^{-1} TGF-β3. Where stated, BMP-2 was supplemented either in the medium (30 ng mL^{-1}) or loaded together with glycosylated SPIONs. Unless otherwise specified, the BMP-2 concentration in the glycosylated SPIONs was 3 µg per mL of hydrogel.

2.3.2 Cytotoxicity AlamarBlue® Assay

In SPION-mediated gradient formation experiments, the cytotoxicity of SPIONs was investigated. Specifically, 9.6×10^3 hMSCs were seeded in a 96 well plate and left to adhere overnight before a 72 h incubation with 2×10^{11} or 10×10^{11} glycosylated SPIONs per mL of culture medium. The cytotoxicity of the glycosylated SPIONs was assessed using an AlamarBlue® assay (Thermo Fisher, USA), as per the manufacturer instructions, with an incubation time of 3 h. The fluorescence was measured at 570/585 nm using an EnVision™ plate reader (Perkin Elmer, USA). The metabolic activity was normalised to an untreated control and averaged across three MSC donors. hMSCs were also stained using a LIVE/DEAD™ assay (L3224, Thermo Fisher) and imaged using a IX51 Inverted microscope

(Olympus, Japan).

In buoyancy-driven gradient formation experiments, the cytotoxicity of Ficoll®, the density-modifier used in the study, was investigated. Specifically, the cytotoxicity of Ficoll® in GelMA hydrogels was assessed using an AlamarBlue® assay (Thermo Fisher Scientific). hMSCs were encapsulated at 5 × 10^5 cells mL^{-1} in 7.5% (w/v) GelMA hydrogels containing 0, 2.5 or 5% (w/v) Ficoll® and 2.5 mg mL^{-1} Irgacure 2959. 25 µL hydrogels were cast using UV irradiation (365 nm, 6 mW cm^{-2}, 5 min) and then cultured for 72 h in MesenPro RS (Thermo Fisher Scientific). The metabolic activity was measured using an alamarBlue assay, as per the manufacturer instructions (incubation time of 3 h). The fluorescence was measured using a microplate reader with an excitation of 570 nm and emission of 585 nm.

2.3.3 BMP-2 Release Kinetics

BMP-2 is crucial during osteogenic differentiation. Accordingly, BMP-2 release kinetics from two carriers, glycosylated SPIONs and HepMA, were studied for both strategies.

Glycosylated SPIONs as carriers

10^{11} glycosylated SPIONs loaded with 300 ng of BMP-2 (R&D System, USA) were cast into a 100 µL 1 wt% agarose hydrogel, to mimic the conditions used for osteochondral tissue engineering. The hydrogel was incubated in PBS with 0.02% of sodium azide (pH 7.4) (Sigma Aldrich, UK) at 37°C for 28 d. 500 µL of PBS was removed at intervals and frozen at -20°C, with 500 µL of fresh PBS added to the hydrogel to ensure that the sink conditions were respected at all times. The concentration of released BMP-2 was then quantified using a BMP-2 specific ELISA kit (R&D System, USA), following the manufacturer protocol. The absorbance was measured at 450 nm using SpectraMax M5 plate reader. After the accumulated release was determined for each time point, the release profile was fitted by Korsmeyer-Peppas model using KinetDs (version 3.0) [187]. The Korsmeyer-Peppas Model was developed to specifically model the release of molecules from a polymeric matrix, such as hydrogel network [188].

HepMA as carriers

12.5 µg mL^{-1} of BMP-2 was mixed for 4 h with an equivalent volume of either 40 µg mL^{-1} heparin or 40 µg mL^{-1} HepMA. These solutions were then mixed with an equivalent volume of 20% (w/v) GelMA with 5 mg mL^{-1} Irgacure 2959. 100 µL of the final mixture were cast using UV irradiation (365 nm, 6 mW cm^{-2}, 5 min) and then incubated for 28 d in PBS with 0.02% (w/v) sodium azide (pH 7.4) at 37°C. 500 µL of PBS was removed at intervals and frozen at -20°C, with 500 µL of fresh PBS added to the hydrogel to ensure that sink conditions were respected at all times. The concentration of released BMP-2 was quantified using a BMP-2 ELISA kit (R&D Systems) as per the manufacturer's protocol, with the absorbance measured at 450 nm using a SpectraMax M5 plate reader.

2.3.4 Tissue Engineering Osteochondral Gradients

Magnetically-formed Gradients

10^{11} glycosylated SPIONs were incubated with 300 ng of BMP-2 at 4°C for at least 5 h and then used to create a gradient in agarose, as described previously (Gradient Formation, section 2.1.1). hMSCs were included in both layers during the fabrication process, at a concentration of 9×10^6 hMSCs per mL, and the final concentration of BMP-2 was 3 μg mL^{-1}. The gradient hydrogel was transferred into a 24-well plate and cultured in 1 mL of osteochondral differentiation medium. The medium was changed after 2 h and the next day after seeding to remove the excess initial burst release BMP-2, and then three times a week for the remaining 27 d.

Buoyancy-driven Gradients

For Buoyancy-based gradients experiments, hMSCs (Lonza) were cultured with MesenPro RS (Thermo Fisher Scientific) and used between passage 4-5. For osteochondral tissue engineering, we used a 90 μL base layer of 5% (w/v) Ficoll-400, 10% (w/v) GelMA, 2.5 mg mL^{-1} Irgacure 2959, and 9×10^6 hMSCs mL^{-1} and a 45 μL injection phase of 12.5 μg mL^{-1} BMP-2 (R&D Systems), 10 μg mL^{-1} HepMA, 10% (w/v) GelMA, 2.5 mg mL^{-1} Irgacure 2959 and 9×10^6 hMSCs mL^{-1}. Note that prior to gradient formation, HepMA and BMP-2 were mixed for at least 4 h to ensure equilibration. We used an injection rate of 16.7 μL s^{-1} and then used a UV lamp to crosslink the hydrogels (365 nm, 6 mW cm^{-2}, 5 min), which were then transferred to a 24 well plate. The constructs were cultured in osteochondral differentiation medium, which was changed three times a week. The osteochondral differentiation medium comprised high glucose Dulbecco's Modified Eagles Medium with pyruvate (Thermo Fisher Scientific), 1 × insulin-transferrin-selenium supplement (ITS+, BD), 100 nM dexamethasone, 50 μg mL^{-1} L-ascorbic acid, 50 μg mL^{-1} L-proline, 2 mM β-glycerophosphate and 10 ng mL^{-1} TGF-β3 (R&D Systems). After 28 d of culture, the constructs were harvested and characterised using histology (Alcian Blue, Alizarin Red), immunofluorescence staining (type II collagen, osteopontin) and Raman spectroscopy. For full details of the tissue engineering and analysis, please refer to Supplementary Materials and Methods.

Gene Expression Analysis

Osteochondral tissue constructs engineered from three donors (N = 3, n = 3) were harvested and dissected into three equal pieces. The cartilage and bone end were rinsed with PBS, homogenized using a TissueLyser II (Qiagen, Germany), and then stored at -80°C. Total RNA was isolated using Trizol with Direct-zol™ RNA Kits, according to the manufacturer protocol, and quantified using a NanoDrop 2000c (Thermo Fisher, UK). RNA was used to generate cDNA using QuantiTect® Reverse Transcripion Kit (Qiagen, Germany), assuming a 1:1 conversion. Quantitative PCR was performed using 3 ng of cDNA, Taqman® probes (Thermo Fisher, USA) and a StepOnePlus™ (Thermo Fisher, USA). The following probes were used: *RPL13A* (Hs04194366_g1), *ACAN* (Hs00153936_m1), *ALPL* (Hs01029144_m1), *COL1A1* (Hs00164004_m1), *COL2A1* (Hs00264051_m1), *COL10A1* (Hs00166657_m1), *RUNX2* (Hs01047973_m1), *SOX9* (Hs00165814_m1), *SP7* (Hs01866874_s1). The $\Delta\Delta$Ct method was used to compare expression at the bone region normalized to the cartilage region.

ALP and DNA Assays

Osteochondral tissue constructs (N = 3, n = 3) were harvested and dissected, as previously described. The ALP activity and quantity of DNA was determined using a protocol modified from the literature [35]. The bone and cartilage ends of the tissue were homogenised separately using a TissueLyser II with ALP lysis buffer, consisting of 1 mM $MgCl_2$ (Sigma Aldrich, UK), 20 µM $ZnCl_2$ (Sigma Aldrich, UK) and 0.1% (w/v) octyl-β-glucopyranoside (Sigma Aldrich, UK) in 10 mM tris(hydroxymethyl)aminomethane buffer (pH 7.4) (Sigma Aldrich, UK) with the sample lysate immediately stored at -80°C. To perform the assay, the samples were thawed on ice and then each sample was incubated with *p*-nitrophenol phosphate (Sigma Aldrich, UK) at 37°C for 30 min. The reaction was terminated using 1 N NaOH and the absorbance measured at 405 nm using SpectraMax M5 plate reader. A standard curve between 0 and 800 µM of *p*-nitrophenol phosphate was used to calculate the sample activity. An equivalent volume from the remainder of the sample was then used for DNA quantification using a PicoGreen™ assay (Thermo Fisher, UK), according to the manufacturer protocol. The fluorescence was measured at 485/535 nm using SpectraMax M5 plate reader. The ALP activity normalised to DNA quantity was compared between the bone and cartilage regions.

Histology and Immunofluorescence Staining

Osteochondral tissue constructs were harvested and washed three times in PBS, fixed with 4% (v/v) paraformaldehyde for 2 h at room temperature, washed a further three times in PBS and then paraffin embedded. 5 µm thick sections on Superfrost Plus slides (Thermo Scientific, UK) were deparaffinised using a 4 min incubation in Histo-Clear (National Diagnostics, USA) and hydrated using 2 min incubations in 100% ethanol, 70% ethanol and then deionised water. These sections were then stained using various protocols. For sulphated glycosaminoglycans, the sections were stained with Alcian Blue (pH 2.5) (Sigma Aldrich, UK) for 30 min, with a hematoxylin nuclear counterstain (Sigma Aldrich, UK). For calcium, Alizarin Red S (Abcam, UK) was used at a concentration of 2% (w/v) at pH 4.3. Alcian Blue and Alizarin Red S were performed on consecutive sections. The slides were mounted in Histomount (National Diagnostics, USA) and then imaged using a Zeiss Axio Observer Inverted Widefield Microscope. Images were superimposed after tiling.

For immunofluorescence staining, the sections were treated with proteinase K (Dako, USA) for 2 min for antigen retrieval, and then blocked with 10% (v/v) donkey or goat serum for 1 h. The samples were incubated overnight with goat anti type I collagen (Southern Biotech, USA) at 1/100 dilution, goat anti type II collagen (Southern Biotech, USA) at 1/20 dilution, rabbit anti SP7 (Abcam, UK) at 1/100 dilution, rabbit anti osteopontin (Abcam) at 1/100 dilution, and goat and rabbit IgG negative controls (Abcam, UK) at 1/20 and 1/100 dilution. Excess primary antibody was then removed by three 10 min washes in PBS and sections were further incubated with secondary donkey anti goat or goat anti rabbit antibodies labelled with AlexaFluor 555 dye (Thermo Fisher, USA). DAPI (Thermo Fisher, USA) was used to counterstain nuclei prior to mounting the sections with Vectashield Antifade Mounting Medium (Vector Lab, USA). Sections were imaged using a Zeiss Axio Observer Inverted Widefield Microscope.

Compression Testing

Osteochondral tissue constructs were harvested, with uniform discs collected from the bone and cartilage regions using 2 mm biopsy punches (Miltex, USA). The biopsy dimensions were measured in the hydrated state using digital calipers for each construct, which were then soaked in cOmplete™ Protease Inhibitor Cocktail (Roche, Switzerland). Unconfined compression testing was performed using a Bose Electroforce 5100 (BOSE, USA) equipped with a 250 g load cell. Samples were preloaded before performing compression stress relaxation by imposing a square wave ramp for 12 steps with 5% strain using Wintest 7 (BOSE, USA). The instantaneous stress-strain response was then fitted to a bilinear curve using Origin software (OriginLab Corporation, USA) to provide a non-biased measure of the E1 and E2. The compressive Young's modulus, calculated from the linear portion of the stress-strain curve, was compared between the bone and cartilage regions.

Raman Spectroscopy

Raman spectroscopic imaging was performed using a confocal Raman microscope (alpha300R+, WITec, Germany) equipped with a 532 nm laser and a × 10/0.25 NA (for full cross-sectional images) or × 20/0.4 NA (for small regions of interest) objective lens (EC Epiplan, Zeiss, Germany). The scattered light was coupled to the spectrometer *via* a 100 µm fiber which functioned as the confocal pinhole. A 600 lines per mm grating spectrograph (UHTS 300, WITec, Germany) and a thermoelectrically cooled back- illuminated CCD camera (Newton DU970N-BV-353, Andor, UK) yielding a spectral resolution of ~10 cm^{-1} (defined at full width at half maximum of mercury argon emission lines) were used to record spectra with 35 mW laser power at the sample. To map the engineered constructs, full cross-sectional images with a 10 × 10 µm (magnetically-formed gradients) or 20 × 20 µm (buoyancy-driven gradients) step-size were acquired with 0.5 s integration time while higher spatial resolution maps were recorded with 2 × 2 µm step-size. Raman spectra were corrected for the instrument response of the system using a traceable Raman standard (STM-2245, National Institute of Standards and Technology).

Engineered osteochondral tissue samples were prepared as previously described [93]. After paraffin embedding and sectioning to 20 µm thickness on Superfrost Plus microscope slides, a standard dewaxing procedure was performed to remove confounding spectral signatures from the paraffin. Substrate signal was apparent in the acquired spectra in regions of low mineralisation but did not affect the determination of mineral or cellular signatures. Full cross-sectional mineral profiles were calculated by integrating the measured HAP and TCP intensities (945 - 975 cm^{-1}) at each position along the construct length. High spatial resolution maps correspond to HAP (v_1 PO4 at 962 cm^{-1}) and β−TCP (v_1 $HPO4^{2-}$ at 948 cm^{-1}), and cellular component of lipids and proteins ($v_{as,s}$ CH_2 at 2850 – 3000 cm^{-1}), which were experimentally validated in agreement with literature [189].

The heterogenous distribution of mineral species was further verified using a Gaussian mixture model. Due to intensity differences in signal strength for different mineral components, each position in the high spatial resolution maps was fitted with a three component Gaussian mixture model *via* expectation maximisation [190] and the relative feature weights for TCP (951 cm^{-1} feature) and HAP (961 cm^{-1} feature) were extracted. Each map position was first cropped to the mineral spectral region previously utilised (940–990 cm^{-1}) and then linearly detrended to account for substrate interference when no mineral was present. A threshold was then applied to mitigate the erroneous fitting of noise and the calculated centre position of each Gaussian was assigned to a feature if it had a position that was within 2 standard deviations of the peak centre for the Gaussian fit of the pure component spectrum mineral peak. Maps corresponded to HAP (v_1 PO_4 at 962 cm^{-1}) and β-TCP (v_1 HPO_4^{2-} at 951 cm^{-1}) which were experimentally validated in agreement with literature [189].

2.4 Statistical Analysis

Comparison between experimental groups was conducted using ordinary least-squares regression based on Generalised Linear Models in the statistical software R using the rms package. When appropriate, the data from the bone end of each individual construct was normalised to the cartilage end for direct pairwise analysis. The normalised data was then modelled as the dependent variable, and regression coefficients were calculated for independent variables. To account for different levels of response due to cell donor variability, generalised estimating equations were used (as previously described) to enable clustering of measurements obtained from constructs derived from a single donor [191-193]. The generated regression coefficients were compared. Specifically for this analysis, the relative changes of interest were the in gene expression, enzyme activity, or mechanical properties (categorical). These descriptors were included as independent variables. Heteroscedasticity in the data set was addressed by using the robust covariance function created in the rms package ("robcov") to adjust the standard errors. Finally, to compare groups, a Welch's t-test (for two group comparisons) or a one sample Student's t-test was performed on the generated GLM regression coefficients from the developed regression model, which were represented with *p*-values. All hypothesis tests were considered one-tailed based on the hypothesis of increased values in the bone end of the construct relative to the cartilage end, with exceptions for cell viability and expression levels of chondrogenic genes (*ACAN*, *COL2A1*, and *SOX9*).

Chapter III: Magnetically-formed Gradients for Osteochondral Tissue Engineering

Abstract

Morphogen and bioactive signal gradients are essential in heterogeneous tissue engineering. In this chapter, a platform using a magnetic field to align superparamagnetic iron oxide nanoparticle (SPION) gradients is reported. The proposed technology could be applied to several general hydrogel systems and the gradient formation process is rapid (< 1 min). The limitations of this platform, such as substrate viscosity and properties of SPIONs, will also be explored.

Nanoparticles have been used as carriers for bioactive signals and can be homogeneously delivered in several tissue engineering systems. In this chapter, it is hypothesised that when the gradient of morphogen loaded nanoparticles is formed, the morphogen gradient can support the generation of an *in vitro* engineered heterogeneous tissue. Specifically, in this chapter, glycosylated SPIONs are used to load and pattern a BMP-2 gradient into an agarose hydrogel laden with mesenchymal stem cells. This gradient of BMP-2 in agarose hydrogels is used to spatially direct the osteogenesis of mesenchymal stem cells and generate robust osteochondral tissue constructs exhibiting a clear mineral transition from bone to cartilage. Interestingly, the smooth gradients in growth factor concentration gave rise to biologically-relevant, emergent structural features including a tidemark transition demarcating mineralised and non-mineralised tissue and an osteochondral interface rich in hypertrophic chondrocytes. This technology could offer a new opportunity for overcoming a range of interfacial tissue engineering challenges.

3.1 Introduction and Objectives

In Chapter 1, different gradient casting strategies were revisited. Most of the strategies, however, only partially match the criteria for being an ideal fabrication technology listed in section 1.4. In this chapter, an alternative fabrication strategy utilising SPIONs and magnetic field will be exploited. Specifically, it was hypothesised that by applying a magnetic field gradient, the SPION gradient can be generated and preserved across different kinds of hydrogel materials in a rather rapid time course (< 1 min) without the requirement of customised devices or equipment. Moreover, it was hypothesised that by tailoring the surface chemistry of SPIONs, SPIONs could be used as a carrier for various cargos. Hence, after loading the cargo of interest with the modified SPIONs, the gradient of the cargo can be generated along with the formation of the SPION gradient.

In this chapter, prior to the results demonstrating the proposed strategy, basic knowledge of SPION and its application in biomedical engineering will be introduced together with their effect on cell metabolism. In the last part of the introduction, the feasibility of creating gradients using SPIONs will be discussed by reviewing related research.

3.1.1 Basics of SPIONs

Classes of magnetic materials

Before introducing the properties of SPIONs, it is necessary to introduce the basics of magnetic properties. Depending on the pairing status of electrons in orbitals, the temperature of the environment and domain structure of a material, materials can present different magnetic capabilities. The magnetisation of a material can be described by the equation:

$$M = \chi H$$

This equation describes that different levels of magnetisation (M / A m^{-1}) can be induced in a material depending on its intrinsic volumetric magnetic susceptibility (χ / unitless) when an external magnetic field (H / A m^{-1}) is applied. Based on the properties of the magnetic susceptibility (χ), materials can be categorised into five categories [194]:

(1) Diamagnetic materials

Based on the principle of molecular orbital theory (*e.g.,* Aufbau principle, Pauli exclusion principle, and Hund's rule) [195], diamagnetic materials such as gold, quartz or copper have no unpaired electron in their orbitals, accordingly, there is no permanent net magnetic moments. However, when exposed to a magnetic field, a negative magnetisation is produced to expel the applied external field, and thus the value of magnetic susceptibility is negative (*e.g.*, volume susceptibility of copper: -9.63×10^{-6}). Diamagnetism is usually weak, and the magnetic susceptibility value of diamagnetic substances remains constant at different temperatures.

(2) Paramagnetic materials

Based on the principle of molecular orbital theory, the atoms of paramagnetic materials such as magnesium, aluminium, and oxygen have unpaired electrons in their orbitals. Consequently, the magnetic fields of each electron can't be cancelled. Accordingly, due to these unpaired electrons in the orbitals, each atom of a paramagnetic material acts like a tiny magnet and supports a net magnetic moment. In the presence of an external magnetic field, the direction of magnetic moments will be aligned to the direction of the field, thus resulting in a net positive magnetisation. However, paramagnetism is usually weak. When aligned in the direction of the applied field, these materials have a positive value of magnetic susceptibility (*e.g.*, volume susceptibility of oxygen at 20°C: 3.7×10^{-7}). It should also be noted that the value of magnetic susceptibility is inversely related to temperature due to the greater thermal vibration that interferes with the alignment of magnetic dipoles at a higher temperature.

(3) Ferromagnetic materials

Ferromagnetic materials also possess unpaired electrons in their orbitals, hence their atoms have a net magnetic moment. Before exposure to an external field, these materials have several magnetic domains in which the magnetisation is in a uniform direction. However, these isotropic magnetic domains are not aligned so there is no net magnetism in any particular direction. After applying the external field, these domains can be aligned into the same direction, and the magnetisation is maintained even after the removal of the external field. When above the Curie Temperature of the material, due to the disruption induced by heat energy, the alignment of a magnetic moment in a single domain will be disrupted, consequently, ferromagnetic materials become paramagnetic. Iron, cobalt, and nickel are common magnetic materials that fall into this category with a greater susceptibility value (*e.g.*, volume susceptibility of iron: 2 × 10^5).

(4) Ferrimagnetic materials

Typically, ionic compounds, such as maghemite (Fe_2O_3) and magnetite (Fe_3O_4) fall into this category. Their properties are very similar to ferromagnetic substances, but usually with a lower magnetic susceptibility value. Like ferromagnetic materials, when above their Curie Temperature, these materials become paramagnetic. In fact, magnetite was considered a ferromagnetic material until 1940.

(5) Antiferromagnetic materials

In these materials, the magnetic domains align in a regular pattern, where neighbouring domains have magnetic moments in opposite directions. However, this pattern is disrupted above the Néel temperature. The magnetic susceptibility value of the material is related to its Néel temperature, which corresponds to the highest value of χ. It should also be noted that ferromagnets, ferrimagnets, and antiferromagnets possess ordered magnetic states even in the absence of a magnetic field, while paramagnetic and diamagnetic materials possess a magnetic state only when an external magnetic field is applied [196].

Superparamagnetism

The concept of superparamagnetism, which describes the behavior of single domain ferromagnetic nanoparticles in the presence of an external field, was first proposed by Bean and Livingston in 1959 [197]. The superparamagnetic behaviour is attributed to the nanometer range diameter of the superparamagnetic materials, at which there is only a single magnetic domain in each particle. For example, when the dimension of bulk magnetic materials, such as magnetite, is less than 20 nm there will only be a single magnetic domain. In this case, each nanoparticle can be considered as a nanoscale magnetic field, and the magnetite particle is in the superparamagnetic state.

The magnetisation direction of superparamagnetic particles is subject to thermal fluctuations when there is no external field applied, and the magnetic moment can flip randomly between two opposite directions at the time interval called Néel relaxation time. Accordingly, without an external field, the time-averaged measured value of magnetisation of superparamagnetic particles is zero. This also implies that without an external field, there will be no magnetic interaction between particles, so no aggregation occurs due to magnetic interaction. While an external magnetic field is applied, however, the overall potential energy of the superparamagnetic materials begins to exceed the energy of thermal fluctuation [198]. As a result, the material is magnetised in the direction aligned to the applied field. Based on this phenomenon, normally the ferromagnetic or ferrimagnetic materials only convert to the paramagnetic state above the Curie temperature (T_C = 585°C for Fe_3O_4 [199]). In contrast, the superparamagnetic material can undergo the transition to paramagnetic state below the Curie temperature, and the magnetic susceptibility is much larger than that of a paramagnetic substance [197]. Overall, superparamagnetic materials have strong magnetic moments in the presence of an external field, but do not have remanence when the magnetic field is removed [200-203].

Among different nanomaterials, superparamagnetic nanoparticles are particularly attractive in recent years. By manipulating the external field, the distinct behaviour of superparamagnetic materials can be utilised in different biomedical applications. Among all the available materials, superparamagnetic iron oxide nanoparticles (SPIONs) made from ferrimagnetic maghemite (Fe_2O_3) or magnetite (Fe_3O_4) iron oxide have shown promising potential for applications *in vivo*, because of their high magnetic moments at physiological temperatures and environmental conditions [204]. It is interesting to note that while most of the applications use ferrimagnetic materials, ferromagnetic materials, such as pure iron nanoparticles, may provide higher magnetisation due to its higher susceptibility [205]. However, the rapid oxidation of ferromagnetic materials will require a more robust coating to protect the core from oxidation.

3.1.2 SPIONs in Biomedical Applications

SPIONs display a distinct superparamagnetic property which can be applied in the field of regenerative medicine such as MRI imaging, drug delivery, hyperthermia therapy and tissue engineering [204, 206-209].

Since SPIONs do not exhibit any magnetisation after removal of the magnetic field near room temperature, the aggregation of SPIONs can be avoided as long as the SPIONs are colloidally stable [204]. The innate spontaneous magnetic responsiveness of SPIONs has been exploited in different *in vivo* applications highlighted in recent biomedical research. In the clinic, SPIONs have been used as iron supplements, without the use of magnetic fields, in severe ischemia patients [210]. However, the classic example of applying SPIONs in a clinical application is their use as contrast agents in Nuclear Magnetic Resonance Imaging (MRI). In fact, there are already FDA approved products for this application (*e.g.,* Feridex®, Sinerem®) [210]. Moreover, labelling cells with SPIONs can also allow the cells to be tracked with MRI both *in vitro* and *in vivo* [211, 212]. In addition to MRI applications, SPIONs have also been used as hyperthermia cancer therapy, in which an oscillating external magnetic field is applied, and local heat is generated by the nanoparticles during the magnetic relaxation process. As a result, the local increase in temperature further trigger cell apoptosis [204].

In addition to the clinical applications of SPIONS outlined above, in the context of regenerative medicine, there are other potential applications utilising SPIONs:

A. Bioactive cargo: targeted delivery and signalling initiation

In regenerative medicine, SPIONs have been applied as the delivery system for bioactive molecules including growth factors and cytokines. For instance, SPIONs have been applied in targeted delivery systems *in vivo*. In these systems, cargo-loaded SPIONs were first systemically delivered, and a magnetic field was applied on the targeted site. The applied magnetic field could then capture the cargo loaded SPIONs to achieve targeted delivery to the desired location [213].

SPIONs can also be an ideal delivery intermediate in a remotely triggered release system because of their large surface area to volume ratio and responsiveness to a magnetic field. This kind of strategy is especially important in tissue engineering applications that require sequential signals to be delivered separately. By applying an alternating magnetic field, significant energy could be transfered onto the surface of cargo-carrying SPIONs, triggering the release of cargo [214]. For instance, a recent study has demonstrated a controlled delivery platform, in which latent TGF-β/LAP complexes were conjugated to SPIONs. In the study, the TGF-β could only be released from the latent complex in the presence of an alternating magnetic field [215].

In addition to the targeted delivery of bioactive cargo across the field of cells at the tissue level, SPIONs could also spatially and temporally trigger the signalling machinery intracellularly [216-218]. Specifically, this has been achieved by conjugating proteins that can recruit and initiate transduction cascades onto the surface of SPIONs. For instance, Etoc *et al*. have demonstrated a platform where the self-assembly process of a signalling complex could be initiated at the SPIONs hot-spot where the magnetic force was applied [218]. Aside from protein delivery, nucleotides could also be delivered intracellularly. For instance, “magnetofection”, an accelerated transfection process utilising SPIONs for vector delivery, has been commercialised [219].

B. Magnetised cell: positioning, patterning and seeding

By appropriately tuning the magnetic field, magnetised cell clusters can be created, patterned or delivered to different substrates. Moreover, with the presence of the magnetic field, unique culture conditions such as a "gravity-free" environment can be supported by technologies like magnetic levitation [220]. Magnetised cells could also be applied in different seeding and patterning applications. For instance, by using the magnetised endothelial cell and the magnetic field generated from a cylindrical magnet, constructs with tubular architecture for vascular engineering application can be fabricated [221, 222]. The strategy of magnetised cell positioning could also be combined with materials that are susceptible to magnetisation. For instance, in a study carried out by Polyak *et al.*, before delivering the magnetized cells, the steel stent that is susceptible to magnetization is implanted in the mouse. After delivering the magnetically responsive cells, the induction of both magnetic field gradient around the implanted steel stent and SPIONs labelled cells could result in cell accumulation around the steel stent surface [223].

To manipulate the cell position with SPIONs, a biocompatible magnetic cell labelling process is needed. While most of the labelling processes are supported by the uptake of SPIONs, the uptake process is usually inefficient [224]. To facilitate the magnetisation process, cationic protein or molecule can be conjugated to the surface of SPIONs, and the positive charge on the surface could then facilitate cell membrane labelling and intracellular uptake of the SPIONs [224-226].

C. Magnetised scaffold: tissue engineering applications

Magnetised scaffolds possess distinct capabilities, for instance, these scaffolds are able to provide controlled release of bioactive cargos, alignment of fibrils in hydrogels, mechanical stimulatation of the attached cells, and regulation of cell differentiation behaviour [206].

In tissue engineering, the magnetised scaffold can be utilised for the targeted delivery of certain bioactive cargos. By applying a localised magnetic field around a magnetised scaffold, accumulation of cargo-carrying SPIONs can be achieved *in vivo*. Moreover, this targeted delivery strategy is more efficient and can reduce off-target delivery. Based on reported simulation results, when a magnetic gradient is more than 13 Oe cm^{-1}, the attractive force generated by the magnetic scaffold with a diameter of 1 cm can attract SPIONs up to 150 nm within a range of 2-4 mm [227].

In addition to cargo delivery, the inclusion of SPIONs in fabrication protocols could also be used to create anisotropic structure. For instance, magnetic fields could be used to align collagen fibrils in the presence of SPIONs. In the reported system, oriented fibrils could induce the co-oriented morphology of the embedded neuron cells [228].

Magnetised scaffolds are also favoured in some tissue engineering applications because of their mechano–magnetic stimulation effect on cells. It has been shown that the differentiation outcome of the residing stem cells could be altered by the SPIONs, especially when an external magnetic stimulation is also applied [206-209, 229, 230]. Research has indicated that the magnetised scaffolds could potentially affect cell metabolism and differentiation through different pathways including BMP, MAPK and NF-kB signalling pathways under an external static magnetic field, however, the exact interaction between these signaling pathways are still elusive [230].

3.1.3 Effects of SPIONs in Biological Systems

The distinct physical properties of SPIONs make them an ideal candidate for both imaging, as well as therapeutic applications. However, it should be noted that SPIONs also elicit several biological effects. For instance, SPIONs can activate mechanosensitive ion channels and alter cytoskeletal mechanics [213]. Indeed, for *in vivo* applications, the biological effect of SPIONs needs to be thoroughly considered.

In this section, the interaction of SPIONs with biological systems will be discussed. The biocompatibility of SPIONs and their effect on cell metabolism will first be introduced. In this chapter, SPIONs will be utilised in an osteochondral tissue engineering application, hence, related literature regarding SPIONs' effect on stem cell differentiation will be separately introduced in this section.

Effects on cell viability

Iron oxide nanoparticles show much lower cytotoxicity when compared to nanoparticles made from zinc, copper or other metals [231]. In several reports of SPIONs with a range of sizes and coatings, SPIONs primarily present low cytotoxicity around 100 µg Fe/mL. The cytotoxicity of SPIONs was found to be related to various factors including surface coating of SPIONs, degraded products of SPIONs, the oxidation state of iron in SPIONs (*i.e.*, Fe_3O_4 or Fe_2O_3), exposure time to SPIONs and the proteins/SPIONs interaction [232]. In general, it is considered that the uptake of SPIONs in a cell can induce a cascade of reactions that produce reactive oxygen species (ROS). The generated ROS could then lead to the damage of lipid, protein or DNA. The potential mechanisms of this process are summarised in Figure 3.1.

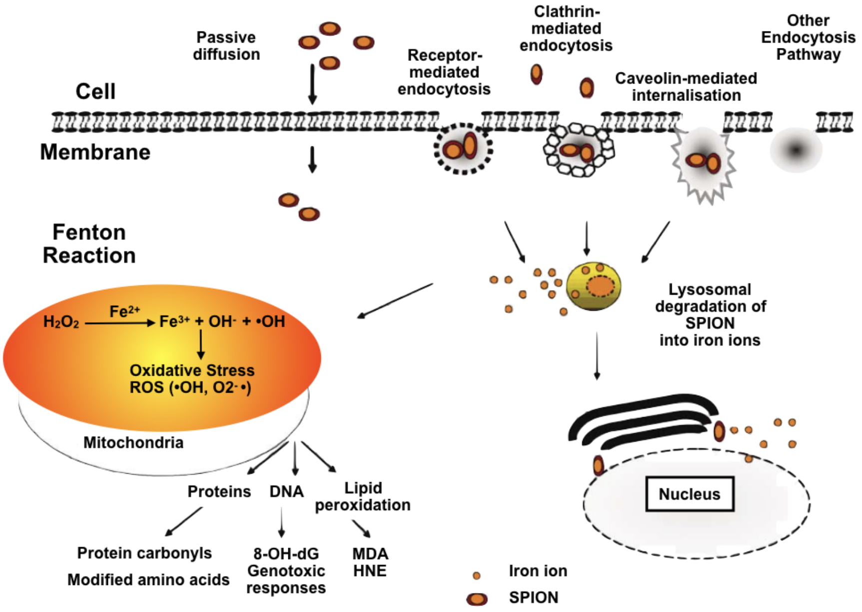

Figure 3.1 Possible mechanisms of uptake and cytotoxicity effects of SPIONs

Summary graphic of possible intracellular uptake mechanics of SPIONs, and the subsequent cascades after uptake. For SPIONs within the lysosome, the degradation of SPIONs produces iron ions which can travel across membranes of organelles and reach the mitochondria. When iron ions are in the mitochondria, the Fenton reaction could take place with the presence of hydrogen peroxide and oxygen. The Fenton reaction could generate free radicals which could damage the cells through different pathways. 8-OH-dG = 8 hydroxy-deoxy-guanosine, MDA = malondialdehyde, HNE = 4-hydroxy-2-nonenal, ROS = reactive oxygen species. Reproduced from Singh et al. [233].

For *in vivo* applications, although the delivered dose of SPIONs only accounts for 1.25-5% of the total body iron storage, most of the SPIONs products are designed to be delivered to a specific site to achieve its therapeutic (*e.g.*, hyperthermia) or diagnostic purpose (*e.g.*, contrast agent) [234]. This usually leads to a high concentration of iron in a localised area. As a result, the iron accumulation could induce damage to the targeted tissue or organ [232]. Despite the potential cytotoxicity, after considering the benefit over potential risk, there are still products approved in the clinic. For instance, Feraheme® is currently approved by the FDA and is used as an iron-replacement and contrast agent [235]. It is thought that their low toxic profile *in vivo* is due to the fact that these nanoparticles are degraded and cleared by endogenous iron metabolism processes. The iron ions may be subsequently used in the formation of red blood cells or alternatively excreted by the kidneys. Another example is Ferumoxtran-10, which is dextran-coated iron oxide nanoparticles used as a contrast agent in the clinic. The use of Ferumoxtran-10 could induce transient and mild side effects including urticaria, diarrhoea, and nausea, however, no severe side effects have been reported in the literature [236].

Effects on proliferation

A system with SPIONs has been shown to boost the proliferation of the residing cells. In several studies, when SPIONs are incorporated into the scaffolds, the system showed significantly enhanced cell proliferation activity. For example, calcium phosphates/SPIONs composites showed good biocompatibility and were able to promote cell proliferation [237]. In another study demonstrated by Bock *et al.*, the rate of cell growth also significantly increased in the magnetised scaffold [227]. A similar result in osteoblastic cell proliferation was also observed for the PLGA/SPIONs porous scaffolds, while cell cycle analysis showed that the presence of SPIONs increased the cell number in S phase, and decreased the cell population in G0/G1 phase. Consequently, these cell cycle changes resulted in a higher cell proliferation activity [238].

While the exact mechanism of enhanced proliferation still needs to be elucidated, there are a few hypotheses. One of the plausible explanations is that the enhanced proliferation is induced by the degraded products of SPIONs. Upon lysosomal degradation, free iron ions may be released, and the released ions may alter the expression of the cell cycle regulatory proteins through CIP/KIP pathways [239]. Another hypothesis of the enhanced proliferation is that SPIONs could diminish intracellular H_2O_2, an inhibitor for cell proliferation [240], through intrinsic peroxidase-like activity, and hence boost the proliferation [239].

Effects on osteogenesis and chondrogenesis

The effects of applied magnetic fields, without the presence of SPIONs, on bone regeneration was found very early. In 1974, Bassett *et al.* reported the application of a magnetic field in osteonecrosis therapy [241]. Recently, in an ovariectomised rat model study, it was found that bone mass becomes higher when the rats were exposed to a static magnetic field. These studies show the beneficial effect of the static magnetic field on osteopenia therapy [242]. In another randomised double-blind study on cervical osteoarthritis patients, it was shown that the magnetic field also possesses a pain-relief effect and increase in the mobility of patients [243]. Moreover, it was found that the magnetic field could also accelerate new bone formation by stimulating the proliferation of osteoblasts [244].

Indeed, these studies demonstrate the beneficial effects when applying the magnetic field to a disease model. To introduce the potential osteoinductive effects of the magnetic field, the strategy of combining SPIONs in bone tissue engineering has become popular recently. By adding the SPIONs into biomaterials, the magnetic property of these composite scaffolds can be utilised [207-209].

The exact mechanism of the osteoinductive property of these composite materials is still unclear. It is postulated that magnetisation could induce local deformation of the scaffold, which in turn, mechanically stimulates the residing cells [245]. Recently, the synergetic effect of the static magnetic field and magnetic scaffold on osteoblastic function and bone formation was examined. In a mouse calvarium osteoblasts/magnetic field set-up, it was found that the expression of bone-associated genes (RUNX-2 and Osterix) and alkaline phosphatase activity were up-regulated, and the activation of integrin pathways and BMP-2 pathway was observed [230]. Moreover, positive effects on osteoinduction remain even after the removal of the external magnetic field.

While SPIONs demonstrate beneficial effects on bone related applications, the effects of SPIONs in other tissue applications are uncertain. In a previous study testing the differentiation altering effect of SPIONs, it is shown that while adipogenesis and osteogenesis are not significantly altered by SPIONs at the iron concentration of 13-16 pg iron per cell, the chondrogenic differentiation pathway can be adversely affected by SPION exposure [246]. One possible explanation of this is that the regulation of iron metabolism is associated with membrane-bound transferrin-like protein (MTf), which is expressed in parallel with collagen type II during the chondrogenesis process. Although the exact physiological function of MTf is still not understood, it is hypothesised that the imbalance of iron metabolism could affect MTf and result in a hindered chondrogenesis process [246, 247].

For a more translational perspective, the comprehensive review by Anselmo *et al*. further provides a detailed outlook on the current clinical products and clinical trials utilising SPIONs [210]. In this thesis, SPIONs will be used to create biochemical gradients. In the next section, related literature on gradient formation using SPIONs will be reviewed.

3.1.4 SPIONs and Gradients

As mentioned previously in *Section 1.4, Engineering Gradients*, a versatile, generalised and reproducible strategy for engineering biochemical gradients is still missing in the field. While SPIONs are particularly attractive and have been applied to several applications in the field of regenerative medicine, there is only limited literature that describes a method using SPIONs for gradient formation.

A suspension of SPIONs is an ideal physical model for studying colloidal phenomena. While most of the research on SPIONs is focused on assessing the bulk properties of ferrofluids, in the context of gradient formation, only a handful of studies have been carried out. The gradient formation of SPIONs within ferrofluids is related to the dynamics of particle clustering. Unlike the transport behaviour of micron-sized magnetic particles, the motion of magnetic nanoparticles is governed by random Brownian motion and other short-range forces including Van der Waals forces and electrostatic forces, in addition to magnetic forces [248, 249]. Indeed, the evolution of particle concentration gradients within ferrofluids is a complex phenomenon to study because the process is a result of a large number of interactions between individual SPION clusters, and also because there are no effective experimental tools to assess concentration gradients on the micron scale. Until now, the mechanism of this magnetic fluid motion has only been partially revealed.

Although the mechanism of gradient formation is still unclear, patterned SPION gradients have been used in the context of biomedical research. For example, Bonnemay *et al.* described a system where SPION gradients were used to generate polarisation of a signalling protein. In the study, the intracellular gradient of RanGTP, a protein controlling assembly of microtubules, was pattered within *Xenopus'* egg extracts. More specifically, in the study, the protein was conjugated to the surface of SPIONs, and the generation of artificial RanGTP gradients was shown to alter the spatial position of microtubule assemblies [250].

Although SPIONs are used in numerous biomedical engineering studies, it should be noted that while the above-mentioned example demonstrates a method of creating a gradient intracellularly, to the best of our knowledge, there have been no reports using SPION gradients as a method for patterning biochemical gradients on the tissue scale, nor any examples in which SPION gradients are applied for a tissue engineering application.

3.1.5 Research Scheme

In this chapter, a new strategy is presented in which externally-applied magnetic fields are used to generate SPION gradients. The advantage of using SPIONs is that it can be applicable for different scaffold systems without the need for customised/special equipment. The proposed system can form continuous gradients instead of layers when SPIONs are incorporated inside the substrate, such as hydrogels. By applying the set-up into different hydrogel precursors, gradients in different hydrogels can be formed.

The proposed platform was also applied and tested in the context of osteochondral tissue engineering. Specifically, a gradient of BMP-2 was decorated in a tissue engineering system. This was achieved by conjugating the SPIONs with heparin, a key ECM component that can effectively load BMP-2. To create constructs with a growth factor gradient, an external magnetic field was then used to pattern BMP-2 loaded SPIONs into an agarose hydrogel, which was pre-laden with human mesenchymal stem cells (hMSCs). Thermal gelation of the hydrogel enabled the system to stably encapsulate a BMP-2 gradient. These engineered constructs were then cultured for 28 d and characterised to verify if the decorated gradient could support spatially-dependent osteogenic gene expression, tissue mineralisation and heterogeneous tissue formation (Figure 3.2).

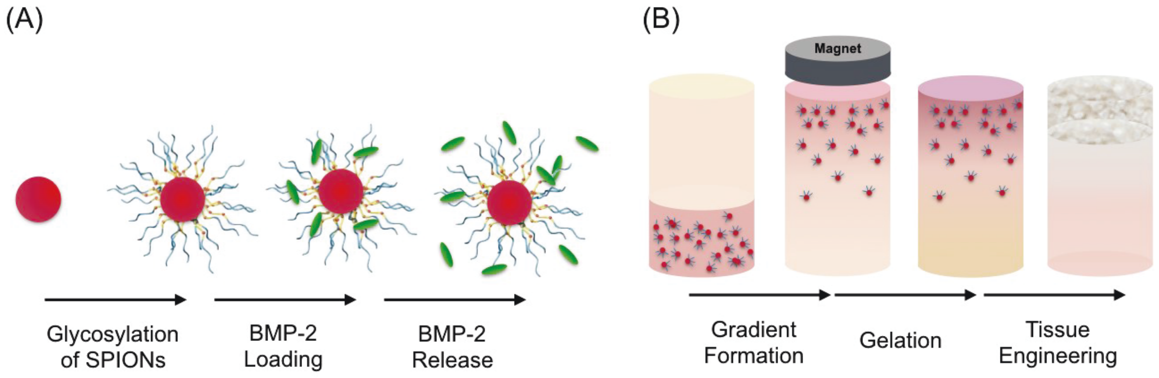

Figure 3.2 Schematic of magnetic nanoparticle-induced biochemical gradients for tissue engineering

Engineering osteochondral tissue using magnetically-aligned glycosylated SPIONs. (A) SPIONs are conjugated with heparin to produce a glycosylated corona that can efficiently sequester and release growth factors. (B) An external magnetic field is used to field-align glycosylated SPIONs in an hMSC-laden agarose hydrogel, which is thermally gelled and cultured for 28 d to generate robust osteochondral constructs comprising both bone and cartilage tissue. The figure is reproduced from Li et al. [93].

3.2 Results and Discussion I: The Platform

3.2.1 Formation of SPION Gradients

Magnetic field modelling and gradient formation

Applying a magnetic field gradient to a liquid system for SPIONs movement and redistribution has been reported in a lot of research [206, 221, 225, 227]. Here, it is hypothesised that when a magnetic field is applied to a solution with suspended SPIONs, the SPIONs will be reorganised into a gradient distribution within the liquid.

The magnetic field gradient is essential to attract the SPIONs within the field [200]. To understand the magnetic field gradient required for this process, finite element magnetic modelling was used to characterise the magnetic field strength and distribution (Figure 3.3 A). This map enabled us to define the magnetic field gradient at relative positions of the magnet and nanoparticle solution. A well-defined field gradient from 0.1 to 0.4 T was generated with the magnet used in this study (Figure 3.3 B). It should be noted that the SPION would only experience magnetic force within a magnetic field gradient but not in a uniform magnetic field.

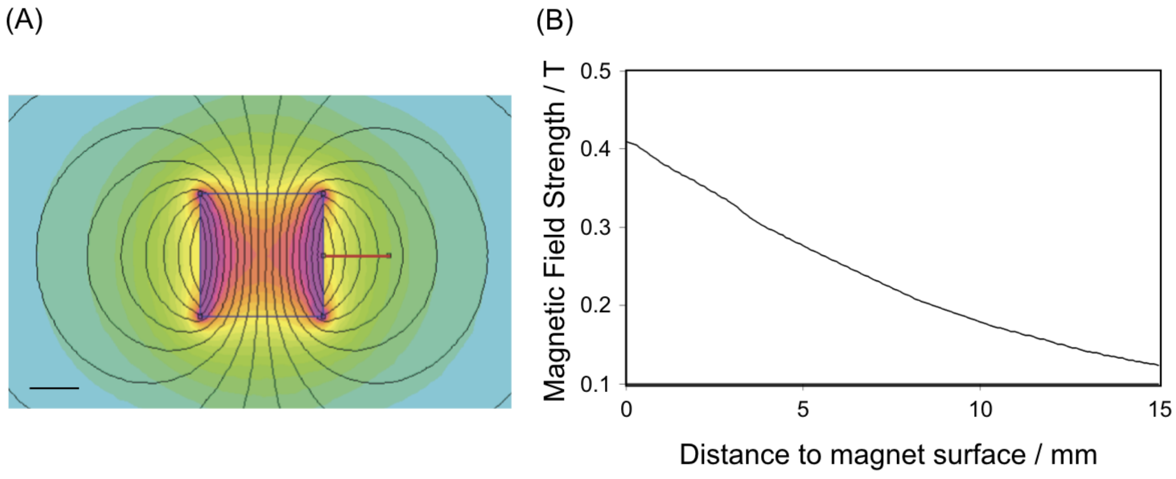

Figure 3.3 Magnetic modelling

A N42 neodymium magnet was used to create gradients (A) Finite element magnetic modelling of the magnetic field. The magnetic field strength along the red line (15 mm) was plotted in (B) as a function of distance from the magnet surface, which revealed a smooth magnetic field gradient across the exposed SPION solution. The figure is reproduced from Li et al. [93]. Scale bar = 10 mm.

To test whether different sizes of SPIONs can form a gradient when in the presence of magnetic field, SPIONs with different diameters (5, 20, 50, 200 nm) have been tested. In this preliminary experiment, different sizes of SPIONs were homogeneously mixed in deionised water and injected into a customised rectangular mould (3 mm × 5 mm × 15 mm). An N42 grade neodymium magnet was then placed 3 mm above the set-up to create a magnetic field gradient across the SPIONs solution. As demonstrated in Figure 3.4, after 30 s exposure to the magnetic field gradient, both the solution of 5 nm and 20 nm SPIONs remained homogeneously distributed instead of forming SPION gradients and accumulation of SPION clusters at the top end were found in the solution of 50 nm and 200 nm SPIONs.

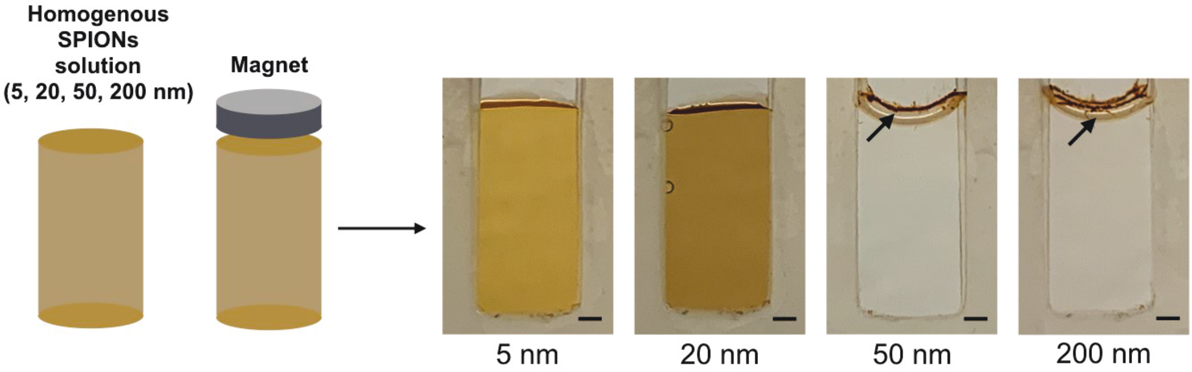

Figure 3.4 Capability of gradient formation with SPIONs of different diameters in aqueous solution

To create SPION gradients, a strong N42 magnet was applied 3 mm above the set-up. 5 nm and 20 nm SPIONs retained a homogeneous distribution in presence of the magnetic field, hence the solution remained brown. In case of 50 nm and 200 nm SPIONs, clusters were formed at the top end (arrows) and the solution became clear. The magnet was placed above the homogeneous SPION solution. Scale bar = 1 mm.

The rapid aggregation of 50 and 200 nm SPIONs is due to the strong attraction induced by the magnetic gradient field and can be explained by the fact that the magnetic force experienced by a particle can be described as:

$$F_m = (m \cdot \nabla) B; m = V_m M$$

A point like magnetic dipole m experiences a magnetic force (F_m) in a field gradient (∇B). The total magnetic moment (m) of a particle can be estimated from the volume of the particle (V_m) and the volumetric magnetisation of the material (M) [200]. Using this equation, it could be deduced that SPIONs with a bigger diameter (50 nm and 200 nm) experience a stronger magnetic force than the smaller particles (5 and 20 nm), and hence the accumulation of bigger particles would form in a shorter period of time. On the other hand, SPIONs of a small diameter do not experience a strong magnetic force in the presence of an external magnetic field. As a result, small SPIONs (5, 20 nm) did not redistribute in a short time frame. Indeed, in this preliminary study, the solutions with suspended small SPIONs did not present observable changes of SPIONs pattern and still remained as a homogeneous distribution after applying a magnet for 30 s (Figure 3.4). Moreover, even a long-term magnetic field exposure (> 16 h) could only produce a thin layer of clustered SPIONs rather than a gradient transition.

An ideal gradient casting platform should enable gradient formation in a short period of time without the formation of aggregates. Accordingly, this rules out the use of larger size SPIONs (*e.g.*, SPIONs with diameters larger than 50 nm) under the current system parameters. While using the SPIONs with a smaller diameter can prevent the formation of aggregates in a short time interval, it does not allow redistribution of the SPIONs from a monophasic suspension to a gradient. This issue was eventually resolved by a step-wise approach which includes a layer of SPION-free materials in the fabrication protocol. Specifically, in this approach, a nanoparticle-free solution was carefully stacked on top of a suspension of SPIONs without disrupting the base layer. Using the same set-up and mould, applying a magnetic field from above resulted in a rapid redistribution of the two layers to generate a smooth nanoparticle gradient within 5 s (Figure 3.5).

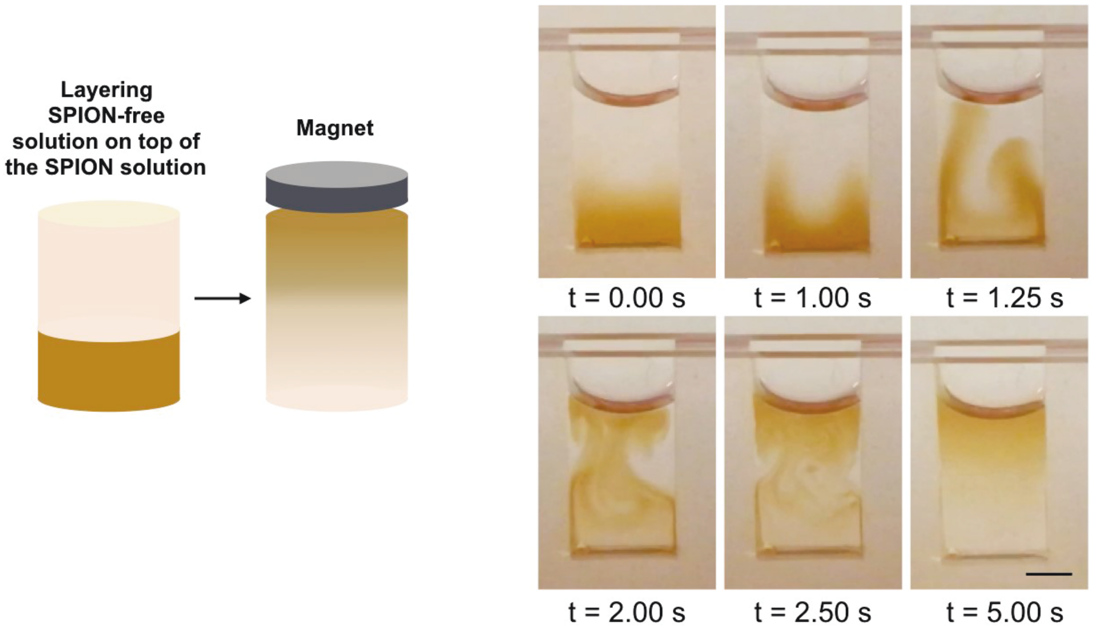

Figure 3.5 SPIONs gradient formation in water

A step-wise approach was implemented, consisting of a layer of SPION-free solution on top of a suspension of SPIONs prior to magnetic field application (t = 0). After applying the magnetic field, time-lapse images show the magnetic field alignment of SPIONs (brown) in water with a clear transition from a stacked bilayer to a smooth gradient. The figure is reproduced from Li et al. [93]. To form the gradient, the magnet was placed above the set-up after the SPION-free solution was injected. Scale bar = 2 mm.

While the magnetic field gradient could enable the movement of the SPIONs and the formation of gradients, the SPIONs reorganised and the gradient pattern was lost due to Brownian motion after removing the magnetic field. However, a system that is able to preserve the patterned gradient is essential for any further application. In this sense, after demonstrating gradient generation in an aqueous solution, it was tested whether these SPION gradients can be created in different hydrogel systems. Moreover, it is hypothesised that by triggering gelation after gradient formation, the gradient can be stably preserved for the intended application.

In this chapter, temperature triggered gelation was chosen to preserve the gradient pattern. The SPION gradient was first formed within type VII-A agarose (gel point: 25°C). To allow redistribution of SPIONs upon magnetic field application, gradient formation was carried out at 37°C, at which the melted agarose is still liquid to allow movement of the SPIONs. By changing the temperature to 4°C, the random coil configuration of agarose molecules reorganises into bundles of double helices and becomes a hydrogel [251]. During this gelation process, SPIONs were trapped in their current position and the gradient was successfully preserved.

Similarly, the temperature-mediated gelation was also applied in hydrogel systems including gelatin and Gelzan (gellan gum). The gradient formation process was carried out at 40°C for gelatin hydrogels, or 60°C for gellan gum hydrogels. To preserve the gradient, both the gelatin and Gelzan constructs with incorporated SPION gradients were cooled to 4°C. For Gelzan hydrogel, calcium ions were added as a gelling agent to stabilise the double helical structure formed after cooling by bridging carboxylic groups on the neighbouring helices [252, 253]. Depending on the exact materials selected, gelation could also be triggered by raising the temperature. For instance, the formation of SPION gradients within Geltrex™ was carried out on ice and the gelation was triggered by moving the construct to 37°C, at which the protein starts to assemble and form a hydrogel network (Figure 3.6). It should be noticed that while only the thermal gelation was used as a trigger here, other gelation mechanisms such as free radical initiated polymerisation (*e.g.,* UV exposure of photo-initiator doped gelatin methacryloyl) could also be used to preserve the gradients.

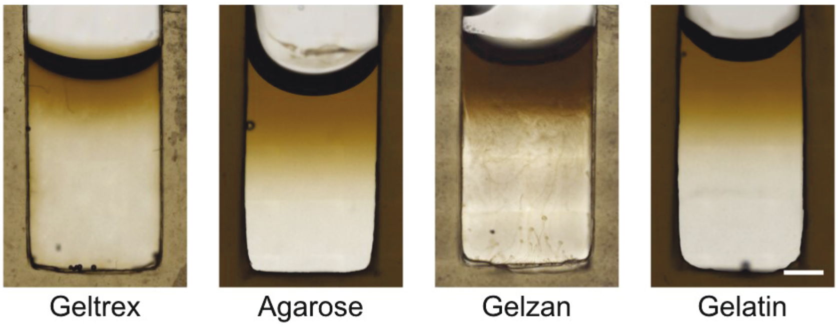

Figure 3.6 SPIONs gradients in different hydrogels

Bright field microscopy images showing gradients of SPIONs (brown colour) immobilised in different biomaterials. Increasing the temperature to 37°C was used to trigger the gelation of Geltrex. Reducing the temperature to 4°C was used to trigger the gelation of agarose, Gelzan and gelatin. The images were acquired after the gelation. The figure is reproduced from Li et *al. [93]. Scale bar = 2 mm.*

Requirements for successful gradient formation in hydrogels

While the proposed fabrication process appears to be largely independent of the material types or crosslinking mechanisms, four key restrictions were identified for the proposed strategy.

The first restriction of the system, as described in the previous sections, is the size of SPIONs. While SPIONs with a smaller diameter can form a gradient, bigger SPIONs will only form aggregates (50 and 200 nm SPIONs). It should also be noted that while small SPIONs could form a gradient within the substrate in a rapid time frame (< 1 min), longer term exposure to the magnetic field eventually resulted in the SPIONs forming dense aggregates close to the magnet. Nevertheless, this transition was a much slower process (> 10 h), which afforded ample time to capture the system in a non-equilibrium state using gelation.

The second restriction of the system is that the SPIONs should be colloidally stable in the precursor solution, which was not the case for certain hydrogels or hydrogels at high weight fractions. For instance, the SPIONs suspension was found to form aggregation after applying the magnetic gradient in a > 5% (w/v) agarose hydrogel, and a norbornene modified 8-arm poly(ethylene glycol) hydrogel. To overcome this restriction, further investigation is needed in modifying the surface chemistry of the SPIONs to make them colloidally stable in the selected hydrogel precursor.

The third restriction of the system is that the precursor solution should not inhibit SPIONs movement through viscous drag. To test the impact of viscosity while keeping the material system largely identical, gradient formation of 1% (w/v) type VII agarose hydrogels (melting temperature: 65°C, gel point: 25°C) at different temperatures (*i.e.*, different viscosities) were tested. In order to characterise the viscosity of agarose at different temperatures, 1% (w/v) agarose was first heated to boil and equilibrated at 27°C, 30°C and 37°C. The viscosity of agarose at these temperatures were then characterised using a rheometer. The viscosity of agarose at 27°C (0.07 Pa·s) was found to be higher than the viscosity of agarose at 30°C and 37°C (0.02 Pa·s) (Figure 3.7 A).

The capability to form gradients was then tested using the same gradient formation protocol. While the gradient formation process can be carried out at 30°C and 37°C in agarose hydrogels, no gradient formation was observed in 1% agarose gels at 27°C (Figure 3.7 B). Indeed, this experiment suggests that the mobility of the SPIONs after applying the magnetic field is crucial in the proposed fabrication method, and the viscosity of the hydrogel precursor solution is an important factor to support gradient formation. However, it should be noted that the relation between viscosity and gradient formation was only investigated here using 20 nm SPIONs within 1% agarose solution and a magnetic field gradient depicted in Figure 3.3. Further optimisation is needed if a different magnetic field or SPIONs are used.

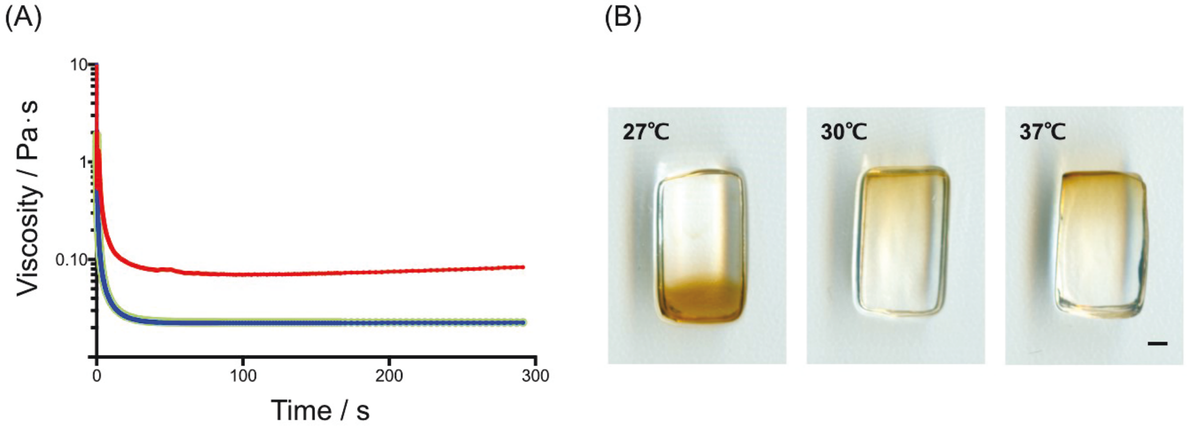

Figure 3.7 The effect of viscosity on gradient formation

To test the effect of viscosity on gradient formation, the gradient formation process was tested using 1% (w/v) agarose solutions at different temperatures. (A) Rheological creep tests confirmed that the 1% agarose solution at 27°C (red trace, 0.07 Pa·s) was of higher viscosity than the 1% agarose solutions at 30°C (blue trace, 0.02 Pa·s) and 37°C (green trace, 0.02 Pa·s). The viscosity was evaluated using the plateau region from 100-300 s of duplicate measurements from separate agarose solutions. (B) The increased viscosity at 27°C appeared to inhibit the gradient formation process. The figure is reproduced from Li et al. [93]. Scale bar = 1 mm.

Finally, the crosslinking mechanism to form the hydrogel should be reasonably rapid (< 1 h), and preferably triggered. Since long-term exposure of SPIONs in a magnetic field will result in the formation of SPION aggregates, a rapid gelation kinetic is preferred. In addition to gelation kinetics, a controllable gelation mechanism that can be triggered right after the formation of the gradient pattern is also favoured. In the current set-up, 10 min cooling in 4°C could trigger the gelation while maintaining gradients.

As long as a selected substrate can fulfil these requirements, the proposed system should able to be applicable. Importantly, these requirements are fulfilled by the majority of hydrogels. However, to adapt the strategy in a different material system or to create different SPION gradient patterns, SPION of different sizes, magnet of different strengths, and hydrogels with different viscosities should be systematically tested.

3.3 Results and Discussion II: Osteochondral Tissue Engineering

3.3.1 Synthesis and Characterisation of Glycosylated SPIONs

After demonstrating that SPION gradients can be formed in hydrogels using an external magnetic field, It was hypothesised that SPIONs can be employed as growth factor carriers for growth factor gradient generation. For this purpose, glycosylated SPIONs were fabricated to sequester and pattern a BMP-2 gradient. As described in chapter 1, key components of ECM, such as proteoglycans, have been used to deliver growth factors in tissue engineering designs. In order to load BMP-2 onto the SPIONs, heparin was used to modify the surface of SPIONs. Heparin is a commonly used carrier for BMP-2 in bone-related tissue engineering constructs. Like many cationic growth factors, BMP-2 exhibits a high affinity for heparin (K_D= 20 nM) [254]. Moreover, it has also been demonstrated to be able to guard against degradation, provide sustained release and prolonged osteogenic stimulation [255, 256].

Synthesis of glycosylated SPIONs

In the previous sections, it has been found that SPIONs with a diameter smaller than 50 nm could be used successfully to form stable gradients in hydrogels. To ensure both the sufficient loading at a reasonable SPIONs concentration (*i.e.*, sufficient surface area to volume ratio for a sufficient BMP-2 loading capability) and a practical synthesis protocol*,* a pragmatic dialysis protocol was employed. The dialysis device should keep the SPIONs within the device while the pore size of the dialysis membrane was big enough for passing the un-reacted byproducts. For this purpose, commercially purchased 20 nm SPIONs with amine groups at the surface were conjugated with heparin.

To conjugate heparin molecules, carbodiimide-based chemistry was used. In the reaction, an excess of heparin was added to react with the SPIONs (*i.e.,* around 1,500 heparin molecules per SPION). In the synthesis protocol, EDC was added and first reacted with the carboxylic groups of heparin to form *o*-acylisourea intermediates in pH 5.4 MES buffer. The active o-acylisourea intermediate could either directly form an amide bond with a primary amine on the SPION surface or react with a Sulfo-NHS molecule. In the latter case, the formed NHS ester on heparin could then further react with a primary amine on the SPIONs surface to form a stable conjugate. After the conjugation, the residual products and un-conjugated heparin molecules were removed by extensive dialysis (72 h) and the SPION solution was concentrated using a 100 kDa cut-off Amicon ultra-centrifugal filter unit. To verify the size distribution of the SPIONs before and after the conjugation, nanoparticle tracking analysis (NTA) was used. As Figure 3.8 demonstrates, NTA measurements verified that the SPIONs were colloidally stable throughout the conjugation process and no aggregation was observed after dialysis and concentration steps. Aside from providing information on size distribution, NTA measurements also determine the particle concentrations.

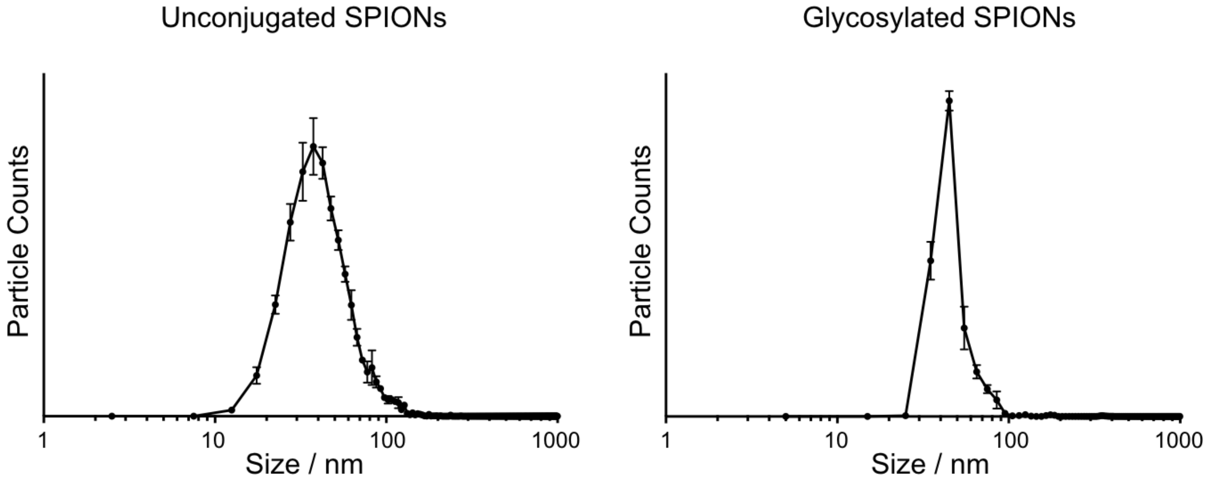

Figure 3.8 Nanoparticle tracking analysis (NTA) of unconjugated and glycosylated SPIONs

NTA demonstrated that no aggregation of SPION was formed after the glycosylation process.

Physical and biochemistry characterisation

As Table 3.1 demonstrates, the size and surface potential were measured using dynamic light scattering before and after conjugation. The hydrodynamic diameter increased from 48.6 ± 0.2 nm for the bare nanoparticles to 72.3 ± 0.9 nm after glycosylation. The increase of the hydrodynamic diameter by about 25 nm can be attributed to the steric bulkiness of the heparin corona. The conjugation of heparin molecules also altered the surface potential of the nanoparticles. The glycosylated SPIONs exhibited a zeta potential of -54.4 ± 1.7 mV compared to -4.7 ± 0.6 mV for the unconjugated nanoparticles. This change in zeta potential could be attributed to the conjugation of heparin, which is a highly anionic polysaccharide, to the surface of nanoparticles.

Next, magnetic properties of the glycosylated SPIONs were assessed using superconducting quantum interference device (SQUID) magnetometry. Magnetic properties were then normalised with the iron content, which was derived from nitric acid digested samples together with inductively coupled plasma optical emission spectroscopy (ICP-OES). The glycosylated SPIONs exhibited a magnetic susceptibility of $5.4 \pm 0.0 \times 10^{-1}$ emu g^{-1} Oe^{-1} and a saturation of 53.6 ± 0.5 emu g^{-1}, values that are very similar to the unconjugated nanoparticles which exhibited a magnetic susceptibility of $5.2 \pm 0.0 \times 10^{-1}$ emu g^{-1} Oe^{-1} and a saturation of 54.9 ± 0.3 emu g^{-1}. These results indicate that while the surface properties such as hydrodynamic diameter size and surface potential were altered after the addition of heparin molecules, the magnetic properties of the core iron oxide nanoparticles remained unchanged (Table 3.1).

Besides physical properties, biochemical properties of modified SPIONs were also determined. Firstly, the degree of glycosylation was assessed. The amount of conjugated heparin per particle is crucial in this study since limited heparin amounts will restrict protein loading and require a higher particle concentration in the system. However, a higher SPIONs concentration could bring the undesirable effects in applications involving hMSCs differentiation [246, 247]. Using a dimethylmethylene blue (DMMB) assay for heparin quantification and nanoparticle tracking analysis (NTA) measurement for the particle concentration, the heparin content per modified SPIONs could be quantified. The normalised results revealed 4.2 ng of heparin per 10^9 nanoparticles, a value that corresponds to approximately 140 heparin chains (18 kDa) bound to the surface of each nanoparticle.

The high density of carboxylic and sulphate groups on heparin provides an anionic network that can be used to sequester many soluble proteins. To assess BMP-2 sequestration capability of the glycosylated SPIONs, avidin was used as a model protein due to its similar isoelectric point (pI of avidin: 6.5; pI of BMP-2: 8.5), comparable dissociation constant with heparin (K_D of BMP-2/heparin: 20 nM; K_D of avidn/heparin: 160 nM) and the fact that it is commonly used as an analogue for studying the interaction between BMP-2 and heparin [257, 258]. To test the loading capacity of the glycosylated SPIONs, avidin was first mixed with glycosylated or unconjugated SPIONs and non-loaded avidin was removed by centrifugation and wash. The final loading was assessed by subtracting the initial loading mass of avidin with the mass of unbounded avidin in the supernatant using a bicinchoninic acid assay in which the total amount peptide bonds in the sample are quantified. With the standards prepared using avidin, the result demonstrates an average loading of 4.7 ± 0.2 ng avidin incorporated per 10^9 nanoparticles, approximately three times greater than the value observed for the unconjugated SPIONs. This is equivalent to approximately 40 sequestered proteins per nanoparticle. This level of loading should offer the opportunity to deliver more than 400 ng of growth factor, a quantity sufficient to influence cell fate, using only 10^{11} nanoparticles [259].

Table 3.1 Biophysical characterisation of unconjugated and glycosylated SPIONs

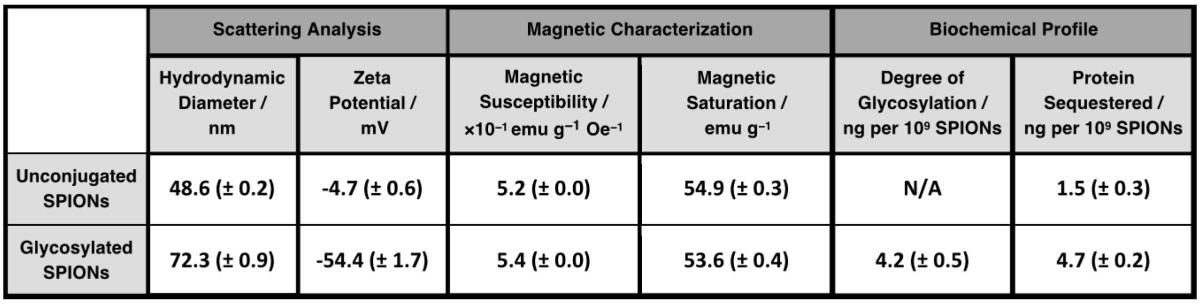

	Scattering Analysis		Magnetic Characterization		Biochemical Profile	
	Hydrodynamic Diameter / nm	Zeta Potential / mV	Magnetic Susceptibility / $\times 10^{-1}$ emu g^{-1} Oe^{-1}	Magnetic Saturation / emu g^{-1}	Degree of Glycosylation / ng per 10^9 SPIONs	Protein Sequestered / ng per 10^9 SPIONs
Unconjugated SPIONs	**48.6 (± 0.2)**	**-4.7 (± 0.6)**	**5.2 (± 0.0)**	**54.9 (± 0.3)**	**N/A**	**1.5 (± 0.3)**
Glycosylated SPIONs	**72.3 (± 0.9)**	**-54.4 (± 1.7)**	**5.4 (± 0.0)**	**53.6 (± 0.4)**	**4.2 (± 0.5)**	**4.7 (± 0.2)**

(mean ± S.D.)

Comparison between gradient and bilayer set-up

While the conventional stacking approach should produce constructs possessing spatial difference in morphogen concentration, the herein proposed fabrication approach should create a more gradual transition than a sharp transition. To demonstrate this, FITC labelled avidin was used as the cargo analogue for visualising protein distribution in the final fabricated construct.

Images of both bilayer and gradient constructs were taken using a fluorescence microscope so the fluorescence channel and bright field channel could be used to determine the distribution of glycosylated SPIONs and FITC labelled avidin, respectively (Figure 3.9). Using the intensity plot profile function in FIJI, the pattern of SPIONs distribution was shown to be different between the gradient set-up and the stepwise stacking approach. While assuming the protein cargo was well co-localised with the glycosylated SPIONs, the magnetic field alignment produced a much smoother transition than a stepwise stacking approach, which resulted in a much sharper boundary at the layer interface. The aim of this research was to create a growth factor gradient in a tissue engineering construct. Based on the result using avidin as an analogue for growth factor protein, the fabrication protocol should be able to create a morphogenetic gradient rather than a sharp transition in protein distribution.

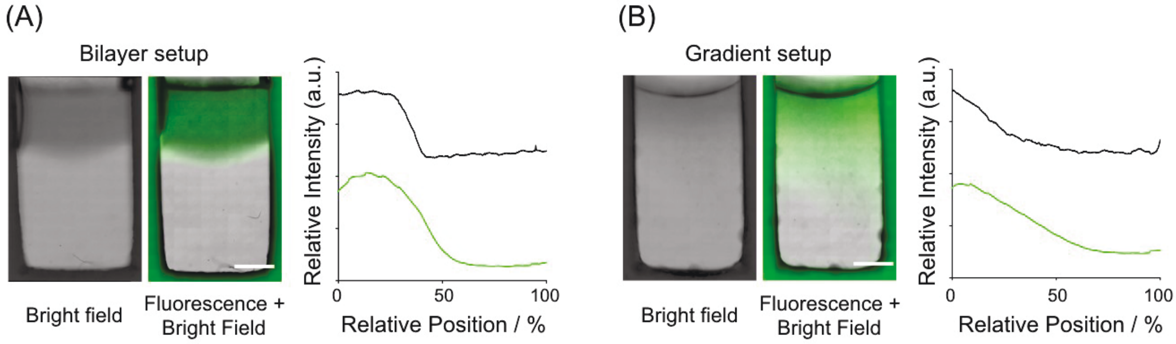

Figure 3.9 Distinct pattern of bilayer and gradient transition

The distribution of glycosylated SPIONs loaded with fluorescently-tagged avidin (green) in agarose was visualised using fluorescence microscopy. Corresponding bright field images revealed the distribution of glycosylated SPIONs (dark grey). (A) Stepwise stacking of hydrogel layers resulted in a much sharper boundary at the layer interface compared to (B) magnetic field alignment, which produced a smooth gradient. The figure is reproduced from Li et al. [93]. SPION/ agarose mixture was slowly injected as the top layer in (A). To form the gradient, magnet was placed on top of the set-up after the SPION-free top layer was injected in (B). Scale bars = 2 mm.

Cytocompatibility test with cells

While the glycosylation of SPIONs enables protein loading, the cytocompatibility of the carrier system needs to be assessed since hMSCs will be incorporated in the system. Here, different concentrations of glycosylated SPIONs, based on the calculation estimating to achieve the required amount for sufficient BMP-2 loading, were used in both the cell metabolic assay (AlamarBlue®) and the LIVE/DEAD™ staining. As Figure 3.10 demonstrates, glycosylated SPIONs did not significantly affect the metabolic activity of hMSCs after a 72 h exposure to glycosylated SPIONs. Subsequently, glycosylated SPIONs were used in the study at the concentration of 10^{12} nanoparticles mL^{-1}.

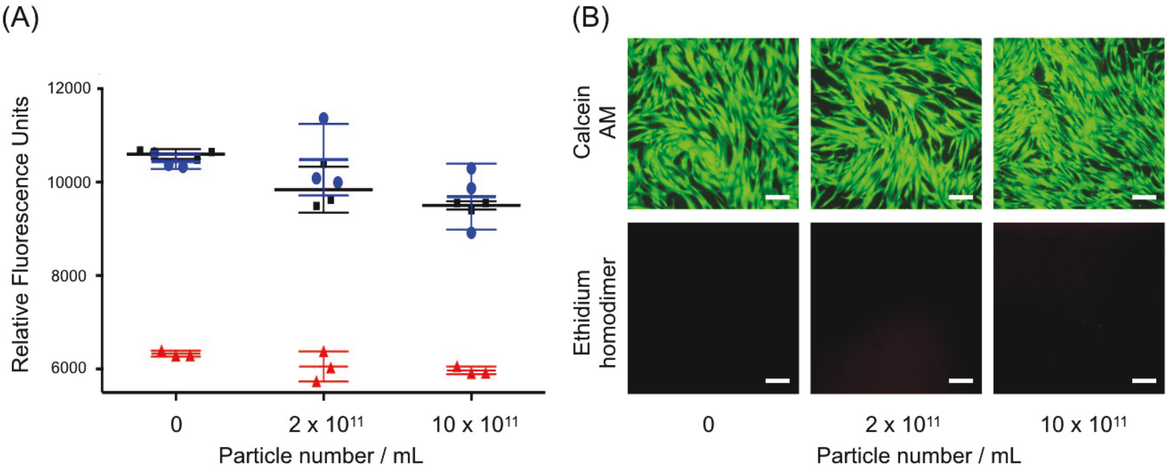

Figure 3.10 Cytotoxicity of the glycosylated SPIONs

Viability analysis of glycosylated SPIONs. (A) An alamarBlue® assay of the effect of glycosylated SPIONs upon hMSCs (3 donors in red, blue, and black), with values representing the metabolic activity of hMSCs exposed to 0, 2 × 10^{11} or 10 × 10^{11} glycosylated SPIONs. (mean ± 95% confidence intervals, N = 3, n = 3). (B) LIVE/DEAD™ staining of hMSCs treated with glycosylated SPIONs showing a large number of viable cells (green, calcein AM) and negligible staining for dead cells (red, ethidium homodimer). The figure is reproduced from Li et al. [93]. Scale bars = 200 µm.

3.3.2 Optimisation for Osteochondral Differentiation

The hMSC laden hydrogels were cultured in individual wells, therefore, a medium cocktail that could support both chondrogenesis (in this study, hMSCs to chondrocytes) and osteogenesis (in this study, hMSCs to osteoblasts) was crucial.

Several established protocols were considered for the final composition of osteochondral medium in this study [68, 137, 260, 261]. To ensure the osteochondral medium can support the cartilage formation of the tissue, TGF-β3, a conventional growth factor for cartilage tissue engineering was included at the commonly used concentration of 10 ng mL^{-1}. Alongside TGF-β3, other suitable protein supplements were also included, such as insulin-transferrin-selenium, which is found to enhance chondrocytes proliferation and retain chondrogenic phenotypes (*i.e.*, lower mRNA levels of Col X and MMP13) [262]) and other small molecule supplements including ascorbic acid and dexamethasone. It has been shown that ascorbic acid is crucial in the generation of hydroxyproline and hydroxylysine, which are both amino acids used for collagen fibril formation [263], and that dexamethasone could potentiate the TGF-β induced chondrogenesis process [264].

To ensure the formation of the characteristic bone ECM (*i.e.*, deposition of minerals) at the high BMP-2 content end within the construct, β-glycerophosphate was included in the optimised osteochondral differentiation medium. It should be noted that, within the study, the β-glycerophosphate was used at a concentration of 2 mM, a level that has been shown to provide a source of phosphate without initiating osteogenesis or nonspecific mineral precipitation [265]. To verify the differentiation effects of the proposed medium, a conventionally used chondrogenic and osteogenic medium were included as a positive control.

Histology assays were performed to effectively determine the differentiation outcome. Firstly, Alcian Blue was used to investigate the production of GAGs, which are one of the main indicators for chondrogenic differentiation. As Figure 3.11 demonstrates, after 28 d culture, the proposed osteochondral medium supported the chondrogenic differentiation of hMSCs within the agarose hydrogel. In addition to the Alcian Blue staining, Alizarin Red S staining was used to investigate the presence of calcium deposits. With the presence of BMP-2, as Figure 3.11

demonstrates, at the commonly used concentration at 30 ng mL^{-1}, osteogenic differentiation could be observed.

In the study, it was vital that the optimised medium could only support the osteogenic process in the presence of BMP-2, to avoid the nonspecific differentiation of cells across the BMP-2 gradient patterned hydrogel. This requirement was tested by using the same differentiation set-up but without the supplement of the BMP-2. Using this set-up, after 28 d of culture, there was no calcium deposition observed in the hydrogels. These results suggest that the osteogenic differentiation triggered in the system was specific, and only triggered in the presence of BMP-2. Indeed, based on these histological observations, the proposed osteochondral medium was able to fulfil the requirements of the system.

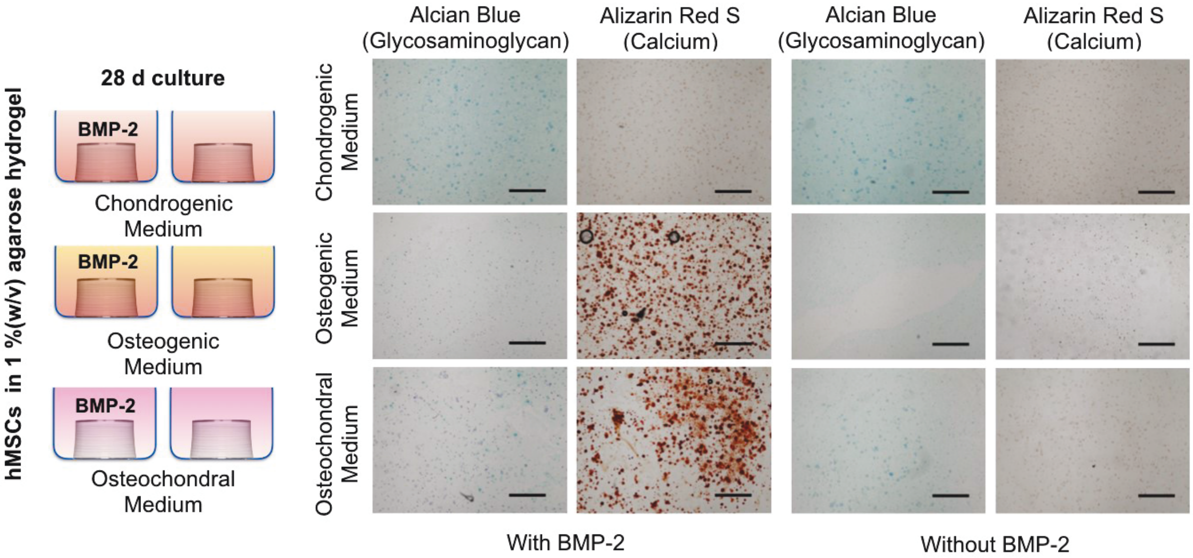

Figure 3.11 Optimisation of osteochondral medium

Effect of medium composition and BMP-2 upon osteochondral tissue engineering. Tissue constructs were engineered for 28 d using hMSC-laden agarose hydrogels. Alizarin Red S staining showed deposition of calcium mineral (red) when exposed to BMP-2 and cultured in osteogenic and osteochondral medium. Alcian Blue staining showed glycosaminoglycan (blue) in chondrogenic and osteochondral medium, either in the presence or absence of BMP-2 (30 ng/mL). The figure is reproduced from Li et al. [93]. Scale bars = 500 µm.

3.3.3 Required Duration of BMP-2 Supplement

While the previous section revealed the optimised osteochondral medium could support both osteogenic and chondrogenic differentiation through supplementation of BMP-2 and TGF-β3, it was important to identify the minimal duration that the BMP-2 supplement was required to achieve osteogenic differentiation. While some literature has suggested the short-term (6 d) addition of BMP-2 could sufficiently trigger osteogenic differentiation [104], the time scale required for differentiation using our optimised BMP-2 containing medium was unclear.

To determine the osteogenic differentiation outcome by varying durations of exposure to BMP-2, Alizarin Red S staining was used after 21 d of culture. Specifically, monolayer cultures of hMSCs were cultured with osteochondral medium supplemented with TGF-β3 and different durations of BMP-2 as shown in Figure 3.12. Supported by the positive staining of Alizarin Red S, the results suggested that in a system with more than 11 d of BMP-2 supplement, mineralisation could take place. Based on this simplified 2D screening result, a sustained release system exceeding 11 d of culture with BMP-2 could be expected to trigger successful osteogenic differentiation.

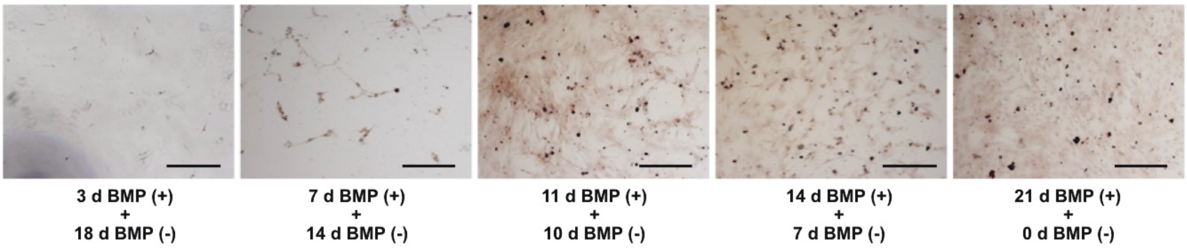

Figure 3.12 Osteogenic differentiation outcome at different BMP-2 supplement durations

Effect of duration of BMP-2 supplement (30 ng/mL) upon osteogenic differentiation. Tissue constructs were engineered for 21 d using hMSC-laden agarose hydrogels exposed to different durations of BMP-2 supplement. Alizarin Red S staining showed deposition of calcium mineral (red) when exposed to more than 11 d of BMP-2 when cultured with the osteochondral medium. Scale bars = 500 µm.

3.3.4 Sustained Release BMP-2 System

In this study, heparin was used as the carrier for BMP-2. While avidin was used as a model protein for estimating the protein loading capacity in section 3.4.1, for a more accurate releasing dynamic, the exact release profile was investigated using BMP-2. The release study was carried out with a fabrication protocol similar to the tissue engineering set-up: BMP-2 was first incubated with glycosylated SPIONs, and the BMP-2 loaded glycosylated SPIONs were encapsulated within the agarose hydrogel. To determine the release profile of BMP-2, an enzyme-linked immunosorbent assay (ELISA) was used.

Samples were collected, and their BMP-2 concentration were measured at different time points. By comparing the BMP-2 quantity to a total release control (a separate vial prepared from directly frozen 100% loaded BMP-2), a cumulative release curve could be established. As shown in Figure 3.13, a sustained release profile of BMP-2 was observed and the quantity of BMP-2 remained within the hydrogel was estimated. It was revealed that 65 ± 3% of encapsulated BMP-2 could be slowly released over a period of 28 d. However, it should be noted that around 20% of loaded BMP-2 was released within the first 24 h. This release profile was further used to inform the tissue engineering experiment, in which the undesired osteogenic differentiation at the cartilage end of the construct may be triggered by this initial burst release of BMP-2. Accordingly, in the final culture protocol, the culture medium was changed at 2 h and 16 h after the cell seeding. In the present study, it was hypothesised that the spatial differentiation could be triggered by the unreleased BMP-2 bound on the glycosylated SPIONs.

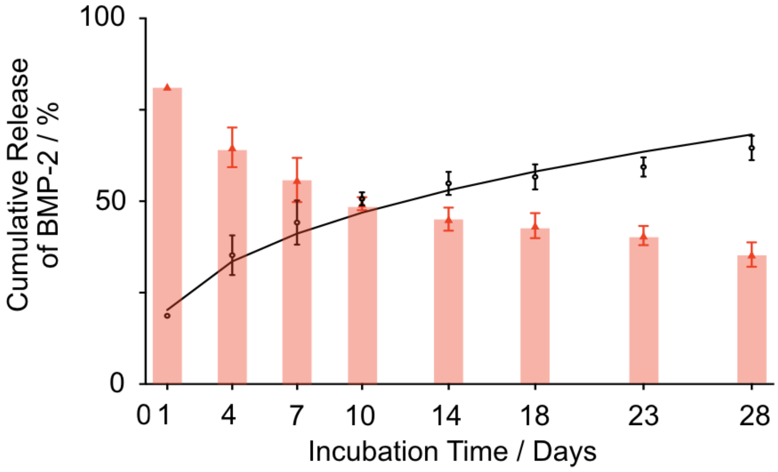

Figure 3.13 Release profile of BMP-2

Release profile of sequestered BMP-2 on glycosylated SPIONs was investigated within agarose hydrogels. While the burst release of 20% loaded BMP-2 was still observed within the first 24 h, the remaining loaded BMP-2 could be gradually released from the glycosylated SPIONs over 28 d (N=3). The amount of unreleased BMP-2 within the hydrogel was estiamted (pink bars). The release curve (black line) was fit using a Korsmeyer-Peppas model, which was developed to specifically model the release of molecules from a polymeric matrix [188] (R^2 = 0.97). The figure is reproduced from Li et al. [93].

3.3.5 Sustained Release of BMP-2 Supports the Local Osteogenic Differentiation

Based on the results described in the previous sections, *i.e.*, the required duration of BMP-2 supplement for osteogenic differentiation and sustained release profile of BMP-2 in the glycosylated SPIONs carrier system, it was hypothesised that the BMP-2 loaded glycosylated SPIONs should support the osteogenic differentiation of the hMSCs encapsulated in the agarose hydrogel. In section 3.4.2 (Optimisation of Osteochondral Differentiation), the osteochondral medium was supplemented with both 10 ng TGF-β3 mL^{-1} and 30 ng mL^{-1} BMP-2. In the final gradient tissue engineering set-up, however, only TGF-β3 was supplemented in the medium. Instead of being supplemented in the medium throughout the culture, the BMP-2 was only delivered initially as the bounded cargo of glycosylated SPIONs. To test if the BMP-2 loaded glycosylated SPIONs could support the osteogenic differentiation, hMSC-laden agarose with glycosylated SPIONs loaded with 6 μg mL^{-1} BMP-2 was first tested.

In this experiment, the osteogenic differentiation outcome was measured under three conditions: (1) osteochondral medium supplemented with 30 ng mL^{-1} BMP-2, (2) BMP-2 bound glycosylated SPIONs at a particle concentration of 10^{12} mL^{-1} and a final BMP-2 concentration of 6 μg mL^{-1}, and (3) glycosylated SPIONs without BMP-2 loading at a particle concentration of 10^{12} mL^{-1}.

Here, 9×10^6 mL^{-1} of hMSCs were encapsulated within the agarose hydrogel. To estimate the loading dose, the total amount of supplemented BMP-2 throughout the culture period in group (1) was calculated. Accordingly, 600 ng of BMP-2 was first incubated for at least 4 h with 10^{11} SPIONs prior to the fabrication of constructs to ensure efficient loading. After the loading, constructs were cast with BMP-2 loaded glycosylated SPIONs and cultured within the designed osteochondral medium for 28 d. As Figure 3.14 demonstrates, the BMP-2 loaded glycosylated SPIONs could trigger calcium deposition (top row, the positive staining of Alizarin Red S) as when the BMP-2 was continuously supplemented (30 ng mL^{-1}) with the osteochondral medium (middle row, the positive staining of Alizarin Red S). The positive staining of Alizarin Red S suggests the osteogenic differentiation of hMSCs, with GAG deposition present in both cases. On the other hand, in the absence of BMP-2 supplement but only glycosylated SPIONs (bottom row, negative staining of Alizarin Red S), calcium deposition was not observed. Taken together, these results verified that BMP-2 released from glycosylated SPIONs could initiate mineralisation to a similar level as BMP-2 supplemented in medium, and the use of glycosylated SPIONs itself did not exhibit the osteogenic effect.

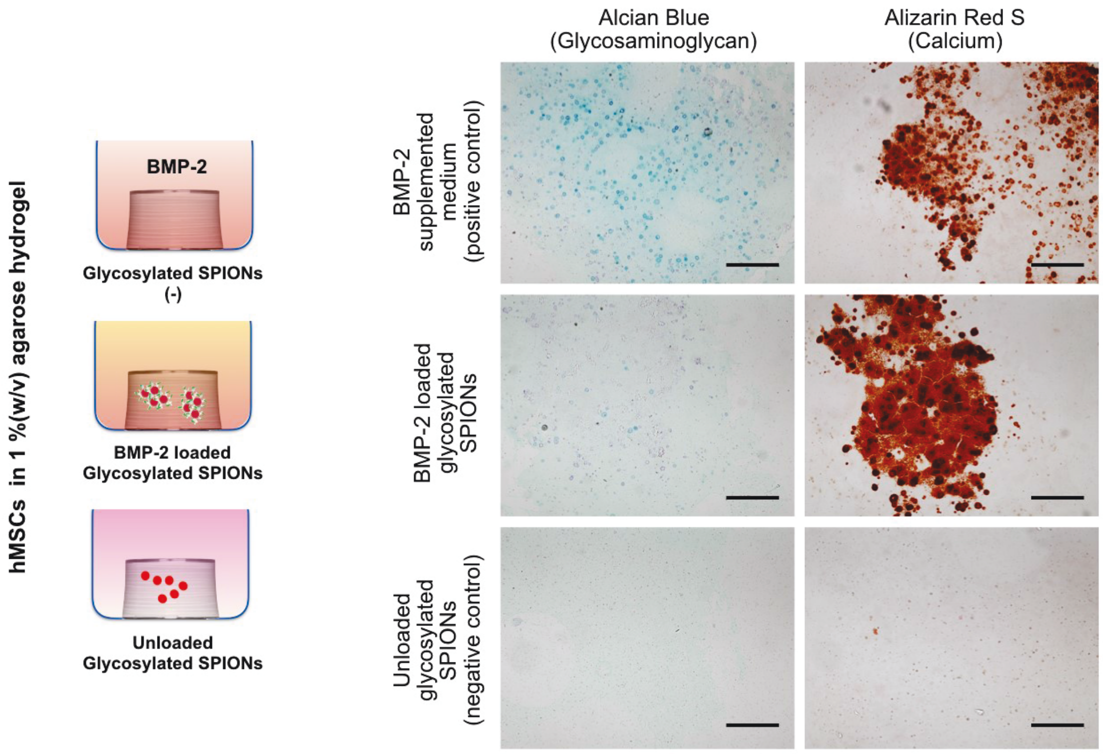

Figure 3.14 BMP-2 loaded glycosylated SPIONs enable the osteogenic differentiation of hMSCs

Effect of BMP-2 delivery mode upon tissue mineralisation. Tissue constructs were engineered for 28 d using hMSC-laden agarose hydrogels. Alizarin Red S staining showed deposition of calcium mineral (red) when BMP-2 was delivered in the medium or from glycosylated SPIONs, but not when exposed to unloaded SPIONs. Alcian Blue staining showed glycosaminoglycan (blue) in all cases. The figure is reproduced from Li et al. [93]. Scale bars = 500 μm.

3.3.6 Optimisation of BMP-2 Loading

Osteochondral tissue engineering: preliminary study

Having verified the osteogenic differentiation triggered by BMP-2 loaded glycosylated SPIONs, the potential of the system in creating gradient tissue constructs was investigated. Agarose hydrogel was used for gradient fabrication in this study. As described in the previous sections, a gellable hydrogel is needed to preserve the patterned gradient within the proposed casting technology. In the study, agarose hydrogel was used for two main reasons. Firstly, the gelation should only be triggered once the gradients are fully established. Secondly, an ideal substrate for this system should be biologically inert. Although using materials with a bioactive signal is becoming attractive in modern tissue engineering, as the first attempt in gradient tissue engineering with a SPIONs-based system, selecting an inert material in the present study could, in fact, help us better understand the influence of the generated growth factor gradient. Considering these factors, thermo-responsive agarose hydrogel was used.

The first batch of gradient constructs was fabricated considering the results from the previous experiments. In brief, 30 μL of agarose hydrogel precursor comprising 9×10^6 mL^{-1} of hMSCs and 10^{12} mL^{-1} SPIONs loaded with 6 μg mL^{-1} of BMP-2 were dispensed into the mould, followed by the careful injection of 60 μL of the agarose hydrogel precursor containing 9×10^6 mL^{-1} of hMSCs. The magnet was subsequently applied from 3 mm above the mould to redistribute the BMP-2 loaded glycosylated SPIONs into a gradient. After the formation of the gradient, the set-up was then moved to from 37°C to 4°C for gelation, with the magnet still placed on top of the set-up. After gelation, the gradient hydrogel was transferred into a 24-well plate and cultured in osteochondral differentiation medium for 28 d.

While a tissue with a distinctive bone and cartilage end was hypothesised to be generated after the culture, it was instead found that after 28 d of culture, the whole tissue was positively stained with Alizarin Red S. Instead of generating heterogeneous constructs, this method produced homogeneous constructs with mineralisation throughout (Figure 3.15).

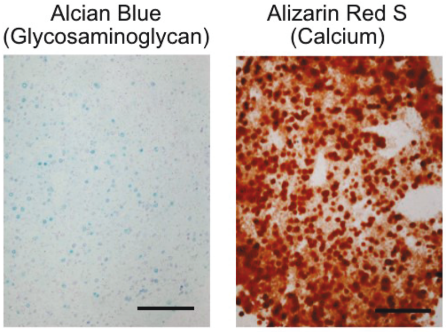

Figure 3.15 Alcian Blue and Alizarin Red S staining of the preliminary osteochondral tissue engineering experiment

The preliminary study of gradient osteochondral tissue prepared by 6 μg mL^{-1} BMP-2 results *in mineralisation of the whole construct after 28 d of culture. Scale bar = 1 mm.*

Optimisation of BMP-2 loading

While there is no literature revealing the exact BMP-2 concentration gradients within osteochondral tissue *in vivo*, the dose of BMP-2 used in the set-up need to be optimised systematically. Based on Figure 3.15, the result of overall mineralisation suggested that the total level of BMP-2 loaded into the glycosylated SPIONs was too high. With a large excess of unconsumed growth factor capable of diffusing out of the hydrogel, the osteogenesis was also triggered in adjacent, nanoparticle-free region of constructs (Figure 3.16 A). To address this, the level of BMP-2 in the glycosylated SPIONs required optimisation, therefore a loading experiment was designed. In the experiment, two independent agarose hydrogels, with one containing both hMSCs and glycosylated SPIONs loaded with BMP-2 and the other containing only hMSCs, were cultured within the same well. Importantly, the culture conditions (28 d in the optimised osteochondral medium) and the volume ratio of the two hydrogels were consistent with the previous gradient set-up (Figure 3.16 B). Different loading amounts including 6 (the concentration used in the preliminary test), 3 and 0.3 μg mL^{-1} of BMP-2 were tested. The aim of this optimisation was to investigate an ideal level of BMP-2 loading that only triggered the mineralisation process in the hydrogel with glycosylated SPIONs, *i.e.*, the diffused BMP-2 shouldn't trigger the undesired osteogenic process on cells embedded in agarose without glycosylated SPIONs.

After 28 d of culture, Alizarin Red S staining was used to identify the occurrence of mineralisation. As demonstrated in Figure 3.16 C, when the same loading level of BMP-2 was used (6 μg mL^{-1} hydrogel) the undesired mineralisation was observed in the adjacent glycosylated SPIONs free hydrogel. However, when this was reduced to 3 μg mL^{-1} of BMP-2, only the hydrogel with glycosylated SPIONs were positively stained. It should be noted that there is a lower limit of BMP-2. For instance, at 0.3 μg mL^{-1}, mineralisation could not be triggered in either construct, with or without loaded glycosylated SPIONs. Henceforth, in the following experiments, BMP-2 at a concentration of 3 μg mL^{-1} was used.

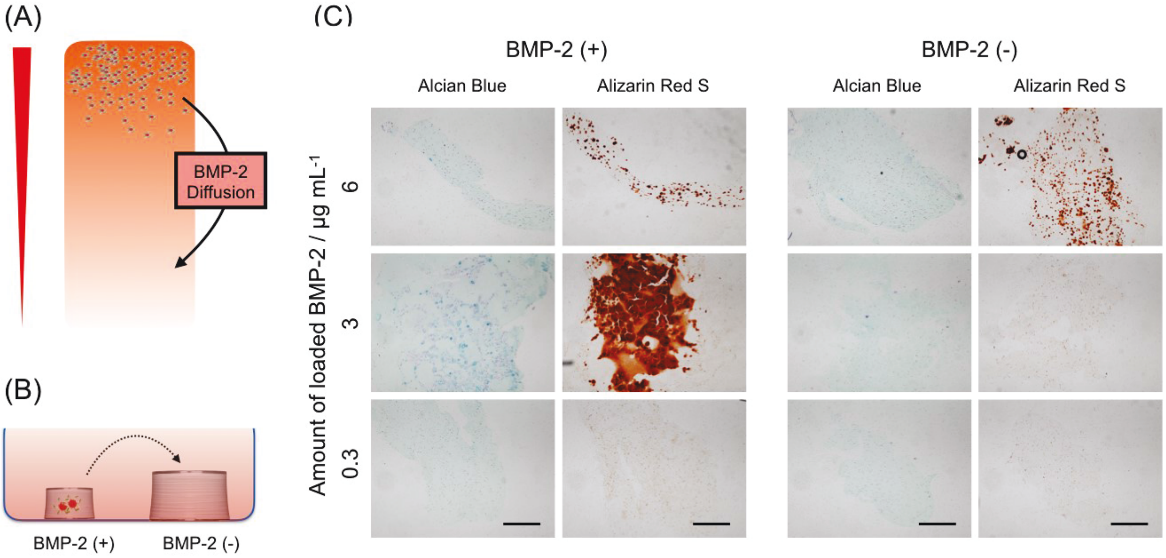

Figure 3.16 Optimised BMP-2 loading triggered mineralisation only when BMP-2 loaded glycosylated SPIONs were present

(A) The excess of BMP-2 released from one end of the construct could trigger the osteogenesis in the adjacent, nanoparticle-free region of the construct. (B) To optimise an appropriate BMP-2 loading level, 2 independent agarose hydrogels (volume ratio: 2:1) with and without BMP-2 loading were cultured in a single well for 28 d using the optimised osteochondral medium (C) Optimising BMP-2 loading to confine regions of tissue mineralisation. Tissue constructs were engineered for 28 d using hMSC-laden agarose hydrogels with BMP-2 loaded glycosylated SPIONs, alongside adjacent hMSC-laden agarose hydrogels without any loaded SPIONs. Alizarin Red S staining showed deposition of calcium mineral (red) in both the SPION laden and the adjacent construct at the highest BMP-2 loading (6 µg mL^{-1} of hydrogel), only in the SPION laden construct at the intermediate BMP-2 loading (3 µg mL^{-1} of hydrogel) and in neither of the constructs at the low BMP-2 loading (0.3 µg mL^{-1} of hydrogel). Alcian Blue staining showed sulphated glycosaminoglycan (blue) in all cases. Scale bars = 500 µm.

3.3.7 Characterisation of Osteochondral Gradient Construct

After all the necessary optimisation steps, including the composition of osteochondral medium, amount of glycosylated SPIONs and amount of loaded BMP-2, the final system was assembled with BMP-2 (3 µg mL^{-1}) loaded glycosylated SPIONs (10^{12} mL^{-1}) magnetically-aligned within a hMSC-laden agarose hydrogel (9×10^6 mL^{-1} hMSCs in 1% (w/v) agarose).

The final set-up should slowly release the active BMP-2 over 28 d and should stimulate hMSC osteogenesis and tissue mineralisation predominantly at one end of the tissue. In the following sections on characterisation results, the construct end that was initially patterned with a higher amount of BMP-2 is referred to as the bone end, and the other end of the construct is referred to as the cartilage end.

Using the set-up, the constructs were cultured in the optimised osteochondral medium for 28 d. After 14 d, the vast majority of the tissue constructs started to develop striking white opacity at the bone end (Figure 3.17 A). It should be noted that approximately 10% of the engineered constructs failed to produce any visible mineralisation, and these were excluded from further study. In all cases, however, the gradient hydrogels produced tissue constructs that were structurally robust, with no macroscopic defects observed between the bone and cartilage ends of the tissue.

To investigate if the gradient set-up could provide an even distribution of embedded cells, both the cell distribution of hydrogels generated from the bilayer stack and magnetically aligned gradients were examined. Interestingly, it was found that there was a distinct 200 µm margin between the two ends of the tissue in the stacked, bilayer constructs. This was in stark contrast with the gradient set-up. Further investigation revealed that these margins were formed prior to tissue culture, with the bilayer interface appearing to exclude hMSCs (Figure 3.17 B). The exact mechanism underpinning this observation is unknown, nevertheless, the ability to avoid such tissue defects represents a major advantage for the developed gradient biomaterial over simple bilayer systems.

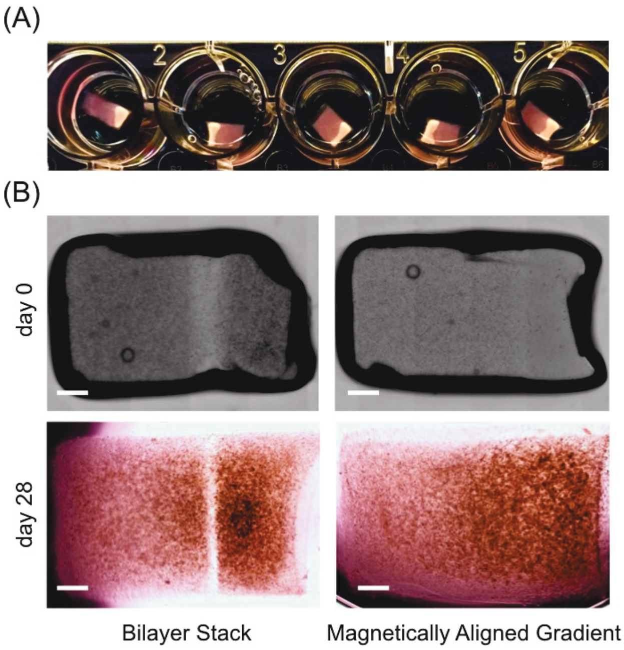

Figure 3.17 Macroscopic view of differentiation outcome after 28 d of culture, and distribution of the cells within gradient and bilayer set-up

(A) The final system was assembled with BMP-2 (3 µg mL^{-1}) loaded glycosylated SPIONs (10^{12} mL^{-1}) magnetically-aligned within a hMSC-laden agarose hydrogel (9 × 10^{6} mL^{-1} hMSCs in 1% (w/v) agarose). Strikingly opaque caps were observed after roughly 14 d of culture. These caps were located at the end with a higher initial BMP-2 loading. The constructs were in 24-well plates. (B) Bright field microscopy images of a magnetically aligned gradient and a bilayer stack, both with hMSCs in agarose, captured immediately after gelation. The gradient material exhibits an even distribution of hMSCs throughout the construct, whereas a margin can be clearly observed between the two phases of a layered stack. The figure is reproduced from Li et al. [93]. Scale bars = 1 mm.

Gene levels

Alongside these macroscopic observations, the osteochondral tissue gradient constructs were characterised after 28 d of culture using gene expression analysis. For both ends of the construct, gene expression analysis using quantitative polymerase chain reaction (qPCR) revealed significant upregulation in the mRNA of both chondrogenic genes (*COL2A1, SOX9, ACAN*) and osteogenic genes (*SP7, RUNX2, COL1A1, ALPL, COL10A1*), compared to undifferentiated hMSCs at day 0 (Figure 3.18). The observed upregulation indicated a positive effect of both the media-supplemented TGF-β3 and the SPION-loaded BMP-2.

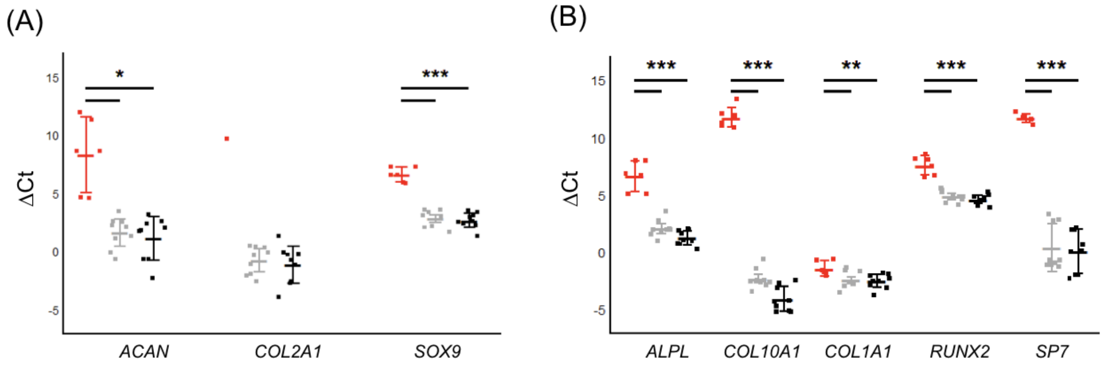

Figure 3.18 Gene expression analysis - comparison with expression on day 0

Gene expression analysis of engineered osteochondral tissue. (A) ΔCt values for the bone region (black), the cartilage region (grey) and a day 0 control (red) for genes associated with cartilage formation and (B) bone formation (mean ± 95% confidence intervals, N = 3, n = 3 for 28 d constructs. N = 3, n = 1 for day 0 control; the COL2A1 gene was only detected in one donor on day 0 but was detected for all 28 d samples). Welch's t-test was used. The statistical analysis was carried out with assistance from Dr. Isaac Pence. The figure is reproduced from Li et al. [93].

More importantly, a higher expression of osteogenic genes in the bone region compared to the cartilage region were observed (N = 3, n = 3) (Figure 3.19 A). Significantly up-regulated genes included *ALPL* and *COL10A1*, which are responsible for the expression of alkaline phosphatase and type X collagen, respectively. Importantly, we observed no significant differences between the bone and cartilage ends of the construct for any of the chondrogenic genes screened (Figure 3.19 B). These gene expression analyses strongly indicated that the soluble TGF-β3 acted globally across the tissue, while the magnetically-aligned gradient of BMP-2 influenced the osteogenic differentiation of hMSCs in a spatially-defined manner.

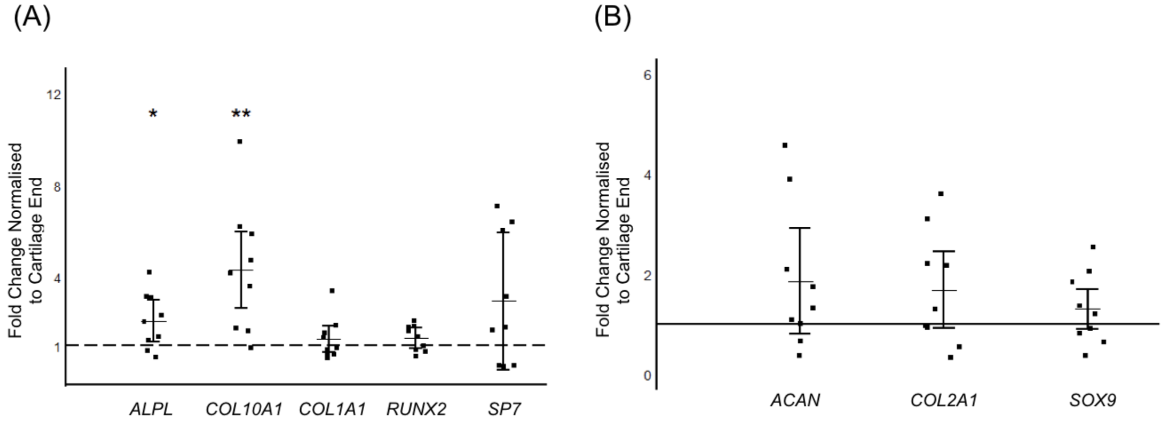

Figure 3.19 Gene expression analysis - comparison between both ends

(A) Gene expression of five osteogenic genes at the bone region of the tissue, compared to the cartilage region. Comparisons of differences were made using a one sample t-test after heteroscedasticity in the dataset was addressed. (B) The bone region was normalised to the cartilage region for three cartilage-associated genes, showing no significant differences between the two regions. Comparison of differences were made using a single sample t-test (mean ± 95% confidence intervals, N = 3, n = 3) where $p < 0.05$ (*), $p < 0.01$ (**), $p < 0.001$ (***). After normalising the gene expression level at the bone region to the expression level at the cartilage region, one sample student t-test was used. The statistical analysis was carried out with assistance from Dr. Isaac Pence. The figure is reproduced from Li et al. [93].

Distribution of Extracellular Matrix

The ECM and protein expression were next investigated using Alcian Blue staining for GAGs and immunofluorescence staining for Collagen type I, II, X, and Osteopontin. Firstly, Alcian Blue and immunofluorescence staining for type I and II collagen revealed extensive extracellular matrix deposition, with cells located in well-defined lacunae (Figure 3.20). The presence of these components was expected since glycosaminoglycans and type II collagen are the two major components of physiological hyaline cartilage, while type I collagen is commonly expressed in engineered cartilage constructs, particularly those grown using hMSCs [266]. Interestingly, although there are no spatial differences observed in the gene expression of *COL1A1* and *COL2A1* (Figure 3.18), the immunostaining appeared to qualitatively show a higher quantity of both type I and type II collagen at the cartilage end of the tissue (Figure 3.20). The discrepancy between the mRNA and protein levels can be attributed to the fact that gene expression and matrix remodelling are dynamic processes that are not always correlated in an end-point tissue analysis [267]. A more thorough investigation on downstream signaling pathways across 28 d culture periods using technique such as spatial transcriptomics could shed light on the spatial and temporal dynamics between mRNA expression and ECM production.

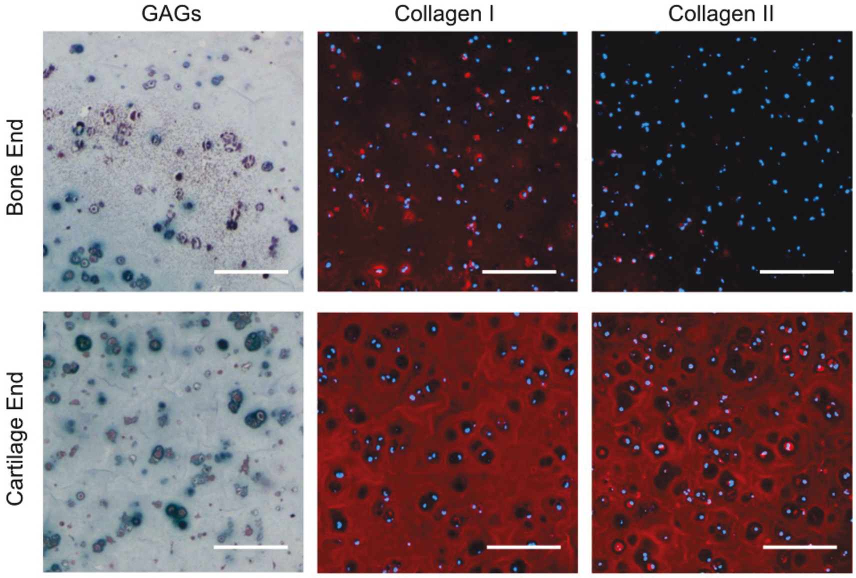

Figure 3.20 Distribution of the ECM – Collagen Type I, II and GAGs

The ECM and protein expression were investigated using Alcian Blue staining (GAGs) and immunofluorescence staining (Collagen type I, and Collagen type II). Histological and immunofluorescence staining of key extracellular matrix proteins present in cartilage and bone revealed deposition of sulphated glycosaminoglycans (blue) and type I and II collagen (red). The presence of well-defined lacunae structure can be found in both collagen I and collagen II staining. DAPI staining was used to stain cell nuclei. Scale bars = 200 μm. The figure is reproduced from Li et al. [93].

Secondly, type X collagen was found predominantly at the region between the bone and cartilage regions, which indicated a zone of hypertrophic chondrocytes, as those found in the deep zone of natural cartilage tissue [268] (Figure 3.21 A). Finally, osteopontin, a key marker of osteogenesis and biomineralisation, was present exclusively in the bone region of the tissue (Figure 3.21 B). In summary, by histology staining and immunofluorescence staining, it is shown that the differences in gene expression could spatially influence matrix composition and structure in the tissue constructs.

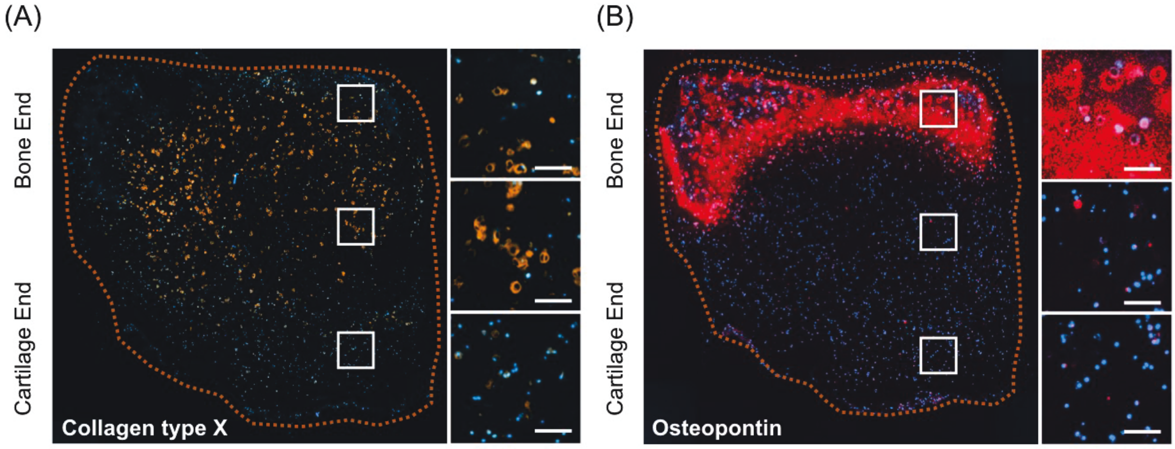

Figure 3.21 Distribution of the ECM – Collagen type X and Osteopontin

The ECM and protein expression were investigated using immunofluorescence staining (Collagen type X, and Osteopontin). (A) By immunofluorescence staining, type X collagen (orange), a protein in hypertrophic chondrocytes, was found mostly located in the middle of the construct. (B) The key mineralisation protein, osteopontin (red), was present specifically at the bone end of the tissue. DAPI staining was used to stain nuclei. Scale bars = 200 μm. The figure is reproduced from Li et al. [93].

Mineral formation and mineral characterisation

Apart from the ECM distribution, the activity of various enzymes was also expected to be at different levels. Among all the enzymes, the alkaline phosphatase, which catalyses the hydrolysis of organic phosphates into inorganic phosphate ions during tissue mineralisation [269], was expected to be higher at the bone end of the construct. Accordingly, the spatially-controlled osteogenic response was further corroborated using an alkaline phosphatase (ALP) activity assay. Indeed, after normalising the ALP activity with the amount of DNA within each sample, the assay revealed a 2.8-fold ALP activity in the bone region compared to the cartilage region (Figure 3.22).

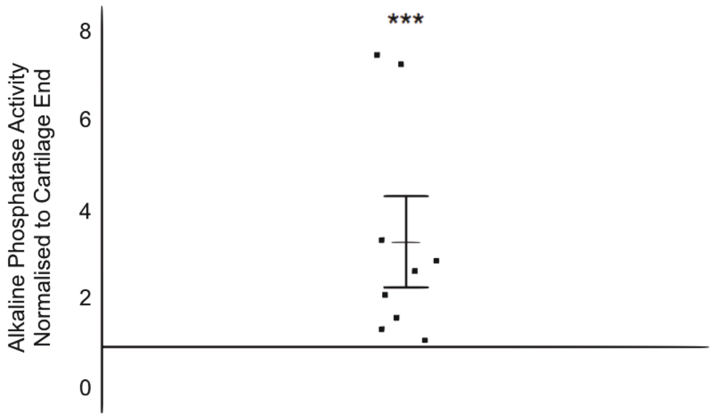

Figure 3.22 Difference in ALP activity at different ends

(A) Alkaline phosphatase measurements showing a significantly higher activity at the bone region, compared to the cartilage region. Comparisons of differences were made using a one sample t-test after heteroscedasticity in the dataset was addressed (mean ± 95% confidence intervals, N = 3, n = 3). After normalising the level of ALP activity at the bone region to the activity at the cartilage region, one sample student t-test was used. p < 0.001 (***).

This result suggested that the mineral deposition should predominately concentrate on the bone-end of the construct. To this sense, Alizarin Red S staining was used to assess the mineral distribution, and the staining revealed that the bone region was comprised of dense calcium-rich nodules (Figure 3.23).

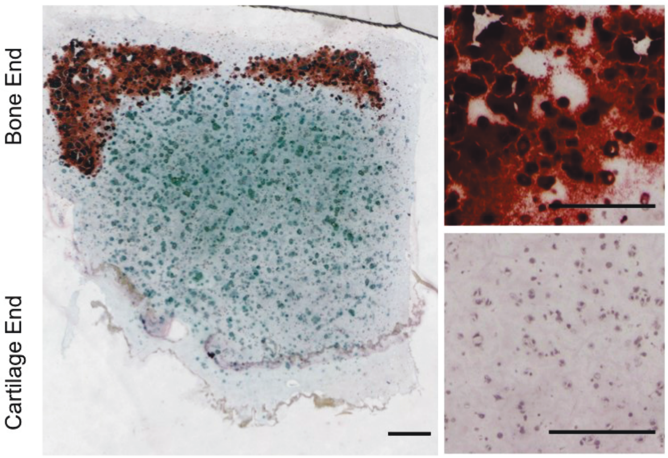

Figure 3.23 Difference in calcium deposition at different ends

Alizarin Red S staining of calcium deposits (red) and Alcian Blue staining of sulphated *glycosaminoglycan (blue) in engineered osteochondral constructs showed mineralisation specifically at the bone end of the tissue while the sulphated glycosaminoglycans were present throughout the engineered tissue. Scale bars = 500 μm. The figure is reproduced from Li et al. [93].*

To further investigate the properties of the mineral species, Raman microscopy was used. Using the Raman microscopy, the presence of two distinct calcium phosphate morphologies: hydroxyapatite (HAP) and β-tricalcium phosphate (β-TCP) in the mineral cap were identified using the reference spectra derived from the mineral standards (Figure 3.24 A). HAP is a non-degradable and mechanically-robust mineral, while β-TCP is a bioresorbable salt with osteoinductive degradation products. Importantly, the presence of both morphologies is desirable during bone formation [270, 271]. Moreover, in both the Alizarin Red S staining and the Raman mapping, negligible calcium phosphate could be detected in the cartilage region. Indeed, by integrating the Raman contributions from β-TCP and HAP, a sharp transition in mineral content from bone to cartilage was able to be detected (Figure 3.24 B). Importantly, this observation was consistent with both the osteopontin immunofluorescence staining and the macroscopic images of the engineered tissue.

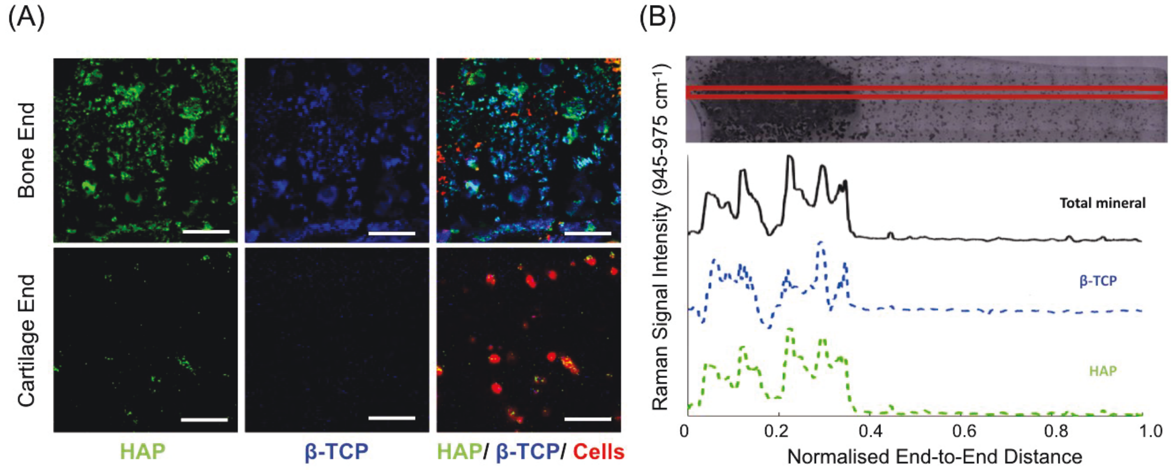

Figure 3.24 Characterisation of mineral in the constructs

With the mineral standard of HAP and TCP, (A) Raman microscopy of HAP (green), β-TCP (blue) and cells (red) also showed mineralisation specifically in the bone region. Scale bars = 100 μm. (B) Profile of Raman intensity corresponding to the integrated signal from HAP and b-TCP (945 - 975 cm^{-1}) across the length of the osteochondral tissue construct, with a bright *field microscopy image for reference. The total mineral signal corresponded to the integrated signal from HAP (v_1 PO_4 at 962 cm^{-1}) and β−TCP (v_1 HPO_4^{2-} at 948 cm^{-1}). The signals were offset to avoid overlapping. Scale bars = 500 µm. The Raman Spectroscopy was conducted by Dr. Isaac Pence. The figure is reproduced from Li et al. [93].*

Mechanical properties

Finally, the mechanical properties of the osteochondral constructs were assessed using unconfined compression (N = 3, n = 3). Representative plots for the mechanical testing are shown in Figure 3.25 A. 5% strain increments were applied to each sample for 12 steps. The reaction force and displacement were measured. The peak stress values for each compression step were then used to plot instantaneous stress versus strain. A bilinear model was fit to the data to derive the instantaneous modulus (Figure 3.25 B). Only the values in the low-strain region, *i.e.,* below the linear fit transition, are reported since engineering stress rather than true stress was measured. By assessing only the low-strain region, artefacts from sample overload at the high-strain region would not bias the data. The instantaneous stress-strain response of the bone and cartilage regions revealed a higher 1.9-fold instantaneous modulus at the bone end compared to that of the cartilage end of the construct. This observation could be attributed to differences in matrix composition, such as the presence of minerals in the bone region [272]. However, this difference in stiffness was not significant, and the higher modulus was only found in one out of three biological replicates (Figure 3.25 C).

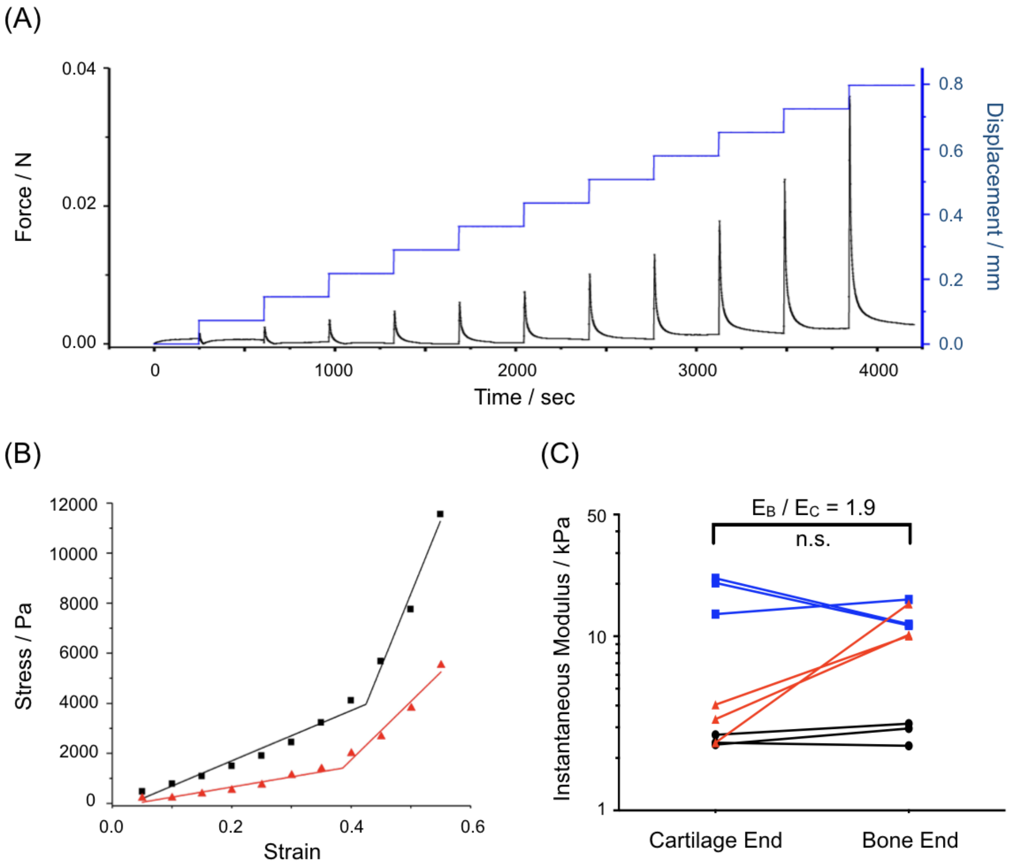

Figure 3.25 Mechanical properties difference between two ends of the engineered constructs

(A) Unconfined compression testing was performed using the engineered osteochondral tissue, with 12 steps of 5% strain increments. The reaction force (black trace, x-axis) and displacement (blue trace, y-axis) were measured. (B) The peak stress of each compression cycle was used to plot instantaneous stress versus strain for the bone end (black square markers) and the cartilage end (red triangle markers). A bilinear model was then fit to the data. The instantaneous modulus was calculated as the slope of the linear regression prior to the transition point. (C) The instantaneous modulus calculated in (B) were used for pairwise comparisons between tissue constructs engineered from three different hMSC donors (denoted by red, black and blue markers). Comparisons of differences were made using a one sample t-test after heteroscedasticity in the dataset was addressed (mean ± 95% confidence intervals, N = 3, n = 3) where $p < 0.05$ (*). The mechanical property measurements were assisted by Dr. Jennfier Puetzer and Dr. Worrapong Kit-Anan. The data analyses were conducted with the assistance from Dr. Axel Moore. The figure is reproduced from Li et al. [93].

3.3.8 Uptake of glycosylated SPIONs

As a system utilising inorganic nanoparticles, the uptake of glycosylated SPIONs was assessed. To this end, transmission electron microscopy (TEM) was used to investigate the distribution of SPIONs within the construct. Hydrogels embedded with hMSCs and glycosylated SPIONs were collected after 10 d of the tissue engineering culture. After fixing the constructs with glutaraldehyde and osmium tetroxide, samples were embedded within resin for ultramicrotome sectioning and 85 nm sections were used for TEM. Cells within agarose hydrogel have a rounded morphology without protrusions required for cell movement. Nevertheless, SPIONs were found within encapsulated cells, which raises the concern for *in vivo* applications. Investigation on nanoparticles metabolism is essential for further translational studies.

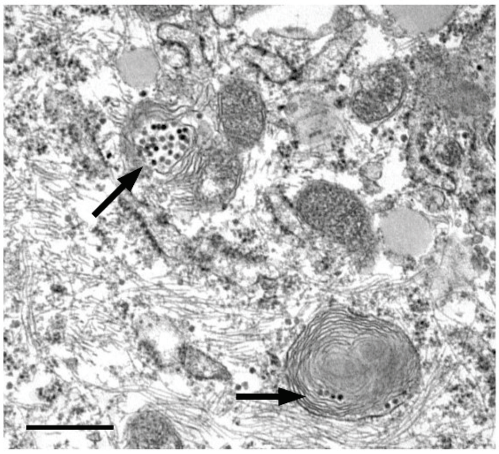

Figure 3.26 Uptake of glycosylated SPIONs

Under the TEM, the presence of the 20 nm inorganic nanoparticles was observed within cells. This was attributed to the intracellular uptake of the glycosylated SPIONs. Scale bar = 500 nm. Ultramicrotome sectioning and images acquisition were assisted by Kerrie Venner, technical manager of EM facility at UCL.

3.4 Conclusions and Future Perspective

Conclusions

There are few gradient-casting strategies that have been exploited to create heterogeneous tissue. Strategies such as combing separate biomaterials layers by suture or solvent have been applied in clinical applications [57, 109], however, discontinuities at the interface are found in these simple bilayer scaffolds, making them highly susceptible to delamination [79]. While smoother transitions can be achieved using strategies such as a gradient maker, the fabrication process is usually slow and complicated. As summarised in section 1.4, an ideal method for gradient casting should be rapid, versatile and doesn’t require any special equipment.

In this chapter, it was demonstrated that a readily available strong magnet can create SPIONs gradients with only a few limitations such as size of SPIONs, the viscosity of substrate, and suitable hydrogel selection. By tailoring surface chemistry of SPIONs, the proposed platform should allow the formation of biological cargo gradients, which are necessary for heterogeneous tissue engineering applications. Specifically, osteochondral tissue was engineered, demonstrating that the approach could be used to resolve the complex and clinically-relevant challenge. To engineer an osteochondral tissue from mesenchymal stem cells, both osteogenic and chondrogenic growth factors are required [273]. Although these signalling molecules could trigger the differentiation process, they cannot, however, provide the necessary spatial information to engineer a heterogeneous tissue. To adapt the system for an osteochondral tissue engineering application, SPIONs were modified with heparin to sequester BMP-2 and create the BMP-2 gradient within cell-laden hydrogels. After all the necessary optimisation, the final system was able to support both osteogenic and chondrogenic differentiation. Moreover, the proposed fabrication strategy can create the BMP-2 distribution in a gradient manner, which more resembles growth factor distribution in nature.

The tissue engineering results demonstrate that BMP-2 signalling gradients can spatially influence osteogenic gene expression to generate robust osteochondral constructs exhibiting both low-stiffness cartilage and higher stiffness mineralised bone. Moreover, histology, immunofluorescence staining and Raman microscopy provide a detailed picture of the engineered osteochondral tissue. In particular, three major zones can be defined; a mineralised bone region that sharply switches into an intermediate region of hypertrophic chondrocytes, which then smoothly transitions into a collagen-rich cartilage region.

Overall, the research provides a rather versatile and rapid fabrication strategy that can be applied to a wide range of hydrogel systems. By modifying the surface chemistry of the nanoparticles, morphogen gradients can be formed, and heterogeneous tissue can be engineered. Taken together, this proposed platform should offer new opportunities for a range of interfacial tissue engineering challenges.

Future Perspective

A. Possible improvements for the system

While results from this chapter demonstrate that the proposed technology is a promising platform for generating heterogeneous osteochondral constructs. There are a few improvements could be made to engineer constructs with more robust properties. First of all, a more bioactive hydrogel material could be used in the system. While the rather bio-inert agarose hydrogel was used in the study, other hydrogel systems such as methacrylated gelatin or methacrylated hyaluronic acid could provide bioactive cues for cell adhesion and differentiation [274, 275]. Accordingly, the differentiation outcome of hMSCs in these hydrogel materials could be tested.

Secondly, the mechanical property of the constructs could be improved. Currently, *in vitro* fabricated constructs don't possess the mechanical properties of natural cartilage. To produce constructs that are more robust, a longer *in vitro* culture protocol could be tested. Alternatively, it is also possible to infiltrate the gradient hydrogels with a second polymer network to create a double network hydrogel using the current set-up [276]. With these approaches, the difference in mechanical properties between the bone end and cartilage end of the constructs after the engineering process can also be investigated.

Finally, the system could further be improved by adding another gradient to form a dual gradient system. For example, in the current design, TGF-β was supplemented in the osteochondral medium during the course of *in vitro* engineering. However, it is possible to incorporate TGF-β when the constructs are cast. To achieve this, another nanoparticle carrier for TGF-β or a substrate modified with TGF-β can be used [277, 278]. Ideally, the loading approach should also support a sustained release profile of TGF-β.

B. Study in ferrofluid movement

Although the research has demonstrated the capability of SPIONs gradients in future tissue engineering applications, the gradient formation mechanism of the initially two-phase system is still elusive. A magnetic-fluid simulation could propose a better hypothesis for gradient formation and could better predict the gradient pattern under different parameters. For instance, the gradient pattern generated from different sizes of SPIONs, magnetic field strength and the viscosity of hydrogel precursor.

C. Biological effects of SPIONs

In the proposed set-up, initially encapsulated glycosylated SPIONs were found within the cells using the ultramicrotome and TEM. Although the use of magnetic field gradient and SPIONs enable the gradient formation in several hydrogels and cargo gradients, the main concern of the present study is the use of metallic nanoparticles. Several reports have suggested that SPIONs could have effect in altering the cell's viability and differentiation fates [230, 232, 245, 247], therefore for any further clinical application, the presence of glycosylated SPIONs in the system, and the effect of glycosylated SPIONs *in vivo* should be tested.

D. Applicable alternative signals for the proposed system

In this chapter, the platform was used to sequester a cationic protein, however, the platform should also support the formation of other cargo gradients. With appropriate modification on surface chemistry of SPIONs, physical adsorption or chemical conjugation could be used to load a wide spectrum of cargos including peptides, small molecules with charges, nucleotides, and growth factors. These cargo gradients can then emulate the gradient observed during the development process *in vivo*. For instance, using the glycosylated SPIONs, besides growth factor, cytokine gradient can also be sequestered and patterned. This could be used in research regarding cell migration, such as the classic cell homing governed by the SDF-1α, which also possesses GAGs binding affinity [279-281]. Besides proteins carrying positive charge, cargo with negative charge including growth factors or nucleotides such as small interfering RNA (siRNA) could also be bound when a positive corona is created on the SPIONs surface. In addition to small molecules, biological nanoparticles could also be loaded using the system. For instance, extracellular vesicle (EVs), which are cell secreted lipid membrane vesicles containing cell regulating function, could be used. In a recent study, the binding affinity between heparin and EVs was demonstrated [282]. This suggests that the glycosylated SPIONs could provide a platform for EVs gradient decoration.

Moreover, it would also be possible to investigate if the sugar modified on SPIONs could itself be a bioactive signal. In a recent study, human articular chondrocytes were studied to verify the influence of cartilage zone specific ECM in both 2D and 3D environment. When chondrocytes were directly exposed to hyaluronic acid in 3D alginate culture, the neocartilage formation was effectively induced with increased production of collagen type II and aggrecan [283]. Besides hyaluronic acid, other kinds of GAGs such as heparin were also investigated for their differentiation effect. Recently, the effect of heparin on hMSCs was demonstrated to enhance osteogenic gene such as BMP-4 and ALP enzyme activity as well as mineralisation *in vitro* [284]. Heparan sulphate proteoglycans (HSPGs) are another crucial component in ECM. Heparan sulphate regulates key developmental signalling pathways, such as the Wnt, Hedgehog, transforming growth factor-β, and fibroblast growth factor pathways [285]. Either actively secreted (perlecan, agrin) or cleaved from the cell surface (syndecans and glypicans), the HSPGs binds to a wide variety of proteins by protein-protein interaction, and by electrostatic interaction with negatively charged haparan sulphate (HS) chains, which covalently couple to the core protein [286]. HS variants possess unique domain structures that target specific protein-ligand interactions and control the phenotype of hMSCs. By creating a gradient of these particular GAGs, the bioactive inductive function can be exploited, and heterogeneous constructs can be fabricated.

Chapter IV: Buoyancy-driven Gradient Fabrication

Abstract

In the previous chapter, a gradient fabrication platform utilising glycosylated SPIONs and magnetic field was developed and applied in the context of tissue engineering. Although the glycosylated SPIONs could efficiently sequester the bioactive cargo of interest (BMP-2), the cell uptake of glycosylated SPIONs is a potential concern for the future translational applications. Moreover, the system could only generate nanoparticle and biochemical gradients. The controlled fabrication of gradient materials is becoming increasingly important as the next generation of tissue engineering seeks to produce heterogeneous constructs with physiological complexity. The current strategies for fabricating gradient materials require highly specialised materials or equipment. A more generalised approach is needed, which can be applied to the wide range of different material systems in tissue engineering.

In this chapter, the physical principle of buoyancy will be used in gradient fabrication. In the first part of this chapter, buoyancy force will be used to create gradient materials bearing well-defined compositional, mechanical or biochemical gradients. As well as versatility, the buoyancy-driven gradient approach is also rapid (< 1 min) and facile (a single injection).I will demonstrate gradient formation across a range of different materials (*e.g.,* polymers, hydrogels) and cargos (*e.g.*, liposomes, inorganic nanoparticles, extracellular vesicles, and macromolecules).

In the second part of this chapter, the novel buoyancy-driven gradient casting platform will be applied to osteochondral tissue engineering. By creating BMP-2 gradients across a gelatin methacryloyl hydrogel laden with hMSCs, the decorated BMP-2 was able to locally stimulate osteogenesis and mineralisation to produce integrated osteochondral tissue constructs. The versatility and accessibility of this fabrication platform should enable the platform to be applied to other gradient materials or in engineering other interfacial tissues.

4.1 Introduction and Objectives

4.1.1 Using Physical Force in Gradient Fabrication

Gradient information can be encoded within gradient constructs using approaches such as a multi-channel microfluidic-based gradient maker or a 3D bio-printer. However, these approaches often require customised apparatus and are usually restricted to certain material properties because of the technology used. For instance, "printability", which is determined by parameters such as the viscosity and gelation kinetics of a material, is crucial for a successful 3D printing application. Other approaches such as photopatterning have also been used to generate gradients. However, this sort of remote field strategy also requires a material to be photoresponsive, *i.e.*, to only undergo bond cleavage, rearrangement or formation upon UV light exposure [89].

As introduced in section 1.4 (Engineering Gradients), gradient casting strategies based on different physical or thermodynamic principles usually don't require a specialised device and can be more universally applied across different materials. For instance, the phenomenon of diffusion, a thermodynamically favourable process, has been used to create protein gradients within 3D-printed microporous scaffolds [76]. Aside from diffusion, centrifugal force has been used to create polymer fibril gradients within a supporting hydrogel [86], while temperature gradients have also been used to create constructs with stiffness gradients [287]. In addition, principles of fluid dynamics, such as the convection between two fluid substrates, has been used to create colloidal particle gradients [82].

To design a more versatile and generalised gradient casting platform, it was hypothesized that physical forces that can be generally applied to different materials can be used. This concept was first demonstrated in the previous chapter: a remote physical force, magnetic force, was used to support the formation of the SPIONs gradients. While the SPIONs-assisted gradient fabrication platform fulfills several criteria stated in 1.4 (*e.g.*, rapid fabrication, without the need of special apparatus, applicable for different materials) and has shown its potential in osteochondral tissue engineering, it still suffers from a few disadvantages. For instance, since the system requires SPIONs to act as protein carriers, modification of the surface chemistry of SPIONs is required. Moreover, as a cell-laden hydrogel system, the uptake of SPIONs raises other potential concerns such as cytotoxicity and DNA damage. With these disadvantages and restrictions, in this chapter, an alternative physical principle, buoyancy force, was sought to controllably fabricate gradients in different materials. As nanoparticle carriers such as SPIONs are not required in the system, it should be more favourable for further translational applications.

4.1.2 Buoyancy and Gradient Casting

Buoyancy force is an upward force generated when materials are immersed in a denser fluid phase [288]. Buoyancy is everywhere in our daily life, for instance, it supports the formation of milk gradient within a glass of coffee [289]. In the context of biomedical research, buoyancy force is also commonly applied. For instance, in order to separate cells or organelles, buoyancy force is used to stabilise the formation of sucrose gradients [290, 291]. Under the same rationale, buoyancy force has also been applied to nanoparticle separation using density-graded organic solvents [292].

In the context of gradients in engineering, however, there are only limited examples in which buoyancy has been used to fabricate gradient materials. For example, Parameswaran and Shukla described a system in which cenospheres (hollow silica-alumina microparticles) were allowed to rise to the top of polyester resin and then immobilized in a solid matrix using a 48 h curing process. This yielded a polymeric material with a graded volume fraction of cenospheres, and a corresponding gradient of compressive and tensile properties [293]. Similarly, Beals and Thompson showed that a gas injected into a molten aluminium alloy could be dispersed into small particulate-stabilised bubbles upon mixing. These bubbles formed a liquid foam at the top of the melt, which was subsequently cooled to form a metallic structure with a porosity gradient [294]. The above-mentioned examples are highly-specific with a focus on hard materials for industrial applications. To the best of our knowledge, there has been no report of any versatile methodology using buoyancy in gradient material fabrication, nor any examples in which buoyancy-driven gradients have been applied to the field of complex tissue engineering.

4.1.3 Research Scheme I: A platform for casting gradients

In this chapter, the application of a buoyancy force-based patterning system for gradient fabrication and tissue engineering applications will be investigated. It is hypothesised that different gradient patterns can be fabricated by controlling sol-gel transition of a hydrogel, *i.e.*, forming the gradient at their liquid state and trigger the gelation to preserve gradient. In addition, as long as substrates possessing a different density, the proposed approach should support the formation of gradients.

In order to rapidly cast different material gradients, in this chapter, a controlled two-component mixing system for gradient fabrication is proposed. In the proposed approach, one material will be introduced at a defined rate into another static base material, and the two mixed phases will be allowed sufficient time to establish a gradient, which could then be preserved by triggering a polymerisation or gelation process. In this chapter, the potential of the platform in fabricating both physical and biochemical gradients will be tested (Figure 4.1).

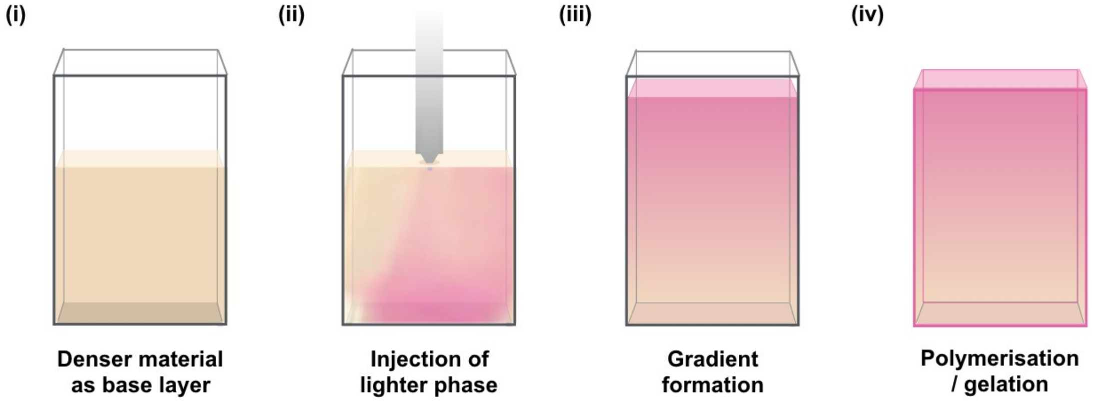

Figure 4.1 Research Scheme: the platform

Buoyancy-driven gradient casting. (A) Schematic showing the steps of gradient formation: (i) a base layer (yellow) is added to a mould, (ii) the injection phase (purple) is introduced during a single injection at a controlled rate, (iii) the system is allowed to equilibrate and form a material gradient, (iv) the gradient is preserved by gelation or polymerization of the material.

4.1.4 Research Scheme II: Osteochondral tissue engineering

In addition to the capability to create different gradients, an ideal fabrication platform should possess potential in engineering complex tissue. A major challenge of regenerative medicine is the engineering of the osteochondral interface that exists between cartilage and bone. In the second part of this chapter, the buoyancy platform will be used to decorate BMP-2 gradient within the hMSCs-laden gelatin methacryloyl (GelMA) hydrogel. To sequester BMP-2, it is hypothesised that heparin methacryloyl (HepMA) could be used. Using the osteochondral medium developed in the previous chapter, osteochondral constructs with distinct cartilage and bone properties are expected to form after a 4-week culture period.

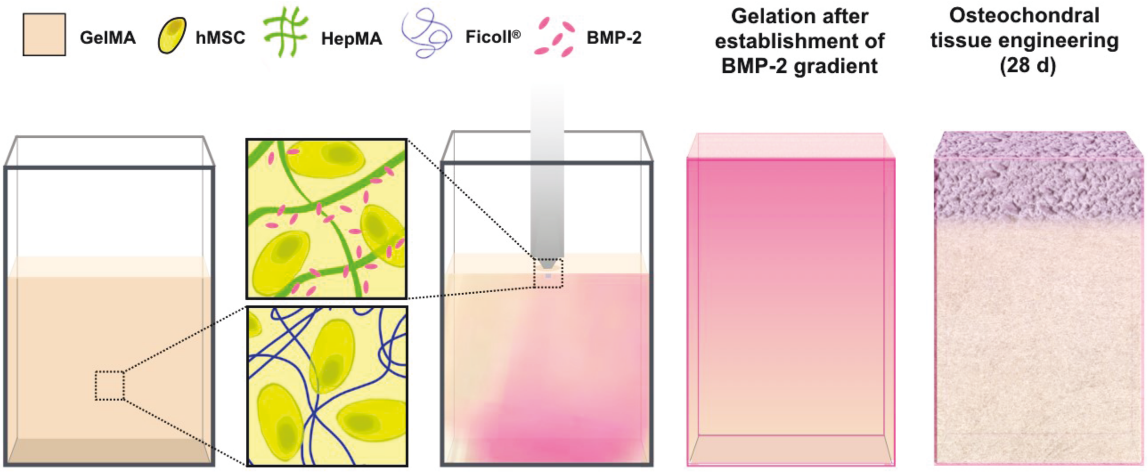

Figure 4.2 Research scheme: osteochondral tissue engineering

Growth factor gradients for osteochondral tissue engineering. Here, BMP-2 loaded HepMA will be co-injected with GelMA and hMSCs into a base layer comprised of GelMA hydrogel and hMSCs. It is hypothesised that the BMP-2 gradient could be preserved after GelMA and HepMA photocrosslinking. The crosslinked hydrogel could then be cultured for 28 d in osteochondral differentiation medium.

4.2 Results and Discussion I: Using Buoyancy to Fabricate Gradients

The essence of this approach is to create a gradient from the sequential injection of two materials with different densities. With buoyancy force, the lighter material is then redistributed into a gradient pattern. For the majority of the study, a rectangular customised mould was used. The rectangular mould was assembled with a pair of transparent glass slides clamping a 3 mm thick silicone sheet with an open rectangular cut-out (5 mm × 15 mm). To cast the gradient, the base layer of materials was first injected into the bottom of the mould prior to injection of the lighter phase. To control the injection rate of the lighter phase, a commercially-available electronic autopipette was used.

4.2.1 Design of Buoyancy Fabrication Platform

Buoyancy-driven gradient in materials with different density

The concept of casting gradients with buoyancy force was first tested using a relatively simple model system comprised of two agarose hydrogels at different agarose concentrations. To visualise the injection phase, rhodamine, a fluorescent dye, was covalently bound to the agarose hydrogel used in the injection phase. More specifically, hydroxyl groups of agarose were reacted with rhodamine B isothiocyanate, and the unconjugated rhodamine B isothiocyanate was removed *via* ethanol precipitation. Using the previously described glass/silicone sheet set-up, 0.2% (w/v) agarose labelled with rhodamine B was injected into a 1.0% (w/v) agarose hydrogel base at the rate of 17 $\mu L\ s^{-1}$. After injection, a gradient of rhodamine B-labelled agarose formed rapidly. Immediately after gradient formation, the whole set-up was then transferred into a 4°C fridge for gelation of the agarose and preservation of the gradient pattern. The gradient of rhodamine B-labelled agarose hydrogel was then imaged using a photo-scanner. After imaging, the intensity of the gradient within the selected ROI was analysed using the plot-profile function within FIJI (Figure 4.3). It was found that the relative intensity of the rhodamine-labelled agarose was distributed along a gradient across the longitudinal coordinate. Indeed, this preliminary attempt demonstrated that the gradient could be attributed to the difference in density between two hydrogels.

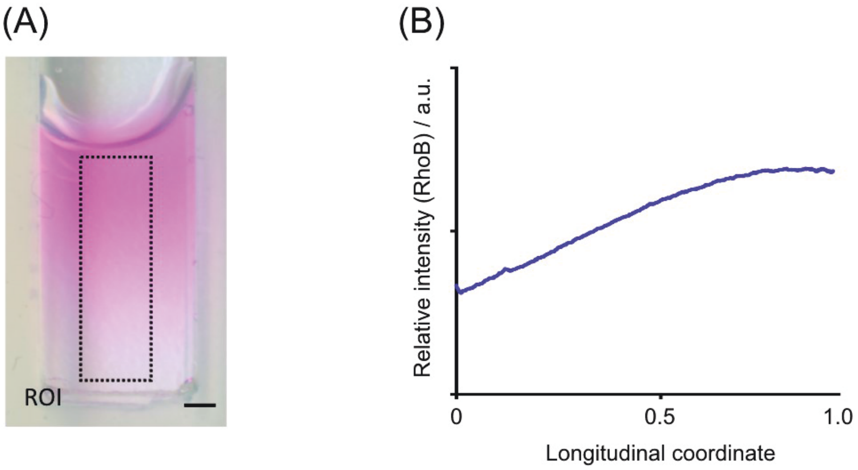

Figure 4.3 Example of buoyancy-driven gradient formation

0.2% (w/v) agarose labelled with rhodamine B and 1% (w/v) agarose were used for the injection phase and base layer respectively, with an injection rate of 17 µL s^{-1}. (A) Scan of a hydrogel showing a clear gradient of agarose labelled with rhodamine B (pink). Scale bar = 1 mm. (B) The relative intensity of rhodamine B signal along the hydrogel confirmed that a smooth gradient was formed under this condition. The figure is reproduced from Li et al. [92].

Using a density modifier in materials with a similar density

Because this platform is reliant on buoyancy force, a gradient can only be formed when the density of the two phases are different. In cases where the density difference between the two phases is too small to create sufficient buoyancy force, a gradient cannot be formed using the proposed approach. To circumvent this restriction, an alternative approach was developed in which a "density modifier" was introduced in the base material to support gradient formation.

The agarose/rhodamine-labelled agarose system was used to test the proposed strategy. In this set-up, instead of using agarose hydrogels of different concentration (*i.e.,* different densities), 1% (w/v) of agarose hydrogel and 1% (w/v) rhodamine-tagged agarose hydrogel were used. To increase the density of the base layer relative to the injection phase, 5% (w/v) sucrose was supplemented to the agarose base layer of 1% (w/v) agarose prior to injection. The same injection set-up used in the previous section was again used to test gradient formation. After injection of the rhodamine-tagged agarose into the sucrose supplemented base, a smooth gradient distribution of 1% (w/v) fluorescently-tagged agarose was rapidly formed together with the sucrose supplemented 1% (w/v) agarose hydrogel under 10 s (Figure 4.4).

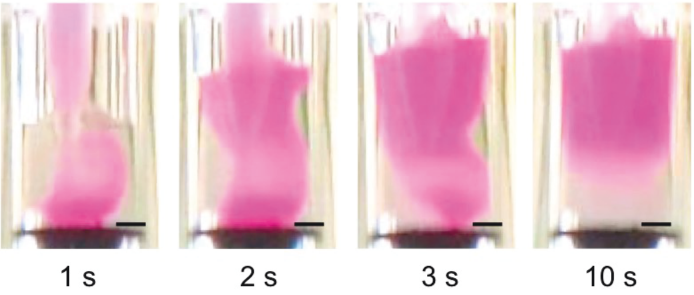

Figure 4.4 Formation of a rhodamine B labelled agarose gradient was supported in a sucrose doped system

The gradient formation process was demonstrated using 1% (w/v) agarose supplemented with 5% (w/v) sucrose as the static phase and 1% (w/v) agarose labelled with Rhodamine B as the injected phase. At the injection rate at 20 μL s^{-1}, gradient could be formed within 10 s after the injection. Scale bar = 1 mm. The figure is reproduced from Li et al. [92].

Indeed, it was demonstrated that introducing sucrose as a density modifier could support gradient formation. Moreover, it was hypothesized that by selecting a density modifier without affinity to the materials used for a given system, the density modifier could be removed after the gradient formation. For instance, small molecular weight sucrose should be removed from the agarose hydrogel after washing. To test this hypothesis, sucrose doped agarose hydrogels were cast and incubated with PBS on a shaker for 72 h. After incubation, the sucrose released into PBS could then be quantified using an enzyme-based assay. In the assay, the sucrose was first converted into glucose and then oxidised for a subsequent reaction with a probe for colourimetric development. Using the assay, it was found that the sucrose could be readily removed from the hydrogel after 72 h of incubation with PBS (Figure 4.5). In this example, sucrose can be considered a temporary density modifier that can template the gradient formation process and be removed after fabrication. This sort of temporary density modifier could be favourable for applications where a simple material composition is required or for the creation of density gradients in materials bearing no final density difference.

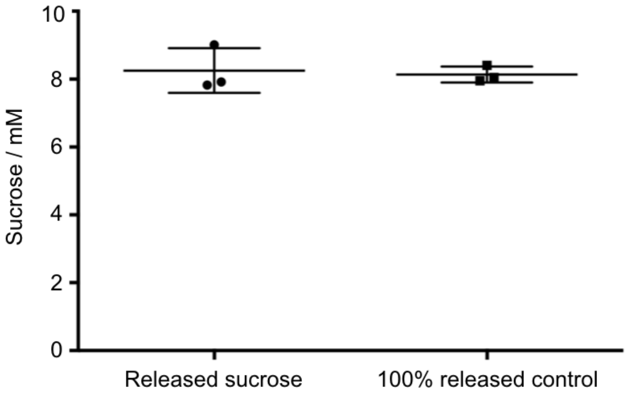

Figure 4.5 Diffuse of sucrose from gradient hydrogels

The amount of sucrose released from the agarose hydrogel was assessed after 72 h of PBS incubation. The sucrose concentration in the supernatant was assessed using an enzyme-based assay. The released sucrose was at the same level as the 100% released control, in which the same amount of sucrose was directly added and measured. The figure is reproduced from Li et al. [92].

Stability of the formed gradient

To preserve the cast gradients, stability of the gradient pattern prior to the gelation is essential. To investigate the stability of the gradient in the liquid state agarose, the rhodamine-labelled agarose gradient within the sucrose-supplemented agarose hydrogel was observed after the gradient formation at 37°C for 30 min. As indicated in Figure 4.6 the buoyancy-driven gradient was stably maintained for at least 30 min post-injection in the liquid state. The stability of the system hence provided an ample window for solidification of the material and preservation of the gradient, in this case, by cooling the system below the gelation temperature of agarose.

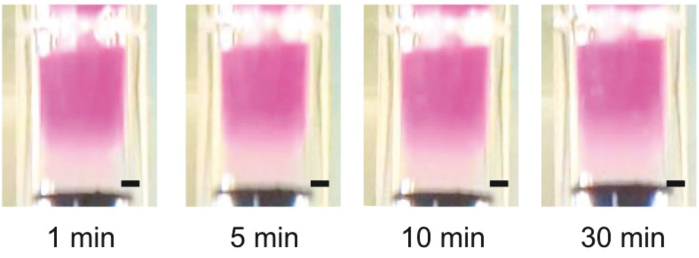

Figure 4.6 The post-injection stability of gradients

Stability of the gradient formation process was demonstrated using 1% (w/v) agarose supplemented with 5% (w/v) sucrose as the static phase and 1% (w/v) agarose labelled with Rhodamine B as the injected phase, with an injection rate of 20 μL s^{-1} at 37°C. The gradient formation process in liquid agarose was completed within 1 min, with the gradient retained for 30 min post injection without gelation. Scale bars = 1 mm. The figure is reproduced from Li et al. [92].

Mechanism of gradient formation

Next, further characterisation of this sucrose-supplemented system was performed in order to elucidate the mechanism behind the gradient formation process. To investigate this, the composition of the hydrogel along the longitudinal axis was analysed. Specifically, the gradient hydrogel fabricated from 1% (w/v) rhodamine B-labelled agarose injected into 5% (w/v) sucrose-supplemented 1% (w/v) agarose was used as the model system. After gelation, the gradient agarose hydrogel was divided into four transverse sections, and their content of sucrose and rhodamine-tagged agarose were analysed (Figure 4.7 A). To determine the content of rhodamine-tagged agarose, the transverse sections of the hydrogel were first heated to 95°C (above the melting temperature of the agarose) and diluted with 1 mL deionised water to inhibit the re-gelation of agarose network. The relative content of rhodamine-tagged agarose of different transections was then determined by the sample's fluorescent intensity. Similarly, to determine the amount of sucrose within each section, the sections were melted prior to an invertase-based sucrose assay.

The fluorescent intensity of rhodamine-tagged agarose and the sucrose contents revealed a sucrose gradient within the hydrogel that was inversely associated to the injected dye-labelled agarose (Figure 4.7 B). These results suggested that sucrose must retain attractive intermolecular interactions (*e.g.*, hydrogen bonding, Van der Waal forces) with the base layer agarose during the fluid-mixing process. These interactions prevent the base layer from completely equilibrating with the injection phase, thus retaining longitudinal density differences, which are capable of supporting buoyancy-driven gradient formation.

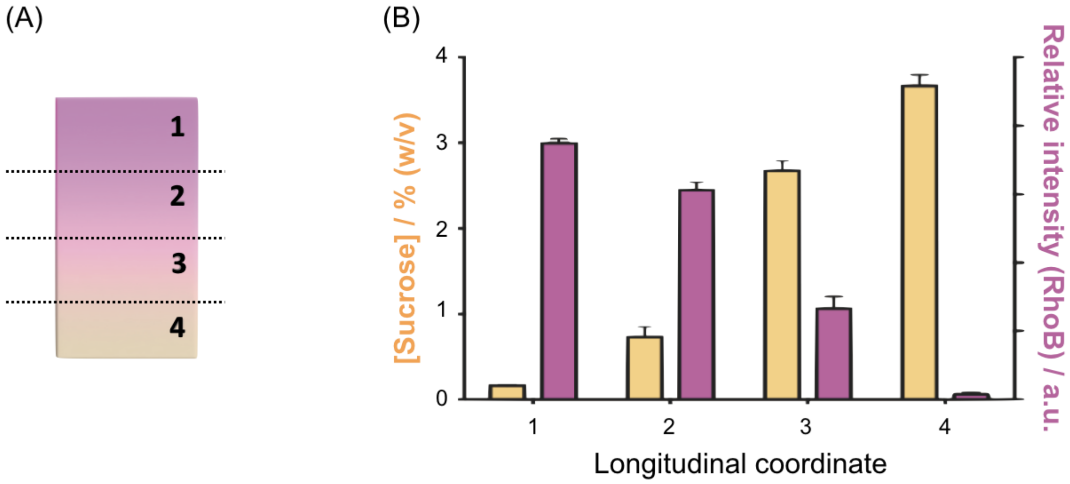

Figure 4.7 The mechanism behind the gradient formation process

(A) After gelation, a gradient hydrogel was equally divided into four transverse sections from the top to the bottom of the hydrogel (1 to 4). (B) These sections were assayed for sucrose (yellow bars) and agarose tagged with rhodamine (RhoB, pink bars), which showed a clear inverse correlation. Data are shown as mean ± S.D., n = 3. The figure is reproduced from Li et al. [92].

Systematic variation of parameter space

Indeed, by introducing a density modifier, the proposed system become more versatile in the sense that a gradient could be formed between two materials with a similar density. Next, the capability of the system to create multiple gradient patterns was investigated. It was hypothesised that while density plays an essential role in gradient formation, another system parameter, the injection rate, could provide additional control over the gradient pattern. Here, by varying the amount of doped sucrose and the injection speed, it was investigated whether systematic variations of these parameters could be used to control the final gradient profile of the materials.

Using the same agarose-sucrose system, it was shown that different combinations of injection rate and density difference could be used to fabricate a range of transitions (Figure 4.8 A). These formed gradient patterns could be illustrated in two examples. First, it was found that at the same amount of doped density modifier, a sharper transition could be formed when a slower injection rate was used. For example, in the base layer doped with 5% (w/v) sucrose, a sharp transition was formed when the injection rates were between 3 and 8 μL s^{-1} (Figure 4.8 B). In other words, a slower injection rate could result in less mixing between phases, and hence achieve a sharper transition. Second, it was found that at a fixed injection rate, a sharper transition could be formed when more density modifier was used. For example, when the injection rate was 8 μL s^{-1}, a sharp transition was formed when the base layer was doped with 20% (w/v) sucrose) (Figure 4.8 C). In other words, a greater difference in density could support a stronger buoyancy force and hence prevent the mixing of phases. In this sense, with this matrix of injection rate and density modifier content, it was also found that while there was no supplement of sucrose in the agarose base layer, no clear structural transitions could be formed at every tested injection rate (pink curve in Figure 4.8 C).

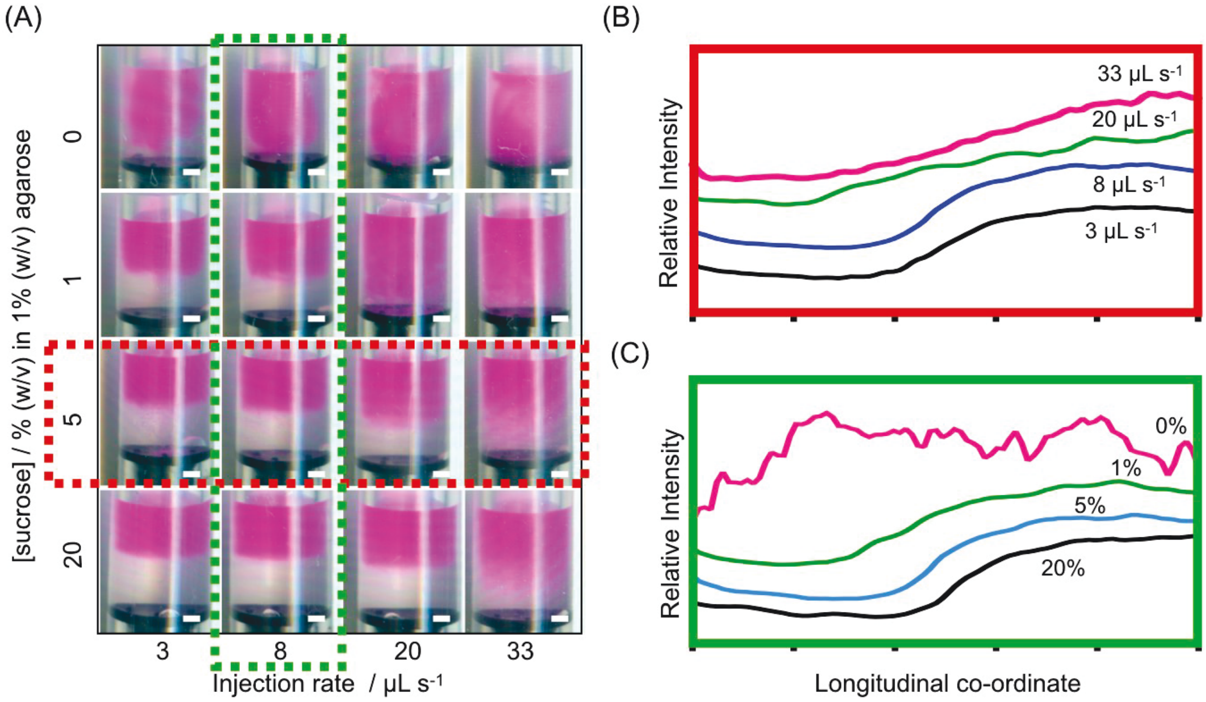

Figure 4.8 Patterns derived from the combination of different densities and injection rates

(A) The gradient pattern could be tuned by varying the injection rate and concentration of

sucrose in the base layer. Here, 1% (w/v) of rhodamine B-labelled agarose was injected into 1% (w/v) agarose solution doped with different concentrations of sucrose (0, 1, 5, or 20%) at different speeds (3, 8, 20 or 33 μL s^{-1}). (B) With base layers doped with the same sucrose concentration (e.g., red dot box), a higher injection speed will result in a more gradual transition. (C) At the same injection speed (e.g., green dot box), a denser base layer will result in a sharper transition. The curves in (B) and (C) were offsetted to for clarity. Scale bars = 1 mm.

Next, using the current system, the minimal density difference required to support gradient formation was investigated. By measuring the mass of samples with a fixed volume, the density of 1% (w/v) agarose and various sucrose concentration doped 1% (w/v) agarose could be derived. As demonstrated in Figure 4.9 the densities of different mixtures used in Figure 4.8 were assessed. Here, it is noteworthy that a small difference in density from the doped sucrose, *e.g.*, $\Delta\rho$ of 0.02 g mL^{-1} between 0% sucrose and 5% sucrose doped agarose was enough to drive gradient formation.

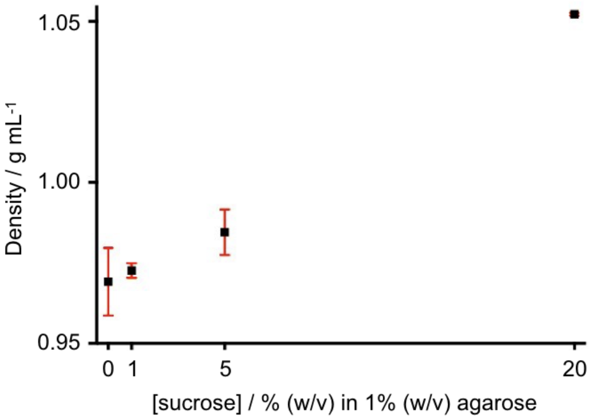

Figure 4.9 Densities of agarose doped with different sucrose concentrations

Density measurements. The density of 1% (w/v) agarose doped with different sucrose concentrations was measured. The mixtures were equilibrated at 37°C and then the mass of a known volume was measured. $\Delta\rho$ of 0.02 g mL^{-1} between 0% sucrose and 5% sucrose doped agarose was enough to drive gradient formation (n = 3, mean ± S.D.). The figure is reproduced from Li et al. [92].

4.2.2 Potential Applications in Gradient Casting

As demonstrated in the previous sections, there are few requirements for the buoyancy-based casting. The system only required two liquid phases that are miscible, curable, and exhibit a sufficient density difference to enable buoyancy-driven gradient formation. Moreover, by varying the amount of doped density modifier and the injection speed, different gradient patterns, from sharp layers to smooth gradients, could be casted using the proposed platform.

Unlike the majority of gradient fabrication strategies, which are usually only applicable to certain materials or cargos, the buoyancy casting platform could adapt to different systems. To illustrate this versatility, seven distinct examples of buoyancy-driven gradient formation were tested. These examples comprise substrate gradients (composition and stiffness gradients), nanoparticle (inorganic, organic, and biological) gradients, and macromolecule (natural polysaccharides and proteins) gradients.

Substrate gradients: composition and stiffness

It is hypothesised that the buoyancy-driven gradient fabrication platform could create both biochemical and physical gradients in a substrate material. In this section both the composition and stiffness gradient casting capability of the platform was tested.

(A) Composition gradients

As demonstrated in the previous example (agarose/rhodamine B-labelled agarose gradients), the composition gradient should be fabricated when the injecting material is miscible with the base materials. Since the buoyancy force could exist in any liquid materials, it was hypothesised that the platform could apply to other systems including organic polymers. To test this hypothesis, a water-free polymer-based gradient was fabricated. In this example, *N,N*-dimethylacrylamide (ρ = 0.96 g mL^{-1}) was used as the base, and lauryl methacrylate (ρ = 0.87 g mL^{-1}) was used for the injected phase. To facilitate the formation of solid polymer plastic, poly(ethylene glycol) dimethacrylate was added as a crosslinker in both phases. In addition to these components, a photo-initiator (Irgacure 2959 in *N,N*-dimethylacrylamide, 2,2-dimethoxy-2-phenylacetophenone in lauryl methacrylate) was also included to allow the photopolymerization to be triggered using 365 nm UV exposure after the establishment of the monomer gradient.

By varying the injection speed, both a sharp and gradual transition of the material composites could be fabricated. Specifically, the sharp transition was generated with an injection rate at 3 μL s^{-1}, and a gradient transition was generated with an injection rate at 20 μL s^{-1}. To visualise material transitions, rhodamine B dye was added to the *N,N*-dimethylacrylamide monomer solution prior to fabrication. This dye is soluble in *N,N*-dimethylacrylamide but not in lauryl methacrylate. After the injection of lauryl methacrylate into *N,N*-dimethylacrylamide, the materials gradient could be visually observed *via* the colour of rhodamine (Figure 4.10 A). The materials transition was then further investigated *via* Raman spectroscopic mapping using the sample set without the addition of rhodamine dye. Based on the reference signature derived from the pure polymer controls, the material distributions were mapped using the Raman scattering signal intensity for v_sCH_2 and v_sCH_3. The composition ratio between two materials is plot across the longitudinal coordinate in Figure 4.10 B-C.

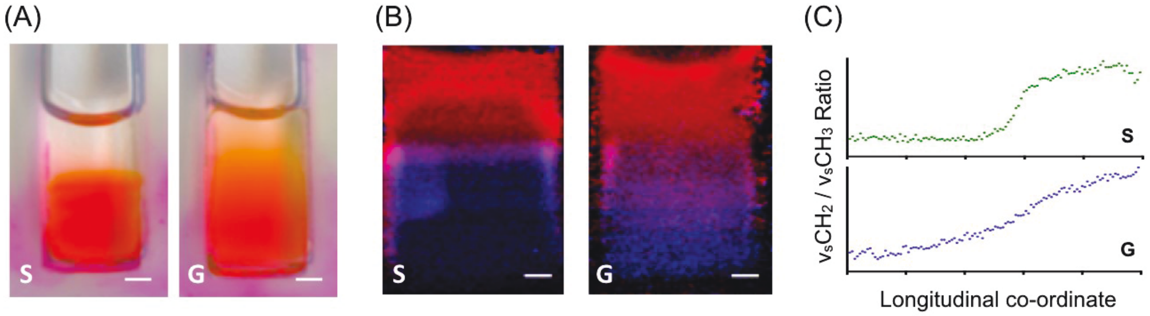

Figure 4.10 Composition gradients

(A) Polymer gradients were formed with two monomers bearing a difference in density: N,N-dimethylacrylamide (0.96 g mL^{-1}*) and lauryl methacrylate (0.87 g* mL^{-1}*). The transition could be visualised using Rhodamine B dye (red), which was soluble only in N,N-dimethylacrylamide. (B) Raman spectroscopy was used to show differences in the intrinsic chemical composition profile along the longitudinal coordinate of an undyed system. (C) Confocal Raman imaging was used to detect the ratio of* CH_2 *and* CH_3 *stretching features, demonstrating the differential profiles for polymers cast with a gradient or sharp transition. The Raman spectroscopy mapping was conducted by Dr. Isaac Pence, who also assisted with data analysis. The figure is reproduced from Li et al. [92].*

(B) Stiffness gradients

Stiffness gradient hydrogels have been a common tool in mechanobiology research. It was hypothesized that the buoyancy gradient platform could also produce stiffness gradients in a hydrogel substrate. To demonstrate this, a gellam gum hydrogel was used. Gellan gum is a biocompatible hydrogel commonly used in the tissue engineering research [295]. The gellan gum solution gels upon cooling and in the presence of a positive ion such as calcium. In this study, a gellan gum solution was heated to 80°C, pre-mixed with 0.01% (w/v) $CaCl_2$ for gelation, and pre-mixed with methylene dye to visualise the gradient formation process.

The buoyancy platform was then used to pattern defined stiffness transitions using a protocol modified from the previous sections. Specifically, the stiffness gradient was formed by injecting 1.0% (w/v) gellan gum hydrogel precursor into 1.5% (w/v) gellan gum hydrogel precursor doped with 5% (w/v) sucrose. The sharp and gradual transition of stiffness gradient was controlled by the injection rate. The sharp transition was produced with an injection rate of 5 $\mu L\ s^{-1}$ and gradient transition of stiffness was fabricated at an injection rate of 20 $\mu L\ s^{-1}$. To prevent any gelation prior to the completion of materials redistribution, the whole gradient formation process was carried out at 80°C. By assessing the re-distribution of dye mixed materials, it was found that the gradient formation process was finished within 10 s. After the gradient formation, the gelation was then triggered by moving the set-up into 4°C for 10 min.

The contact modulus was then measured along the longitudinal axis using a 3 mm diameter spherical indenter with a fixed indenting rate at 1.4 mm s^{-1}. By applying the Hertzian indentation model, the contact modulus was calculated along the longitudinal coordinate at a spacing of 0.5 mm. The calculated modulus revealed that controlled stiffness transitions could be achieved by varying the injection rate (Figure 4.11).

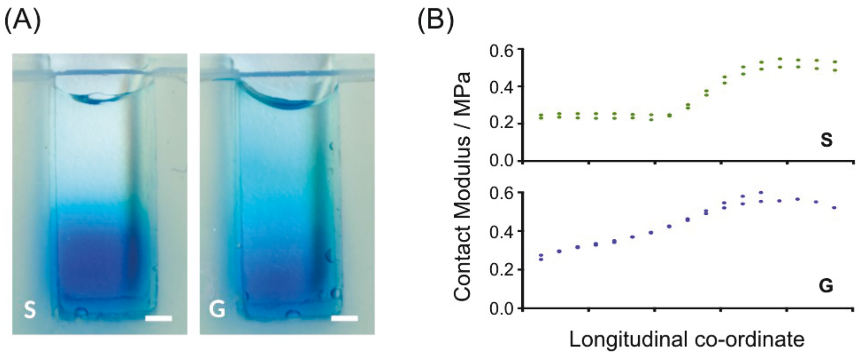

Figure 4.11 Stiffness gradients

(A) Stiffness gradients were formed by injecting 1.0% (w/v) gellan gum solution into a 1.5% (w/v) gellan gum base doped with 5% (w/v) sucrose. Gradients could be visualised by the addition of methylene blue dye in the base. (B) Spherical indentions along the longitudinal coordinate were used to quantify the local contact modulus for the gradient and sharp transition hydrogels. The contact modulus measurements were conducted by Dr. Axel Moore, who also assisted with data analysis. The figure is reproduced from Li et al. [92].

Nanoparticles gradients: inorganic, organic and biological

After demonstrating the ability to create material transitions (*e.g.*, composition, stiffness gradient), the proposed buoyancy platform was investigated for its ability to fabricate materials bearing nanoparticle gradients.

For this purpose, a wide range of nanoparticles including organic nanoparticles (1-palmitoyl-2-oleoyl-glycero-3-phosphocholine (POPC) liposomes), inorganic nanoparticles (gold nanoparticles) and biological nanoparticles (cell-derived extracellular vesicles, EVs) were prepared. Due to the surface plasmon resonance phenomenon, citrate-capped gold nanoparticles with a diameter smaller than 50 nm reflect the red light and are visible in the gradient constructs. To visualise nanoparticle gradients of liposomes, POPC liposomes were prepared with the inclusion of Lissamine™ Rhodamine B in the lipid film prior to hydration. To visualise extracellular vesicles, the cell-line for EV production was transfected to express red fluorescence protein-fused LAMP1.

Using the established agarose-sucrose system with the controlled injection rates, both sharp and gradient transitions were successfully generated and visualised with brightfield and fluorescence imaging (Figure 4.12). These three examples encompassed a broad range of nanoparticles, and importantly, each of these nanoparticles are commonly used as hosts for cargo delivery or as functional entities in their own right, for instance, as bioactive signal, or as small molecule drug carrier [296-298].

The capability of the fabrication in these nanoparticle gradients further broadens the possible applications for gradient construct fabrication. It should also be noted that while the SPIONs/magnetic field approach elaborated in the previous chapters are also able to pattern the nanoparticles gradient, the buoyancy approach doesn't rely on the specific physical features of the desired nanoparticles (*e.g.*, magnetic susceptibility of SPIONs).

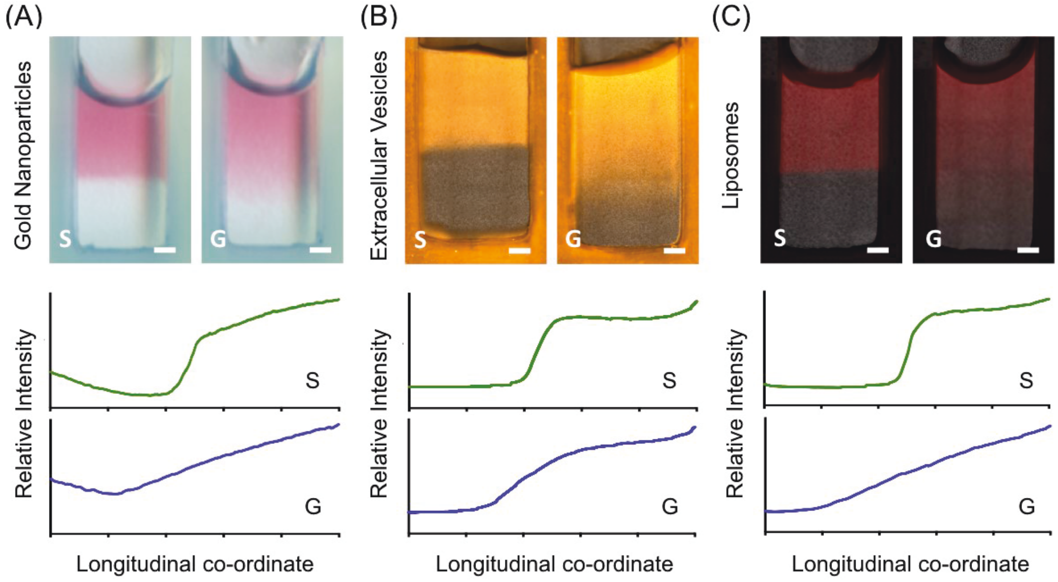

Figure 4.12 Nanoparticles gradients

Sucrose was used to create density differences between the base layer and injection phase of agarose hydrogel in order to create transitions of (A) gold nanoparticles (pink), (B) RFP-extracellular vesicles (orange), and (C) liposomes labelled with Rhodamine B (red). Scale bars = 1 mm. The RFP-labelled EVs were prepared by Charles Winter. The gold nanoparticles were prepared by Dr. Yiyang Lin. The extracellular vesicles were prepared by Charles Winter. The figure is reproduced from Li et al. [92].

Macromolecule gradients: polysaccharides and protein

After demonstrating the proposed platform could support the formation of nanoparticle gradients, I next sought to investigate if the platform could create gradients of other commonly used bioactive cargos in regenerative medicine research. For this purpose, natural polymers such as polysaccharides and proteins, which together encompass a wide range of applications, were tested.

Here, FITC-labelled dextran (200 kDa) and Texas Red labelled avidin (66 kDa) were selected as the model cargo for polysaccharides and proteins respectively. With the fluorescent tag, these cargos could then be visualised using a fluorescence microscope. To fabricate buoyancy driven gradients, the agarose-sucrose system was again used. Specifically, the cargo, 1 mg mL^{-1} FITC-labelled dextran or 50 μg mL^{-1} Texas Red labelled avidin, were loaded within the injection phase of 1% (w/v) prior to the rate-controlled injection. Similar to the previous applications, the base phase consisted of 1% (w/v) agarose doped with 5% (w/v) sucrose. By mapping the fabricated constructs using a wide-field fluorescence microscope, the gradient of both cargos could be visualised within the agarose hydrogel. However, due to the absence of any strong attractive interactions between cargos and the agarose network, the loaded cargos were expected to be released in a short period. Indeed, by incubating the casted hydrogels within PBS, it was found that the avidin and dextran were only temporarily entrapped within the hydrogel. Moreover, the smaller size globular avidin was released from the agarose hydrogel in a much shorter time period than the 200 kDa linear dextran (Figure 4.13).

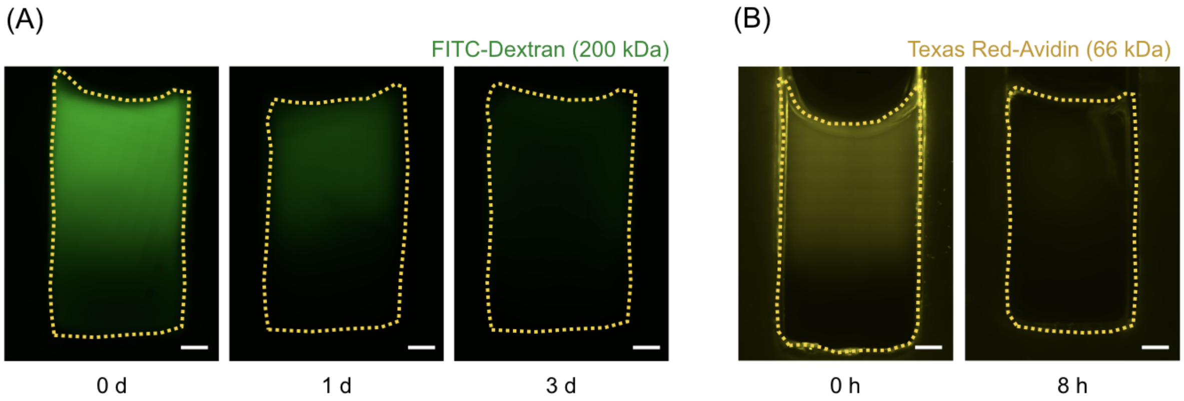

Figure 4.13 Stability of dextran and avidin gradients

With a base layer doped with sucrose, agarose hydrogels were cast with gradients of (A) 200 kDa dextran labelled with FITC (green) and (B) avidin labelled with Texas Red (yellow). The hydrogels were incubated with PBS in the dark at room temperature. Wide-field fluorescence micrographs showing loss of fluorescence over time, which was attributed to the leaching of the cargo from the hydrogel. Scale bars = 1 mm. The figure is reproduced from Li et al. [92].

4.3 Results and Discussion II: Osteochondral Tissue Engineering

4.3.1 Strategy for a Prolonged Gradient

In the previous section, two macromolecule gradients could be cast using the buoyancy platform, however, only temporarily gradients could be created. While two macromolecules with different molecular weights and structure (globular and linear) have been tested, it should be noted that aside from steric hindrance, other factors such as electrostatic interaction and hydrogen bonding between the cargo and hydrogel network are also affecting release kinetics.

In the context of tissue engineering applications, a system with prolonged gradients is more desirable. To design a system with prolonged gradients requires further adaption and tailoring of the buoyancy method previously described. To this end, it was hypothesised that a much prolonged releasing profile could be achieved by introducing a macromolecular host that could be covalently crosslinked to the surrounding hydrogel network. The strategy was investigated here by using heparin methacryloyl (HepMA) as a macromolecular host. While heparin has been widely used to sequester cationic proteins [258, 299], the addition of methacrylate groups provided a means to covalently crosslink HepMA with itself and the surrounding methacrylate substrate. For the surrounding methacrylate substrate, gelatin methacryloyl (GelMA), a photo-crosslinkable and biocompatible hydrogel, was used as the bulk substrate. Aside from providing binding sites, GelMA hydrogel is also favourable in this research because it has been shown to support the hMSCs differentiation for both cartilage and bone based on several previous studies [300].

Since orthogonal methacrylate chemistry could covalently cross-link the HepMA and GelMA without forming covalent linkages with the protein cargo, this approach should also reduce the chance of denaturation while retaining the possibility for slow cargo release. Moreover, since the gelation of GelMA and crosslinking of HepMA are both triggered by photo-polymerisation using UV light, both the processes could be controllably activated after the gradient formation process was complete.

HepMA and GelMA were prepared by the reaction of methacrylic anhydride with heparin and gelatin respectively. Specifically, under the basic conditions, the methacrylic anhydride could react with amine groups on gelatin and hydroxyl groups on heparin. After reaction, the byproducts were removed through extensive dialysis, and the final product was lyophilised and kept at -20°C before use. To determine if the conjugation was successful, ^{1}H NMR was used to verify the proton signal from the hydrogens of methacrylate vinyl groups. As demonstrated in Figure 4.14, both GelMA and HepMA were successfully prepared. It should be noted that the difference in chemical shift could be attributed to the electronegativity of the element bonding with methacrylate group: methacrylate anhydride reacted with hydroxyl group of the heparin, accordingly, the methacrylate group is bond with an oxygen; methacrylate anhydride reacted with amine group of the gelatin, accordingly, the methacrylate group is bond with a nitrogen.

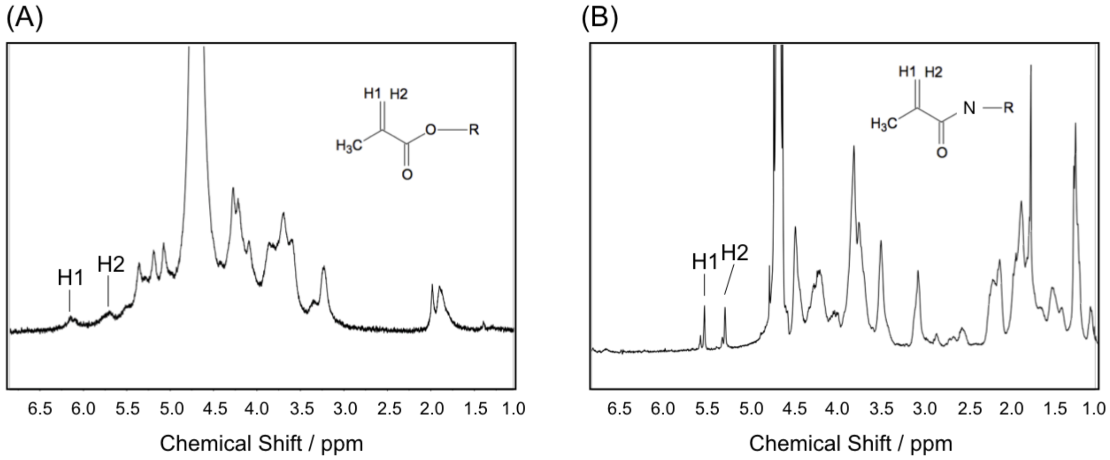

Figure 4.14 Characterisation of HepMA and GelMA

(A) The representative ^{1}H NMR spectrum of HepMA, showing conjugation of the methacrylate group (H1 and H2; 6.1 ppm and 5.7 ppm) on heparin. The chemical shifts of the protons of methacrylate group were identical to the locations reported in Nilasaroya et al., [301] (B) Representative NMR spectrum of GelMA, showing conjugation of the methacrylate groups. (H1 and H2; 5.4 ppm and 5.7 ppm). The chemical shifts were identical as locations reported in Sarem et al., [302]. NMR spectrums were generated with the assistance of Dr. Liliang Ouyang.

To test if the HepMA could be retained longer within the GelMA hydrogel, an equal amount of HepMA and heparin was separately mixed with GelMA to form two kinds of hydrogels: heparin/GelMA and HepMA/GelMA. Both heparin/GelMA and HepMA/GelMA hydrogels were then incubated with PBS over a period of 28 d. At different time points, the supernatant solution was collected, and the amount of heparin or HepMA in the solution was quantified using a DMMB assay based on standards prepared from heparin and HepMA respectively. As Figure 4.15 demonstrates, the cumulative release of HepMA from GelMA was greatly limited compared to unmodified heparin. While the HepMA could support the retention of more than 70% of initial loading after 28 d, majority of unmodified heparin (> 75% of initial loading) was released from the GelMA network after just 1 day of incubation.

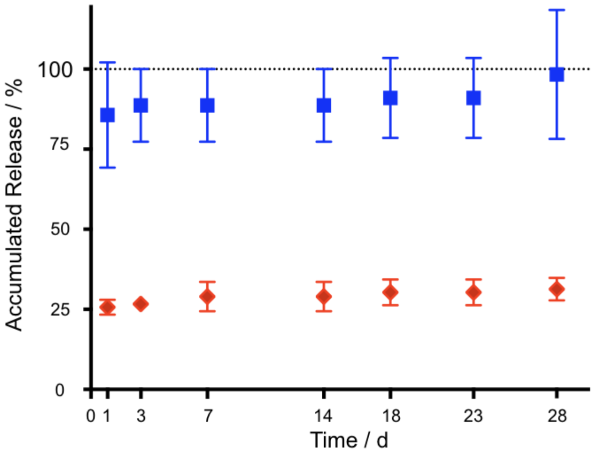

Figure 4.15 Characterisation of heparin methacryloyl release

Heparin or HepMA was mixed with GelMA to form either heparin/GelMA or HepMA/GelMA hydrogels. Release profiles of heparin (blue markers) and HepMA (red markers) from GelMA hydrogels were investigated by collecting sample at different time points and DMMB assays. The releasing profile indicate that HepMA could be retained to a greater degree than unmodified heparin (n = 3, mean ± S.D.). The figure is reproduced from Li et al. [92].

After demonstrating that the majority proportion of HepMA could be retained within the GelMA hydrogel, the capability of HepMA to load protein cargo was investigated. To test the cargo-loading capability, 66 kDa Texas Red-tagged avidin was again used as a model protein due to its binding affinity with heparin (pI = 6.5, heparin K_D = 160 nM) [257]. Prior to the fabrication process, the Texas Red-tagged avidin was allowed to incubate with HepMA for sequestration.

To fabricate the avidin gradient, a mixture comprised of 10% (w/v) GelMA, 50 µg mL^{-1} avidin and 1 mg mL^{-1} HepMA was injected into a base layer of 10% (w/v) GelMA doped with 5% (w/v) sucrose. A protein gradient with a sharp transition was fabricated using a rate of 3 µL s^{-1}, and a gradient transition was fabricated at a rate of 17 µL s^{-1}. By verifying the fabricated constructs with fluorescent imaging and image analysis, both sharp and gradual transition of protein gradients were successfully generated (Figure 4.16).

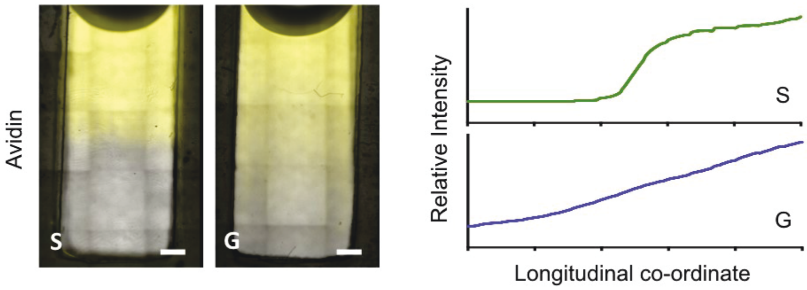

Figure 4.16 Gradient patterning of avidin labelled with Texas Red®

HepMA was used to sequester protein and form protein gradients within GelMA hydrogel. Both sharp and gradient transition of protein could be fabricated by varying injection speed. Using a fluorescence microscope and FIJI, intensity profiles along the longitudinal coordinate were used to characterise the hydrogels bearing Texas Red labelled avidin. A gradient or a sharp transition were revealed. Scale bars = 1 mm. The figure is reproduced from Li et al. [92].

4.3.2 Sustained BMP-2 Releasing System

After demonstrating that HepMA could sequester protein and cast gradients within GelMA hydrogels, the release profile of HepMA sequestered protein was investigated. In this research, BMP-2 gradients will be patterned to generate osteochondral tissue. Given that BMP-2 is also a low molecular weight cationic protein with affinity to heparin (M.W. = 13 kDa, pI = 8.5, K_D= 20 nM), instead of using avidin as the model protein, here, release profile of BMP-2 was directly investigated.

It was hypothesised that due to the covalent crosslinking between HepMA and GelMA, HepMA could support a more sustained release of BMP-2 than unmodified heparin. To test this, the unmodified heparin or HepMA (10 µg mL^{-1}) was first mixed with BMP-2 (3 µg mL^{-1}) to ensure the loading of BMP-2. The mixture was then added to the 10% (w/v) GelMA substrate supplemented with the photo-initiator. This final mixture was then exposed to 5 min of UV (365 nm) to photo-crosslink the HepMA and GelMA. It should also be noted that in the proposed approach, the orthogonal crosslinking mechanism between methacrylate groups should avoid the covalent bond formation between the BMP-2 and the hydrogels, which should prevent the denaturing of the loaded BMP-2 and allow slow release. The formed hydrogels were then incubated with PBS for 28 d, and the samples were collected at a different time interval to assess the releasing profile of BMP-2 from homogeneous HepMA-GelMA and Heparin-GelMA hydrogels. To test the amount of released BMP-2, an ELISA was used to measure the cumulative release of BMP-2. As Figure 4.17 demonstrates, a slow release that reached completion at 28 d of incubation was observed within the GelMA-HepMA system. On the other hand, a much more rapid releasing profile was observed in the GelMA-Heparin system. Based on the result from chapter 2, the releasing profile of the GelMA-HepMA system should support the osteochondral tissue engineering application, in which the BMP-2 elevated at one end of the hydrogel throughout the culture period.

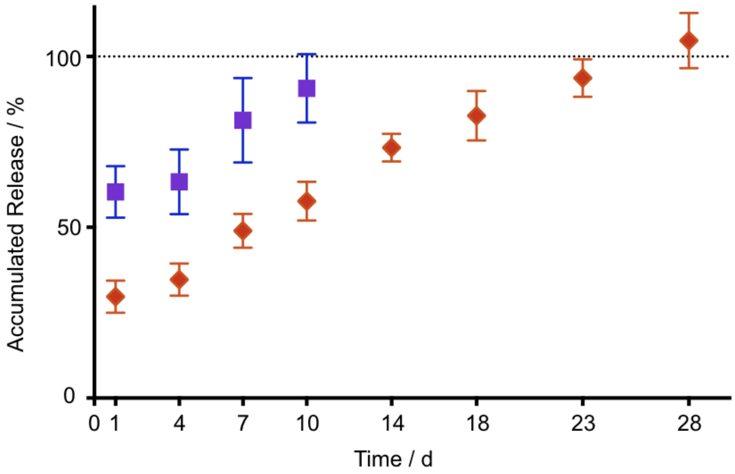

Figure 4.17 BMP-2 release profile

BMP-2 was mixed with either heparin (blue markers) or HepMA (red markers) and then mixed with 10% (w/v) GelMA to form the hydrogel. The hydrogels were immersed in PBS with aliquots collected at various time points and analysed using an enzyme-linked immunosorbent assay (ELISA) for BMP-2. This study showed a prolonged release of BMP-2 from the HepMA-GelMA constructs (n = 3, mean ± S.D.). The figure is reproduced from Li et al. [92].

4.3.3 A Biocompatible Density Modifier

In the first part of the chapter, sucrose was used as the density modifier while the base layer and injecting layer have similar densities. Although sucrose is ideal for fabricating gradients in cell-free systems, it is known to exert an osmotic pressure that can be highly cytotoxic. To tailor the system into a cell-laden one, other density modifiers need to be selected. Accordingly, it is investigated whether the sucrose could be substituted with the more cytocompatible polysaccharide Ficoll® in order to raise the density of GelMA in the base layer while maintaining cell viability. Ficoll® is a neutral hydrophilic polysaccharide that is highly branched, high mass (M.W. = 400 kDa) and commonly used reagent in zonal centrifugation studies [303]. With the low membrane permeability and low osmotic pressure, it was hypothesised that using Ficoll® rather than sucrose should provide a lower cytotoxicity profile in long-term culture conditions.

To verify the biocompatibility of Ficoll® in the system, hMSCs were encapsulated at 5×10^5 cells mL^{-1} in 7.5% (w/v) GelMA hydrogels containing 0, 2.5 or 5% (w/v) Ficoll® and cultured for 72 h. The encapsulated hMSCs cultured within Ficoll® doped GelMA hydrogels were first assessed using Calcein AM staining, which revealed that the hMSCs cultured in all conditions presented similar cell density and morphology (Figure 4.18 A). Aside from the cell morphology, the metabolic activity of hMSCs was also assessed using an alamarBlue® assay. As expected, the result confirmed that when Ficoll® was doped at 5% (w/v) in GelMA hydrogels, no significant cytotoxicity was presented to the encapsulated hMSCs (Figure 4.18 B).

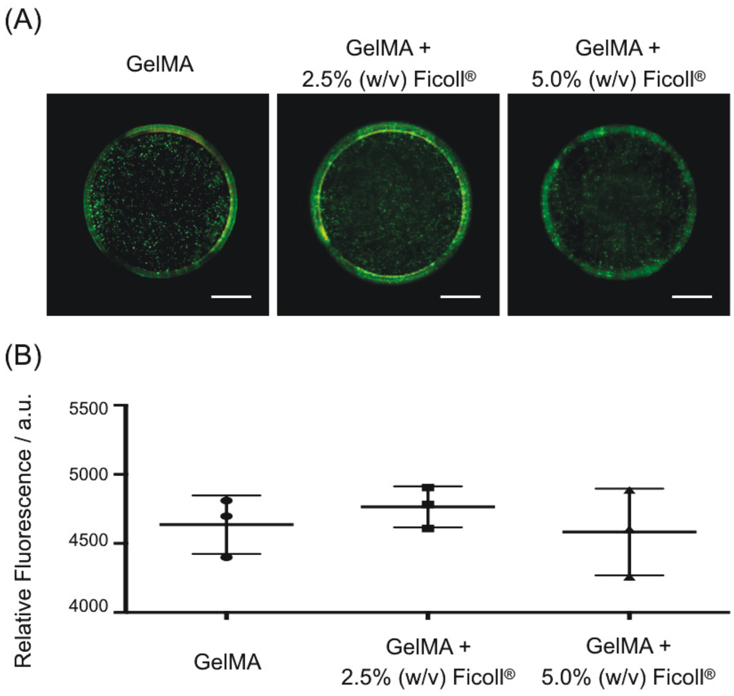

Figure 4.18 Ficoll® as a biocompatible density modifier

Ficoll® was tested to be non-cytotoxic in the present study. (A) Calcein AM staining was performed to assess hMSC density and morphology after 72 h of culture. The hMSCs were initially seeded within GelMA, GelMA + 2.5% (w/v) Ficoll® or GelMA + 5% (w/v) Ficoll® at the same cell density (5 × 10^5 cells mL^{-1}). Scale bar = 1 mm (B) An alamarBlue® assay performed on hMSCs in GelMA supplemented with different concentrations of Ficoll®. No significant difference in metabolic activity was measured between samples (n = 3, mean ± S.D.). Statistical comparison was made using a Wilcoxon matched-pairs signed rank test.

4.3.4 Ficoll in Gradient Casting

Next, replacing sucrose as the density modifier, the gradient casting protocol using Ficoll® was tested with GelMA. In the gradient casting set-up, 10% (w/v) GelMA solution was injected in to a base comprised of 10% (w/v) GelMA and 5% (w/v) Ficoll®. While the base was doped with 5% Ficoll®, the distribution of the initial base materials after gradient fabrication process could be visualised by the opaque Ficoll®-doped GelMA. As Figure 4.19 demonstrates, under the different injection rates of 10% GelMA, various gradient pattern hydrogels could be formed. In addition to being biocompatible, more crucially, Ficoll® can be used in the same way as sucrose to produce gradients in GelMA that was dependent upon injection rate.

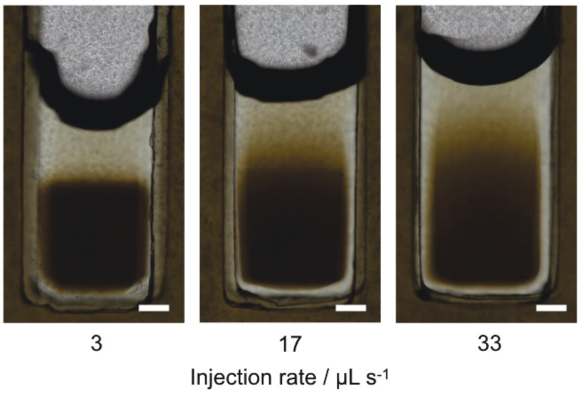

Figure 4.19 Ficoll® could support gradient casting

Ficoll® was used to increase the density of the GelMA base layer. With different injection rates, different gradient patterns could be fabricated. After the injection, gelation was triggered by exposing the set-up to UV light for 5 min. Distinct gradient patterns can be visualised due to the opacity developed after the gelation of Ficoll® infiltrated GelMA. Scale bar = 1 mm. The figure is reproduced from Li et al. [92].

4.3.5 Osteochondral Tissue Engineering

The optimised final set-up

While there is no literature revealing the exact BMP-2 concentration within osteochondral tissue *in vivo*, in the final set-up, adequate BMP-2 loading was estimated by the optimised parameters in the previous chapter. The final optimised system for osteochondral tissue engineering comprised the injection phase of 3.1 μg mL^{-1} BMP-2, 2.5 μg mL^{-1} HepMA, and 10% (w/v) GelMA and a base layer of 10% (w/v) GelMA thickened with 5% (w/v) Ficoll®, with both phases containing 9×10^6 mL^{-1} hMSCs and 2.5 mg mL^{-1} photoinitiator. To create a smooth gradient, the injection rate of 17 μL s^{-1}, derived from the avidin-HepMA-GelMA system (section 4.4.1) was used.

With these conditions, smooth gradients of BMP-2 loaded HepMA could be established. Moreover, the gradient distribution of BMP-2 loaded HepMA could be immobilised in GelMA using UV light irradiation (5 min, 365 nm, 6 mW cm^{-2}). These constructs were then subjected to a 28 d course of osteochondral tissue engineering using a defined osteochondral differentiation medium that has been optimised and described in Chapter 3.

Extracellular matrix characterisation

Using the optimised osteochondral medium, after approximately 15 d of tissue engineering culture, the emergence of a strikingly opaque cap on the cultured constructs was observed. By the end of the culture period (28 d), this cap was present on all tissue constructs, a strong indication that the BMP-2 gradient had guided a localised mineralisation process. Indeed, when sections of osteochondral tissue were examined using Alizarin Red S staining, a mineralised cap exclusively at one end of the tissue was observed (Figure 4.20 A). On the other hand, Alcian Blue staining revealed the entire tissue to contain sulphated glycosaminoglycans, a key extracellular matrix component naturally presents in both cartilage and bone (Figure 4.20 B) [304]. These findings were corroborated using immunofluorescent staining for key proteins associated with chondrogenesis and osteogenesis (Figure 4.20 C-D). While osteopontin, a key marker of osteogenesis, was observed only in the mineralised cap [305], type II collagen, a key component of hyaline cartilage ECM [306], was present throughout the tissue construct.

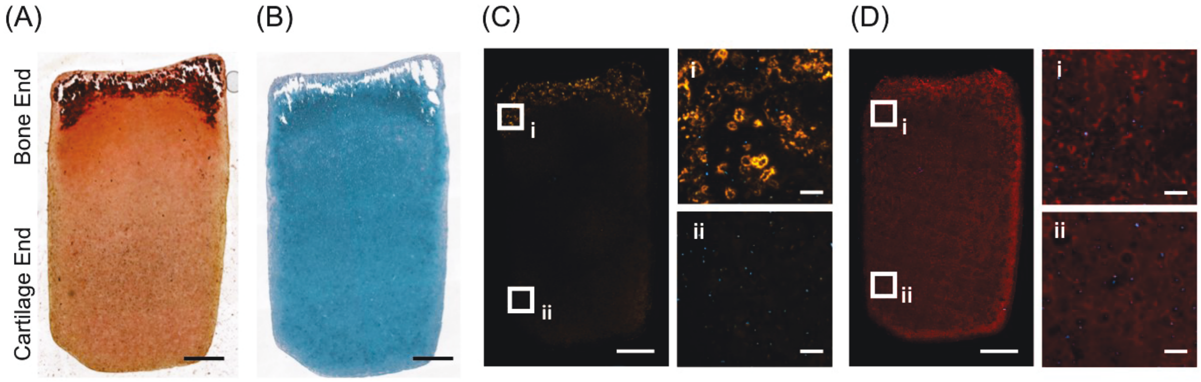

Figure 4.20 ECM distribution of the engineered osteochondral tissue

(A) Alizarin Red S staining revealed localised mineral deposition at one end of the tissue; (B) Alcian Blue staining revealed tissue-wide staining for glycosaminoglycans, a component of both cartilage and bone; (C) The bone-specific marker osteopontin was also localised exclusively at the mineralised cap; (D) type II collagen, a component of hyaline cartilage, was present throughout the tissue. Scale bars = 1 mm in low magnification images, 100 µm in high magnification images. The figure is reproduced from Li et al. [92].

Mineral characterisation

The composition and distribution of minerals were further investigated using Raman spectroscopy imaging. The presence of both hydroxyapatite (HAP) and β-tricalcium phosphate (β-TCP) were found exclusively at the bone end of the construct (Figure 4.21 A-B). While the signal of HAP was stronger than that of TCP throughout the mineral cap region, spectral unmixing of Raman features indicated a heterogeneous presentation of mineral species that formed co-locally within the cultured construct.

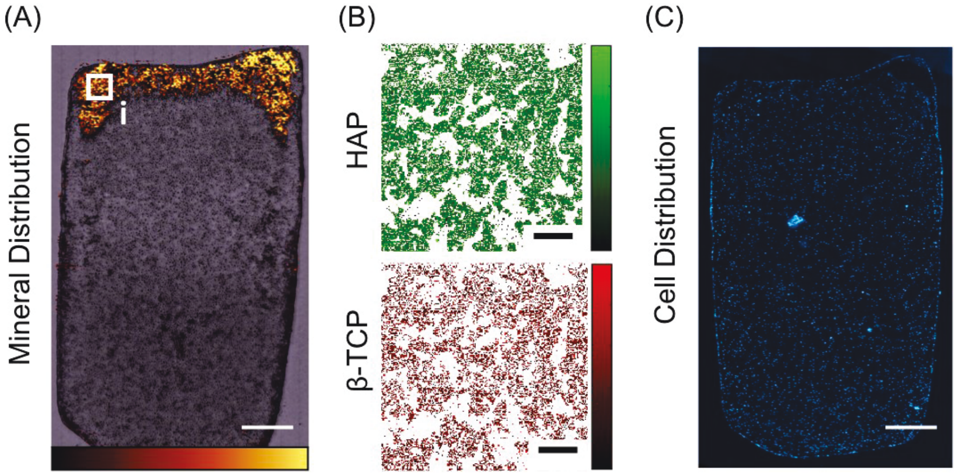

Figure 4.21 Mineral of the engineered osteochondral tissue

(A) Raman spectroscopic imaging was used to reveal the spatial distribution of mineral and (B) identify the presence and heterogenous presentation of both hydroxyapatite and tri-calcium phosphate in the mineralised cap. Scale bar = 1 mm in low magnification images, 100 µm in high magnification images. The colour scales in (A) and (B) show the relative intensity of the signal, with brighter colour representing higher intensity. The Raman Spectroscopy mapping was conducted by Dr. Isaac Pence, who also assisted with data analysis. (C) Cell distribution. DAPI staining (nuclei, blue) performed on the osteochondral tissue constructs showed an even distribution of hMSCs throughout the tissue construct, with no visible margin or interface. Scale bar = 1 mm. The figure is reproduced from Li et al. [92].

Taken together, the histology, immunofluorescence staining and Raman spectroscopic mapping strongly suggested that the soluble TGF-β3 had stimulated tissue-wide chondrogenesis of the hMSCs, while BMP-2 gradients had initiated a localised osteogenic response. Interestingly, the results demonstrated here are similar to that of chapter 2: the mineralisation took the form of an abrupt transition between bone and cartilage, despite the initially smooth BMP-2 gradient and the homogenous distribution of cells (Figure 4.21 C). These results suggest that the platform could mimic the natural process of endochondral ossification, in which concentration gradients of osteoinductive factors (*e.g.,* BMP-2, BMP-6) produce a sharp mineral transition at the developed osteochondral interface.

4.4 Conclusions and Future Perspective

Conclusions

In this chapter, a buoyancy-driven gradient casting technology using basic physical force was demonstrated. As in the gradient technology utilising magnetic field and SPIONs discussed in Chapter 3, the buoyancy-driven gradient casting agrees with the criteria summarized in section 1.4 (criteria for robust gradient casting) and was used to fabricate several gradients across different hydrogels systems. Specifically, in this chapter, it was shown that a single injection event of one fluid material into another is sufficient to generate material transitions that can be preserved by subsequent gelation or polymerisation. Moreover, materials exhibiting either a sharp transition or a smooth gradient could be fabricated by systematically varying the material characteristics and injection parameters.

The proposed platform was used to cast gradients in several different materials (gelatin methacryloyl, gellan gum, agarose, acrylate polymers) and generated tunable transitions in composition, biochemical profile and compressive stiffness. Moreover, it was also demonstrated that several cargo species could be incorporated in gradient form, including inorganic nanoparticles, liposomes, cell-derived extracellular vesicles, macromolecules and proteins. The proposed buoyancy-drive gradient casting provides a platform for further research and in diverse applications. For instance, stiffness gradient hydrogel could be used as platform for studying hMSCs development biology [23], the extracellular vesicles and liposome gradient, when loaded with functional motifs, could be used to gradient-pattern bioactive signals within the tissue engineering scaffold [296-298].

As mentioned at the beginning of this chapter, native osteochondral tissue, which has a structural transition from hyaline cartilage to the underlying subchondral bone, provides distinct physiological function and developed from an initial growth factor gradient. In this chapter, in addition to various gradients generated with the buoyancy-driven gradient casting platform, the new method was also used to resolve the complex and clinically-relevant challenge of osteochondral tissue engineering. In this application, buoyancy was used to pattern BMP-2 gradients using one simple injection event. Moreover, the presentation of BMP-

2 gradients has successfully produced osteochondral tissue. The resulting tissue constructs possessed distinct regions of bone and cartilage, along with a structural transition that resembled the tidemark observed at the native osteochondral interface.

It should be noted that alterations are still needed to adapt the proposed platform to other applications. For instance, an intermediate host may be required (in this chapter: HepMA) to sequester other cargo of interest. In addition, the proposed system might not be suitable for creating a precise architecture gradient that could be more easily fabricated using a technique such as 3D printing. Nevertheless, for a hydrogel-based system, the versatility, speed and ease of use of the buoyancy-based platform provide the opportunity for many different applications in gradient material fabrication and interfacial tissue engineering.

Future Perspective

A. Producing more robust constructs

The proposed buoyancy-based technology provides more advantages when compared to the SPIONs-based system, and it provides opportunities for further study. However, additional work is still required for translation of this technology; in particular, the overall mechanical properties of the engineered tissue construct must better match to native tissue to be compatible with in vivo transplantation. While GelMA was used as the gel material in the present study, other hydrogels or double network hydrogel, which provides better mechanical properties could be tested [307]. In addition to using a cell-laden hydrogel, bio-inert polymers could also be considered, since the proposed technology could also support the materials gradient of water-free polymers. For instance, hybrid polymers of silica/poly(tetrahydrofuran)/poly(ε-caprolactone), which have superior mechanical property comparing to natural derived hydrogel, could be used [308].

B. Platform for studying osteochondral development

In both chapter 2 (magnetically aligned BMP-2 gradient) and this chapter (buoyancy-driven BMP-2 gradient), the structural complexity of the engineered osteochondral tissue, most notably the sharp transition between bone and cartilage, was generated from an initially smooth concentration gradient of BMP-2. This emergent structural feature is fascinating considering the developmental biology of the osteochondral interface, in which concentration gradients of osteoinductive factors produce a sharp transition (tidemark) that separates the subchondral bone/calcified cartilage from hyaline cartilage.

Using this nanoparticle-free platform as a model system, further studies related to osteochondral tissue development biology could be conducted. For instance, the differentiation dynamics during the tide-mark formation can be investigated. In the *in vitro* engineered constructs, it is hypothesised that the tide mark emerged from the initial BMP-2 gradient in the system. It is thought that a threshold level of BMP-2 is required to initiate and sustain mineralisation of the osteochondral tissue, which may, in turn, produce a positive feedback loop whereby the deposited mineral (HAP or resorbed β-TCP) act to further stimulate osteogenesis. Using the developed platform as a model system, molecular cross-talks (*e.g.*, regulations of different genes, secretion of downstream growth factors) could be extracted using a technique like single cell sequencing and may provide a sound mechanistic basis for engineering of osteochondral constructs and other structurally complex tissues. Further work is required to test this theory, which could shed light on some of the key developmental processes that occur during endochondral ossification.

Chapter V: Conclusion

5.1 Toward a More Complex Tissue Engineering

Since the 90s, the field of tissue engineering has extensively progressed from casting simple constructs to systems with a more complex structure. Numerous studies have optimised the combination of biomaterial, signals and culture protocol for different engineered tissues, however, many of these protocols use a homogeneous distribution of components that produces constructs with a uniform structure. To engineer complex tissues, the heterogeneous character of the target tissue must be considered. This is especially crucial for the engineering of gradient constructs, such as osteochondral tissue, from a single cell population, such as mesenchymal stem cells. In this case, one tissue engineering approach is to spatially and temporally decorate a biomaterial with a morphogen signal gradient.

Physical Forces for Gradient Tissue Engineering

In this thesis, the literature surrounding gradient tissue engineering was reviewed in chapter 1. By considering the gradients present in nature, the logic of gradient interpretation, and the current gradient casting approaches, it is clear that a generalised gradient fabrication technology for heterogenous tissue engineering is still missing. An ideal gradient fabrication technology should provide a system with distinct spatial information that supports the generation of the final heterogeneous tissue. However, while several gradient fabrication technologies have been reported, most of them require specialist or customised equipment (*e.g.*, gradient maker, microfluidics, 3D bioprinter) and often have relatively complicated or lengthy fabrication protocols. To enable widespread use and support future translational applications, an ideal gradient casting technology should be simple, rapid and applicable to different scenarios. Under this rationale, two forces (magnetism and buoyancy) were exploited for gradient casting and heterogeneous tissue engineering.

In chapter 3, a magnetic gradient casting platform was introduced. It was demonstrated that application of a magnetic field gradient could be used to create gradients of SPIONs in a short period of time (< 1 min) across several common hydrogels (*e.g.*, gelatin, agarose, gellan gum and matrigel). This technology is versatile and could be used for a number of applications. For instance, the SPIONs could be modified to sequester alternative cargos, including proteins, small molecules, oligonucleotides, or macromolecules. Although this strategy provides several advantages, the use of metallic nanoparticles presents a concern for *in vivo* applications, which led me to investigate alternative, nanoparticle-free systems.

In chapter 4, a buoyancy gradient casting platform was developed. One liquid was injected into another liquid at a defined rate, and the whole system was cast after the formation of a buoyancy-driven gradient. Buoyancy can be applied more broadly than magnetism, and as a result, a wider range of applications could be investigated. The system was still capable of forming nanoparticle gradients, but this was not restricted to SPIONs: using this fabrication strategy the platform was able to pattern gradients of non-magnetic inorganic nanoparticles, synthetic liposomes, and biological extracellular vesicles. This system also supported the formation of bulk material gradients, macromolecule gradients and, with the help of a suitable polymer intermediate, small molecule gradients. When the density of the two materials were insufficient to create a buoyancy gradient, a temporary density modifier could be used to template a gradient. Overall, this buoyancy-driven casting platform is versatile with a relatively straight-forward and rapid fabrication protocol.

Engineering Osteochondral Tissue

As introduced in chapter 1, physiological osteochondral tissue possesses a complex architecture and several different natural gradients. The formation of these gradients is largely dictated by a heterogeneous distribution of growth factors present during embryological development and pre-adolescent growth. For instance, the formation of the cartilage-bone interface in osteochondral tissue is heavily influenced by a polarised distribution of pro-osteogenic growth factors, such as BMP-2. The local difference of growth factor concentration produces a spatial variance in cell signalling, which can, in turn, lead to distinct cell phenotypes across the tissue (*e.g.*, osteoblasts and chondrocytes). In a structural system such as osteochondral tissue, the different cell types sculpt the final tissue composition *via* the production and remodelling of different extracellular matrix components. These structural features play a critically important role in the functional performance of the tissue.

The key to create osteochondral tissue from hMSCs is to provide both osteogenic and chondrogenic differentiation signals. Complex systems, such as compartmentalized culture chambers, could supply different regions of the tissue with different media, however, a system using scaffolds pre-decorated with morphogen gradients is more favourable because it can be supported by conventional culture conditions. To this end, both the magnetic and buoyancy-driven gradient casting for osteochondral tissue engineering were tailored using an optimised osteochondral culture medium. In the magnetic platform, the SPION surface was first modified with heparin, which acted as an intermediate host for BMP-2. This was used to create a nanoparticle/BMP-2 gradient using an applied magnetic field. Indeed, this set-up generated osteochondral tissue with several features similar to physiological tissue (*e.g.*, gene expression, osteogenic and chondrogenic ECM distribution, alkaline phosphatase activity and mineral formation). In buoyancy-driven gradient casting, heparin-sequestered BMP-2 was once again used to locally stimulate osteogenesis. A gradient of heparin methacryloyl, mixed with BMP-2, was cast in a gelatin methacryloyl hydrogel and the two methacrylated biopolymers were photocrosslinked to form a biomaterial with a gradient of BMP-2. This set-up also generated osteochondral tissue with natural features.

It was interesting to observe that despite presenting a morphogen *gradient*, both technologies generated osteochondral tissue with a sharp transition between the mineralized and non-mineralized tissue. This “tide mark” is observed in native osteochondral tissue and future work is needed to understand this emergent structural behaviour. By combining techniques such as single cell transcriptomics and fluorescence in-situ hybridization, the established osteochondral tissue engineering platforms could further shed light upon the mechanism of osteochondral tissue development process.

Overall, both the proposed technologies have demonstrated their potential for osteochondral tissue engineering, however, a lot of further optimisation is required for any future clinical translation. More generally, clinical translation of these gradient biomaterials would require the use of materials, cells and media approved by the Food and Drug Administration (FDA) and other relevant international agencies, and tissue fabrication procedures to be brought in line with good manufacturing practice (GMP) guidelines.

Next Chapter of Heterogeneous Tissue Engineering

Decades of research progress in tissue engineering has generated several clinical products that have improved the quality of life of patients. In this thesis, two gradient-casting technologies using magnetic and buoyancy forces are introduced and applied to the engineering of heterogeneous tissue. Since these technologies use broad physical principles, rather than complex fabrication procedures, these technologies offer a more universal platform for building gradient materials and tissues. The technologies introduced in this thesis are relatively straight-forward, cost-effective and widely applicable. These protocols should offer general benefit to the field, and these technologies could be adopted in further research in order to emulate other mesmerising gradients seen in nature.

"Simplicity is the Ultimate Sophistication".

References

1. R. Langer, J.P. Vacanti, Tissue engineering, *Science* **260**(5110) (1993) 920-6.
2. J.E. Murray, J.P. Merrill, J.H. Harrison, Renal homotransplantation in identical twins. 1955, *J Am Soc Nephrol* **12**(1) (2001) 201-4.
3. J.E. Murray, R.E. Wilson, N.L. Tilney, J.P. Merrill, W.C. Cooper, A.G. Birtch, C.B. Carpenter, E.B. Hager, G.J. Dammin, J.H. Harrison, Five years' experience in renal transplantation with immunosuppressive drugs: survival, function, complications, and the role of lymphocyte depletion by thoracic duct fistula, *Ann Surg* **168**(3) (1968) 416-35.
4. E. Bell, H.P. Ehrlich, D.J. Buttle, T. Nakatsuji, Living tissue formed in vitro and accepted as skin-equivalent tissue of full thickness, *Science* **211**(4486) (1981) 1052-4.
5. Y. Cao, J.P. Vacanti, K.T. Paige, J. Upton, C.A. Vacanti, Transplantation of chondrocytes utilizing a polymer-cell construct to produce tissue-engineered cartilage in the shape of a human ear, *Plast Reconstr Surg* **100**(2) (1997) 297-302; discussion 303-4.
6. A.G. Mikos, S.W. Herring, P. Ochareon, J. Elisseeff, H.H. Lu, R. Kandel, F.J. Schoen, M. Toner, D. Mooney, A. Atala, M.E.V. Dyke, D. Kaplan, G. Vunjak-Novakovic, Engineering Complex Tissues, *Tissue Engineering* **12**(12) (2006) 3307-3339.
7. A. Atala, F.K. Kasper, A.G. Mikos, Engineering Complex Tissues, *Science Translational Medicine* **4**(160) (2012) 160rv12-160rv12.
8. J.L. Christian, Morphogen gradients in development: from form to function, *Wiley Interdiscip Rev Dev Biol* **1**(1) (2012) 3-15.
9. V. Vogel, M. Sheetz, Local force and geometry sensing regulate cell functions, *Nat Rev Mol Cell Biol* **7**(4) (2006) 265-75.
10. H.L. Ashe, J. Briscoe, The interpretation of morphogen gradients, *Development* **133**(3) (2006) 385-94.
11. H.H. Lu, S. Thomopoulos, Functional attachment of soft tissues to bone: development, healing, and tissue engineering, *Annu Rev Biomed Eng* **15** (2013) 201-26.
12. P.B. Messersmith, Materials science. Multitasking in tissues and materials, *Science* **319**(5871) (2008) 1767-8.
13. F. Ulloa, J. Briscoe, Morphogens and the control of cell proliferation and patterning in the spinal cord, *Cell Cycle* **6**(21) (2007) 2640-9.
14. P. Garrison, S. Yue, J. Hanson, J. Baron, J.C. Lui, Spatial regulation of bone morphogenetic proteins (BMPs) in postnatal articular and growth plate cartilage, *PLoS One* **12**(5) (2017) e0176752.
15. L.G. Griffith, M.A. Swartz, Capturing complex 3D tissue physiology in vitro, *Nat Rev Mol Cell Biol* **7**(3) (2006) 211-24.
16. S. Sant, M.J. Hancock, J.P. Donnelly, D. Iyer, A. Khademhosseini, Biomimetic Gradient Hydrogels for Tissue Engineering, *Can J Chem Eng* **88**(6) (2010) 899-911.
17. R.O. Hynes, The extracellular matrix: not just pretty fibrils, *Science* **326**(5957) (2009) 1216-9.
18. S.F. Badylak, Regenerative medicine and developmental biology: the role of the extracellular matrix, *Anat Rec B New Anat* **287**(1) (2005) 36-41.
19. M. Singh, C. Berkland, M.S. Detamore, Strategies and applications for incorporating physical and chemical signal gradients in tissue engineering, *Tissue Eng Part B Rev* **14**(4) (2008) 341-66.
20. A.J. Engler, S. Sen, H.L. Sweeney, D.E. Discher, Matrix elasticity directs stem cell lineage specification, *Cell* **126**(4) (2006) 677-89.
21. R. McBeath, D.M. Pirone, C.M. Nelson, K. Bhadriraju, C.S. Chen, Cell shape, cytoskeletal tension, and RhoA regulate stem cell lineage commitment, *Dev Cell* **6**(4) (2004) 483-95.
22. J.G. Jacot, A.D. McCulloch, J.H. Omens, Substrate stiffness affects the functional maturation of neonatal rat ventricular myocytes, *Biophys J* **95**(7) (2008) 3479-87.
23. J.R. Tse, A.J. Engler, Stiffness gradients mimicking in vivo tissue variation regulate mesenchymal stem cell fate, *PLoS One* **6**(1) (2011) e15978.
24. A. Di Luca, B. Ostrowska, I. Lorenzo-Moldero, A. Lepedda, W. Swieszkowski, C. Van Blitterswijk, L. Moroni, Gradients in pore size enhance the osteogenic differentiation of human mesenchymal stromal cells in three-dimensional scaffolds, *Sci Rep* **6** (2016) 22898.

25. A.G. Mikos, S.W. Herring, P. Ochareon, J. Elisseeff, H.H. Lu, R. Kandel, F.J. Schoen, M. Toner, D. Mooney, A. Atala, M.E. Van Dyke, D. Kaplan, G. Vunjak-Novakovic, Engineering complex tissues, *Tissue Eng* **12**(12) (2006) 3307-39.
26. S. Thomopoulos, G.R. Williams, J.A. Gimbel, M. Favata, L.J. Soslowsky, Variation of biomechanical, structural, and compositional properties along the tendon to bone insertion site, *J Orthop Res* **21**(3) (2003) 413-9.
27. P.J. Yang, J.S. Temenoff, Engineering orthopedic tissue interfaces, *Tissue Eng Part B Rev* **15**(2) (2009) 127-41.
28. A. Di Luca, C. Van Blitterswijk, L. Moroni, The osteochondral interface as a gradient tissue: from development to the fabrication of gradient scaffolds for regenerative medicine., *Birth defects research. Part C, Embryo today : reviews* **105**(1) (2015) 34-52.
29. S.P. Ho, S.J. Marshall, M.I. Ryder, G.W. Marshall, The tooth attachment mechanism defined by structure, chemical composition and mechanical properties of collagen fibers in the periodontium, *Biomaterials* **28**(35) (2007) 5238-45.
30. A.J. Pope, G.B. Sands, B.H. Smaill, I.J. LeGrice, Three-dimensional transmural organization of perimysial collagen in the heart, *Am J Physiol Heart Circ Physiol* **295**(3) (2008) H1243-H1252.
31. C. Alber, B.D. Brandner, S. Bjorklund, P. Billsten, R.W. Corkery, J. Engblom, Effects of water gradients and use of urea on skin ultrastructure evaluated by confocal Raman microspectroscopy, *Biochim Biophys Acta* **1828**(11) (2013) 2470-8.
32. B.G. Fuller, Self-organization of intracellular gradients during mitosis, *Cell Div* **5**(1) (2010) 5.
33. M. Caudron, G. Bunt, P. Bastiaens, E. Karsenti, Spatial coordination of spindle assembly by chromosome-mediated signaling gradients, *Science* **309**(5739) (2005) 1373-6.
34. N. McDowell, J.B. Gurdon, D.J. Grainger, Formation of a functional morphogen gradient by a passive process in tissue from the early Xenopus embryo, *Int J Dev Biol* **45**(1) (2001) 199-207.
35. K.M. Cadigan, M.P. Fish, E.J. Rulifson, R. Nusse, Wingless repression of Drosophila frizzled 2 expression shapes the Wingless morphogen gradient in the wing, *Cell* **93**(5) (1998) 767-77.
36. C. Torroja, N. Gorfinkiel, I. Guerrero, Patched controls the Hedgehog gradient by endocytosis in a dynamin-dependent manner, but this internalization does not play a major role in signal transduction, *Development* **131**(10) (2004) 2395-408.
37. J. Filmus, M. Capurro, J. Rast, Glypicans, *Genome Biol* **9**(5) (2008) 224.
38. T. Akiyama, K. Kamimura, C. Firkus, S. Takeo, O. Shimmi, H. Nakato, Dally regulates Dpp morphogen gradient formation by stabilizing Dpp on the cell surface, *Dev Biol* **313**(1) (2008) 408-19.
39. D.L. Kooyman, G.W. Byrne, S. McClellan, D. Nielsen, M. Tone, H. Waldmann, T.M. Coffman, K.R. McCurry, J.L. Platt, J.S. Logan, In vivo transfer of GPI-linked complement restriction factors from erythrocytes to the endothelium, *Science* **269**(5220) (1995) 89-92.
40. J. Steinhauer, J.E. Treisman, Lipid-modified morphogens: functions of fats, *Curr Opin Genet Dev* **19**(4) (2009) 308-14.
41. X. Zeng, J.A. Goetz, L.M. Suber, W.J. Scott, Jr., C.M. Schreiner, D.J. Robbins, A freely diffusible form of Sonic hedgehog mediates long-range signalling, *Nature* **411**(6838) (2001) 716-20.
42. V. Greco, M. Hannus, S. Eaton, Argosomes: a potential vehicle for the spread of morphogens through epithelia, *Cell* **106**(5) (2001) 633-45.
43. D. Panakova, H. Sprong, E. Marois, C. Thiele, S. Eaton, Lipoprotein particles are required for Hedgehog and Wingless signalling, *Nature* **435**(7038) (2005) 58-65.
44. A. Kicheva, P. Pantazis, T. Bollenbach, Y. Kalaidzidis, T. Bittig, F. Julicher, M. Gonzalez-Gaitan, Kinetics of morphogen gradient formation, *Science* **315**(5811) (2007) 521-5.
45. F. Wang, The signaling mechanisms underlying cell polarity and chemotaxis, *Cold Spring Harb Perspect Biol* **1**(4) (2009) a002980.
46. M. Sharma, F. Afrin, N. Satija, R.P. Tripathi, G.U. Gangenahalli, Stromal-derived factor-1/CXCR4 signaling: indispensable role in homing and engraftment of hematopoietic stem cells in bone marrow, *Stem Cells Dev* **20**(6) (2011) 933-46.
47. M.F. Berry, A.J. Engler, Y.J. Woo, T.J. Pirolli, L.T. Bish, V. Jayasankar, K.J. Morine, T.J. Gardner, D.E. Discher, H.L. Sweeney, Mesenchymal stem cell injection after myocardial infarction improves myocardial compliance, *Am J Physiol Heart Circ Physiol* **290**(6) (2006) H2196-203.
48. L.L. Gao, C.Q. Zhang, H. Gao, Z.D. Liu, P.P. Xiao, Depth and rate dependent mechanical behaviors for articular cartilage: experiments and theoretical predictions, *Mater Sci Eng C Mater Biol Appl* **38** (2014) 244-51.
49. H. Sakuta, R. Suzuki, H. Takahashi, A. Kato, T. Shintani, S. Iemura, T.S. Yamamoto, N. Ueno, M. Noda,

Ventroptin: a BMP-4 antagonist expressed in a double-gradient pattern in the retina, *Science* **293**(5527) (2001) 111-5.

50. S. Shimozono, T. Iimura, T. Kitaguchi, S. Higashijima, A. Miyawaki, Visualization of an endogenous retinoic acid gradient across embryonic development, *Nature* **496**(7445) (2013) 363-6.
51. P.V. Lidsky, K.A. Lukyanov, T. Misra, B. Handke, A.S. Mishin, C.F. Lehner, A genetically encoded fluorescent probe for imaging of oxygenation gradients in living Drosophila, *Development* **145**(4) (2018).
52. J. Zinski, Y. Bu, X. Wang, W. Dou, D. Umulis, M.C. Mullins, Systems biology derived source-sink mechanism of BMP gradient formation, *Elife* **6** (2017).
53. H.P. Makarenkova, M.P. Hoffman, A. Beenken, A.V. Eliseenkova, R. Meech, C. Tsau, V.N. Patel, R.A. Lang, M. Mohammadi, Differential interactions of FGFs with heparan sulfate control gradient formation and branching morphogenesis, *Sci Signal* **2**(88) (2009) ra55.
54. S. Dyson, J.B. Gurdon, The interpretation of position in a morphogen gradient as revealed by occupancy of activin receptors, *Cell* **93**(4) (1998) 557-68.
55. J. Ericson, P. Rashbass, A. Schedl, S. Brenner-Morton, A. Kawakami, V. van Heyningen, T.M. Jessell, J. Briscoe, Pax6 controls progenitor cell identity and neuronal fate in response to graded Shh signaling, *Cell* **90**(1) (1997) 169-80.
56. J. Jullien, J. Gurdon, Morphogen gradient interpretation by a regulated trafficking step during ligand-receptor transduction, *Genes Dev* **19**(22) (2005) 2682-94.
57. A. Di Luca, C. Van Blitterswijk, L. Moroni, The osteochondral interface as a gradient tissue: from development to the fabrication of gradient scaffolds for regenerative medicine, *Birth Defects Res C Embryo Today* **105**(1) (2015) 34-52.
58. T.J. Levingstone, E. Thompson, A. Matsiko, A. Schepens, J.P. Gleeson, F.J. O'Brien, Multi-layered collagen-based scaffolds for osteochondral defect repair in rabbits, *Acta Biomater* **32** (2016) 149-160.
59. L.H. Nguyen, A.K. Kudva, N.S. Saxena, K. Roy, Engineering articular cartilage with spatially-varying matrix composition and mechanical properties from a single stem cell population using a multi-layered hydrogel, *Biomaterials* **32**(29) (2011) 6946-52.
60. J.K. Sherwood, S.L. Riley, R. Palazzolo, S.C. Brown, D.C. Monkhouse, M. Coates, L.G. Griffith, L.K. Landeen, A. Ratcliffe, A three-dimensional osteochondral composite scaffold for articular cartilage repair, *Biomaterials* **23**(24) (2002) 4739-51.
61. T.B. Woodfield, J. Malda, J. de Wijn, F. Peters, J. Riesle, C.A. van Blitterswijk, Design of porous scaffolds for cartilage tissue engineering using a three-dimensional fiber-deposition technique, *Biomaterials* **25**(18) (2004) 4149-61.
62. A. Di Luca, K. Szlazak, I. Lorenzo-Moldero, C.A. Ghebes, A. Lepedda, W. Swieszkowski, C. Van Blitterswijk, L. Moroni, Influencing chondrogenic differentiation of human mesenchymal stromal cells in scaffolds displaying a structural gradient in pore size, *Acta Biomater* **36** (2016) 210-9.
63. L.G. Bracaglia, B.T. Smith, E. Watson, N. Arumugasaamy, A.G. Mikos, J.P. Fisher, 3D printing for the design and fabrication of polymer-based gradient scaffolds, *Acta Biomater* **56** (2017) 3-13.
64. W. Liu, Y.S. Zhang, M.A. Heinrich, F. De Ferrari, H.L. Jang, S.M. Bakht, M.M. Alvarez, J. Yang, Y.C. Li, G. Trujillo-de Santiago, A.K. Miri, K. Zhu, P. Khoshakhlagh, G. Prakash, H. Cheng, X. Guan, Z. Zhong, J. Ju, G.H. Zhu, X. Jin, S.R. Shin, M.R. Dokmeci, A. Khademhosseini, Rapid Continuous Multimaterial Extrusion Bioprinting, *Adv Mater* **29**(3) (2017) 1604630.
65. L. Ouyang, R. Yao, Y. Zhao, W. Sun, Effect of bioink properties on printability and cell viability for 3D bioplotting of embryonic stem cells, *Biofabrication* **8**(3) (2016) 035020.
66. N.H. Dormer, M. Singh, L. Zhao, N. Mohan, C.J. Berkland, M.S. Detamore, Osteochondral interface regeneration of the rabbit knee with macroscopic gradients of bioactive signals, *J Biomed Mater Res A* **100**(1) (2012) 162-70.
67. S. Nemir, H.N. Hayenga, J.L. West, PEGDA hydrogels with patterned elasticity: Novel tools for the study of cell response to substrate rigidity, *Biotechnol Bioeng* **105**(3) (2010) 636-44.
68. N.H. Dormer, M. Singh, L. Wang, C.J. Berkland, M.S. Detamore, Osteochondral interface tissue engineering using macroscopic gradients of bioactive signals, *Ann Biomed Eng* **38**(6) (2010) 2167-82.
69. N. Mohan, V. Gupta, B. Sridharan, A. Sutherland, M.S. Detamore, The potential of encapsulating "raw materials" in 3D osteochondral gradient scaffolds, *Biotechnol Bioeng* **111**(4) (2014) 829-41.
70. A. Seidi, M. Ramalingam, I. Elloumi-Hannachi, S. Ostrovidov, A. Khademhosseini, Gradient biomaterials for soft-to-hard interface tissue engineering, *Acta Biomater* **7**(4) (2011) 1441-51.
71. X. Zhang, X. Gao, L. Jiang, J. Qin, Flexible generation of gradient electrospinning nanofibers using a microfluidic assisted approach, *Langmuir* **28**(26) (2012) 10026-32.

72. L.W. Chow, A. Armgarth, J.-P. St-Pierre, S. Bertazzo, C. Gentilini, C. Aurisicchio, S.D. McCullen, J.A.M. Steele, M.M. Stevens, Peptide-directed spatial organization of biomolecules in dynamic gradient scaffolds., *Advanced healthcare materials* **3**(9) (2014) 1381-1386.

73. S.D. McCullen, H. Autefage, A. Callanan, E. Gentleman, M.M. Stevens, Anisotropic Fibrous Scaffolds for Articular Cartilage Regeneration, *Tissue Engineering Part A* **18**(19-20) (2012) 2073-2083.

74. J.K. Hong, J.Y. Bang, G. Xu, J.H. Lee, Y.J. Kim, H.J. Lee, H.S. Kim, S.M. Kwon, Thickness-controllable electrospun fibers promote tubular structure formation by endothelial progenitor cells, *Int J Nanomedicine* **10** (2015) 1189-200.

75. M.C. Dodla, R.V. Bellamkonda, Anisotropic scaffolds facilitate enhanced neurite extension in vitro, *J Biomed Mater Res A* **78**(2) (2006) 213-21.

76. M.K. Gunnewiek, A. Di Luca, H.Z. Bollemaat, C.A. van Blitterswijk, G.J. Vancso, L. Moroni, E.M. Benetti, Creeping proteins in microporous structures: polymer brush-assisted fabrication of 3D gradients for tissue engineering, *Adv Healthc Mater* **4**(8) (2015) 1169-74.

77. H.C. Yang, Q.Y. Wu, L.S. Wan, Z.K. Xu, Polydopamine gradients by oxygen diffusion controlled autoxidation, *Chem Commun (Camb)* **49**(89) (2013) 10522-4.

78. S. Sant, M.J. Hancock, J.P. Donnelly, D. Iyer, A. Khademhosseini, BIOMIMETIC GRADIENT HYDROGELS FOR TISSUE ENGINEERING., *The Canadian journal of chemical engineering* **88**(6) (2010) 899-911.

79. J.E. Phillips, K.L. Burns, J.M. Le Doux, R.E. Guldberg, A.J. Garcia, Engineering graded tissue interfaces, *Proc Natl Acad Sci U S A* **105**(34) (2008) 12170-5.

80. J. Shi, L. Wang, F. Zhang, H. Li, L. Lei, L. Liu, Y. Chen, Incorporating protein gradient into electrospun nanofibers as scaffolds for tissue engineering, *ACS Appl Mater Interfaces* **2**(4) (2010) 1025-30.

81. Y. Du, M.J. Hancock, J. He, J.L. Villa-Uribe, B. Wang, D.M. Cropek, A. Khademhosseini, Convection-driven generation of long-range material gradients, *Biomaterials* **31**(9) (2010) 2686-94.

82. R.F. Canadas, T. Ren, A.P. Marques, J.M. Oliveira, R.L. Reis, U. Demirci, Biochemical Gradients to Generate 3D Heterotypic-Like Tissues with Isotropic and Anisotropic Architectures, *Advanced Functional Materials* **28**(48) (2018) 1804148.

83. N. Zaari, P. Rajagopalan, S.K. Kim, A.J. Engler, J.Y. Wong, Photopolymerization in Microfluidic Gradient Generators: Microscale Control of Substrate Compliance to Manipulate Cell Response, *Advanced Materials* **16**(23-24) (2004) 2133-2137.

84. B.P. Mahadik, T.D. Wheeler, L.J. Skertich, P.J. Kenis, B.A. Harley, Microfluidic generation of gradient hydrogels to modulate hematopoietic stem cell culture environment, *Adv Healthc Mater* **3**(3) (2014) 449-58.

85. S.H. Oh, I.K. Park, J.M. Kim, J.H. Lee, In vitro and in vivo characteristics of PCL scaffolds with pore size gradient fabricated by a centrifugation method, *Biomaterials* **28**(9) (2007) 1664-71.

86. S.H. Oh, T.H. Kim, J.H. Lee, Creating growth factor gradients in three dimensional porous matrix by centrifugation and surface immobilization, *Biomaterials* **32**(32) (2011) 8254-60.

87. R. Sunyer, A.J. Jin, R. Nossal, D.L. Sackett, Fabrication of hydrogels with steep stiffness gradients for studying cell mechanical response, *PLoS One* **7**(10) (2012) e46107.

88. X. Tong, J. Jiang, D. Zhu, F. Yang, Hydrogels with dual gradients of mechanical and biochemical cues for deciphering cell-niche interactions, *ACS Biomaterials Science & Engineering* **2**(5) (2016) 845-852.

89. K.A. Mosiewicz, L. Kolb, A.J. van der Vlies, M.M. Martino, P.S. Lienemann, J.A. Hubbell, M. Ehrbar, M.P. Lutolf, In situ cell manipulation through enzymatic hydrogel photopatterning, *Nat Mater* **12**(11) (2013) 1072-8.

90. S.V. Vlierberghe, V. Cnudde, P. Dubruel, B. Masschaele, A. Cosijns, I.D. Paepe, P.J. Jacobs, L.V. Hoorebeke, J.P. Remon, E. Schacht, Porous gelatin hydrogels: 1. Cryogenic formation and structure analysis, *Biomacromolecules* **8**(2) (2007) 331-7.

91. S.H. Oh, D.B. An, T.H. Kim, J.H. Lee, Wide-range stiffness gradient PVA/HA hydrogel to investigate stem cell differentiation behavior, *Acta Biomater* **35** (2016) 23-31.

92. C. Li, L. Ouyang, I.J. Pence, A.C. Moore, Y. Lin, C.W. Winter, J.P.K. Armstrong, M.M. Stevens, Buoyancy-Driven Gradients for Biomaterial Fabrication and Tissue Engineering, *Advanced Materials* **31**(17) (2019) 1900291.

93. C. Li, J.P.K. Armstrong, I.J. Pence, W. Kit-Anan, J.L. Puetzer, S. Correia Carreira, A.C. Moore, M.M. Stevens, Glycosylated superparamagnetic nanoparticle gradients for osteochondral tissue engineering, *Biomaterials* **176** (2018) 24-33.

94. Y. Usami, A.T. Gunawardena, M. Iwamoto, M. Enomoto-Iwamoto, Wnt signaling in cartilage development and diseases: lessons from animal studies, *Lab Invest* **96**(2) (2016) 186-96.

95. E.J. Mackie, Y.A. Ahmed, L. Tatarczuch, K.S. Chen, M. Mirams, Endochondral ossification: how cartilage

is converted into bone in the developing skeleton, *Int J Biochem Cell Biol* **40**(1) (2008) 46-62.

96. F. Las Heras, H.K. Gahunia, K.P. Pritzker, Articular cartilage development: a molecular perspective, *Orthop Clin North Am* **43**(2) (2012) 155-71, v.
97. M.A. Cleary, G.J.V.M. van Osch, P.A. Brama, C.A. Hellingman, R. Narcisi, FGF, TGF β and Wnt crosstalk: embryonic to in vitrocartilage development from mesenchymal stem cells, *Journal of Tissue Engineering and Regenerative Medicine* **9**(4) (2013) 332-342.
98. M. Demoor, D. Ollitrault, T. Gomez-Leduc, M. Bouyoucef, M. Hervieu, H. Fabre, J. Lafont, J.M. Denoix, F. Audigie, F. Mallein-Gerin, F. Legendre, P. Galera, Cartilage tissue engineering: molecular control of chondrocyte differentiation for proper cartilage matrix reconstruction, *Biochim Biophys Acta* **1840**(8) (2014) 2414-40.
99. L. Yang, K.Y. Tsang, H.C. Tang, D. Chan, K.S. Cheah, Hypertrophic chondrocytes can become osteoblasts and osteocytes in endochondral bone formation, *Proc Natl Acad Sci U S A* **111**(33) (2014) 12097-102.
100. E.B. Hunziker, E. Kapfinger, J. Geiss, The structural architecture of adult mammalian articular cartilage evolves by a synchronized process of tissue resorption and neoformation during postnatal development, *Osteoarthritis Cartilage* **15**(4) (2007) 403-13.
101. C. Crowder, D. Austin, Age ranges of epiphyseal fusion in the distal tibia and fibula of contemporary males and females, *J Forensic Sci* **50**(5) (2005) 1001-7.
102. H.M. Kronenberg, Developmental regulation of the growth plate, *Nature* **423**(6937) (2003) 332-6.
103. O. Nilsson, E.A. Parker, A. Hegde, M. Chau, K.M. Barnes, J. Baron, Gradients in bone morphogenetic protein-related gene expression across the growth plate, *J Endocrinol* **193**(1) (2007) 75-84.
104. D. Noel, D. Gazit, C. Bouquet, F. Apparailly, C. Bony, P. Plence, V. Millet, G. Turgeman, M. Perricaudet, J. Sany, C. Jorgensen, Short-term BMP-2 expression is sufficient for in vivo osteochondral differentiation of mesenchymal stem cells, *Stem Cells* **22**(1) (2004) 74-85.
105. J.C. Leijten, J. Emons, C. Sticht, S. van Gool, E. Decker, A. Uitterlinden, G. Rappold, A. Hofman, F. Rivadeneira, S. Scherjon, J.M. Wit, J. van Meurs, C.A. van Blitterswijk, M. Karperien, Gremlin 1, frizzled-related protein, and Dkk-1 are key regulators of human articular cartilage homeostasis, *Arthritis Rheum* **64**(10) (2012) 3302-12.
106. S. Murakami, M. Kan, W.L. McKeehan, B. de Crombrugghe, Up-regulation of the chondrogenic Sox9 gene by fibroblast growth factors is mediated by the mitogen-activated protein kinase pathway, *Proc Natl Acad Sci U S A* **97**(3) (2000) 1113-8.
107. E.B. Hunziker, Articular cartilage repair: basic science and clinical progress. A review of the current status and prospects, *Osteoarthritis Cartilage* **10**(6) (2002) 432-63.
108. S. Ansari, S. Khorshidi, A. Karkhaneh, Engineering of gradient osteochondral tissue: From nature to lab, *Acta Biomater* (2019).
109. P. Nooeaid, V. Salih, J.P. Beier, A.R. Boccaccini, Osteochondral tissue engineering: scaffolds, stem cells and applications, *J Cell Mol Med* **16**(10) (2012) 2247-70.
110. M. Tamaddon, L. Wang, Z. Liu, C. Liu, Osteochondral tissue repair in osteoarthritic joints: clinical challenges and opportunities in tissue engineering, *Biodes Manuf* **1**(2) (2018) 101-114.
111. S.P. Nukavarapu, D.L. Dorcemus, Osteochondral tissue engineering: Current strategies and challenges, *Biotechnology Advances* **31**(5) (2013) 706-721.
112. C. Di Bella, A. Fosang, D.M. Donati, G.G. Wallace, P.F. Choong, 3D Bioprinting of Cartilage for Orthopedic Surgeons: Reading between the Lines, *Front Surg* **2** (2015) 39.
113. A.J. Sophia Fox, A. Bedi, S.A. Rodeo, The basic science of articular cartilage: structure, composition, and function, *Sports Health* **1**(6) (2009) 461-8.
114. R. Florencio-Silva, G.R.d.S. Sasso, E. Sasso-Cerri, Sim, #xf5, M.J. es, P.S. Cerri, #xe9, rgio, Biology of Bone Tissue: Structure, Function, and Factors That Influence Bone Cells, 2015.
115. T.M. Quinn, H.J. Hauselmann, N. Shintani, E.B. Hunziker, Cell and matrix morphology in articular cartilage from adult human knee and ankle joints suggests depth-associated adaptations to biomechanical and anatomical roles, *Osteoarthritis Cartilage* **21**(12) (2013) 1904-12.
116. E.B. Hunziker, T.M. Quinn, H.J. Hauselmann, Quantitative structural organization of normal adult human articular cartilage, *Osteoarthritis Cartilage* **10**(7) (2002) 564-72.
117. A.M. Bhosale, J.B. Richardson, Articular cartilage: structure, injuries and review of management, *Br Med Bull* **87** (2008) 77-95.
118. R. Teshima, M. Ono, Y. Yamashita, H. Hirakawa, K. Nawata, Y. Morio, Immunohistochemical collagen analysis of the most superficial layer in adult articular cartilage, *Journal of Orthopaedic Science* **9**(3) (2004) 270-273.
119. C.B. Knudson, W. Knudson, Cartilage proteoglycans, *Seminars in Cell & Developmental Biology* **12**(2)

(2001) 69-78.

120. M.S. Bergholt, J.P. St-Pierre, G.S. Offeddu, P.A. Parmar, M.B. Albro, J.L. Puetzer, M.L. Oyen, M.M. Stevens, Raman Spectroscopy Reveals New Insights into the Zonal Organization of Native and Tissue-Engineered Articular Cartilage, *ACS Cent Sci* **2**(12) (2016) 885-895.

121. S. Saarakkala, R.K. Korhonen, M.S. Laasanen, J. Töyräs, J. Rieppo, J.S. Jurvelin, Mechano-acoustic determination of Young' s modulus of articular cartilage, *Biorheology* **41**(3-4) (2004) 167-179.

122. C.W. Archer, E.H. Morrison, M.T. Bayliss, M.W. Ferguson, The development of articular cartilage: II. The spatial and temporal patterns of glycosaminoglycans and small leucine-rich proteoglycans, *J Anat* **189 (Pt 1)** (1996) 23-35.

123. X. Feng, Chemical and Biochemical Basis of Cell-Bone Matrix Interaction in Health and Disease, *Curr Chem Biol* **3**(2) (2009) 189-196.

124. Y. Zhang, F. Wang, H. Tan, G. Chen, L. Guo, L. Yang, Analysis of the mineral composition of the human calcified cartilage zone, *Int J Med Sci* **9**(5) (2012) 353-60.

125. R.K. Korhonen, M.S. Laasanen, J. Töyräs, R. Lappalainen, H.J. Helminen, J.S. Jurvelin, Fibril reinforced poroelastic model predicts specifically mechanical behavior of normal, proteoglycan depleted and collagen degraded articular cartilage, *Journal of Biomechanics* **36**(9) (2003) 1373-1379.

126. J.S. Jurvelin, M.D. Buschmann, E.B. Hunziker, Mechanical anisotropy of the human knee articular cartilage in compression, *Proc Inst Mech Eng H* **217**(3) (2003) 215-9.

127. V.L. Ferguson, A.J. Bushby, A. Boyde, Nanomechanical properties and mineral concentration in articular calcified cartilage and subchondral bone, *J Anat* **203**(2) (2003) 191-202.

128. F. McCormick, J.D. Harris, G.D. Abrams, R. Frank, A. Gupta, K. Hussey, H. Wilson, B. Bach, Jr., B. Cole, Trends in the surgical treatment of articular cartilage lesions in the United States: an analysis of a large private-payer database over a period of 8 years, *Arthroscopy* **30**(2) (2014) 222-6.

129. W. Widuchowski, J. Widuchowski, T. Trzaska, Articular cartilage defects: study of 25,124 knee arthroscopies, *Knee* **14**(3) (2007) 177-82.

130. P. Aichroth, Osteochondritis dissecans of the knee. A clinical survey, *J Bone Joint Surg Br* **53**(3) (1971) 440-7.

131. O.S. Schindler, Osteochondritis dissecans of the knee, *Current Orthopaedics* **21**(1) (2007) 47-58.

132. B.J. Huang, J.C. Hu, K.A. Athanasiou, Cell-based tissue engineering strategies used in the clinical repair of articular cartilage, *Biomaterials* **98** (2016) 1-22.

133. N. Hawi, C. Haasper, "Long-term results after microfracture treatment for full-thickness knee chondral lesions in athletes" Knee Surg Sports Traumatol Arthrosc (2014) 22:1986-1996 DOI 10.1007/s00167-013-2676-8, *Knee Surg Sports Traumatol Arthrosc* **23**(4) (2015) 1268-9.

134. L. Hangody, G.K. Rathonyi, Z. Duska, G. Vasarhelyi, P. Fules, L. Modis, Autologous osteochondral mosaicplasty. Surgical technique, *J Bone Joint Surg Am* **86-A Suppl 1** (2004) 65-72.

135. T. Minas, Autologous Chondrocyte Implantation for Focal Chondral Defects of the Knee, *Clinical Orthopaedics and Related Research®* **391** (2001) S349-S361.

136. T. Minas, A. Von Keudell, T. Bryant, A.H. Gomoll, The John Insall Award: A minimum 10-year outcome study of autologous chondrocyte implantation, *Clin Orthop Relat Res* **472**(1) (2014) 41-51.

137. J.L. Puetzer, J.N. Petitte, E.G. Loboa, Comparative review of growth factors for induction of three-dimensional in vitro chondrogenesis in human mesenchymal stem cells isolated from bone marrow and adipose tissue, *Tissue Eng Part B Rev* **16**(4) (2010) 435-44.

138. K. Johnson, S. Zhu, M.S. Tremblay, J.N. Payette, J. Wang, L.C. Bouchez, S. Meeusen, A. Althage, C.Y. Cho, X. Wu, P.G. Schultz, A stem cell-based approach to cartilage repair, *Science* **336**(6082) (2012) 717-21.

139. A. Valiani, M.A. Izadi, H. Bahramian, E. Esfandiari, B. Hashemibeni, Comparison between the effect of kartogenin and TGFbeta3 on chondrogenesis of human adipose- derived stem cells in fibrin scaffold, *Bratisl Lek Listy* **118**(10) (2017) 591-597.

140. D.F. Williams, Challenges With the Development of Biomaterials for Sustainable Tissue Engineering, *Front Bioeng Biotechnol* **7** (2019) 127.

141. R. Longley, A.M. Ferreira, P. Gentile, Recent Approaches to the Manufacturing of Biomimetic Multi-Phasic Scaffolds for Osteochondral Regeneration, *Int J Mol Sci* **19**(6) (2018).

142. J.M. Polak, A.E. Bishop, Stem cells and tissue engineering: past, present, and future, *Ann N Y Acad Sci* **1068** (2006) 352-66.

143. M.M. Caron, P.J. Emans, M.M. Coolsen, L. Voss, D.A. Surtel, A. Cremers, L.W. van Rhijn, T.J. Welting, Redifferentiation of dedifferentiated human articular chondrocytes: comparison of 2D and 3D cultures, *Osteoarthritis Cartilage* **20**(10) (2012) 1170-8.

144. H.C. Tribe, J. McEwan, H. Taylor, R.O.C. Oreffo, R.S. Tare, Mesenchymal Stem Cells: Potential Role in the

Treatment of Osteochondral Lesions of the Ankle, *Biotechnol J* **12**(12) (2017).

145. M. Abad, L. Mosteiro, C. Pantoja, M. Canamero, T. Rayon, I. Ors, O. Grana, D. Megias, O. Dominguez, D. Martinez, M. Manzanares, S. Ortega, M. Serrano, Reprogramming in vivo produces teratomas and iPS cells with totipotency features, *Nature* **502**(7471) (2013) 340-5.
146. M. Owen, A.J. Friedenstein, Stromal stem cells: marrow-derived osteogenic precursors, *Ciba Found Symp* **136** (1988) 42-60.
147. Y. Sakaguchi, I. Sekiya, K. Yagishita, T. Muneta, Comparison of human stem cells derived from various mesenchymal tissues: superiority of synovium as a cell source, *Arthritis Rheum* **52**(8) (2005) 2521-9.
148. B.A. Jones, M. Pei, Synovium-derived stem cells: a tissue-specific stem cell for cartilage engineering and regeneration, *Tissue Eng Part B Rev* **18**(4) (2012) 301-11.
149. S.C. Dickinson, C.A. Sutton, K. Brady, A. Salerno, T. Katopodi, R.L. Williams, C.C. West, D. Evseenko, L. Wu, S. Pang, R. Ferro de Godoy, A.E. Goodship, B. Peault, A.W. Blom, W. Kafienah, A.P. Hollander, The Wnt5a Receptor, Receptor Tyrosine Kinase-Like Orphan Receptor 2, Is a Predictive Cell Surface Marker of Human Mesenchymal Stem Cells with an Enhanced Capacity for Chondrogenic Differentiation, *Stem Cells* **35**(11) (2017) 2280-2291.
150. A. Uccelli, V. Pistoia, L. Moretta, Mesenchymal stem cells: a new strategy for immunosuppression?, *Trends Immunol* **28**(5) (2007) 219-26.
151. S. Aggarwal, M.F. Pittenger, Human mesenchymal stem cells modulate allogeneic immune cell responses, *Blood* **105**(4) (2005) 1815-22.
152. W. Wang, D. Rigueur, K.M. Lyons, TGFbeta signaling in cartilage development and maintenance, *Birth Defects Res C Embryo Today* **102**(1) (2014) 37-51.
153. M. Wu, G. Chen, Y.P. Li, TGF-beta and BMP signaling in osteoblast, skeletal development, and bone formation, homeostasis and disease, *Bone Res* **4** (2016) 16009.
154. E. Augustyniak, T. Trzeciak, M. Richter, J. Kaczmarczyk, W. Suchorska, The role of growth factors in stem cell-directed chondrogenesis: a real hope for damaged cartilage regeneration, *Int Orthop* **39**(5) (2015) 995-1003.
155. M.B. Sporn, A.B. Roberts, L.M. Wakefield, R.K. Assoian, Transforming growth factor-beta: biological function and chemical structure, *Science* **233**(4763) (1986) 532-4.
156. H. Madry, A. Rey-Rico, J.K. Venkatesan, B. Johnstone, M. Cucchiarini, Transforming growth factor Beta-releasing scaffolds for cartilage tissue engineering, *Tissue Eng Part B Rev* **20**(2) (2014) 106-25.
157. M.B. Mueller, M. Fischer, J. Zellner, A. Berner, T. Dienstknecht, L. Prantl, R. Kujat, M. Nerlich, R.S. Tuan, P. Angele, Hypertrophy in mesenchymal stem cell chondrogenesis: effect of TGF-beta isoforms and chondrogenic conditioning, *Cells Tissues Organs* **192**(3) (2010) 158-66.
158. Q.O. Tang, K. Shakib, M. Heliotis, E. Tsiridis, A. Mantalaris, U. Ripamonti, E. Tsiridis, TGF-beta3: A potential biological therapy for enhancing chondrogenesis, *Expert Opin Biol Ther* **9**(6) (2009) 689-701.
159. A.C. Carreira, F.H. Lojudice, E. Halcsik, R.D. Navarro, M.C. Sogayar, J.M. Granjeiro, Bone morphogenetic proteins: facts, challenges, and future perspectives, *J Dent Res* **93**(4) (2014) 335-45.
160. F. Deschaseaux, L. Sensebe, D. Heymann, Mechanisms of bone repair and regeneration, *Trends Mol Med* **15**(9) (2009) 417-29.
161. B. Keller, T. Yang, Y. Chen, E. Munivez, T. Bertin, B. Zabel, B. Lee, Interaction of TGFbeta and BMP signaling pathways during chondrogenesis, *PLoS One* **6**(1) (2011) e16421.
162. A.W. James, G. LaChaud, J. Shen, G. Asatrian, V. Nguyen, X. Zhang, K. Ting, C. Soo, A Review of the Clinical Side Effects of Bone Morphogenetic Protein-2, *Tissue Eng Part B Rev* **22**(4) (2016) 284-97.
163. N. Shintani, K.A. Siebenrock, E.B. Hunziker, TGF-ss1 enhances the BMP-2-induced chondrogenesis of bovine synovial explants and arrests downstream differentiation at an early stage of hypertrophy, *PLoS One* **8**(1) (2013) e53086.
164. T.F. Li, M. Darowish, M.J. Zuscik, D. Chen, E.M. Schwarz, R.N. Rosier, H. Drissi, R.J. O'Keefe, Smad3-deficient chondrocytes have enhanced BMP signaling and accelerated differentiation, *J Bone Miner Res* **21**(1) (2006) 4-16.
165. I. Kawamura, S. Maeda, K. Imamura, T. Setoguchi, M. Yokouchi, Y. Ishidou, S. Komiya, SnoN suppresses maturation of chondrocytes by mediating signal cross-talk between transforming growth factor-beta and bone morphogenetic protein pathways, *J Biol Chem* **287**(34) (2012) 29101-13.
166. K. Tachi, M. Takami, H. Sato, A. Mochizuki, B. Zhao, Y. Miyamoto, H. Tsukasaki, T. Inoue, S. Shintani, T. Koike, Y. Honda, O. Suzuki, K. Baba, R. Kamijo, Enhancement of bone morphogenetic protein-2-induced ectopic bone formation by transforming growth factor-beta1, *Tissue Eng Part A* **17**(5-6) (2011) 597-606.
167. C.A. Simmons, E. Alsberg, S. Hsiong, W.J. Kim, D.J. Mooney, Dual growth factor delivery and controlled scaffold degradation enhance in vivo bone formation by transplanted bone marrow stromal cells, *Bone*

35(2) (2004) 562-9.

168. M.J. Dalby, A.J. García, M. Salmeron-Sanchez, Receptor control in mesenchymal stem cell engineering, *Nature Reviews Materials* **3**(3) (2018) 17091.

169. K. Hauff, C. Zambarda, M. Dietrich, M. Halbig, A.L. Grab, R. Medda, E.A. Cavalcanti-Adam, Matrix-Immobilized BMP-2 on Microcontact Printed Fibronectin as an in vitro Tool to Study BMP-Mediated Signaling and Cell Migration, *Front Bioeng Biotechnol* **3** (2015) 62.

170. K. Lee, E.A. Silva, D.J. Mooney, Growth factor delivery-based tissue engineering: general approaches and a review of recent developments, *J R Soc Interface* **8**(55) (2011) 153-70.

171. P. Farkaš, S. Bystrický, Chemical conjugation of biomacromolecules: A mini-review, *Chemical Papers* **64**(6) (2010) 683-695.

172. J. Kalia, R.T. Raines, Advances in Bioconjugation, *Curr Org Chem* **14**(2) (2010) 138-147.

173. E.S. Place, N.D. Evans, M.M. Stevens, Complexity in biomaterials for tissue engineering, *Nat Mater* **8**(6) (2009) 457-70.

174. S.H. Kim, J. Turnbull, S. Guimond, Extracellular matrix and cell signalling: the dynamic cooperation of integrin, proteoglycan and growth factor receptor, *J Endocrinol* **209**(2) (2011) 139-51.

175. O. Jeon, S.J. Song, S.W. Kang, A.J. Putnam, B.S. Kim, Enhancement of ectopic bone formation by bone morphogenetic protein-2 released from a heparin-conjugated poly(L-lactic-co-glycolic acid) scaffold, *Biomaterials* **28**(17) (2007) 2763-71.

176. Y. Liang, K.L. Kiick, Heparin-functionalized polymeric biomaterials in tissue engineering and drug delivery applications, *Acta Biomater* **10**(4) (2014) 1588-600.

177. N.S. Gandhi, R.L. Mancera, Prediction of heparin binding sites in bone morphogenetic proteins (BMPs), *Biochimica et Biophysica Acta (BBA) - Proteins and Proteomics* **1824**(12) (2012) 1374-1381.

178. A. Shafiee, A. Atala, Tissue Engineering: Toward a New Era of Medicine, *Annu Rev Med* **68** (2017) 29-40.

179. A.N. de Belder, K.O. Wik, Preparation and properties of fluorescein-labelled hyaluronate, *Carbohydrate Research* **44**(2) (1975) 251-257.

180. D. Loessner, C. Meinert, E. Kaemmerer, L.C. Martine, K. Yue, P.A. Levett, T.J. Klein, F.P. Melchels, A. Khademhosseini, D.W. Hutmacher, Functionalization, preparation and use of cell-laden gelatin methacryloyl-based hydrogels as modular tissue culture platforms, *Nat Protoc* **11**(4) (2016) 727-46.

181. D.S. Benoit, K.S. Anseth, Heparin functionalized PEG gels that modulate protein adsorption for hMSC adhesion and differentiation, *Acta Biomater* **1**(4) (2005) 461-70.

182. D.M. Templeton, The basis and applicability of the dimethylmethylene blue binding assay for sulfated glycosaminoglycans, *Connect Tissue Res* **17**(1) (1988) 23-32.

183. E. Butchert, T.R. Manley, The vibrational spectra of n-dodecyl methacrylate, *Spectrochimica Acta Part A: Molecular Spectroscopy* **34**(7) (1978) 781-784.

184. H. Edwards, A. Johnson, E. E. Lawson, A Raman spectroscopic study of N,N-dimethylacrylamide, 1994.

185. A.C. Moore, J.F. DeLucca, D.M. Elliott, D.L. Burris, Quantifying Cartilage Contact Modulus, Tension Modulus, and Permeability With Hertzian Biphasic Creep, *J Tribol* **138**(4) (2016) 0414051-414057.

186. H. Hertz, On the Contact of Elastic Solids, *J. Reine Angew Math.* **92** (1881) 156-171.

187. A. Mendyk, R. Jachowicz, Unified methodology of neural analysis in decision support systems built for pharmaceutical technology, *Expert Systems with Applications* **32**(4) (2007) 1124-1131.

188. N.A. Peppas, E.W. Merrill, Crosslinked poly(vinyl alcohol) hydrogels as swollen elastic networks, *Journal of Applied Polymer Science* **21**(7) (1977) 1763-1770.

189. S. Koutsopoulos, Synthesis and characterization of hydroxyapatite crystals: a review study on the analytical methods, *J Biomed Mater Res* **62**(4) (2002) 600-12.

190. R.O. Duda, P.E. Hart, D.G. Stork, Pattern Classification (2nd Edition), Wiley-Interscience2000.

191. S.L. Zeger, K.Y. Liang, Longitudinal data analysis for discrete and continuous outcomes, *Biometrics* **42**(1) (1986) 121-30.

192. J.A. Hanley, A. Negassa, M.D. Edwardes, J.E. Forrester, Statistical analysis of correlated data using generalized estimating equations: an orientation, *Am J Epidemiol* **157**(4) (2003) 364-75.

193. C.M. O'Brien, J.L. Herington, N. Brown, I.J. Pence, B.C. Paria, J.C. Slaughter, J. Reese, A. Mahadevan-Jansen, *in vivo* Raman spectral analysis of impaired cervical remodeling in a mouse model of delayed parturition, *Sci Rep* **7**(1) (2017) 6835.

194. J.M.D. Coey, Magnetism and magnetic materials, Cambridge University Press, Cambridge
Cambridge, UK
New York, 2010.

195. M. Reis, Chapter 3 - Angular Momenta, in: M. Reis (Ed.), Fundamentals of Magnetism, Academic Press,

Boston, 2013, pp. 25-43.

196. D. Jiles, Introduction to magnetism and magnetic materials, 2nd ed., Chapman & Hall, London, 1998.

197. C.P. Bean, J.D. Livingston, Superparamagnetism, *Journal of Applied Physics* **30**(4) (1959) S120-S129.

198. B. Polyak, G. Friedman, Magnetic targeting for site-specific drug delivery: applications and clinical potential, *Expert Opinion on Drug Delivery* **6**(1) (2009) 53-70.

199. K. Okada, S. Kohiki, S. Nishi, H. Shimooka, H. Deguchi, M. Mitome, Y. Bando, T. Shishido, Room Temperature Ferromagnetism of Fe Doped Indium Tin Oxide Based on Dispersed Fe3O4Nanoparticles, *Japanese Journal of Applied Physics* **46**(No. 35) (2007) L823-L825.

200. Q.A. Pankhurst, J. Connolly, S.K. Jones, J. Dobson, Applications of magnetic nanoparticles in biomedicine, *Journal of Physics D: Applied Physics* **36**(13) (2003) R167.

201. E.A. Lee, H. Yim, J. Heo, H. Kim, G. Jung, N.S. Hwang, Application of magnetic nanoparticle for controlled tissue assembly and tissue engineering, *Arch Pharm Res* **37**(1) (2014) 120-8.

202. A. Gloria, T. Russo, U. D'Amora, S. Zeppetelli, T. D'Alessandro, M. Sandri, M. Banobre-Lopez, Y. Pineiro-Redondo, M. Uhlarz, A. Tampieri, J. Rivas, T. Herrmannsdorfer, V.A. Dediu, L. Ambrosio, R. De Santis, Magnetic poly(epsilon-caprolactone)/iron-doped hydroxyapatite nanocomposite substrates for advanced bone tissue engineering, *J R Soc Interface* **10**(80) (2013) 20120833.

203. Y. Gao, J. Lim, S.-H. Teoh, C. Xu, Emerging translational research on magnetic nanoparticles for regenerative medicine, *Chemical Society Reviews* **44**(17) (2015) 6306-6329.

204. X. Li, J. Wei, K.E. Aifantis, Y. Fan, Q. Feng, F.Z. Cui, F. Watari, Current investigations into magnetic nanoparticles for biomedical applications, *J Biomed Mater Res A* **104**(5) (2016) 1285-96.

205. S. Laurent, D. Forge, M. Port, A. Roch, C. Robic, L. Vander Elst, R.N. Muller, Magnetic Iron Oxide Nanoparticles: Synthesis, Stabilization, Vectorization, Physicochemical Characterizations, and Biological Applications, *Chemical Reviews* **108**(6) (2008) 2064-2110.

206. R. Sensenig, Y. Sapir, C. MacDonald, S. Cohen, B. Polyak, Magnetic nanoparticle-based approaches to locally target therapy and enhance tissue regeneration in vivo, *Nanomedicine (Lond)* **7**(9) (2012) 1425-42.

207. J. Meng, B. Xiao, Y. Zhang, J. Liu, H. Xue, J. Lei, H. Kong, Y. Huang, Z. Jin, N. Gu, H. Xu, Super-paramagnetic responsive nanofibrous scaffolds under static magnetic field enhance osteogenesis for bone repair in vivo, *Sci Rep* **3** (2013) 2655.

208. A. Tampieri, M. Iafisco, M. Sandri, S. Panseri, C. Cunha, S. Sprio, E. Savini, M. Uhlarz, T. Herrmannsdorfer, Magnetic bioinspired hybrid nanostructured collagen-hydroxyapatite scaffolds supporting cell proliferation and tuning regenerative process, *ACS Appl Mater Interfaces* **6**(18) (2014) 15697-707.

209. R.A. Perez, K.D. Patel, H.-W. Kim, Novel magnetic nanocomposite injectables: calcium phosphate cements impregnated with ultrafine magnetic nanoparticles for bone regeneration, *RSC Advances* **5**(18) (2015) 13411-13419.

210. A.C. Anselmo, S. Mitragotri, A Review of Clinical Translation of Inorganic Nanoparticles, *AAPS J* **17**(5) (2015) 1041-54.

211. I.J. de Vries, W.J. Lesterhuis, J.O. Barentsz, P. Verdijk, J.H. van Krieken, O.C. Boerman, W.J. Oyen, J.J. Bonenkamp, J.B. Boezeman, G.J. Adema, J.W. Bulte, T.W. Scheenen, C.J. Punt, A. Heerschap, C.G. Figdor, Magnetic resonance tracking of dendritic cells in melanoma patients for monitoring of cellular therapy, *Nat Biotechnol* **23**(11) (2005) 1407-13.

212. S. Correia Carreira, J.P. Armstrong, A.M. Seddon, A.W. Perriman, R. Hartley-Davies, W. Schwarzacher, Ultra-fast stem cell labelling using cationised magnetoferritin, *Nanoscale* **8**(14) (2016) 7474-83.

213. J. Dobson, Magnetic nanoparticles for drug delivery, *Drug Development Research* **67**(1) (2006) 55-60.

214. Y. Gao, J. Lim, S.H. Teoh, C. Xu, Emerging translational research on magnetic nanoparticles for regenerative medicine, *Chem Soc Rev* **44**(17) (2015) 6306-29.

215. A. Monsalve, A.C. Bohórquez, C. Rinaldi, J. Dobson, Remotely triggered activation of TGF-beta with magnetic nanoparticles, *IEEE Magnetics Letters* **6** (2015) 1-4.

216. M. Cruz-Acuna, J.R. Halman, K.A. Afonin, J. Dobson, C. Rinaldi, Magnetic nanoparticles loaded with functional RNA nanoparticles, *Nanoscale* **10**(37) (2018) 17761-17770.

217. D. Lisse, C. Monzel, C. Vicario, J. Manzi, I. Maurin, M. Coppey, J. Piehler, M. Dahan, Engineered Ferritin for Magnetogenetic Manipulation of Proteins and Organelles Inside Living Cells, *Adv Mater* **29**(42) (2017).

218. F. Etoc, D. Lisse, Y. Bellaiche, J. Piehler, M. Coppey, M. Dahan, Subcellular control of Rac-GTPase signalling by magnetogenetic manipulation inside living cells, *Nature Nanotechnology* **8** (2013) 193.

219. C. Plank, O. Zelphati, O. Mykhaylyk, Magnetically enhanced nucleic acid delivery. Ten years of magnetofection-progress and prospects, *Adv Drug Deliv Rev* **63**(14-15) (2011) 1300-31.

220. W.L. Haisler, D.M. Timm, J.A. Gage, H. Tseng, T.C. Killian, G.R. Souza, Three-dimensional cell culturing by magnetic levitation, *Nat Protoc* **8**(10) (2013) 1940-9.
221. H. Perea, J. Aigner, U. Hopfner, E. Wintermantel, Direct magnetic tubular cell seeding: a novel approach for vascular tissue engineering, *Cells Tissues Organs* **183**(3) (2006) 156-65.
222. A. Ito, K. Ino, M. Hayashida, T. Kobayashi, H. Matsunuma, H. Kagami, M. Ueda, H. Honda, Novel methodology for fabrication of tissue-engineered tubular constructs using magnetite nanoparticles and magnetic force, *Tissue Eng* **11**(9-10) (2005) 1553-61.
223. B. Polyak, I. Fishbein, M. Chorny, I. Alferiev, D. Williams, B. Yellen, G. Friedman, R.J. Levy, High field gradient targeting of magnetic nanoparticle-loaded endothelial cells to the surfaces of steel stents, *Proc Natl Acad Sci U S A* **105**(2) (2008) 698-703.
224. S. Correia Carreira, J.P.K. Armstrong, A.M. Seddon, A.W. Perriman, R. Hartley-Davies, W. Schwarzacher, Ultra-fast stem cell labelling using cationised magnetoferritin, *Nanoscale* (2016) 1-10.
225. S.P. Grogan, C. Pauli, P. Chen, J. Du, C.B. Chung, S.D. Kong, C.W. Colwell, Jr., M.K. Lotz, S. Jin, D.D. D'Lima, In situ tissue engineering using magnetically guided three-dimensional cell patterning, *Tissue Eng Part C Methods* **18**(7) (2012) 496-506.
226. B. Steitz, H. Hofmann, S.W. Kamau, P.O. Hassa, M.O. Hottiger, B. von Rechenberg, M. Hofmann-Amtenbrink, A. Petri-Fink, Characterization of PEI-coated superparamagnetic iron oxide nanoparticles for transfection: Size distribution, colloidal properties and DNA interaction, *Journal of Magnetism and Magnetic Materials* **311**(1) (2007) 300-305.
227. N. Bock, A. Riminucci, C. Dionigi, A. Russo, A. Tampieri, E. Landi, V.A. Goranov, M. Marcacci, V. Dediu, A novel route in bone tissue engineering: magnetic biomimetic scaffolds, *Acta Biomater* **6**(3) (2010) 786-96.
228. M. Antman-Passig, O. Shefi, Remote Magnetic Orientation of 3D Collagen Hydrogels for Directed Neuronal Regeneration, *Nano Letters* **16**(4) (2016) 2567-2573.
229. K. Shimizu, A. Ito, T. Yoshida, Y. Yamada, M. Ueda, H. Honda, Bone tissue engineering with human mesenchymal stem cell sheets constructed using magnetite nanoparticles and magnetic force, *J Biomed Mater Res B Appl Biomater* **82**(2) (2007) 471-80.
230. H.M. Yun, S.J. Ahn, K.R. Park, M.J. Kim, J.J. Kim, G.Z. Jin, H.W. Kim, E.C. Kim, Magnetic nanocomposite scaffolds combined with static magnetic field in the stimulation of osteoblastic differentiation and bone formation, *Biomaterials* **85** (2016) 88-98.
231. H.L. Karlsson, P. Cronholm, J. Gustafsson, L. Moller, Copper oxide nanoparticles are highly toxic: a comparison between metal oxide nanoparticles and carbon nanotubes, *Chem Res Toxicol* **21**(9) (2008) 1726-32.
232. N. Singh, G.J. Jenkins, R. Asadi, S.H. Doak, Potential toxicity of superparamagnetic iron oxide nanoparticles (SPION), *Nano Rev* **1** (2010).
233. N. Singh, G.J.S. Jenkins, R. Asadi, S.H. Doak, Potential toxicity of superparamagnetic iron oxide nanoparticles (SPION), *Nano Reviews* **1**(0) (2010) 1-15.
234. A. Elias, A. Tsourkas, Imaging circulating cells and lymphoid tissues with iron oxide nanoparticles, *Hematology Am Soc Hematol Educ Program* (2009) 720-6.
235. A.C. Anselmo, S. Mitragotri, Nanoparticles in the clinic, *Bioeng Transl Med* **1**(1) (2016) 10-29.
236. Y. Anzai, C.W. Piccoli, E.K. Outwater, W. Stanford, D.A. Bluemke, P. Nurenberg, S. Saini, K.R. Maravilla, D.E. Feldman, U.P. Schmiedl, J.A. Brunberg, I.R. Francis, S.E. Harms, P.M. Som, C.M. Tempany, Group, Evaluation of neck and body metastases to nodes with ferumoxtran 10-enhanced MR imaging: phase III safety and efficacy study, *Radiology* **228**(3) (2003) 777-88.
237. Y. Wu, W. Jiang, X. Wen, B. He, X. Zeng, G. Wang, Z. Gu, A novel calcium phosphate ceramic-magnetic nanoparticle composite as a potential bone substitute, *Biomed Mater* **5**(1) (2010) 15001.
238. K. Lai, W. Jiang, J.Z. Tang, Y. Wu, B. He, G. Wang, Z. Gu, Superparamagnetic nano-composite scaffolds for promoting bone cell proliferation and defect reparation without a magnetic field, *RSC Advances* **2**(33) (2012) 13007-13017.
239. D.M. Huang, J.K. Hsiao, Y.C. Chen, L.Y. Chien, M. Yao, Y.K. Chen, B.S. Ko, S.C. Hsu, L.A. Tai, H.Y. Cheng, S.W. Wang, C.S. Yang, Y.C. Chen, The promotion of human mesenchymal stem cell proliferation by superparamagnetic iron oxide nanoparticles, *Biomaterials* **30**(22) (2009) 3645-51.
240. A.M. Rodriguez, P.M. Carrico, J.E. Mazurkiewicz, J.A. Melendez, Mitochondrial or cytosolic catalase reverses the MnSOD-dependent inhibition of proliferation by enhancing respiratory chain activity, net ATP production, and decreasing the steady state levels of H(2)O(2), *Free Radic Biol Med* **29**(9) (2000) 801-13.
241. C.A. Bassett, R.J. Pawluk, A.A. Pilla, Acceleration of fracture repair by electromagnetic fields. A surgically

noninvasive method, *Ann N Y Acad Sci* **238** (1974) 242-62.

242. N. Taniguchi, S. Kanai, Efficacy of static magnetic field for locomotor activity of experimental osteopenia, *Evid Based Complement Alternat Med* **4**(1) (2007) 99-105.
243. S.T. Sutbeyaz, N. Sezer, B.F. Koseoglu, The effect of pulsed electromagnetic fields in the treatment of cervical osteoarthritis: a randomized, double-blind, sham-controlled trial, *Rheumatol Int* **26**(4) (2006) 320-4.
244. Y. Yamamoto, Y. Ohsaki, T. Goto, A. Nakasima, T. Iijima, Effects of static magnetic fields on bone formation in rat osteoblast cultures, *J Dent Res* **82**(12) (2003) 962-6.
245. L.J. Santos, R.L. Reis, M.E. Gomes, Harnessing magnetic-mechano actuation in regenerative medicine and tissue engineering, *Trends Biotechnol* **33**(8) (2015) 471-9.
246. J.W. Bulte, D.L. Kraitchman, A.M. Mackay, M.F. Pittenger, Chondrogenic differentiation of mesenchymal stem cells is inhibited after magnetic labeling with ferumoxides, *Blood* **104**(10) (2004) 3410-2; author reply 3412-3.
247. L. Kostura, D.L. Kraitchman, A.M. Mackay, M.F. Pittenger, J.W. Bulte, Feridex labeling of mesenchymal stem cells inhibits chondrogenesis but not adipogenesis or osteogenesis, *NMR Biomed* **17**(7) (2004) 513-7.
248. R.M. Erb, D.S. Sebba, A.A. Lazarides, B.B. Yellen, Magnetic field induced concentration gradients in magnetic nanoparticle suspensions: Theory and experiment, *Journal of Applied Physics* **103**(6) (2008) 063916.
249. O. Hovorka, B. Yellen, N. Dan, G. Friedman, Self-consistent model of field gradient driven particle aggregation in magnetic fluids, *Journal of Applied Physics* **97**(10) (2005) 10Q306.
250. L. Bonnemay, S. Hostachy, C. Hoffmann, J. Gautier, Z. Gueroui, Engineering spatial gradients of signaling proteins using magnetic nanoparticles, *Nano Lett* **13**(11) (2013) 5147-52.
251. D.A. Rees, Shapely polysaccharides. The eighth Colworth Medal Lecture, *Biochemical Journal* **126**(2) (1972) 257.
252. E.R. Morris, K. Nishinari, M. Rinaudo, Gelation of gellan - a review, *Food Hydrocolloids* **28**(2) (2012) 373-411.
253. H. Grasdalen, O. Smidsrød, Gelation of gellan gum, *Carbohydrate Polymers* **7**(5) (1987) 371-393.
254. R. Ruppert, E. Hoffmann, W. Sebald, Human bone morphogenetic protein 2 contains a heparin-binding site which modifies its biological activity, *Eur J Biochem* **237**(1) (1996) 295-302.
255. B. Zhao, T. Katagiri, H. Toyoda, T. Takada, T. Yanai, T. Fukuda, U.I. Chung, T. Koike, K. Takaoka, R. Kamijo, Heparin potentiates the in vivo ectopic bone formation induced by bone morphogenetic protein-2, *J Biol Chem* **281**(32) (2006) 23246-53.
256. Z. Wang, K. Wang, X. Lu, M. Li, H. Liu, C. Xie, F. Meng, O. Jiang, C. Li, W. Zhi, BMP-2 encapsulated polysaccharide nanoparticle modified biphasic calcium phosphate scaffolds for bone tissue regeneration, *J Biomed Mater Res A* **103**(4) (2015) 1520-32.
257. W.C. Kett, R.I. Osmond, L. Moe, S.E. Skett, B.F. Kinnear, D.R. Coombe, Avidin is a heparin-binding protein. Affinity, specificity and structural analysis, *Biochim Biophys Acta* **1620**(1-3) (2003) 225-34.
258. S.A. Abbah, J. Liu, R.W. Lam, J.C. Goh, H.K. Wong, In vivo bioactivity of rhBMP-2 delivered with novel polyelectrolyte complexation shells assembled on an alginate microbead core template, *J Control Release* **162**(2) (2012) 364-72.
259. H. Lysdahl, A. Baatrup, C.B. Foldager, C. Bunger, Preconditioning human mesenchymal stem cells with a low concentration of BMP2 stimulates proliferation and osteogenic differentiation in vitro, *Biores Open Access* **3**(6) (2014) 278-85.
260. X. Wang, E. Wenk, X. Zhang, L. Meinel, G. Vunjak-Novakovic, D.L. Kaplan, Growth factor gradients via microsphere delivery in biopolymer scaffolds for osteochondral tissue engineering, *J Control Release* **134**(2) (2009) 81-90.
261. J. Li, S. Mareddy, D.M. Tan, R. Crawford, X. Long, X. Miao, Y. Xiao, A minimal common osteochondrocytic differentiation medium for the osteogenic and chondrogenic differentiation of bone marrow stromal cells in the construction of osteochondral graft, *Tissue Eng Part A* **15**(9) (2009) 2481-90.
262. X. Liu, J. Liu, N. Kang, L. Yan, Q. Wang, X. Fu, Y. Zhang, R. Xiao, Y. Cao, Role of insulin-transferrin-selenium in auricular chondrocyte proliferation and engineered cartilage formation in vitro, *Int J Mol Sci* **15**(1) (2014) 1525-37.
263. Y. Sato, H. Mera, D. Takahashi, T. Majima, N. Iwasaki, S. Wakitani, M. Takagi, Synergistic effect of ascorbic acid and collagen addition on the increase in type 2 collagen accumulation in cartilage-like MSC sheet, *Cytotechnology* **69**(3) (2017) 405-416.
264. N. Shintani, E.B. Hunziker, Differential effects of dexamethasone on the chondrogenesis of

mesenchymal stromal cells: influence of microenvironment, tissue origin and growth factor, *Eur Cell Mater* **22** (2011) 302-19; discussion 319-20.

265. J. Hwang, E.M. Kyubwa, W.C. Bae, W.D. Bugbee, K. Masuda, R.L. Sah, in vitro calcification of immature bovine articular cartilage: formation of a functional zone of calcified cartilage, *Cartilage* **1**(4) (2010) 287-297.
266. J.P. Armstrong, R. Shakur, J.P. Horne, S.C. Dickinson, C.T. Armstrong, K. Lau, J. Kadiwala, R. Lowe, A. Seddon, S. Mann, J.L. Anderson, A.W. Perriman, A.P. Hollander, Artificial membrane-binding proteins stimulate oxygenation of stem cells during engineering of large cartilage tissue, *Nat Commun* **6** (2015) 7405.
267. P.A. Parmar, L.W. Chow, J.P. St-Pierre, C.M. Horejs, Y.Y. Peng, J.A. Werkmeister, J.A. Ramshaw, M.M. Stevens, Collagen-mimetic peptide-modifiable hydrogels for articular cartilage regeneration, *Biomaterials* **54** (2015) 213-25.
268. G. Shen, The role of type X collagen in facilitating and regulating endochondral ossification of articular cartilage, *Orthod Craniofac Res* **8**(1) (2005) 11-7.
269. E.E. Golub, G. Harrison, A.G. Taylor, S. Camper, I.M. Shapiro, The role of alkaline phosphatase in cartilage mineralization, *Bone Miner* **17**(2) (1992) 273-8.
270. S. Yamada, D. Heymann, J.M. Bouler, G. Daculsi, Osteoclastic resorption of calcium phosphate ceramics with different hydroxyapatite/beta-tricalcium phosphate ratios, *Biomaterials* **18**(15) (1997) 1037-41.
271. H.E. Koepp, S. Schorlemmer, S. Kessler, R.E. Brenner, L. Claes, K.P. Gunther, A.A. Ignatius, Biocompatibility and osseointegration of beta-TCP: histomorphological and biomechanical studies in a weight-bearing sheep model, *J Biomed Mater Res B Appl Biomater* **70**(2) (2004) 209-17.
272. S. Ahmed, F.R. Jones, A review of particulate reinforcement theories for polymer composites, *Journal of Materials Science* **25**(12) (1990) 4933-4942.
273. G. Chen, C. Deng, Y.P. Li, TGF-beta and BMP signaling in osteoblast differentiation and bone formation, *Int J Biol Sci* **8**(2) (2012) 272-88.
274. J. Yang, Y.S. Zhang, K. Yue, A. Khademhosseini, Cell-laden hydrogels for osteochondral and cartilage tissue engineering, *Acta Biomater* **57** (2017) 1-25.
275. I.L. Kim, R.L. Mauck, J.A. Burdick, Hydrogel design for cartilage tissue engineering: a case study with hyaluronic acid, *Biomaterials* **32**(34) (2011) 8771-82.
276. S.L. Vega, M.Y. Kwon, J.A. Burdick, Recent advances in hydrogels for cartilage tissue engineering, *Eur Cell Mater* **33** (2017) 59-75.
277. M.S. Liang, S.T. Andreadis, Engineering fibrin-binding TGF-beta1 for sustained signaling and contractile function of MSC based vascular constructs, *Biomaterials* **32**(33) (2011) 8684-93.
278. C. Bellamy, S. Shrestha, C. Torneck, A. Kishen, Effects of a Bioactive Scaffold Containing a Sustained Transforming Growth Factor-beta1-releasing Nanoparticle System on the Migration and Differentiation of Stem Cells from the Apical Papilla, *J Endod* **42**(9) (2016) 1385-92.
279. A.J. Pelletier, L.J. van der Laan, P. Hildbrand, M.A. Siani, D.A. Thompson, P.E. Dawson, B.E. Torbett, D.R. Salomon, Presentation of chemokine SDF-1 alpha by fibronectin mediates directed migration of T cells, *Blood* **96**(8) (2000) 2682-90.
280. C.P. Addington, J.M. Heffernan, C.S. Millar-Haskell, E.W. Tucker, R.W. Sirianni, S.E. Stabenfeldt, Enhancing neural stem cell response to SDF-1alpha gradients through hyaluronic acid-laminin hydrogels, *Biomaterials* **72** (2015) 11-9.
281. A. Amara, O. Lorthioir, A. Valenzuela, A. Magerus, M. Thelen, M. Montes, J.-L. Virelizier, M. Delepierre, F. Baleux, H. Lortat-Jacob, F. Arenzana-Seisdedos, Stromal Cell-derived Factor-1 α Associates with Heparan Sulfates through the First β-Strand of the Chemokine, *Journal of Biological Chemistry* **274**(34) (1999) 23916-23925.
282. L. Balaj, N.A. Atai, W. Chen, D. Mu, B.A. Tannous, X.O. Breakefield, J. Skog, C.A. Maguire, Heparin affinity purification of extracellular vesicles, *Sci Rep* **5** (2015) 10266.
283. S.P. Grogan, X. Chen, S. Sovani, N. Taniguchi, C.W. Colwell Jr., M.K. Lotz, D.D. D'Lima, Influence of Cartilage Extracellular Matrix Molecules on Cell Phenotype and Neocartilage Formation, *Tissue Engineering Part A* **20**(1-2) (2014) 264-274.
284. M. Simann, V. Schneider, S. Le Blanc, J. Dotterweich, V. Zehe, M. Krug, F. Jakob, T. Schilling, N. Schütze, Heparin affects human bone marrow stromal cell fate: Promoting osteogenic and reducing adipogenic differentiation and conversion, *Bone* **78** (2015) 102-113.
285. X. Lin, Functions of heparan sulfate proteoglycans in cell signaling during development, *Development* **131**(24) (2004) 6009-21.
286. S.H. Kim, J. Turnbull, S. Guimond, Extracellular matrix and cell signalling: the dynamic cooperation of

integrin, proteoglycan and growth factor receptor, *Journal of Endocrinology* **209**(2) (2011) 139-151.

287. T.H. Kim, D.B. An, S.H. Oh, M.K. Kang, H.H. Song, J.H. Lee, Creating stiffness gradient polyvinyl alcohol hydrogel using a simple gradual freezing-thawing method to investigate stem cell differentiation behaviors, *Biomaterials* **40** (2015) 51-60.
288. J.S. Turner, Jets and plumes with negative or reversing buoyancy, *Journal of Fluid Mechanics* **26**(4) (1966) 779-792.
289. N. Xue, S. Khodaparast, L. Zhu, J.K. Nunes, H. Kim, H.A. Stone, Laboratory layered latte, *Nat Commun* **8**(1) (2017) 1960.
290. R.J. Britten, R.B. Roberts, High-Resolution Density Gradient Sedimentation Analysis, *Science* **131**(3392) (1960) 32-3.
291. A. Boyum, Isolation of mononuclear cells and granulocytes from human blood. Isolation of monuclear cells by one centrifugation, and of granulocytes by combining centrifugation and sedimentation at 1 g, *Scand J Clin Lab Invest Suppl* **97** (1968) 77-89.
292. L. Bai, X. Ma, J. Liu, X. Sun, D. Zhao, D.G. Evans, Rapid separation and purification of nanoparticles in organic density gradients, *J Am Chem Soc* **132**(7) (2010) 2333-7.
293. V. Parameswaran, A. Shukla, Processing and characterization of a model functionally gradient material, *Journal of Materials Science* **35**(1) (2000) 21-29.
294. J.T. BEALS, M.S. THOMPSON, Density gradient effects on aluminium foam compression behaviour, *Journal of Materials Science* **32**(13) (1997) 3595-3600.
295. J.T. Oliveira, L. Martins, R. Picciochi, P.B. Malafaya, R.A. Sousa, N.M. Neves, J.F. Mano, R.L. Reis, Gellan gum: A new biomaterial for cartilage tissue engineering applications, *Journal of Biomedical Materials Research Part A* **93A**(3) (2010) 852-863.
296. J.P.K. Armstrong, M.M. Stevens, Strategic design of extracellular vesicle drug delivery systems, *Adv Drug Deliv Rev* **130** (2018) 12-16.
297. T.M. Allen, P.R. Cullis, Liposomal drug delivery systems: from concept to clinical applications, *Adv Drug Deliv Rev* **65**(1) (2013) 36-48.
298. P. Ghosh, G. Han, M. De, C.K. Kim, V.M. Rotello, Gold nanoparticles in delivery applications, *Adv Drug Deliv Rev* **60**(11) (2008) 1307-15.
299. Y.I. Chung, K.M. Ahn, S.H. Jeon, S.Y. Lee, J.H. Lee, G. Tae, Enhanced bone regeneration with BMP-2 loaded functional nanoparticle-hydrogel complex, *J Control Release* **121**(1-2) (2007) 91-9.
300. J. Yang, Y.S. Zhang, K. Yue, A. Khademhosseini, Cell-laden hydrogels for osteochondral and cartilage tissue engineering, *Acta Biomater* (2017).
301. A. Nilasaroya, L.A. Poole-Warren, J.M. Whitelock, P. Jo Martens, Structural and functional characterisation of poly(vinyl alcohol) and heparin hydrogels, *Biomaterials* **29**(35) (2008) 4658-64.
302. X. Li, S. Chen, J. Li, X. Wang, J. Zhang, N. Kawazoe, G. Chen, 3D Culture of Chondrocytes in Gelatin Hydrogels with Different Stiffness, *Polymers (Basel)* **8**(8) (2016).
303. P.N. Lavrenko, O.I. Mikriukova, O.V. Okatova, On the separation ability of various Ficoll gradient solutions in zonal centrifugation, *Anal Biochem* **166**(2) (1987) 287-97.
304. V.M. Mania, A.G. Kallivokas, C. Malavaki, A.P. Asimakopoulou, J. Kanakis, A.D. Theocharis, G. Klironomos, G. Gatzounis, A. Mouzaki, E. Panagiotopoulos, N.K. Karamanos, A comparative biochemical analysis of glycosaminoglycans and proteoglycans in human orthotopic and heterotopic bone, *IUBMB Life* **61**(4) (2009) 447-52.
305. J. Sodek, B. Ganss, M.D. McKee, Osteopontin, *Critical Reviews in Oral Biology & Medicine* **11**(3) (2000) 279-303.
306. E.H. Morrison, M.W. Ferguson, M.T. Bayliss, C.W. Archer, The development of articular cartilage: I. The spatial and temporal patterns of collagen types, *J Anat* **189 (Pt 1)** (1996) 9-22.
307. J. Li, A.D. Celiz, J. Yang, Q. Yang, I. Wamala, W. Whyte, B.R. Seo, N.V. Vasilyev, J.J. Vlassak, Z. Suo, D.J. Mooney, Tough adhesives for diverse wet surfaces, *Science* **357**(6349) (2017) 378.
308. F. Tallia, L. Russo, S. Li, A.L.H. Orrin, X. Shi, S. Chen, J.A.M. Steele, S. Meille, J. Chevalier, P.D. Lee, M.M. Stevens, L. Cipolla, J.R. Jones, Bouncing and 3D printable hybrids with self-healing properties, *Materials Horizons* **5**(5) (2018) 849-860.

Appendices

A. List of Publications and Conferences

B. **C. Li**, J.P.K. Armstrong, I.J. Pence, W. Kit-Anan, J.L. Puetzer, S. Correia Carreira, A.C. Moore, M.M. Stevens, Glycosylated superparamagnetic nanoparticle gradients for osteochondral tissue engineering, ***Biomaterials*** 176 (2018) 24-33.

C. **C. Li**, L. Ouyang, I.J. Pence, A.C. Moore, Y. Lin, C.W. Winter, J.P.K. Armstrong, M.M. Stevens, Buoyancy-Driven Gradients for Biomaterial Fabrication and Tissue Engineering, ***Advanced Materials*** 31(17) (2019) e1900291.

D. Reproduction Permissions

A. List of Publications and Conferences

Conferences:

C Li, JPK Armstrong, IJ Pence, W Kit-Anan, JL Puetzer, S Correia Correira, MM Stevens "Superparamagnetic Nanoparticle in Gradient Tissue Engineering" (5th TERMIS World Congress, Kyoto, Japan, 2018)

C Li, L Ouyang, IJ Pence, AC Moore, Y Lin, CW Winter, JPK Armstrong, MM Stevens "Force-based Engineering of Osteochondral Gradients" (TERMIS European Chapter Meeting, Rhodes, Greece, 2019)

Publications:

C. Li, J.P.K. Armstrong, I.J. Pence, W. Kit-Anan, J.L. Puetzer, S. Correia Carreira, A.C. Moore, M.M. Stevens, Glycosylated superparamagnetic nanoparticle gradients for osteochondral tissue engineering, ***Biomaterials*** 176 (2018) 24-33.

C. Li, L. Ouyang, I.J. Pence, A.C. Moore, Y. Lin, C.W. Winter, J.P.K. Armstrong, M.M. Stevens, Buoyancy-Driven Gradients for Biomaterial Fabrication and Tissue Engineering, ***Advanced Materials*** 31(17) (2019) e1900291.

Biomaterials 176 (2018) 24–33

Contents lists available at ScienceDirect

Biomaterials

journal homepage: www.elsevier.com/locate/biomaterials

Glycosylated superparamagnetic nanoparticle gradients for osteochondral tissue engineering

Chunching Li [a], James PK. Armstrong [a], Isaac J. Pence [a], Worrapong Kit-Anan [a], Jennifer L. Puetzer [a], Sara Correia Carreira [b], Axel C. Moore [a], Molly M. Stevens [a, *]

[a] *Department of Materials, Department of Bioengineering and Institute of Biomedical Engineering, Imperial College London, Prince Consort Road, London, SW7 2AZ, United Kingdom*
[b] *H. H. Wills Physics Laboratory, University of Bristol, Tyndall Avenue, Bristol, BS8 1TL, United Kingdom*

ARTICLE INFO

Article history:
Received 16 February 2018
Received in revised form
27 April 2018
Accepted 19 May 2018
Available online 21 May 2018

Keywords:
Magnetic
Nanoparticles
Gradients
Osteochondral
Tissue engineering

ABSTRACT

In developmental biology, gradients of bioactive signals direct the formation of structural transitions in tissue that are key to physiological function. Failure to reproduce these native features in an *in vitro* setting can severely limit the success of bioengineered tissue constructs. In this report, we introduce a facile and rapid platform that uses magnetic field alignment of glycosylated superparamagnetic iron oxide nanoparticles, pre-loaded with growth factors, to pattern biochemical gradients into a range of biomaterial systems. Gradients of bone morphogenetic protein 2 in agarose hydrogels were used to spatially direct the osteogenesis of human mesenchymal stem cells and generate robust osteochondral tissue constructs exhibiting a clear mineral transition from bone to cartilage. Interestingly, the smooth gradients in growth factor concentration gave rise to biologically-relevant, emergent structural features, including a tidemark transition demarcating mineralized and non-mineralized tissue and an osteochondral interface rich in hypertrophic chondrocytes. This platform technology offers great versatility and provides an exciting new opportunity for overcoming a range of interfacial tissue engineering challenges.

1. Introduction

Biological gradients play an essential role in defining the functional role of a wide range of tissues, including tendon, cartilage and the central nervous system [1–3]. These gradients are largely dictated by an anisotropic distribution of growth factors present during embryological development and pre-adolescent growth. For instance, the formation of the cartilage-bone interface in osteochondral tissue is heavily influenced by a polarized distribution of pro-osteogenic growth factors, such as bone morphogenetic protein 2 (BMP-2) [3,4]. These local differences in growth factor concentration produce spatial variance in cell signaling, which can, in turn, lead to distinct cell phenotypes across the tissue (*e.g.* osteoblasts and chondrocytes). In a structural system such as osteochondral tissue, the different cell types sculpt the final tissue composition *via* the production and remodeling of different extracellular matrix components. These structural features play a critically important role in the functional performance of the tissue; for instance, the gradual transition between bone and cartilage enables the smooth transmission and distribution of compressive loads through the osteochondral tissue [5,6].

Despite these well-known considerations, the overwhelming majority of *in vitro* engineering strategies use uniform scaffolds and homogeneous growth factor delivery to produce isotropic tissue constructs. It is clear that more sophisticated fabrication processes are required to replicate the native complexity and fulfill the functional requirements of tissue grafts. A few material strategies have been developed that can heterogeneously deliver biological or mechanical cues [7–11]. A simplistic strategy, which has found clinical application, is to laminate separate biomaterials by suture or other approaches such as using a small amount of solvent after preparation [4,12]. This approach uses the material composition and structure of the different scaffold layers to direct cell fate and tissue formation, however, discontinuities at the interface make these biphasic materials highly susceptible to delamination [8]. A smoother transition can be achieved using a gradient maker, in which microspheres laden with growth factors are distributed in

---

* Corresponding author.
E-mail address: m.stevens@imperial.ac.uk (M.M. Stevens).

https://doi.org/10.1016/j.biomaterials.2018.05.029

graded fashion throughout a hydrogel [13], or through specialist techniques, such as photo-patterning [14] and microfluidics [14]. These systems can produce excellent gradients, but can often be limited by complex micro-fabrication procedures or compatibility with different material systems. It is clear that there is an urgent and unmet need for a simple and versatile gradient casting method that can be universally applied to different biomaterial and tissue engineering protocols.

To this end, we present a new strategy in which externally-applied magnetic fields are used to decorate different biomaterials with continuous gradients of growth factor loaded glycosylated superparamagnetic iron oxide nanoparticles (SPIONs) (Fig. 1). SPIONs have previously been used to generate polarization of the signaling protein RanGTP within *Xenopus* egg extracts to spatially modify the assembly of microtubule networks [15]. To the best of our knowledge, however, SPIONs have not yet been investigated as a method for patterning biochemical gradients for *in vitro* tissue engineering. Here, we report the use of magnetically-aligned gradients of BMP-2 to spatially direct mineralization during osteochondral tissue engineering. Specifically, we used an external magnetic field to pattern glycosylated SPIONs into an agarose hydrogel, pre-laden with human mesenchymal stem cells (hMSCs). Thermal gelation of the hydrogel enabled us to stably encapsulate a BMP-2 gradient, which was used to spatially stimulate osteogenic gene expression and tissue mineralization over a 28-day culture. The resulting tissues exhibited a cartilage region, rich in type II collagen and glycosaminoglycan, with a transition into a mineralized, bone region exhibiting extensive distribution of β-tricalcium phosphate (β-TCP) and hydroxyapatite (HAP). In certain cases, these differences in extracellular matrix provided an increased compressive instantaneous modulus at the bone region compared to the cartilage region. This approach required no specialized equipment, other than a magnet, and offered great versatility in patterning different hydrogel or scaffold systems. The ability to produce tissue-scale biochemical gradients in under a minute across different biomaterials should afford this platform technology wide applicability across a range of complex tissue engineering systems.

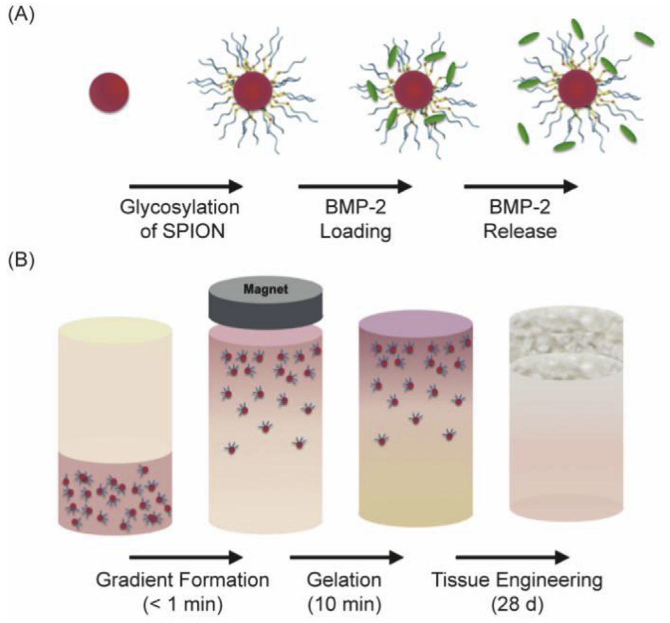

Fig. 1. Engineering osteochondral tissue using magnetically-aligned glycosylated SPIONs. (A) SPIONs are conjugated with heparin to produce a glycosylated corona that can efficiently sequester and release growth factors. (B) An external magnetic field is used to field-align glycosylated SPIONs in a hMSC-laden agarose hydrogel, which is thermally gelled and cultured for 28 days to generate robust osteochondral constructs comprising both bone and cartilage tissue.

2. Materials and methods

2.1. Glycosylated SPION synthesis and characterization

A 0.9 mL solution of 1.5 mg mL^{-1} of heparin (Sigma Aldrich, UK) was prepared in pH 5.4 4-morpholineethanesulfonic acid buffer (MES, Thermo Fisher, USA), and mixed for 15 min with 5 mg of *N*-(3-dimethylaminopropyl)-*N′*-ethylcarbodiimide hydrochloride (EDC, Sigma Aldrich, UK) and 1 mg of *N*-hydroxysuccinimide (NHS, Sigma Aldrich, UK). 0.1 mL of 5 mg mL^{-1} amine-functionalized 20 nm SPIONs (SHA-20, Ocean NanoTech, USA) were then added and mixed for 24 h at room temperature. After the conjugation, the product was dialyzed against 5 L of phosphate-buffered saline (PBS, Thermo Fisher, USA) for 3 days with two daily buffer changes to ensure complete removal of unconjugated heparin. The conjugated SPIONs were then concentrated to 2 mg mL^{-1} using 100 kDa cut-off Amicon ultra-centrifugal filter unit (Merck Millipore, USA).

Zeta potential and hydrodynamic diameter measurements were performed using a Zetasizer Zen 3600 (Malvern Instruments, UK), with samples in pH 7 deionized water at a concentration of 40 μg mL^{-1}. Heparin quantification was performed using dimethylmethylene blue (DMMB, Sigma Aldrich, UK), with standards ranging between 0 and 25 μg mL^{-1} and an unconjugated SPION reference. The absorbance was measured at 525 nm using a SpectraMax M5 microplate reader (Molecular Devices, USA). The sulfated glycosaminoglycan content was normalized to the nanoparticle number, which was measured using a Nanosight (Ns300, Malvern Instruments, UK) equipped with Nanoparticle Tracking Analysis 3.0 software. Magnetic analysis was performed using a SQUID magnetometer (MPMS-7, Quantum Design, UK) on 1.5 mg mL^{-1} samples. These values were normalized by iron content, which was measured by digesting the nanoparticles in 2 N nitric acid (Sigma Aldrich, UK) at 40 °C for 24 h to ensure complete digestion and analyzing samples using inductively coupled plasma optical emission spectrometry (ICAP 6300 Duo, Thermo Fisher, USA).

The protein loading capacity of the glycosylated SPIONs was assessed by mixing avidin (Thermo Fisher, USA) with glycosylated and unconjugated SPIONs at room temperature for 10 min, and then centrifuging the sample at 20,817 g for 100 min. The concentration of avidin was detected using a Micro BCA™ Protein Assay Kit (Thermo Fisher, USA) following the manufacturer's protocol, using avidin standards between 0 and 20 μg mL^{-1}. The loading capacity was determined by subtracting the initial loading mass of avidin with the mass of avidin detected in the supernatant.

2.2. Magnetic field alignment and simulation

Finite element magnetic modeling (FEMM, D. C. Meeker, Finite Element Method Magnetics, Version 4.2.) was used to characterize the magnetic field based on the dimensions and physical properties of the cylindrical N42 magnet (eMagnets, UK) used throughout the study (ø = 20 mm, height = 20 mm, HcB = 915 kA/m). All gradients were formed in a customized mold composed of two glass slides and a cut 2 mm silicone spacer (final well dimensions = 13 × 5 × 2 mm). 30 μL of solution or hydrogel precursor containing SPIONs were dispensed into the mold, followed by 60 μL of the same components minus the SPIONs. The magnetic field was subsequently applied from approximately 2 mm above the mold to redistribute the SPIONs into a gradient. To image the gradient formation process, gradients were formed in deionized water using a layer of 0.5 mg mL^{-1} SPIONs.

To examine the gradient forming capability in different hydrogels, a layer of 0.5 mg mL^{-1} SPIONs was used. After the formation of the gradient, the hydrogel precursor was gelled and the constructs were imaged using an Axio Observer inverted widefield microscope (Zeiss, Germany). Type VII-A Agarose (Sigma Aldrich, UK) was used at 1 wt% and gelled at room temperature. Geltrex (Thermo Fisher, USA) was used undiluted and gelled at 37 °C. Gellum gum (Sigma Aldrich, UK) was used at 0.75 wt% and crosslinked by the addition of a 0.06 wt% solution of calcium chloride. Gelatin (Sigma Aldrich, UK) was used at 5 wt% and gelled at 4 °C. To visualize the distribution of loaded protein, 10^{11} SPIONs were first loaded with 300 ng of fluorescein-labelled avidin (Thermo Fisher, USA) prior to gradient formation. Intensity plots were produced using the plot profile function on FIJI software using images acquired with an Axio Observer inverted widefield microscope (Zeiss, Germany). 1 wt% agarose was used to test the influence of viscosity on pattern formation, with the gradient forming process carried out in a temperature-controlled water bath (27, 30, 37 °C) and the resulting gels imaged using a desktop scanner. The viscosity of the agarose solutions at these temperatures was measured by rheological creep tests performed at 2 Pa stress over 5 min using an AR2000ex rheometer (TA Instruments, USA).

2.3. BMP-2 release kinetics

10^{11} glycosylated SPIONs loaded with 300 ng of BMP-2 (R&D System, USA) were cast into a 100 μL 1 wt% agarose hydrogel, to mimic the conditions used for osteochondral tissue engineering. The hydrogel was incubated in PBS with 0.02% of sodium azide (pH 7.4) (Sigma Aldrich, UK) at 37 °C for 28 days. 500 μL of PBS was removed at intervals and frozen at −20 °C, with 500 μL of fresh PBS added to the hydrogel to ensure that sink conditions were respected at all times. The concentration of released BMP-2 was then quantified using a BMP-2 specific ELISA kit (R&D System, USA), following the manufacturer's protocol. The absorbance was measured at 450 nm using a SpectraMax M5 plate reader. After the accumulated release was determined for each time point, the release profile was fitted by a Korsmeyer-Peppas model using KinetDs (version 3.0) [16]. The Korsmeyer-Peppas Model was developed to specifically model the release of molecules from a polymeric matrix, such as hydrogel network [17].

2.4. Stem cell culture and differentiation

hMSCs from three donors (Lonza, Switzerland) were expanded using Mesenchymal Stem Cell Growth Medium (MSCGM™, Lonza, Switzerland) in sterile culture at 37 °C/5% CO_2. The culture medium was changed every 2–3 days, and hMSCs cultured up to passage 5. Differentiation was induced after encapsulating the hMSCs into agarose hydrogels at a cell density of 9×10^6 hMSCs per mL. Osteogenic differentiation was triggered using high glucose Dulbecco's Modified Eagles Medium with pyruvate supplement (HG-DMEM 31966021, Thermo Fisher, UK) together with 10% (v/v) fetal bovine serum (FBS, Thermo Fisher, USA), 100 nM dexamethasone (Sigma Aldrich, UK), 50 μg mL^{-1} L-ascorbic acid 2-phosphate sesquimagnesium salt (L-ascorbic acid, Sigma Aldrich, UK) and 10 mM β-glycerophosphate (Sigma Aldrich, UK). Chondrogenic differentiation was triggered using HG-DMEM supplemented with 1X ITS$^+$ (BD, USA), 100 nM dexamethasone, 50 μg mL^{-1} L-ascorbic acid, 50 μg mL^{-1} L-proline (Sigma Aldrich, UK) and 10 ng mL^{-1} transforming growth factor β3 (TGF-β3) (R&D System, USA). Osteochondral differentiation was triggered using HG-DMEM supplemented with 1X ITS$^+$, 100 nM dexamethasone, 50 μg mL^{-1} L-ascorbic acid, 50 μg mL^{-1} L-proline, 2 mM β-glycerophosphate and 10 ng mL^{-1} TGF-β3. Where stated, BMP-2 was supplemented either in the medium (30 ng mL^{-1}) or loaded together with glycosylated SPIONs. Unless otherwise specified, the BMP-2 concentration in the glycosylated SPIONs was 3 μg per mL of hydrogel.

2.5. Tissue engineering osteochondral gradients

10^{11} glycosylated SPIONs were incubated with 300 ng of BMP-2 at 4 °C for at least 5 h and then used to create a gradient in agarose, as described previously. hMSCs were included in both layers during the fabrication process, at a concentration of 9×10^6 hMSCs per mL, and the final concentration of BMP-2 was 3 μg mL^{-1}. The gradient hydrogel was transferred into a 24-well plate and cultured in 1 mL of osteochondral differentiation medium. The medium was changed after 2 h and the next day after seeding to remove the excess initial burst release BMP-2, and then three times a week for the remaining 27 days.

2.6. Gene expression analysis

Osteochondral tissue constructs engineered from three donors ($N = 3$, $n = 3$) were harvested and dissected into three equal pieces. The cartilage and bone ends were rinsed with PBS, homogenized using a TissueLyser II (Qiagen, Germany), and then stored at −80 °C. Total RNA was isolated using Trizol with Direct-zol™ RNA Kits, according to the manufacturer's protocol, and quantified using a NanoDrop 2000c (Thermo Fisher, UK). RNA was used to generate cDNA using a QuantiTect® Reverse Transcription Kit (Qiagen, Germany), assuming a 1:1 conversion. Quantitative PCR was performed using 3 ng of cDNA, Taqman® probes (Thermo Fisher, USA) and a StepOnePlus™ (Thermo Fisher, USA). The following probes were used: *RPL13A* (Hs04194366_g1), *ACAN* (Hs00153936_m1), *ALPL* (Hs01029144_m1), *COL1A1* (Hs00164004_m1), *COL2A1* (Hs00264051_m1), *COL10A1* (Hs00166657_m1), *RUNX2* (Hs01047973_m1), *SOX9* (Hs00165814_m1), *SP7* (Hs01866874_s1). The ΔΔCt method was used to compare expression at the bone region normalized to the cartilage region.

2.7. ALP and DNA assays

Osteochondral tissue constructs ($N = 3$, $n = 3$) were harvested and dissected, as previously described. The ALP activity and quantity of DNA was determined using a protocol modified from the literature [18]. The bone and cartilage ends of the tissue were homogenized separately using a TissueLyser II with ALP lysis buffer, consisting of 1 mM $MgCl_2$ (Sigma Aldrich, UK), 20 μM $ZnCl_2$ (Sigma Aldrich, UK) and 0.1% (w/v) octyl-β-glucopyranoside (Sigma Aldrich, UK) in 10 mM tris(hydroxymethyl)aminomethane buffer (pH 7.4) (Sigma Aldrich, UK) with the sample lysate immediately stored at −80 °C. To perform the assay, the samples were thawed on ice and then each sample was incubated with *p*-nitrophenol phosphate (Sigma Aldrich, UK) at 37 °C for 30 min. The reaction was terminated using 1 N NaOH and the absorbance measured at 405 nm using a SpectraMax M5 plate reader. A standard curve between 0 and 800 μM of *p*-nitrophenol phosphate was used to calculate the sample activity. An equivalent volume from the remainder of the sample was then used for DNA quantification using a PicoGreen™ assay (Thermo Fisher, UK), according to the manufacturer's protocol. The fluorescence was measured at 485/535 nm using a SpectraMax M5 plate reader. The ALP activity normalized to DNA quantity was compared between the bone and cartilage regions.

2.8. Histology and immunofluorescence staining

Osteochondral tissue constructs were harvested and washed three times in PBS, fixed with 4% (v/v) paraformaldehyde for 2 h at room temperature, washed a further three times in PBS and then paraffin embedded. 5 μm thick sections on Superfrost Plus slides (Thermo Scientific, UK) were deparaffinized using a 4 min incubation in Histo-Clear (National Diagnostics, USA) and hydrated using 2 min incubations in 100% ethanol, 70% ethanol and then deionized water. These sections were then stained using various protocols. For sulfated glycosaminoglycans, the sections were stained with Alcian Blue (pH 2.5) (Sigma Aldrich, UK) for 30 min, with a hematoxylin nuclear counterstain (Sigma Aldrich, UK). For calcium, Alizarin Red S (Abcam, UK) was used at a concentration of 2% (w/v) at pH 4.3. Alcian Blue and Alizarin Red S were performed on consecutive sections. The slides were mounted in Histomount (National Diagnostics, USA) and then imaged using a Zeiss Axio Observer Inverted Widefield Microscope. Images were superimposed after tiling.

For immunofluorescence staining, the sections were treated with proteinase K (Dako, USA) for antigen retrieval, and then blocked with 10% (v/v) donkey or goat serum. The samples were incubated overnight with goat anti type I collagen (Southern Biotech, USA) at 1/100 dilution, goat anti type II collagen (Southern Biotech, USA) at 1/20 dilution, rabbit anti osteopontin and rabbit anti type X collagen (Abcam, UK) at 1/100 dilution and goat and rabbit IgG negative controls (Abcam, UK) at 1/20 and 1/100 dilution. Excess primary antibody was then removed by three washes in PBS and sections were further incubated with secondary donkey anti goat or goat anti rabbit antibodies labelled with AlexaFluor 555 dye (Thermo Fisher, USA). DAPI (Thermo Fisher, USA) was used to counterstain the nucleus prior to mounting the sections with Vectashield Antifade Mounting Medium (Vector Lab, USA). Sections were imaged using a Zeiss Axio Observer Inverted Widefield Microscope.

2.9. Compression testing

Osteochondral tissue constructs were harvested, with uniform discs collected from the bone and cartilage regions using 2 mm biopsy punches (Miltex, USA). The biopsy dimensions were measured in the hydrated state using digital calipers for each construct, which were then soaked and tested in cOmplete™ Protease Inhibitor Cocktail (Roche, Switzerland). Unconfined compression testing was performed using a Bose Electroforce 3200 (BOSE, USA) equipped with a 250 g load cell. Compression stress relaxation tests were performed by imposing a square wave ramp for 12 steps of 5% strain with a 360 s hold using Wintest 7 (BOSE, USA). The instantaneous load was recorded at the beginning of each step and used to produce an instantaneous stress-strain data set, which was fitted with a bilinear model using Origin (OriginLab Corporation, USA). The instantaneous compressive modulus was then calculated using the low-strain linear region of the stress-strain curve and compared between the bone and cartilage regions.

2.10. Raman spectroscopy

Raman spectroscopic imaging was performed using a confocal Raman microscope (alpha300R+, WITec, Germany) equipped with a 532 nm laser and a x 20/0.4 NA objective lens (EC Epiplan, Zeiss, Germany). The scattered light was coupled to the spectrometer *via* a 100 μm fiber which functioned as the confocal pinhole. A 600 lines per mm grating spectrograph (UHTS 300, WITec, Germany) and a thermoelectrically cooled back-illuminated CCD camera (Newton DU970N-BV-353, Andor, UK) yielding a spectral resolution of ~10 cm^{-1} (defined at full width at half maximum of mercury argon emission lines) were used to record spectra with 35 mW laser power at the sample. Full cross-sectional images with a 10 × 10 μm step-size were acquired with 0.5 s integration time while higher spatial resolution maps were recorded with 2 × 2 μm step size. Raman spectra were corrected for the instrument response of the system using a traceable Raman standard (STM-2245, National Institute of Standards and Technology). Engineered osteochondral tissue samples were prepared as previously described. After paraffin embedding and sectioning to 20 μm thickness on Superfrost Plus microscope slides, a standard dewaxing procedure was performed to remove confounding spectral signatures from the paraffin. Substrate signal was apparent in the acquired spectra in regions of low mineralization but did not affect the determination of mineral or cellular signatures. Full cross-sectional mineral profiles were calculated by integrating the measured HAP and TCP intensities (945 - 975 cm^{-1}) at each position along the construct length. High spatial resolution maps correspond to HAP (ν_1 PO_4 at 962 cm^{-1}), β–TCP (ν_1 HPO_4^{2-} at 948 cm^{-1}), and cellular components of lipids and proteins ($\nu_{as,s}$ CH_2 at 2850–3000 cm^{-1}), which were experimentally validated in agreement with literature [19].

2.11. Cytotoxicity of glycosylated SPIONs

9.6×10^3 hMSCs were seeded in a 96 well plate and left to adhere overnight before a 72 h incubation with 2×10^{11} or 10×10^{11} glycosylated SPIONs per mL of culture medium. The cytotoxicity of the glycosylated SPIONs was assessed using an alamarBlue assay (Thermo Fisher, USA), as per the manufacturer's instructions, with an incubation time of 3 h. The fluorescence was measured at 570/585 nm using an EnVision™ plate reader (Perkin Elmer, USA). The metabolic activity was normalized to an untreated control and averaged across three hMSC donors. hMSCs were also stained using a LIVE/DEAD™ assay (L3224, Thermo Fisher) and imaged using an IX51 Inverted microscope (Olympus, Japan).

2.12. Statistical analysis

Comparison between experimental groups was conducted using ordinary least-squares regression based on Generalized Linear Models in the statistical software R using the rms package. When appropriate, the data from the bone end of each individual construct was normalized to the cartilage end for direct pairwise analysis. The normalized data was then modelled as the dependent variable, and regression coefficients were calculated for independent variables. To account for different levels of response due to cell donor variability, generalized estimating equations were used (as previously described) to enable clustering of measurements obtained from constructs derived from a single donor [20–22]. The generated regression coefficients were compared. Specifically for this analysis, the relative changes of interest were the gene expression, enzyme activity, or mechanical properties (categorical). These descriptors were included as independent variables. Heteroscedasticity in the data set was addressed by using the robust covariance function created in the rms package ("robcov") to adjust the standard errors. Finally, to compare groups, a Welch's *t*-test (for two group comparisons) or a one sample Student's t-test was performed on the generated GLM regression coefficients from the developed regression model, which were represented with *p*-values. All hypothesis tests were considered one-tailed based on the hypothesis of increased values in the bone end of the construct relative to the cartilage end, with exceptions for cell viability and expression levels of chondrogenic genes (*ACAN*, *COL2A1*, and *SOX9*).

Table 1
Biophysical characterization of glycosylated SPIONs (mean ± standard deviation).

	Scattering Analysis		Magnetic Characterization		Biochemical Profile	
	Hydrodynamic Diameter/nm	Zeta Potential/mV	Magnetic Susceptibility/$\times 10^{-1}$ emu g^{-1} Oe^{-1}	Magnetic Saturation/emu g^{-1}	Degree of Glycosylation/ng per 10^9 SPIONs	Protein Sequestered/ng per 10^9 SPIONs
Unconjugated SPIONs	48.6 (±0.2)	−4.7 (±0.6)	5.2 (±0.0)	54.9 (±0.3)	N/A	1.5 (±0.3)
Glycosylated SPIONs	72.3 (±0.9)	−54.4 (±1.7)	5.4 (±0.0)	53.6 (±0.4)	4.2 (±0.5)	4.7 (±0.2)

3. Results and discussion

In order to generate biochemical gradients, we glycosylated 20 nm SPIONs with a protein-binding corona of heparin. Briefly, we used a carbodiimide-based coupling to conjugate the carboxylate groups of heparin to primary amines present on the nanoparticle surface. We then characterized the glycosylated SPIONs, which were colloidally stable, using dynamic light scattering in order to determine the size and surface charge potential (Table 1). The hydrodynamic diameter increased from 48.6 ± 0.2 nm for the bare nanoparticles to 72.3 ± 0.9 nm after glycosylation, which was attributed to the steric bulk of the heparin corona. The glycosylated SPIONs exhibited a zeta potential of −54.4 ± 1.7 mV compared to −4.7 ± 0.6 mV for the unconjugated nanoparticles, which was further evidence for the binding of heparin, a highly anionic polysaccharide. We assessed the magnetic properties of the glycosylated SPIONS using superconducting quantum interference device (SQUID) magnetometry correlated with inductively coupled plasma optical emission spectroscopy (ICP-OES). The glycosylated SPIONs exhibited a magnetic susceptibility of $5.4 \pm 0.0 \times 10^{-1}$ emu g^{-1} Oe^{-1} and a saturation of 53.6 ± 0.4 emu g^{-1}, values that were very similar to the unconjugated nanoparticles ($5.2 \pm 0.0 \times 10^{-1}$ emu g^{-1} Oe^{-1}, 54.9 ± 0.3 emu g^{-1}) (Table 1).

Next, we measured the degree of glycosylation using nanoparticle tracking analysis and a dimethylmethylene blue (DMMB) assay (Supplementary Figure 1 and Table 1). These results revealed 4.2 ng of heparin per 10^9 nanoparticles, a value that corresponded to approximately 140 heparin chains bound to the surface of each nanoparticle. The high density of carboxylate groups on heparin provides an anionic network that can be used to sequester many soluble proteins. For example, our protein of interest, bone morphogenetic protein 2, exhibits highly basic N-terminal peptide domains that confer a high binding affinity with heparin (kD ≈ 20 nM) [23]. To assess the sequestration of the glycosylated SPIONs, we used avidin as a model protein, due to its similar isoelectric point, comparable dissociation constant (kD ≈ 160 nM) and the fact that it is commonly used as an analogue for studying the interaction between BMP-2 and heparin [24,25]. A bicinchoninic acid assay of avidin revealed an average of 4.7 ± 0.2 ng of avidin incorporated per 10^9 nanoparticles, approximately four times greater than observed for the unconjugated SPIONs, and equivalent to approximately 40 sequestered proteins per nanoparticle. This loading capacity offered the opportunity to deliver more than 400 ng of growth factors, a quantity sufficient to influence cell fate, using only 10^{11} nanoparticles [26]. Importantly, the glycosylated SPIONs did not significantly affect the viability of hMSCs, as demonstrated using alamarBlue and LIVE-DEAD™ assays performed after a 72-h exposure to glycosylated SPIONS (10^{12} nanoparticles per mL) (Supplementary Figure 2).

Next, we investigated the nanoparticle response to externally-applied magnetic fields in aqueous solution and different hydrogels commonly used for *in vitro* tissue engineering. Here, we used finite element magnetic modeling to characterize the magnetic field strength and distribution (Fig. 2A). This map enabled us to define the relative positions of the magnet and nanoparticle solution, in order to expose the SPIONs to a well-defined field gradient (from 0.1 to 0.4 T) (Supplementary Figure 3). We initially used these field parameters to attract SPIONs dispersed in a monophasic

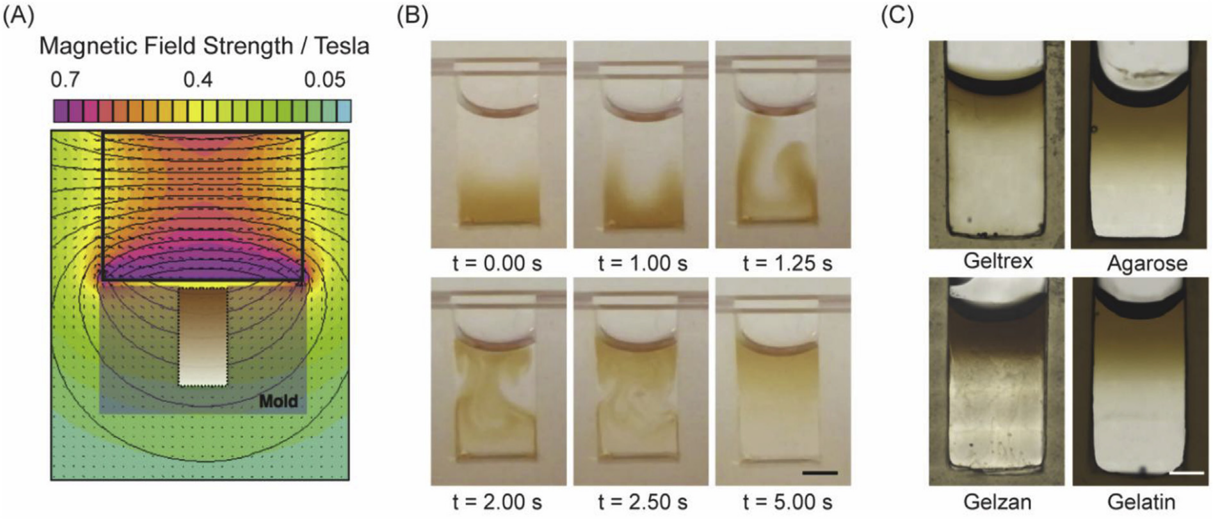

Fig. 2. Magnetic field alignment of SPIONs. (A) Finite element modeling of the magnetic field strength and distribution. (B) Time-lapse images showing the magnetic field alignment of SPIONs (brown) in water, with a clear transition from a biphasic stack to a smooth gradient. (C) Bright field microscopy images showing gradients of SPIONs (brown) immobilized in different biomaterials. Scale bar in all images = 2 mm. (For interpretation of the references to colour in this figure legend, the reader is referred to the Web version of this article.)

suspension, however, this process took several hours (>16 h) to reach completion and produced a thin layer of aggregated SPIONs rather than a gradient transition. We resolved this issue by starting with a two-phase system, in which nanoparticle-free solution was stacked on top of a suspension of nanoparticles. Applying a magnetic field from above resulted in a rapid redistribution of the two layers to generate a smooth nanoparticle gradient (<5 s) (Fig. 2B). Continued exposure to the magnetic field eventually resulted in the SPIONs forming dense aggregates close to the magnet. This transition was a slow process (>10 h), which afforded ample time to capture the system in a non-equilibrium state by encapsulating the nanoparticle gradient in a hydrogel. Indeed, this process appeared to be largely independent of the material type or crosslinking mechanism, however, we did identify three key characteristics that favored gradient formation. First, the SPIONs should be colloidally stable in the precursor solution; which was not the case for certain gels at high weight fraction (*e.g.* > 5 wt% agarose). Second, the precursor solution should not inhibit SPION movement through viscous drag; no gradient formation was observed in 1% agarose gels maintained as a highly viscous solution at 27 °C (Supplementary Figure 4). Third, the crosslinking mechanism should be reasonably rapid (<1 h), and preferably triggered, in order to capture the SPIONs in a non-equilibrium gradient distribution. These characteristics are exhibited by the majority of hydrogels used for tissue engineering. Indeed, we successfully demonstrated the formation of SPION gradients in a range of biomaterials, including gelatin, Geltrex™, Gelzan™ and agarose (Fig. 2C). Importantly, we could use this system to generate protein gradients in biomaterials, as demonstrated by fluorescent microscopy of an agarose hydrogel patterned with glycosylated SPIONs containing fluorescently-tagged avidin (Supplementary Figure 5A). The protein cargo was well co-localized with the nanoparticles, and importantly, the magnetic field alignment produced a much smoother transition than a biphasic stacking approach, which resulted in a much sharper boundary at the layer interface (Supplementary Figure 5B).

We applied this hydrogel patterning approach to the complex and clinically-relevant challenge of osteochondral tissue engineering. Native osteochondral tissue possesses a structural transition from hyaline cartilage to the underlying subchondral bone that is generated in the developmental process of endochondral ossification. A key biochemical cue present during tissue development is the pro-osteogenic growth factor BMP-2. Gradients of BMP-2 in the growth plate play an important role in spatially regulating chondrocyte proliferation and hypertrophic differentiation *in vivo* [3,27], while *in vitro* studies have shown that BMP-2 can trigger bone formation in a concentration-dependent manner [28]. Like many cationic growth factors, BMP-2 exhibits a high affinity for heparin (kD = 20 nM) [23], which has been used in tissue engineering systems to guard against degradation and provide sustained release and stimulation [29,30]. To test whether our system could be used to release growth factors in a biomaterial system, we immobilized BMP-2 loaded glycosylated SPIONs in agarose hydrogels and then monitored the release into solution using an enzyme-linked immunosorbent assay (ELISA). This analysis revealed a sustained diffusion-driven release (Korsmeyer-Peppas model fitting, $R^2 = 0.97$) of BMP-2 over 28 days, with 20% released after the first 24 h (Fig. 3A). It should be noted that these measurements do not account for any possible denaturation of BMP-2. Accordingly, we sought to test the functional activity of the loaded glycosylated SPIONs in a tissue engineering set up.

Here, we intend to use magnetic alignment to present glycosylated SPIONs loaded with BMP-2 as a gradient across a hMSC-laden agarose hydrogel. The subsequent slow release of active BMP-2 over 28 days should stimulate hMSC osteogenesis and tissue mineralization predominantly at one end of the engineered construct [31]. To ensure cartilage formation at the other end of the tissue, we included TGF-β3 alongside insulin-transferrin-selenium, ascorbic acid, dexamethasone and β-glycerophosphate in an optimized osteochondral differentiation medium based on similar compositions reported in the literature [13,32,33]. We used β-glycerophosphate at a concentration of 2 mM, a level that can provide a source of phosphate without initiating osteogenesis or nonspecific mineral precipitation [34]. Indeed, we showed that this osteochondral medium could support either osteogenic or chondrogenic differentiation of hMSCs in agarose, depending on the presence or absence of BMP-2 in the culture medium

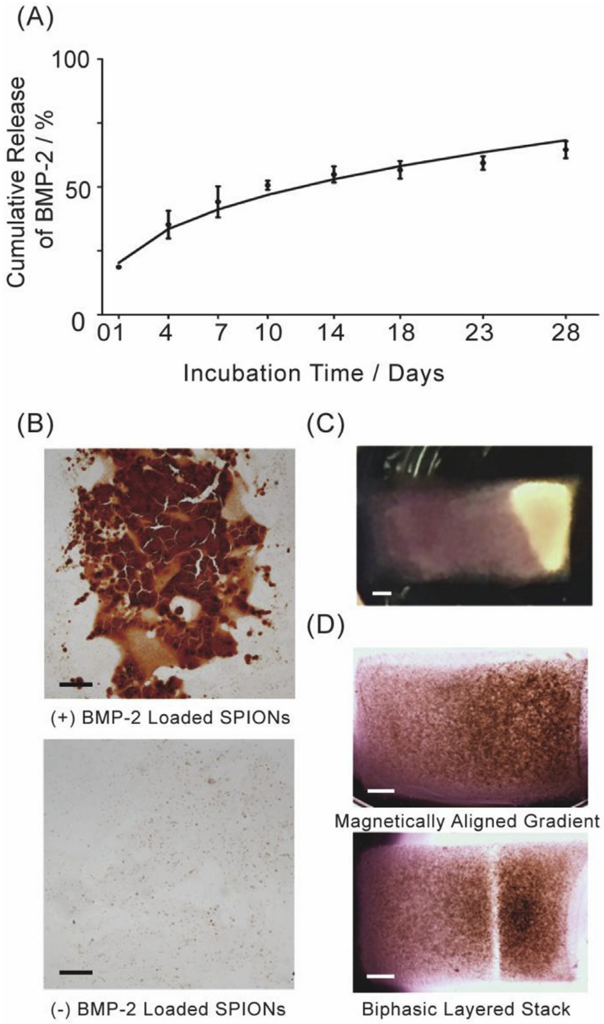

Fig. 3. BMP-2 release and action in agarose hydrogels. (A) An ELISA was used to detect the release of BMP-2 from glycosylated SPIONs immobilized in 1 wt% agarose, over a period of 28 days. (mean ± S.D., n = 3). The BMP-2 release profile from agarose to the surrounding medium was fitted using the Korsmeyer-Peppas model ($R^2 = 0.97$). (B) Alizarin Red S staining in tissue engineered hMSC-laden agarose constructs with or without glycosylated SPIONs loaded with BMP-2. Extensive calcium deposition (red) was observed in the hydrogel with BMP-2 present, with no staining in the system without BMP-2. Scale bars = 200 μm. (C) Macroscopic view of a representative osteochondral tissue construct engineered using agarose hydrogels patterned with a SPION gradient of BMP-2. An opaque mineralized region can be clearly observed at the bone end of the tissue construct. Scale bars = 1 mm (D) For the gradient constructs, bright field microscopy showed a smooth transition from the cartilage region to the bone region. A control system using a biphasic layered stack, rather than a gradient, exhibited a clear margin between the two regions of the tissue. Scale bars = 1 mm. (For interpretation of the references to colour in this figure legend, the reader is referred to the Web version of this article.)

(Supplementary Figure 6). More importantly, the osteochondral medium supported tissue mineralization in a 28-day culture of hMSCs in agarose with BMP-2 delivered exclusively *via* glycosylated SPIONs (Supplementary Figure 7). Indeed, the total level of BMP-2 loaded into the glycosylated SPIONs was often too high, with a large excess of unconsumed growth factor capable of diffusing out of the hydrogel and stimulating osteogenesis in adjacent, nanoparticle-free constructs. We addressed this issue by optimizing the level of BMP-2 in the glycosylated SPIONs to identify a growth factor concentration (3 μg mL^{-1}) capable of producing only local mineralization (Fig. 3B and Supplementary Figure 8).

Having optimized the gradient formation, growth factor release, cell viability and differentiation for osteochondral tissue engineering, we assembled the final system with BMP-2 loaded glycosylated SPIONs magnetically-aligned within a hMSC-laden agarose hydrogel. Over 28 days of differentiation, the vast majority of the tissue constructs developed striking white opacity at the bone end of the constructs (Fig. 3C). It should be noted that approximately 10% of the engineered constructs failed to produce any visible mineralization, and these were excluded from further study. In all cases, however, the gradient hydrogels produced tissue constructs that were structurally robust, with no macroscopic defects observed between the bone and cartilage ends of the tissue. This was in stark contrast with osteochondral tissue engineered from stacked, biphasic constructs, which produced a distinct 200 μm margin between the two ends of the tissue (Fig. 3D). Further investigation revealed that these margins were formed prior to tissue culture, with the biphasic interface appearing to exclude hMSCs (Supplementary Figure 9). The exact mechanism underpinning this observation is unknown, but nevertheless, the ability to avoid such tissue defects represents a major advantage for our gradient biomaterial over simple biphasic systems.

Alongside these macroscopic observations, we characterized the osteochondral tissue gradient constructs after 28 days of culture using gene expression analysis, histology and immunostaining. Gene expression analysis using quantitative polymerase chain reaction (qPCR) revealed significant upregulation in the mRNA of both chondrogenic genes (*COL2A1*, *SOX9*, *ACAN*) and osteogenic genes (*SP7*, *RUNX2*, *COL1A1*, *ALPL*, *COL10A1*), compared to undifferentiated hMSCs at day 0 (Supplementary Figure 10). The observed upregulation indicated a positive effect of both the media-supplemented TGF-β3 and the SPION-loaded BMP-2. More importantly, we observed a higher expression of osteogenic genes in the bone region compared to the cartilage region (N = 3, n = 3) (Fig. 4A). Significantly upregulated genes included *ALPL* and *COL10A1*, which are responsible for the expression of alkaline phosphatase and type X collagen, respectively. Importantly, we observed no significant differences between the bone and cartilage

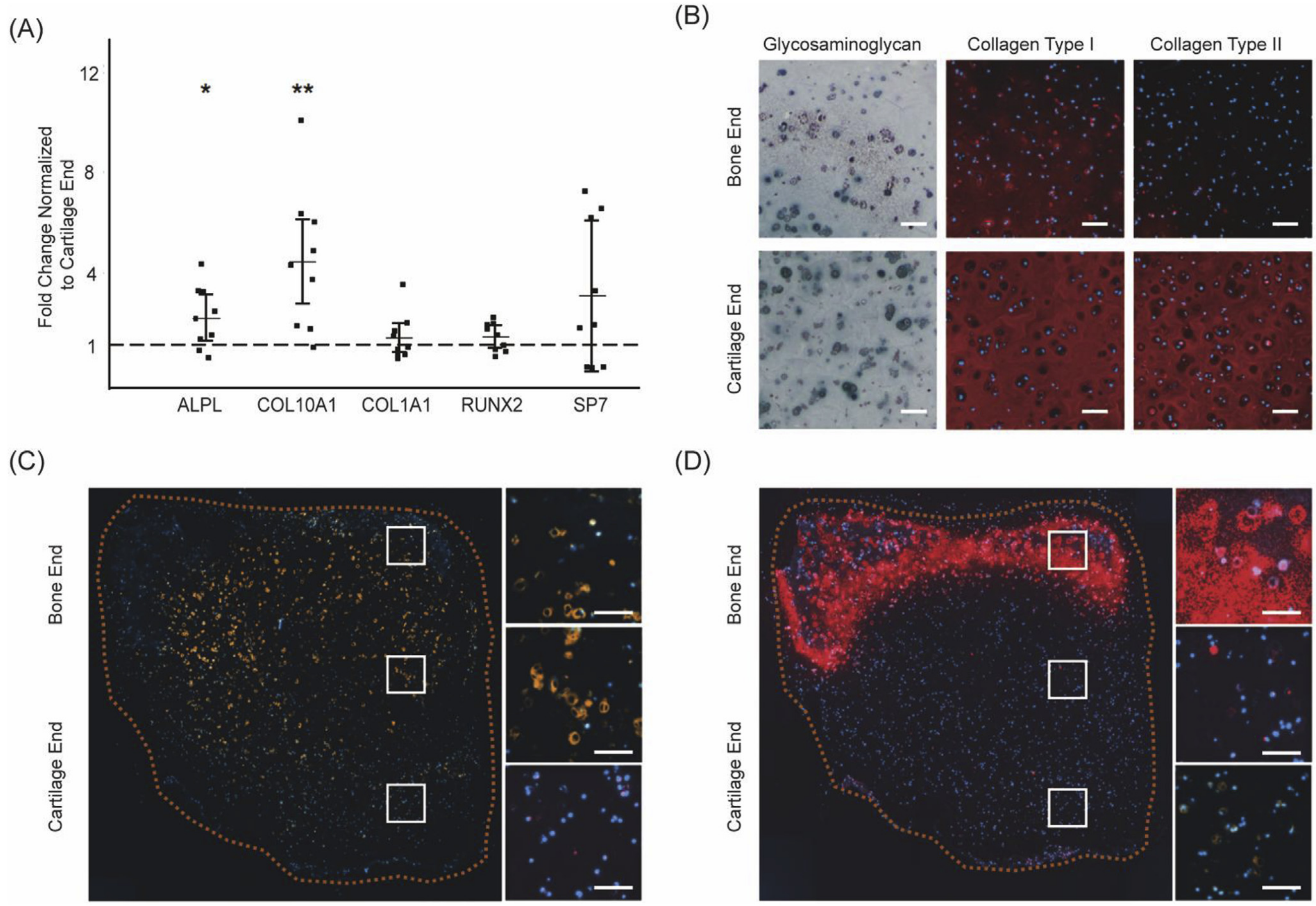

Fig. 4. Gene and protein expression in osteochondral tissue engineering. (A) Gene expression of five osteogenic genes at the bone region of the tissue, compared to the cartilage region. Comparison of differences were made using a one sample *t*-test after heteroscedasticity in the dataset was addressed (mean ± 95% confidence intervals, N = 3, n = 3) where $p < 0.05$ (*), $p < 0.01$ (**). (B) Histological and immunofluorescence staining of key extracellular matrix proteins present in cartilage and bone revealed deposition of sulfated glycosaminoglycans (blue) and type I and II collagen (red). Scale bars = 200 μm. (C) Immunofluorescence staining of the hypertrophic protein type X collagen (orange), and (D) the key mineralization protein osteopontin (red), which were present specifically at the bone end of the tissue. Scale bars = 200 μm. (For interpretation of the references to colour in this figure legend, the reader is referred to the Web version of this article.)

ends of the construct for any of the chondrogenic genes screened (Supplementary Figure 11). This gene expression analysis strongly indicated that the soluble TGF-β3 acted globally across the tissue, while the magnetically-aligned gradient of BMP-2 influenced the osteogenic differentiation of hMSCs in a spatially-defined manner.

Furthermore, we showed that these differences in gene expression could spatially influence matrix composition and structure in the tissue constructs. Alcian Blue staining for sulfated glycosaminoglycans and immunofluorescence staining for type I and II collagen revealed extensive extracellular matrix deposition, with cells located in well-defined lacunae (Fig. 4B). The presence of these components was expected; glycosaminoglycan and type II collagen are the two major components of physiological hyaline cartilage, while type I collagen is commonly expressed in engineered cartilage constructs, particularly those grown using hMSCs [35]. Although we observed no spatial differences in the gene expression of *COL1A1* and *COL2A1*, the immunostaining appeared to show a higher quantity of both type I and II collagen at the cartilage end of the tissue. The discrepancy between the mRNA and protein levels can be attributed to the fact that gene expression and matrix remodeling are dynamic processes that are not always correlated in an end-point tissue analysis [36]. Interestingly, we observed type X collagen predominantly at the interface between the bone and cartilage regions, which indicated a zone of hypertrophic chondrocytes [37] (Fig. 4C). Furthermore, osteopontin, a key marker of osteogenesis and biomineralization, was present exclusively in the bone region of the tissue (Fig. 4D).

This spatially-controlled osteogenic response was further corroborated using an alkaline phosphatase assay, which revealed a higher enzymatic activity in the bone region, compared to the cartilage region (Supplementary Figure 12). Alkaline phosphatase catalyzes the hydrolysis of organic phosphates into inorganic phosphate ions, which are used in tissue mineralization [38]. Accordingly, we further investigated the mineral formation in the engineered tissue. Alizarin Red S staining revealed the bone region to be comprised of dense calcium-rich nodules (Fig. 5A), while Raman microscopy identified the presence of two distinct calcium phosphate morphologies: hydroxyapatite (HAP) and β-tricalcium phosphate (β-TCP) (Fig. 5B). HAP is a non-degradable and mechanically-robust mineral, while β-TCP is a bioresorbable salt with osteoinductive degradation products; the presence of both morphologies is desirable during bone formation [39,40]. Importantly, in both the Alizarin Red S staining and the Raman mapping, we detected negligible calcium phosphate in the cartilage region. Indeed, by integrating the Raman contributions from β-TCP and HAP, we were able to detect a sharp transition in mineral content

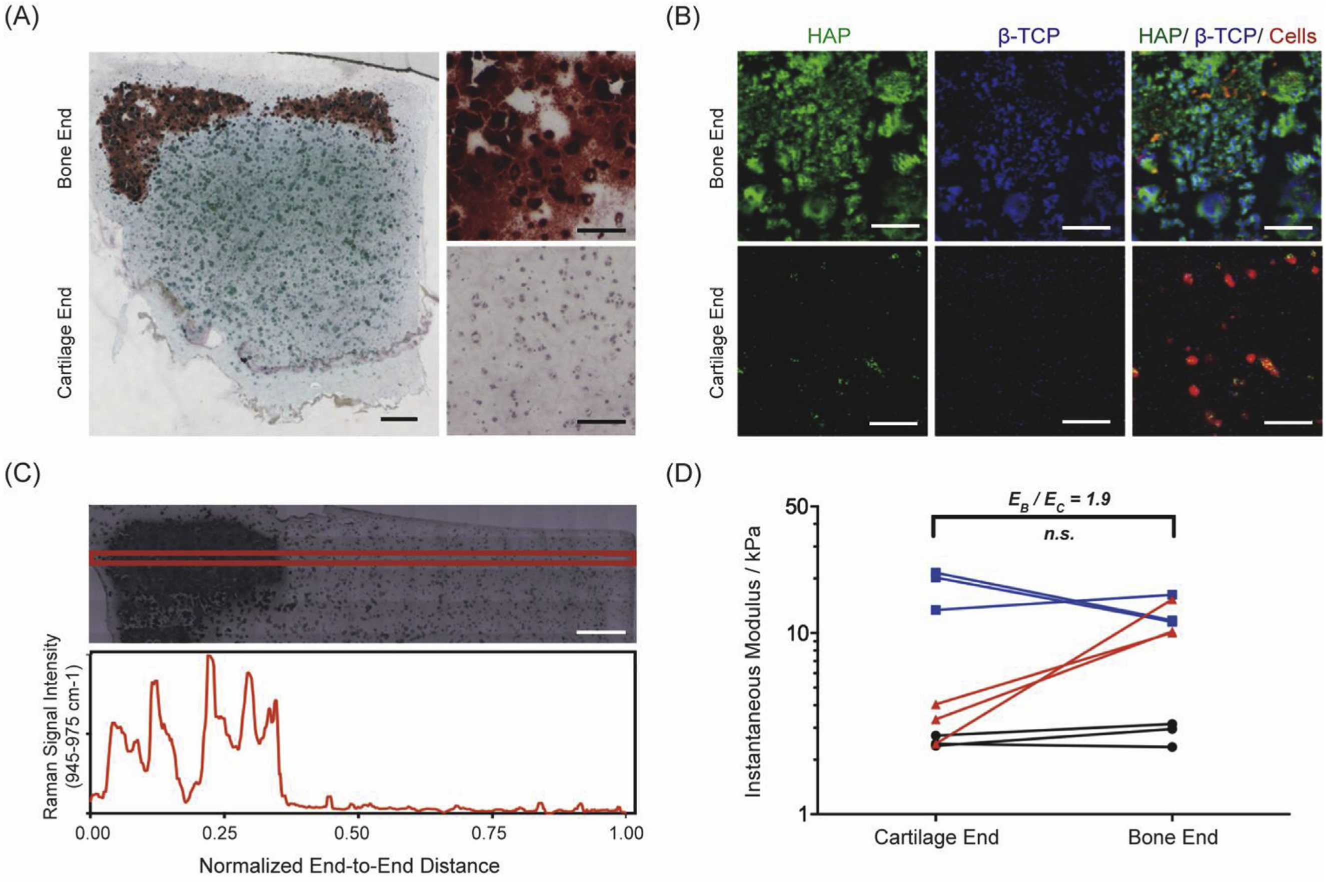

Fig. 5. Mineralization and mechanical analysis of engineered osteochondral tissue. (A) Alizarin Red S staining of calcium deposits (red) and Alcian Blue staining of sulfated glycosaminoglycan (blue) in engineered osteochondral constructs showed mineralization specifically at the bone end of the tissue. Scale bars = 500 μm. (B) Raman microscopy of HAP (green), β-TCP (blue) and cells (red) also showed mineralization specifically in the bone region. Scale bars = 100 μm. (C) Profile of Raman intensity corresponding to integrated signal from HAP and β-TCP (945 - 975 cm^{-1}) across the length of the osteochondral tissue construct, with a bright field microscopy image for reference. Scale bar = 500 μm. (D) Unconfined compression testing of the engineered osteochondral constructs showing the instantaneous modulus and the pairwise comparison between tissue constructs engineered from three different hMSC donors (denoted by red, black and blue markers). Comparison of differences were made using a one sample *t*-test after heteroscedasticity in the dataset was addressed (mean ± 95% confidence intervals, N = 3, n = 3) where $p < 0.05$ (*). (For interpretation of the references to colour in this figure legend, the reader is referred to the Web version of this article.)

from bone to cartilage that resembles the tidemark of the osteochondral interface [41] (Fig. 5C, Supplementary Figure 13). This observation was consistent with both the osteopontin immunofluorescence staining and the macroscopic images of the engineered tissue. Finally, we assessed the mechanical properties of the osteochondral constructs using an unconfined compression test ($N = 3$). The instantaneous stress-strain response of the bone and cartilage regions revealed a higher instantaneous modulus at the bone end than at the cartilage end in one of the biological replicates (Fig. 5D and Supplementary Figure 14). This observation could be attributed to differences in matrix composition, such as the presence of mineral in the bone region [42].

Overall, our results indicate that BMP-2 signaling gradients patterned using glycosylated SPIONs can spatially influence osteogenic gene expression to generate robust osteochondral constructs exhibiting low-stiffness cartilage and higher stiffness mineralized bone. Moreover, the histology, immunofluorescence staining and Raman microscopy provide a detailed picture of the engineered osteochondral tissue. In particular, we can define three major zones; a mineralized *bone region* that sharply switches into an *intermediate region* of hypertrophic chondrocytes, which then smoothly transitions into a collagen-rich *cartilage region*. To the best of our knowledge, such complexity has not been demonstrated using biphasic hydrogel systems. Interestingly, the structural complexity of our tissue, most notably the sharp transition between bone and cartilage followed by the region of hypertrophic chondrocytes, was generated from an initially smooth concentration gradient of BMP-2. These emergent structural properties are fascinating considering the developmental biology of the osteochondral interface, in which concentration gradients of osteoinductive factors produce a sharp transition (tidemark) that separates the subchondral bone/calcified cartilage from hyaline cartilage. We hypothesize that a threshold level of BMP-2 may be required to initiate and sustain mineralization of our tissue, which may in turn produce a positive feedback loop whereby the deposited mineral (HAP or resorbed β-TCP) act to further stimulate osteogenesis. Further work is required to test this theory, information that will provide a sound mechanistic basis for engineering of osteochondral constructs and other structurally complex tissues using our gradient technology. Additional work is also required for translation of this technology; in particular, the overall mechanical properties of our tissue construct must be raised to a level that is compatible with *in vivo* transplantation. More generally, clinical translation of our gradient biomaterials will require the use of materials, cells and media approved by the Food and Drug Administration (FDA) and other relevant international agencies, and the fabrication procedures to be brought in line with good manufacturing and clinical practice (GMP/GCP) guidelines.

4. Conclusions

Any robust and relevant engineered graft must recapture the complex hierarchical microstructure of the physiological tissue. In this report, we introduce a novel platform based on magnetic field alignment that can be used to rapidly produce smooth biochemical gradients for osteochondral tissue engineering. Specifically, the osteogenic growth factor BMP-2 was sequestered into glycosylated SPIONs, which were magnetically patterned across an agarose hydrogel laden with hMSCs. Diffusion of BMP-2 from the glycosylated corona provided spatially-directed osteogenesis to generate robust osteochondral tissue constructs. The initial gradient of BMP-2 gave rise to emergent structural features that highly resembled the osteochondral interface: mineralized bone transitioning to cartilage *via* a region of hypertrophic chondrocytes. The osteochondral constructs exhibited distinct cell phenotypes (chondrocytes and osteoblasts), protein expression (presence of osteopontin, alkaline phosphatase activity) and tissue mineralization (presence of β-TCP and HAP mineral). Taken together, the gene expression, biochemical profile, matrix distribution and Raman microscopy suggested that the interplay between the released BMP-2 and the solution factors (TGF-β3, β-glycerophosphate) were at a point where the tissue calcification could be achieved in a local fashion governed entirely by the patterned gradient. This technology offers great versatility and could be readily tailored to other growth factors and hydrogel systems, offering new opportunities for a range of interfacial tissue engineering challenges.

Author contributions

The study was designed by C.L., J.P.K.A. and S.C.C., with C.L. performing the majority of experimental work. C.L., J.P.K.A. and S.C.C. performed preliminary feasibility studies, I.J.P. performed all Raman spectroscopy experiments and assisted with the statistical analysis. S.W.K., J.L.P. and A.C.M. assisted with mechanical characterization and J.L.P. also provided guidance on histology and ALP assays. M.M.S. supervised the project and C.L., J.P.K.A. and M.M.S. wrote the paper, with contributions from all authors.

Acknowledgments

C.L. was supported by a Top University Strategic Alliance PhD Scholarship from Taiwan. J.P.K.A. acknowledges support from the Arthritis Research U.K. Foundation (21138). I.J.P., J.L.P. and A.C.M. were supported by the Whitaker International Program, Institute of International Education, U.S.A. W.K.-A. was supported by the British Heart Foundation Centre of Research Excellence (RE/13/4/30184). S.C.C. acknowledges funding from the Bristol Centre for Functional Nanomaterials, sponsored by the Engineering and Physical Sciences Research Council (EP/G036780/1). M.M.S. was funded by the grant from the UK Regenerative Medicine Platform “Acellular Approaches for Therapeutic Delivery” (MR/K026682/1). M.M.S. also acknowledges the grant “State of the Art Biomaterials Development and Characterization of the Cell-Biomaterial Interface” (MR/L012677/1) from the Medical Research Council, the European Research Council Seventh Framework Programme Consolidator grant “Naturale CG” (616417) and the Wellcome Trust Senior Investigator Award (098411/Z/12/Z). We also thank the Facility for Imaging by Light Microscopy (FILM) at Imperial College London. We acknowledge the assistance provided by Dr. Ioanna Mylonaki in analyzing the growth factor release data. Raw data are available upon request from rdm-enquiries@imperial.ac.uk.

Appendix A. Supplementary data

Supplementary data related to this article can be found at https://doi.org/10.1016/j.biomaterials.2018.05.029.

References

[1] F. Ulloa, J. Briscoe, Morphogens and the control of cell proliferation and patterning in the spinal cord, Cell Cycle 6 (21) (2007) 2640–2649.
[2] H.H. Lu, S. Thomopoulos, Functional attachment of soft tissues to bone: development, healing, and tissue engineering, Annu. Rev. Biomed. Eng. 15 (2013) 201–226.
[3] P. Garrison, et al., Spatial regulation of bone morphogenetic proteins (BMPs) in postnatal articular and growth plate cartilage, PLoS One 12 (5) (2017), e0176752.
[4] A. Di Luca, C. Van Blitterswijk, L. Moroni, The osteochondral interface as a gradient tissue: from development to the fabrication of gradient scaffolds for regenerative medicine, Birth Def. Res. C Embryo Today 105 (1) (2015) 34–52.
[5] S. Thomopoulos, et al., Variation of biomechanical, structural, and compositional properties along the tendon to bone insertion site, J. Orthop. Res. 21 (3) (2003) 413–419.

[6] P.J. Yang, J.S. Temenoff, Engineering orthopedic tissue interfaces, Tissue Eng. B Rev. 15 (2) (2009) 127–141.
[7] B. Sharma, J.H. Elisseeff, Engineering structurally organized cartilage and bone tissues, Ann. Biomed. Eng. 32 (1) (2004) 148–159.
[8] J.E. Phillips, et al., Engineering graded tissue interfaces, Proc. Natl. Acad. Sci. U. S. A. 105 (34) (2008) 12170–12175.
[9] M. Singh, et al., Three-dimensional macroscopic scaffolds with a gradient in stiffness for functional regeneration of interfacial tissues, J. Biomed. Mater. Res. 94 (3) (2010) 870–876.
[10] S.H. Oh, T.H. Kim, J.H. Lee, Creating growth factor gradients in three dimensional porous matrix by centrifugation and surface immobilization, Biomaterials 32 (32) (2011) 8254–8260.
[11] K.A. Mosiewicz, et al., In situ cell manipulation through enzymatic hydrogel photopatterning, Nat. Mater. 12 (11) (2013) 1072–1078.
[12] P. Nooeaid, et al., Osteochondral tissue engineering: scaffolds, stem cells and applications, J. Cell Mol. Med. 16 (10) (2012) 2247–2270.
[13] N.H. Dormer, et al., Osteochondral interface tissue engineering using macroscopic gradients of bioactive signals, Ann. Biomed. Eng. 38 (6) (2010) 2167–2182.
[14] N. Zaari, et al., Photopolymerization in microfluidic gradient generators: microscale control of substrate compliance to manipulate cell response, Adv. Mater. 16 (23–24) (2004) 2133–2137.
[15] L. Bonnemay, et al., Engineering spatial gradients of signaling proteins using magnetic nanoparticles, Nano Lett. 13 (11) (2013) 5147–5152.
[16] A. Mendyk, R. Jachowicz, Unified methodology of neural analysis in decision support systems built for pharmaceutical technology, Expert Syst. Appl. 32 (4) (2007) 1124–1131.
[17] N.A. Peppas, E.W. Merrill, Crosslinked poly(vinyl alcohol) hydrogels as swollen elastic networks, J. Appl. Polym. Sci. 21 (7) (1977) 1763–1770.
[18] L.D. Solorio, et al., Spatially organized differentiation of mesenchymal stem cells within biphasic microparticle-incorporated high cell density osteochondral tissues, Adv. Health Mater. 4 (15) (2015) 2306–2313.
[19] S. Koutsopoulos, Synthesis and characterization of hydroxyapatite crystals: a review study on the analytical methods, J. Biomed. Mater. Res. 62 (4) (2002) 600–612.
[20] S.L. Zeger, K.Y. Liang, Longitudinal data analysis for discrete and continuous outcomes, Biometrics 42 (1) (1986) 121–130.
[21] J.A. Hanley, et al., Statistical analysis of correlated data using generalized estimating equations: an orientation, Am. J. Epidemiol. 157 (4) (2003) 364–375.
[22] C.M. O'Brien, et al., In vivo Raman spectral analysis of impaired cervical remodeling in a mouse model of delayed parturition, Sci. Rep. 7 (1) (2017) 6835.
[23] R. Ruppert, E. Hoffmann, W. Sebald, Human bone morphogenetic protein 2 contains a heparin-binding site which modifies its biological activity, Eur. J. Biochem. 237 (1) (1996) 295–302.
[24] W.C. Kett, et al., Avidin is a heparin-binding protein. Affinity, specificity and structural analysis, Biochim. Biophys. Acta 1620 (1–3) (2003) 225–234.
[25] S.A. Abbah, et al., In vivo bioactivity of rhBMP-2 delivered with novel polyelectrolyte complexation shells assembled on an alginate microbead core template, J. Contr. Release 162 (2) (2012) 364–372.
[26] H. Lysdahl, et al., Preconditioning human mesenchymal stem cells with a low concentration of BMP2 stimulates proliferation and osteogenic differentiation in vitro, Biores. Open Access 3 (6) (2014) 278–285.
[27] O. Nilsson, et al., Gradients in bone morphogenetic protein-related gene expression across the growth plate, J. Endocrinol. 193 (1) (2007) 75–84.
[28] Y. Ma, et al., Concentration-dependent hMSC differentiation on orthogonal concentration gradients of GRGDS and BMP-2 peptides, Biomacromolecules 17 (4) (2016) 1486–1495.
[29] B. Zhao, et al., Heparin potentiates the in vivo ectopic bone formation induced by bone morphogenetic protein-2, J. Biol. Chem. 281 (32) (2006) 23246–23253.
[30] Z. Wang, et al., BMP-2 encapsulated polysaccharide nanoparticle modified biphasic calcium phosphate scaffolds for bone tissue regeneration, J. Biomed. Mater. Res. 103 (4) (2015) 1520–1532.
[31] G. Chen, C. Deng, Y.P. Li, TGF-beta and BMP signaling in osteoblast differentiation and bone formation, Int. J. Biol. Sci. 8 (2) (2012) 272–288.
[32] J.L. Puetzer, J.N. Petitte, E.G. Loboa, Comparative review of growth factors for induction of three-dimensional in vitro chondrogenesis in human mesenchymal stem cells isolated from bone marrow and adipose tissue, Tissue Eng. B Rev. 16 (4) (2010) 435–444.
[33] U. Noth, et al., Chondrogenic differentiation of human mesenchymal stem cells in collagen type I hydrogels, J. Biomed. Mater. Res. 83 (3) (2007) 626–635.
[34] J. Hwang, et al., In vitro calcification of immature bovine articular cartilage: formation of a functional zone of calcified cartilage, Cartilage 1 (4) (2010) 287–297.
[35] J.P. Armstrong, et al., Artificial membrane-binding proteins stimulate oxygenation of stem cells during engineering of large cartilage tissue, Nat. Commun. 6 (2015) 7405.
[36] P.A. Parmar, et al., Collagen-mimetic peptide-modifiable hydrogels for articular cartilage regeneration, Biomaterials 54 (2015) 213–225.
[37] G. Shen, The role of type X collagen in facilitating and regulating endochondral ossification of articular cartilage, Orthod. Craniofac. Res. 8 (1) (2005) 11–17.
[38] E.E. Golub, et al., The role of alkaline phosphatase in cartilage mineralization, Bone Miner. 17 (2) (1992) 273–278.
[39] S. Yamada, et al., Osteoclastic resorption of calcium phosphate ceramics with different hydroxyapatite/beta-tricalcium phosphate ratios, Biomaterials 18 (15) (1997) 1037–1041.
[40] H.E. Koepp, et al., Biocompatibility and osseointegration of beta-TCP: histomorphological and biomechanical studies in a weight-bearing sheep model, J. Biomed. Mater. Res. B Appl. Biomater. 70 (2) (2004) 209–217.
[41] A.J. Sophia Fox, A. Bedi, S.A. Rodeo, The basic science of articular cartilage: structure, composition, and function, Sports Health 1 (6) (2009) 461–468.
[42] S. Ahmed, F.R. Jones, A review of particulate reinforcement theories for polymer composites, J. Mater. Sci. 25 (12) (1990) 4933–4942.

COMMUNICATION

Gradient Materials

ADVANCED MATERIALS

www.advmat.de

Buoyancy-Driven Gradients for Biomaterial Fabrication and Tissue Engineering

Chunching Li, Liliang Ouyang, Isaac J. Pence, Axel C. Moore, Yiyang Lin, Charles W. Winter, James P. K. Armstrong, and Molly M. Stevens**

The controlled fabrication of gradient materials is becoming increasingly important as the next generation of tissue engineering seeks to produce inhomogeneous constructs with physiological complexity. Current strategies for fabricating gradient materials can require highly specialized materials or equipment and cannot be generally applied to the wide range of systems used for tissue engineering. Here, the fundamental physical principle of buoyancy is exploited as a generalized approach for generating materials bearing well-defined compositional, mechanical, or biochemical gradients. Gradient formation is demonstrated across a range of different materials (e.g., polymers and hydrogels) and cargos (e.g., liposomes, nanoparticles, extracellular vesicles, macromolecules, and small molecules). As well as providing versatility, this buoyancy-driven gradient approach also offers speed (<1 min) and simplicity (a single injection) using standard laboratory apparatus. Moreover, this technique is readily applied to a major target in complex tissue engineering: the osteochondral interface. A bone morphogenetic protein 2 gradient, presented across a gelatin methacryloyl hydrogel laden with human mesenchymal stem cells, is used to locally stimulate osteogenesis and mineralization in order to produce integrated osteochondral tissue constructs. The versatility and accessibility of this fabrication platform should ensure widespread applicability and provide opportunities to generate other gradient materials or interfacial tissues.

In nature, gradients play an essential role in guiding the function of a wide range of tissues, including tendon, cartilage, and the central nervous system.[1–4] Strategies that seek to engineer tissues in vitro must strive to recreate these natural gradients in order to produce fully functional grafts or physiologically relevant models. In doing so, one must consider the numerous gradients present in native tissue, including transitions in biochemical composition (e.g., extracellular matrix and soluble growth factors) and physical environment (e.g., stiffness and topography). These transitions play a major role in defining the formation of cellular gradients by spatially regulating the morphology, behavior, and differentiation of local cells.[5–8] Accordingly, intensive research effort has been invested in designing materials with well-defined gradients. For instance, material gradients have been fabricated using multichannel microfluidic devices or 3D printing.[9–11] However, these approaches require specialist apparatus and are usually restricted by certain material parameters, such as viscosity or gelation kinetics. Approaches such as photopatterning and magnetic field alignment have also been used to generate gradients; however, these remote field strategies require even more specific material properties (photoresponsivity and magnetic susceptibility).[12,13] Indeed, a generalized method that can be universally applied to different systems has thus far remained elusive.

In this work, we sought to employ a more universal physical principle that could be applied broadly across different material systems. Specifically, we investigated whether we could fabricate material transitions using buoyancy, the upward force generated on materials immersed in a denser fluid phase.[14] Buoyancy is commonly used to stabilize the formation of sucrose gradients used for the fractionation of cells and organelles.[15,16] This approach has been extended to nanoparticle separation using density-graded organic solvents.[17] There are, however, only a limited number of examples in which buoyancy has been used to fabricate gradient materials. For example, Parameswaran and Shukla described a system in which cenospheres (hollow silica–alumina microparticles) were allowed to rise to the top of a polyester resin and then immobilized in a solid matrix using a 48 h curing process. This yielded a polymeric material with a graded volume fraction of cenospheres, and a corresponding gradient of compressive and tensile properties.[18] Similarly, Beals and Thompson showed that a gas injected into a molten aluminum alloy could be dispersed into small particulate-stabilized bubbles upon mixing. These bubbles formed a liquid foam at the top of the melt, which was subsequently cooled to

---

C. Li, L. Ouyang, I. J. Pence, A. C. Moore, Y. Lin, C. W. Winter,
J. P. K. Armstrong, M. M. Stevens
Department of Materials
Department of Bioengineering and Institute of Biomedical Engineering
Imperial College London
Prince Consort Road, London SW7 2AZ, UK
E-mail: james.armstrong@imperial.ac.uk; m.stevens@imperial.ac.uk

The ORCID identification number(s) for the author(s) of this article can be found under https://doi.org/10.1002/adma.201900291.

DOI: 10.1002/adma.201900291

form a metallic structure with a gradient of porosity.[19] However, these examples are highly specific with a focus on solid materials for industrial applications. To the best of our knowledge, there has been no report of any versatile methodology using buoyancy in gradient material fabrication, nor any examples in which buoyancy-driven gradients have been applied to the field of complex tissue engineering.

To this end, we sought to develop a generalized buoyancy-driven approach for casting gradients that could be applied to real-world tissue engineering applications. Here we show that a single injection event of one fluid material into another is sufficient to generate material transitions that can be preserved by subsequent gelation or polymerization. Moreover, we were able to fabricate materials exhibiting either a sharp transition or a smooth gradient by systematically varying the material characteristics and injection parameters. We used this platform to cast gradients in several different materials (gelatin methacryloyl, gellan gum, agarose, and acrylate polymers) and generated tunable transitions in composition, biochemical profile, and compressive stiffness. We also demonstrated that several cargo species could be incorporated in gradient form, including inorganic nanoparticles, liposomes, cell-derived extracellular vesicles, macromolecules, and proteins. We applied this method to cast bone morphogenetic protein 2 (BMP-2) gradients for the in vitro engineering of osteochondral tissue constructs.[20] In this system, the encapsulated BMP-2 was slowly released over 28 d of tissue engineering to locally stimulate osteogenesis of human mesenchymal stem cells and produce osteochondral tissue bearing a defined mineral cap. The versatility and simplicity of this gradient casting platform should enable a range of applications in complex material fabrication and interfacial tissue engineering.

In order to rapidly cast different material gradients, we sought to develop and optimize a controlled two-component mixing system. Specifically, we used a commercially available electronic autopipette to introduce one material at a defined rate into another static base material. The two phases were allowed time to establish a gradient, which could then be preserved by triggering a polymerization or gelation process. This system only required two liquid phases that were miscible and curable, as well as a sufficient density difference to enable buoyancy-driven gradient formation (**Figure 1**A). This can be illustrated using the relatively simple case of 0.2 and 1% (w/v) agarose in the injection phase and base layer, respectively (Figure S1, Supporting Information). However, in scenarios where the density difference between the two phases was too small to create sufficient buoyancy, we used a third component to increase the density of the base layer relative to the injection phase. Using this approach, we were able to form smooth gradients using 1% (w/v) fluorescently tagged agarose and 1% (w/v) unlabeled agarose by adding 5% (w/v) sucrose to the base layer. Moreover, gradients could be rapidly established in 10 s, with the resulting structure remaining stable for at least 30 min post injection (Figure 1B; Figure S2 and Video S1, Supporting Information). This provided us with an ample window of opportunity to solidify the material and preserve the gradient, in this case, by cooling the system below the gelation temperature of agarose.

To characterize this system and elucidate the mechanism behind gradient formation, we analyzed the composition of the hydrogel along the longitudinal axis. We divided the hydrogels

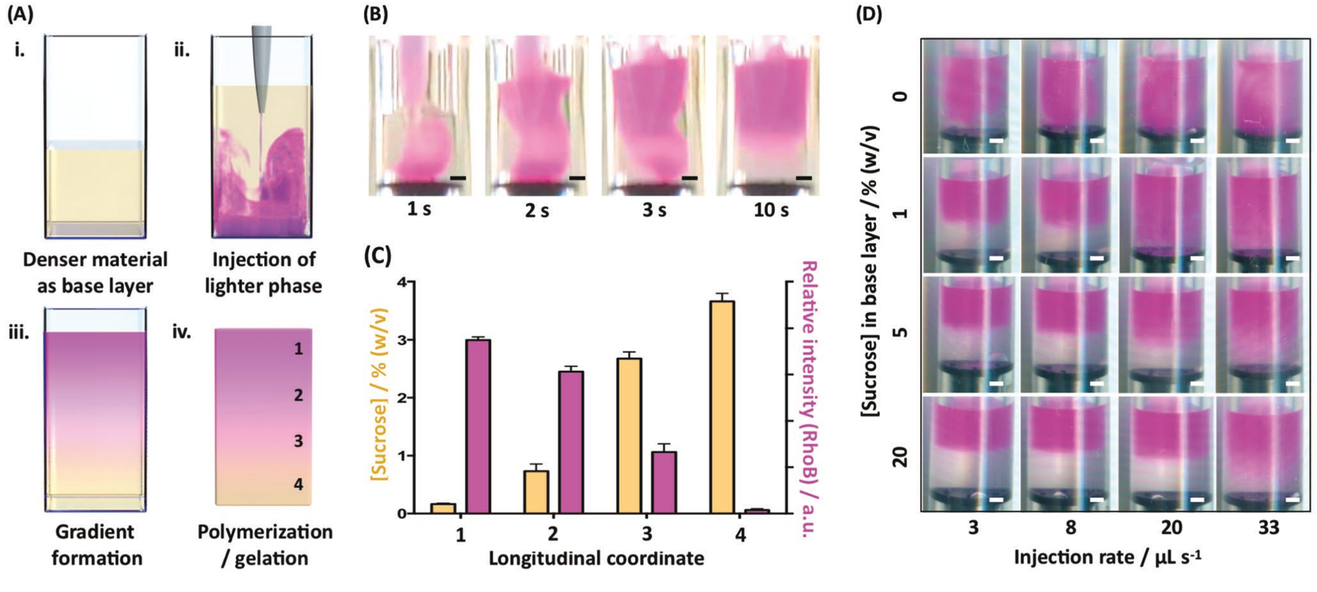

Figure 1. Buoyancy-driven gradient casting. A) Schematic showing the steps of gradient formation: i) a base layer (yellow) is added to a mold, ii) the injection phase (purple) is introduced during a single injection at a controlled rate, iii) the system is allowed to equilibrate and form a material gradient, and iv) the gradient is preserved by gelling or polymerizing the material. B) An example of gradient formation using 1% (w/v) agarose tagged with rhodamine B (pink) injected at a rate of 20 µL s^{-1} into a base layer of 1% (w/v) agarose supplemented with 5% (w/v) sucrose as a density modifier. An observable gradient can be established within 10 s. C) Immediately after gelation, a gradient hydrogel was equally divided into four transverse sections from the top to the bottom of the hydrogel (1–4). These sections were assayed for sucrose (yellow bars) and agarose tagged with rhodamine (RhoB, pink bars), which showed a clear inverse correlation. Data shown as mean ± S.D., *n* = 3. D) The gradient pattern could be tuned by varying the injection rate and concentration of sucrose in the base layer. For measured densities, see Figure S4 in the Supporting Information. Scale bars = 1 mm.

into four transverse sections, which we analyzed using an enzymatic assay for sucrose and fluorescence spectroscopy for dye-labeled agarose (Figure 1C). These measurements revealed a sucrose gradient within the hydrogel that was inversely associated with the injected dye-labeled agarose. These results suggest that sucrose must retain attractive intermolecular interactions with the base layer agarose during the fluid-mixing process. These interactions prevent the base layer from completely equilibrating with the injection phase, thus retaining longitudinal density differences capable of supporting buoyancy-driven gradient formation. It should also be noted that sucrose, as a small molecule, could be readily removed by washing the agarose hydrogel in phosphate buffered saline (PBS) (Figure S3, Supporting Information). In this sense, sucrose can be considered as a temporary density modifier that can template the gradient formation process. Moreover, we observed that systematic variation of different parameters could be used to control the final profile of the material gradient. Using the same agarose–sucrose system, we showed that different combinations of injection rate and density difference could be used to fabricate a range of transitions, from sharp layers to smooth gradients (Figure 1D; Figure S4, Supporting Information). Indeed, small differences in density from the doped sucrose ($\Delta\rho = 0.02$ g mL^{-1}) were enough to drive gradient formation, while no clear structural transitions could be formed without addition of sucrose to the agarose base layer.

Unlike the majority of gradient fabrication strategies, which are only applicable to certain materials or cargos, our buoyancy platform could be widely applied across different systems. To illustrate this versatility, we demonstrated seven distinct examples of buoyancy-driven gradient formation (Table S1, Supporting Information). First, we generated gradients in solid polymers using two miscible monomers bearing a slight difference in material density, *N*,*N*-dimethylacrylamide ($\rho = 0.96$ g mL^{-1}) and lauryl methacrylate ($\rho = 0.87$ g mL^{-1}), together with poly(ethylene glycol) dimethacrylate as a crosslinker. Inclusion of photoinitiator allowed us to trigger photopolymerization after establishment of the monomer gradient. We visualized this transition by adding rhodamine B dye, which is soluble in *N*,*N*-dimethylacrylamide but not in lauryl methacrylate (**Figure 2**A). We further characterized this transition using Raman spectroscopy based on the distinct signature of the two polymers (Figure 2A; Figure S5, Supporting Information). Next, we used our buoyancy platform to pattern defined stiffness transitions into 1% and 1.5% (w/v) gellan gum hydrogels, using 5% (w/v) sucrose as a density modifier. We measured the contact modulus along the longitudinal axis using a spherical indenter, which revealed the different stiffness transitions that we could achieve by varying the injection rate (Figure 2B). As well as creating transitions in the bulk material structure, we also used our buoyancy platform to fabricate materials bearing gradients of encapsulated

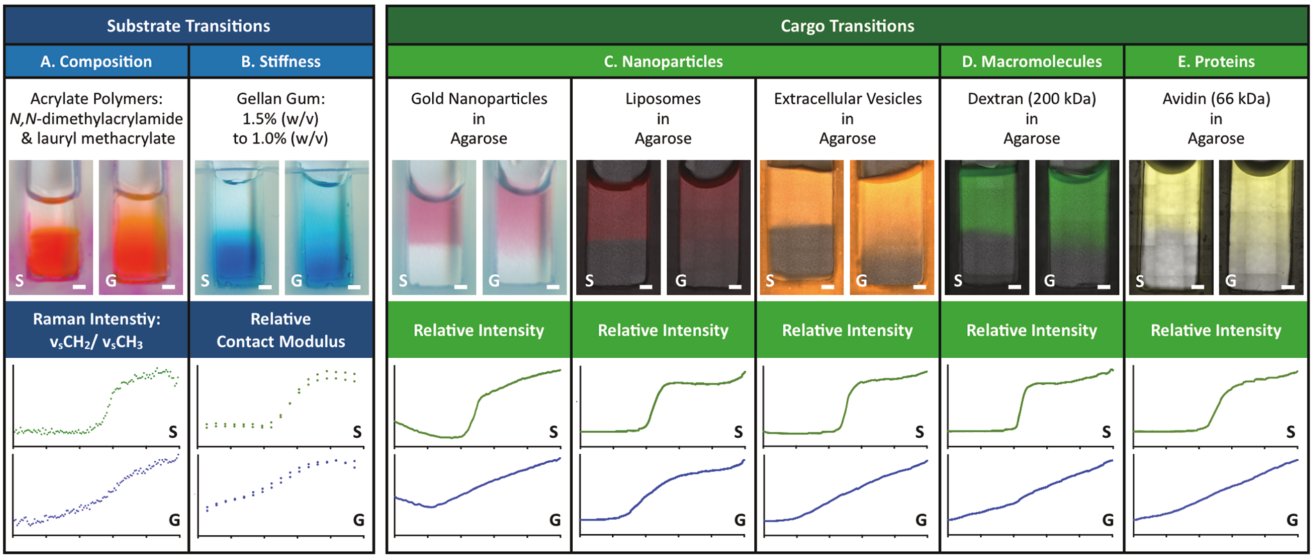

Figure 2. Versatility of buoyancy-driven gradient formation. For all fabricated materials, we generated sharp transitions (S, green traces) and gradient transitions (G, blue traces). A) Polymer gradients were formed with two monomers bearing a difference in density: *N*,*N*-dimethylacrylamide (0.96 g mL^{-1}) and lauryl methacrylate (0.87 g mL^{-1}). The transition could be visualized using Rhodamine B dye (red), which was soluble only in the latter monomer. Raman spectroscopy was used to show differences in the intrinsic chemical composition profile along the longitudinal coordinate of an undyed system. Confocal Raman imaging was used to detect the ratio of CH_2 and CH_3 stretching features, demonstrating the different profiles obtained for polymers cast with a gradient or sharp transition. B) Gradients were formed with two different concentrations of gellan gum hydrogel, which could be visualized by the addition of methylene blue dye. Spherical indentations along the longitudinal coordinate were used to calculate contact modulus profiles for the gradient and sharp transition hydrogels. Sucrose was used to create density differences between the base layer and injection phase of agarose hydrogels in order to create transitions of: C) nanoparticles including gold nanoparticles (pink), liposomes labeled with Rhodamine B (red) and RFP-extracellular vesicles (orange) as well as D) 200 kDa FITC-dextran (green) and E) avidin labeled with Texas Red (yellow). Intensity profiles along the longitudinal coordinate were used to characterize the hydrogels bearing a gradient or a sharp transition. Scale bars = 1 mm. All profile plots show normalized transitions along the longitudinal coordinate, with equivalent axes scales used for each pair of graphs. For fabrication detail please refer to Table S1 in the Supporting Information.

nano-particles. For this study, we used our established agarose–sucrose system to generate gradients of gold nanoparticles, 1-palmitoyl-2-oleoyl-glycero-3-phosphocholine (POPC) liposomes, and cell-derived extracellular vesicles (Figure 2C). These three examples encompassed a broad range of inorganic, organic, and biological nanoparticles, each of which can be used as a host for cargo delivery or as a functional entity in its own right.[13,21–23] We next investigated whether our buoyancy platform could support the formation of biomolecular gradients. Again using our agarose–sucrose system, we patterned gradients of both macromolecules (fluorescently tagged 200 kDa dextran) and proteins (fluorescently tagged avidin) (Figure 2D). It should be noted, however, that due to the absence of any strong attractive interactions with the agarose network, the avidin and dextran were only temporarily entrapped within the hydrogel (Figure S6, Supporting Information). To establish a more prolonged gradient, we investigated whether we could pattern cargo associated with a macromolecular host that was covalently crosslinked to the surrounding hydrogel network. We demonstrated this concept using gelatin methacryloyl (GelMA) as the bulk hydrogel and heparin methacryloyl (HepMA) as a macromolecular host. While heparin has been widely used to sequester cationic proteins,[24,25] the addition of methacryloyl groups provided a means to covalently crosslink HepMA with itself and the surrounding GelMA. Indeed, this approach limited the cumulative release of HepMA from GelMA to just 26 ± 3% after 28 d of incubation, compared to an 86 ± 16% release of unmodified heparin from GelMA after just 1 d of incubation (Figure S7, Supporting Information). To demonstrate the cargo-loading capability, we used fluorescently tagged avidin ($M_W = 66$ kDa, $pI = 6.5$, heparin dissociation constant = 160×10^{-9} M) as a model protein.[26] By coinjecting 10% (w/v) GelMA and avidin sequestered with HepMA into a base layer of 10% (w/v) GelMA with 5% (w/v) sucrose, we successfully generated well-defined protein gradients (Figure 2E). It is important to note that orthogonal methacrylate chemistry was chosen in order to bind HepMA and GelMA without forming covalent linkages with the protein cargo. Consequently, this approach reduces the chance of denaturation while retaining the possibility for slow cargo release.

The ability of our buoyancy platform to rapidly cast biomaterial gradients offers great potential for the engineering of complex tissue structures. For instance, a major challenge of regenerative medicine is the engineering of the osteochondral interface that exists between cartilage and bone. In nature, this transition arises, in part, by an anisotropic distribution of growth factors present during the process of endochondral ossification.[27] Accordingly, we sought to use our buoyancy platform to present a gradient distribution of BMP-2, a key developmental growth factor that can be used to initiate osteogenesis in human mesenchymal stem cells (hMSCs).[28] Given that BMP-2 is a low molecular weight cationic protein ($M_W = 13$ kDa, $pI = 8.5$, heparin dissociation constant = 20×10^{-9} M),[29] we elected to use HepMA as a macromolecular host patterned within a GelMA hydrogel (similar to our previous example using avidin). As a bulk material, GelMA has been used extensively to support hMSCs during cartilage, bone and osteochondral tissue engineering,[30] while heparin has been used to electrostatically bind and slowly release functionally active BMP-2.[31] To test this behavior, we used an enzyme-linked immunosorbent assay to measure the cumulative release of BMP-2 from homogeneous HepMA–GelMA hydrogels (Figure S8, Supporting Information). We observed a slow release that reached completion at 28 d of incubation, which should ensure that BMP-2 is elevated at one end of the hydrogel throughout the culture period.

The only aspect of the HepMA–GelMA system that was not suitable for tissue engineering was the density modifier: although sucrose is ideal for fabricating gradients in cell-free systems, it is known to exert an osmotic pressure that can be highly cytotoxic. Accordingly, we investigated whether we could substitute sucrose for the more cytocompatible polysaccharide Ficoll in order to raise the density of GelMA in the base layer while maintaining a stable osmotic pressure. Indeed, an alamarBlue assay confirmed that doping up to 5% (w/v) Ficoll in GelMA hydrogels presented no significant cytotoxicity to the encapsulated hMSCs (Figure S9A, Supporting Information). Crucially, Ficoll could be used in the same way as sucrose to produce gradients in GelMA with a longitudinal profile that was dependent upon injection rate (Figure S9B, Supporting Information). Thus, our optimized system for osteochondral tissue engineering comprised 3.1 µg mL^{-1} BMP-2, 2.5 µg mL^{-1} HepMA and 10% (w/v) GelMA injected into a base layer of 10% (w/v) GelMA doped with 5% (w/v) Ficoll, with both phases containing 9×10^6 hMSCs mL^{-1} and 2.5 mg mL^{-1} photoinitiator. Using these conditions, and an injection rate of 17 µL s^{-1}, we were able to establish smooth gradients of HepMA and BMP-2 that could be immobilized in GelMA using UV light irradiation (5 min, 365 nm, 6 mW cm^{-2}) (**Figure 3**A). We used these constructs for a 28 d course of osteochondral tissue engineering using a defined osteochondral differentiation medium that we have previously shown to be capable of supporting both osteogenesis and chondrogenesis (Figure 3A).[13] This medium included 2×10^{-3} M β-glycerophosphate as a phosphate source,[32] transforming growth factor β3 (TGF-β3) to stimulate chondrogenesis, alongside supporting components such as insulin–transferrin–selenium, ascorbic acid, and dexamethasone.

We started to observe the formation of a strikingly opaque cap on the cultured constructs after approximately 15 d of tissue engineering. By the end of the culture period (28 d), this cap was present on all tissue constructs, a strong indication that the BMP-2 gradient had guided a localized mineralization process. Indeed, when we examined sections of osteochondral tissue using Alizarin Red S staining, we observed a mineralized cap exclusively at one end of the tissue (Figure 3B). On the other hand, Alcian Blue staining revealed that the entire tissue contained sulfated glycosaminoglycans, a key extracellular matrix component naturally present in both cartilage and bone (Figure 3C).[33] These findings were corroborated using immunofluorescence staining for key proteins associated with chondrogenesis and osteogenesis (Figure 3D,E). While type II collagen, found exclusively in hyaline cartilage,[34] was present throughout the tissue construct, osteopontin, a key marker of osteogenesis, was observed only in the mineralized cap.[35] We further investigated the mineral composition and distribution using Raman spectroscopic imaging, which revealed the presence of both hydroxyapatite (HAP) and β-tricalcium phosphate (β-TCP), exclusively at the bone end of the construct

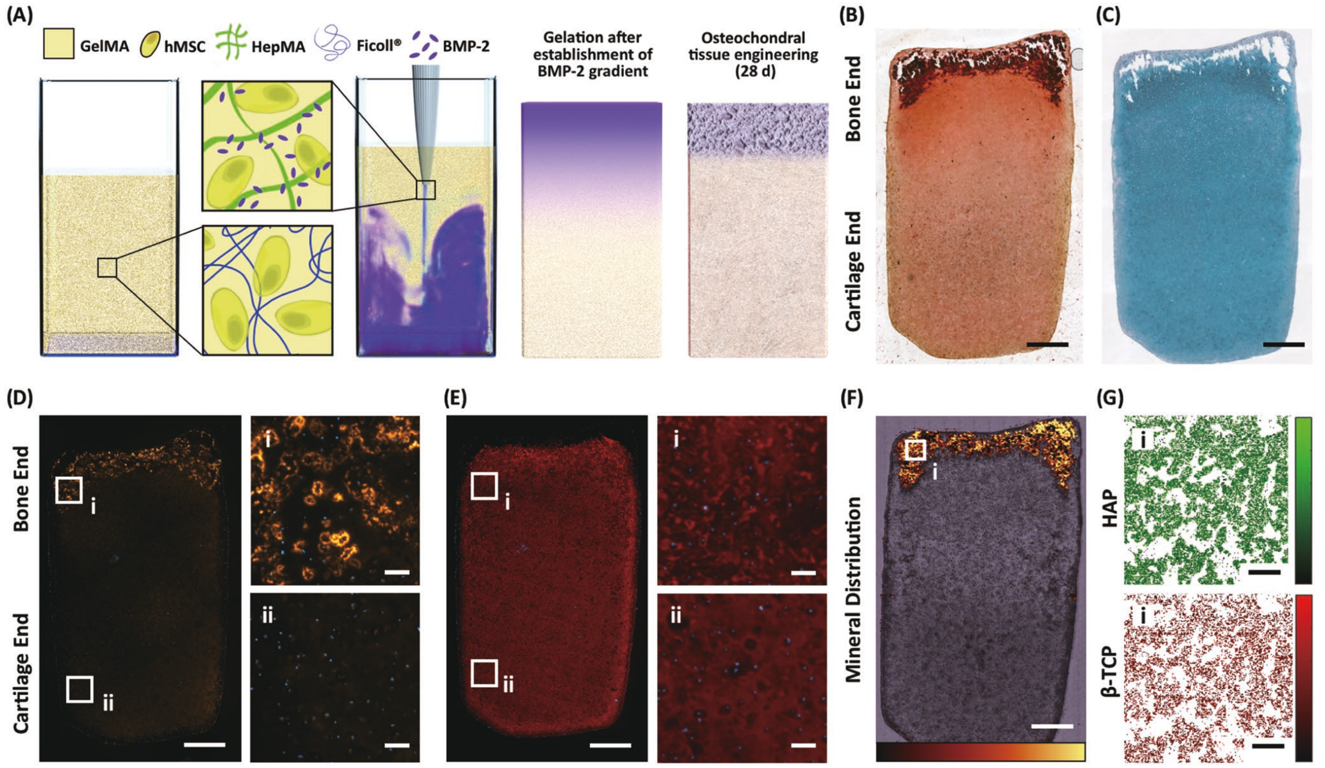

Figure 3. Growth factor gradients for osteochondral tissue engineering. A) BMP-2 was sequestered by HepMA and coinjected with 10% (w/v) GelMA and hMSCs into a base layer of 10% (w/v) GelMA, 5% (w/v) Ficoll and hMSCs. The GelMA and HepMA were photo-crosslinked to preserve the BMP-2 gradient in a self-supporting hydrogel, which was cultured for 28 d in osteochondral differentiation medium. Note that the components in the inset images are not drawn to scale. Histology and immunofluorescence staining confirmed the formation of osteochondral tissue: B) Alizarin Red S staining revealed localized mineral deposition at one end of the tissue; C) Alcian Blue staining revealed tissue-wide staining for glycosaminoglycans, a component of both cartilage and bone; D) the bone-specific marker osteopontin was also localized exclusively at the mineralized cap; E) Type II collagen, a component of hyaline cartilage, was present throughout the tissue. F) Raman spectroscopic imaging was used to reveal the spatial distribution of mineral and G) identify the presence and heterogeneous presentation of both hydroxyapatite and tri-calcium phosphate in the mineralized cap. Scale bar = 1 mm in low-magnification images, 100 µm in high magnification images. The color scales in (F) and (G) show the relative intensity of signal, with brighter color representing higher intensity.

(Figure 3F,G). While the HAP signature was stronger throughout the mineral cap region, spectral unmixing of these features indicated a heterogeneous presentation of mineral species that formed colocally within the cultured construct. Taken together, the histology, immunofluorescence staining and Raman spectroscopic mapping strongly suggested that the soluble TGF-β3 had stimulated tissue-wide chondrogenesis of the hMSCs, while the BMP-2 released from the HepMA gradient had initiated a localized osteogenic response. Interestingly, the mineralization took the form of an abrupt biphasic transition between bone and cartilage, despite the initially smooth BMP-2 gradient and the homogenous distribution of cells (Figure S10, Supporting Information). This observation mimics the natural process of endochondral ossification, in which concentration gradients of osteoinductive factors (e.g., BMP-2 and BMP-6) produce a sharp transition at the osteochondral interface. This transition, known as a tidemark, separates subchondral bone and calcified cartilage from the other cartilage zones and is a hallmark feature of the osteochondral interface. Interestingly, we have observed a similar phenomenon in previous osteochondral tissue engineering systems[13] and hypothesize that a threshold level of BMP-2 may be required to initiate and sustain mineralization, which could in turn produce a positive feedback loop whereby the deposited mineral acts to further stimulate osteogenesis. Further work is required to test this theory, which could shed light upon some of the key developmental processes that occur during endochondral ossification.

In conclusion, we have introduced a versatile platform that uses the fundamental force of buoyancy to pattern materials with tunable gradients using one simple injection event. We demonstrated gradient formation with a range of different materials (polymers and hydrogels) and cargos (liposomes, inorganic nanoparticles, extracellular vesicles, macromolecules, and small molecules). We also demonstrated the applicability of this platform in a tissue engineering context, specifically, the presentation of a BMP-2 gradient for the production of osteochondral tissue. The resulting tissue constructs possessed distinct regions of bone and cartilage, along with a structural transition that resembled the tidemark observed at the native osteochondral interface. Overall, the versatility, speed, and ease of use of our platform technology offer the opportunity for many different applications in gradient material fabrication and interfacial tissue engineering.

Experimental Section

Buoyancy-Driven Gradient Casting and Characterization: Unless stated otherwise, all chemicals used were from Sigma Aldrich. To create the gradient constructs, the denser liquid was added to a mold as a base layer. An electronic dispenser (Multipette E3/E3x, Eppendorf) was used to inject the lighter liquid at a defined flow rate, with the injection outlet maintained at the liquid–air interface of the base layer. Injection rates were measured manually. Immediately after injection, the dispenser was removed, and the gradients were preserved by gelation or polymerization. Two molds were used in this communication: a cuboid mold ($5 \times 15 \times 3$ mm) and a cylindrical mold ($\varnothing = 5$ mm, $h = 15$ mm). Polymer gradients were characterized using Raman spectroscopic mapping. Briefly, a confocal Raman microspectroscopy system (WITec alpha 300R+) was used to raster map the entire surface of the gradient construct and obtain spectra comprising compositional information at 50 μm steps.[36,37] The resulting data was analyzed via peak ratio to reveal the location and relative concentration of the construct polymers. Stiffness gradients were characterized using spherical indentation mapping. Briefly, a 3 mm diameter stainless steel sphere was indented along the gradient in 0.5 mm steps, and the contact modulus of each indent was characterized by a modified Hertzian solution to account for substrate effects.[38] All other gradients were characterized by imaging the constructs using a wide field microscope, converting the images to 16-bit and then using the plot profile function in Image J. For full details of the fabrication and characterization of each gradient system, see Table S1 and the Experimental Section in the Supporting Information.

Osteochondral Tissue Engineering: hMSCs (Lonza) were cultured with MesenPro RS medium (Thermo Fisher Scientific) and used between passage 4–5. For osteochondral tissue engineering, we used a 90 μL base layer of 5% (w/v) Ficoll-400, 10% (w/v) GelMA, 2.5 mg mL^{-1} Irgacure 2959, and 9×10^6 hMSCs mL^{-1} and a 45 μL injection phase of 12.5 μg mL^{-1} BMP-2 (R&D Systems), 10 μg mL^{-1} HepMA, 10% (w/v) GelMA, 2.5 mg mL^{-1} Irgacure 2959 and 9×10^6 hMSCs mL^{-1}. Note that prior to gradient formation, HepMA and BMP-2 were mixed for at least 4 h to ensure equilibration. We used an injection rate of 16.7 μL s^{-1} and then used a UV lamp to crosslink the hydrogels (365 nm, 6 mW cm^{-2}, 5 min), which were then transferred to a 24 well plate. The constructs were cultured in osteochondral differentiation medium, which was changed three times a week. The osteochondral differentiation medium comprised high glucose Dulbecco's modified Eagle medium with pyruvate (Thermo Fisher Scientific), 1× insulin–transferrin–selenium supplement (ITS+, BD), 100×10^{-9} M dexamethasone, 50 μg mL^{-1} L-ascorbic acid, 50 μg mL^{-1} L-proline, 2×10^{-3} M β-glycerophosphate and 10 ng mL^{-1} TGF-β3 (R&D Systems). After 28 d of culture, the constructs were harvested and characterized using histology (Alcian Blue, Alizarin Red), immunofluorescence staining (type II collagen, osteopontin) and Raman spectroscopy. For full details of the tissue engineering and analysis, please refer to the Materials and Methods section in the Supporting Information.

Supporting Information

Supporting Information is available from the Wiley Online Library or from the author.

Acknowledgements

C.L. was supported by a Top University Strategic Alliance Ph.D. Scholarship from Taiwan. L.O. acknowledges support from the Engineering and Physical Sciences Research Council (EPSRC) Programme Grant "Engineering growth factor microenvironments—a new therapeutic paradigm for regenerative medicine" (EP/P001114/1). I.J.P. and A.C.M. acknowledge support from the Whitaker International Program, Institute of International Education, USA. C.W.W. acknowledges support from the Biotechnology and Biological Sciences Research Council Doctoral Training Partnership (BB/N503952/1). J.P.K.A. acknowledges support from the Arthritis Research U.K. Foundation (21138) and the Medical Research Council (MRC) (MR/S00551X/1). M.M.S. and Y.L. acknowledge support from the European Research Council Seventh Framework Programme Consolidator grant "Naturale CG" (616417). M.M.S. acknowledges support from the grant from the UK Regenerative Medicine Platform "Acellular/Smart Materials—3D Architecture" (MR/R015651/1) and the Wellcome Trust Senior Investigator Award (098411/Z/12/Z). We thank the Facility for Imaging by Light Microscopy (FILM) at Imperial College London, and acknowledge the assistance provided by Dr. Vincent Leonardo in producing the fluorescent cell line used to generate extracellular vesicles, Dr. Yunqing Zhu for advice in polymer experiments, and Dr. John Goertz for assistance with graphic design in Figures 1 and 3. Raw data are available online at https://doi.org/10.5281/zenodo.2578001. C.L. conceived the project and carried out the majority of experimental work; C.L. and L.O. performed the tissue engineering experiments; I.J.P. performed all Raman spectroscopy experiments; A.C.M. performed all mechanical characterization; Y.L. and L.O. assisted on the material modification and synthesis; C.W.W. assisted with extracellular vesicle production; J.P.K.A. and M.M.S. supervised the work; and C.L., J.P.K.A., and L.O. wrote the paper with contributions from all authors.

Conflict of Interest

The authors declare no conflict of interest.

Keywords

biomaterials, buoyancy, gradients, osteochondral, tissue engineering

Received: January 14, 2019
Revised: February 18, 2019
Published online: March 7, 2019

---

[1] H. H. Lu, S. Thomopoulos, *Annu. Rev. Biomed. Eng.* **2013**, *15*, 201.
[2] P. B. Messersmith, *Science* **2008**, *319*, 1767.
[3] F. Ulloa, J. Briscoe, *Cell Cycle* **2007**, *6*, 2640.
[4] P. Garrison, S. Yue, J. Hanson, J. Baron, J. C. Lui, *PLoS One* **2017**, *12*, e0176752.
[5] J. L. Christian, *Wiley Interdisp. Rev.: Dev. Biol.* **2012**, *1*, 3.
[6] V. Vogel, M. Sheetz, *Nat. Rev. Mol. Cell Biol.* **2006**, *7*, 265.
[7] H. L. Ashe, J. Briscoe, *Development* **2006**, *133*, 385.
[8] M. Singh, C. Berkland, M. S. Detamore, *Tissue Eng., Part B* **2008**, *14*, 341.
[9] J. Shi, L. Wang, F. Zhang, H. Li, L. Lei, L. Liu, Y. Chen, *ACS Appl. Mater. Interfaces* **2010**, *2*, 1025.
[10] X. Zhang, X. Gao, L. Jiang, J. Qin, *Langmuir* **2012**, *28*, 10026.
[11] L. G. Bracaglia, B. T. Smith, E. Watson, N. Arumugasaamy, A. G. Mikos, J. P. Fisher, *Acta Biomater.* **2017**, *56*, 3.
[12] K. A. Mosiewicz, L. Kolb, A. J. van der Vlies, M. M. Martino, P. S. Lienemann, J. A. Hubbell, M. Ehrbar, M. P. Lutolf, *Nat. Mater.* **2013**, *12*, 1072.
[13] C. Li, J. P. K. Armstrong, I. J. Pence, W. Kit-Anan, J. L. Puetzer, S. Correia Carreira, A. C. Moore, M. M. Stevens, *Biomaterials* **2018**, *176*, 24.
[14] J. S. Turner, *J. Fluid Mech.* **1966**, *26*, 779.
[15] A. Boyum, *Scand. J. Clin. Lab. Invest., Suppl.* **1968**, *97*, 77.
[16] R. J. Britten, R. B. Roberts, *Science* **1960**, *131*, 32.

[17] L. Bai, X. Ma, J. Liu, X. Sun, D. Zhao, D. G. Evans, *J. Am. Chem. Soc.* **2010**, *132*, 2333.
[18] V. Parameswaran, A. Shukla, *J. Mater. Sci.* **2000**, *35*, 21.
[19] J. T. Beals, M. S. Thompson, *J. Mater. Sci.* **1997**, *32*, 3595.
[20] A. Di Luca, C. Van Blitterswijk, L. Moroni, *Birth Defects Res., Part C* **2015**, *105*, 34.
[21] J. P. K. Armstrong, M. M. Stevens, *Adv. Drug Delivery Rev.* **2018**, *130*, 12.
[22] T. M. Allen, P. R. Cullis, *Adv. Drug Delivery Rev.* **2013**, *65*, 36.
[23] P. Ghosh, G. Han, M. De, C. K. Kim, V. M. Rotello, *Adv. Drug Delivery Rev.* **2008**, *60*, 1307.
[24] Y. I. Chung, K. M. Ahn, S. H. Jeon, S. Y. Lee, J. H. Lee, G. Tae, *J. Controlled Release* **2007**, *121*, 91.
[25] S. A. Abbah, J. Liu, R. W. Lam, J. C. Goh, H. K. Wong, *J. Controlled Release* **2012**, *162*, 364.
[26] W. C. Kett, R. I. Osmond, L. Moe, S. E. Skett, B. F. Kinnear, D. R. Coombe, *Biochim. Biophys. Acta, Gen. Subj.* **2003**, *1620*, 225.
[27] F. Las Heras, H. K. Gahunia, K. P. Pritzker, *Orthop. Clin. North Am.* **2012**, *43*, 155.
[28] D. Noel, D. Gazit, C. Bouquet, F. Apparailly, C. Bony, P. Plence, V. Millet, G. Turgeman, M. Perricaudet, J. Sany, C. Jorgensen, *Stem Cells* **2004**, *22*, 74.
[29] R. Ruppert, E. Hoffmann, W. Sebald, *Eur. J. Biochem.* **1996**, *237*, 295.
[30] J. Yang, Y. S. Zhang, K. Yue, A. Khademhosseini, *Acta Biomater.* **2017**, *57*, 1.
[31] B. Zhao, T. Katagiri, H. Toyoda, T. Takada, T. Yanai, T. Fukuda, U. I. Chung, T. Koike, K. Takaoka, R. Kamijo, *J. Biol. Chem.* **2006**, *281*, 23246.
[32] J. Hwang, E. M. Kyubwa, W. C. Bae, W. D. Bugbee, K. Masuda, R. L. Sah, *Cartilage* **2010**, *1*, 287.
[33] V. M. Mania, A. G. Kallivokas, C. Malavaki, A. P. Asimakopoulou, J. Kanakis, A. D. Theocharis, G. Klironomos, G. Gatzounis, A. Mouzaki, E. Panagiotopoulos, N. K. Karamanos, *IUBMB Life* **2009**, *61*, 447.
[34] E. H. Morrison, M. W. Ferguson, M. T. Bayliss, C. W. Archer, *J. Anat.* **1996**, *189*, 9.
[35] J. Sodek, B. Ganss, M. D. McKee, *Crit. Rev. Oral Biol. Med.* **2000**, *11*, 279.
[36] E. Butchert, T. R. Manley, *Spectrochim. Acta, Part A* **1978**, *34*, 781.
[37] H. Edwards, A. Johnson, E. E. Lawson, *Spectrochim. Acta, Part A* **1994**, *50*, 255.
[38] A. C. Moore, J. F. DeLucca, D. M. Elliott, D. L. Burris, *J. Tribol.* **2016**, *138*, 041405.

D. Reproduction Permissions

JOHN WILEY AND SONS LICENSE
TERMS AND CONDITIONS

Aug 21, 2019

This Agreement between Imperial College London -- Chunching Li ("You") and John Wiley and Sons ("John Wiley and Sons") consists of your license details and the terms and conditions provided by John Wiley and Sons and Copyright Clearance Center.

License Number	4653670130318
License date	Aug 21, 2019
Licensed Content Publisher	John Wiley and Sons
Licensed Content Publication	WILEY INTERDISCIPLINARY REVIEWS: DEVELOPMENTAL BIOLOGY
Licensed Content Title	Morphogen gradients in development: from form to function
Licensed Content Author	Jan L. Christian
Licensed Content Date	Nov 17, 2011
Licensed Content Volume	1
Licensed Content Issue	1
Licensed Content Pages	13
Type of use	Dissertation/Thesis
Requestor type	University/Academic
Format	Print and electronic
Portion	Figure/table
Number of figures/tables	6
Original Wiley figure/table number(s)	Figure 1, 3, 4, 5, 6, 7
Will you be translating?	No
Title of your thesis / dissertation	Force-based Engineering of Gradients
Expected completion date	Nov 2019
Expected size (number of pages)	200
Requestor Location	Imperial College London South Kensington Campus London, SW7 2AZ, UK United Kingdom Attn: Imperial College London
Publisher Tax ID	EU826007151
Total	0.00 USD
Terms and Conditions	

TERMS AND CONDITIONS

This copyrighted material is owned by or exclusively licensed to John Wiley & Sons, Inc. or one of its group companies (each a"Wiley Company") or handled on behalf of a society with which a Wiley Company has exclusive publishing rights in relation to a particular work (collectively "WILEY"). By clicking "accept" in connection with completing this licensing transaction, you agree that the following terms and conditions apply to this transaction (along with the billing and payment terms and conditions established by the Copyright Clearance Center Inc., ("CCC's Billing and Payment terms and conditions"), at the time that you opened your RightsLink account (these are available at any time at http://myaccount.copyright.com).

Terms and Conditions

- The materials you have requested permission to reproduce or reuse (the "Wiley Materials") are protected by copyright.

- You are hereby granted a personal, non-exclusive, non-sub licensable (on a stand-alone basis), non-transferable, worldwide, limited license to reproduce the Wiley Materials for the purpose specified in the licensing process. This license, **and any CONTENT (PDF or image file) purchased as part of your order,** is for a one-time use only and limited to any maximum distribution number specified in the license. The first instance of republication or reuse granted by this license must be completed within two years of the date of the grant of this license (although copies prepared before the end date may be distributed thereafter). The Wiley Materials shall not be used in any other manner or for any other purpose, beyond what is granted in the license. Permission is granted subject to an appropriate acknowledgement given to the author, title of the material/book/journal and the publisher. You shall also duplicate the copyright notice that appears in the Wiley publication in your use of the Wiley Material. Permission is also granted on the understanding that nowhere in the text is a previously published source acknowledged for all or part of this Wiley Material. Any third party content is expressly excluded from this permission.

- With respect to the Wiley Materials, all rights are reserved. Except as expressly granted by the terms of the license, no part of the Wiley Materials may be copied, modified, adapted (except for minor reformatting required by the new Publication), translated, reproduced, transferred or distributed, in any form or by any means, and no derivative works may be made based on the Wiley Materials without the prior permission of the respective copyright owner.**For STM Signatory Publishers clearing permission under the terms of the STM Permissions Guidelines only, the terms of the license are extended to include subsequent editions and for editions in other languages, provided such editions are for the work as a whole in situ and does not involve the separate exploitation of the permitted figures or extracts,** You may not alter, remove or suppress in any manner any copyright, trademark or other notices displayed by the Wiley Materials. You may not license, rent, sell, loan, lease, pledge, offer as security, transfer or assign the Wiley Materials on a stand-alone basis, or any of the rights granted to you hereunder to any other person.

- The Wiley Materials and all of the intellectual property rights therein shall at all times remain the exclusive property of John Wiley & Sons Inc, the Wiley Companies, or their respective licensors, and your interest therein is only that of having possession of and the right to reproduce the Wiley Materials pursuant to Section 2 herein during the continuance of this Agreement. You agree that you own no right, title or interest in or to the Wiley Materials or any of the intellectual property rights therein. You shall have no rights hereunder other than the license as provided for above in Section 2. No right, license or interest to any trademark, trade name, service mark or other branding ("Marks") of WILEY or its licensors is granted hereunder, and you agree that you shall not assert any such right, license or interest with respect thereto

- NEITHER WILEY NOR ITS LICENSORS MAKES ANY WARRANTY OR REPRESENTATION OF ANY KIND TO YOU OR ANY THIRD PARTY, EXPRESS, IMPLIED OR STATUTORY, WITH RESPECT TO THE MATERIALS OR THE ACCURACY OF ANY INFORMATION CONTAINED IN THE MATERIALS, INCLUDING, WITHOUT LIMITATION, ANY IMPLIED WARRANTY OF MERCHANTABILITY, ACCURACY, SATISFACTORY QUALITY, FITNESS FOR A PARTICULAR PURPOSE, USABILITY, INTEGRATION OR NON-INFRINGEMENT AND ALL SUCH WARRANTIES ARE HEREBY EXCLUDED BY WILEY AND ITS LICENSORS AND WAIVED BY YOU.

- WILEY shall have the right to terminate this Agreement immediately upon breach of this Agreement by you.

- You shall indemnify, defend and hold harmless WILEY, its Licensors and their respective directors, officers, agents and employees, from and against any actual or threatened claims, demands, causes of action or proceedings arising from any breach of this Agreement by you.

- IN NO EVENT SHALL WILEY OR ITS LICENSORS BE LIABLE TO YOU OR ANY OTHER PARTY OR ANY OTHER PERSON OR ENTITY FOR ANY SPECIAL, CONSEQUENTIAL, INCIDENTAL, INDIRECT, EXEMPLARY OR PUNITIVE DAMAGES, HOWEVER CAUSED, ARISING OUT OF OR IN CONNECTION WITH THE DOWNLOADING, PROVISIONING, VIEWING OR USE OF THE MATERIALS REGARDLESS OF THE FORM OF ACTION, WHETHER FOR BREACH OF CONTRACT, BREACH OF WARRANTY, TORT, NEGLIGENCE, INFRINGEMENT OR OTHERWISE (INCLUDING, WITHOUT LIMITATION, DAMAGES BASED ON LOSS OF PROFITS, DATA, FILES, USE, BUSINESS OPPORTUNITY OR CLAIMS OF THIRD PARTIES), AND WHETHER OR NOT THE PARTY HAS BEEN ADVISED OF THE POSSIBILITY OF SUCH DAMAGES. THIS LIMITATION SHALL APPLY NOTWITHSTANDING ANY FAILURE OF ESSENTIAL PURPOSE OF ANY LIMITED REMEDY PROVIDED HEREIN.

- Should any provision of this Agreement be held by a court of competent jurisdiction to be illegal, invalid, or unenforceable, that provision shall be deemed amended to achieve as nearly as possible the same economic effect as the original provision, and the legality, validity and enforceability of the remaining provisions of this Agreement shall not be affected or impaired thereby.

- The failure of either party to enforce any term or condition of this Agreement shall not constitute a waiver of either party's right to enforce each and every term and condition of this Agreement. No breach under this agreement shall be deemed waived or excused by either party unless such waiver or consent is in writing signed by the party granting such waiver or consent. The waiver by or consent of a party to a breach of any provision of this Agreement shall not operate or be construed as a waiver of or consent to any other or subsequent breach by such other party.

- This Agreement may not be assigned (including by operation of law or otherwise) by you without WILEY's prior written consent.

- Any fee required for this permission shall be non-refundable after thirty (30) days from receipt by the CCC.

- These terms and conditions together with CCC's Billing and Payment terms and conditions (which are incorporated herein) form the entire agreement between you and WILEY concerning this licensing transaction and (in the absence of fraud) supersedes all prior agreements and representations of the parties, oral or written. This Agreement may not be amended except in writing signed by both parties. This Agreement shall be binding upon and inure to the benefit of the parties' successors, legal representatives, and authorized assigns.

- In the event of any conflict between your obligations established by these terms and conditions and those established by CCC's Billing and Payment terms and conditions, these terms and conditions shall prevail.

- WILEY expressly reserves all rights not specifically granted in the combination of (i) the license details provided by you and accepted in the course of this licensing transaction, (ii) these terms and conditions and (iii) CCC's Billing and Payment terms and conditions.

- This Agreement will be void if the Type of Use, Format, Circulation, or Requestor Type was misrepresented during the licensing process.

- This Agreement shall be governed by and construed in accordance with the laws of the State of New York, USA, without regards to such state's conflict of law rules. Any legal action, suit or proceeding arising out of or relating to these Terms and Conditions or the breach thereof shall be instituted in a court of competent jurisdiction in New York County in the State of New York in the United States of America and each party hereby consents and submits to the personal jurisdiction of such court, waives any objection to venue in such court and consents to service of process by registered or certified mail, return receipt requested, at the last known address of such party.

WILEY OPEN ACCESS TERMS AND CONDITIONS

Wiley Publishes Open Access Articles in fully Open Access Journals and in Subscription journals offering Online Open. Although most of the fully Open Access journals publish open access articles under the terms of the Creative Commons Attribution (CC BY) License only, the subscription journals and a few of the Open Access Journals offer a choice of Creative Commons Licenses. The license type is clearly identified on the article.

The Creative Commons Attribution License

The Creative Commons Attribution License (CC-BY) allows users to copy, distribute and transmit an article, adapt the article and make commercial use of the article. The CC-BY license permits commercial and non-

Creative Commons Attribution Non-Commercial License

The Creative Commons Attribution Non-Commercial (CC-BY-NC)License permits use, distribution and reproduction in any medium, provided the original work is properly cited and is not used for commercial purposes.(see below)

Creative Commons Attribution-Non-Commercial-NoDerivs License

The Creative Commons Attribution Non-Commercial-NoDerivs License (CC-BY-NC-ND) permits use, distribution and reproduction in any medium, provided the original work is properly cited, is not used for commercial purposes and no modifications or adaptations are made. (see below)

Use by commercial "for-profit" organizations

Use of Wiley Open Access articles for commercial, promotional, or marketing purposes requires further explicit permission from Wiley and will be subject to a fee.

Further details can be found on Wiley Online Library

http://olabout.wiley.com/WileyCDA/Section/id-410895.html

Other Terms and Conditions:

v1.10 Last updated September 2015

Questions? customercare@copyright.com or +1-855-239-3415 (toll free in the US) or +1-978-646-2777.

SPRINGER NATURE LICENSE TERMS AND CONDITIONS

Aug 21, 2019

This Agreement between Imperial College London -- Chunching Li ("You") and Springer Nature ("Springer Nature") consists of your license details and the terms and conditions provided by Springer Nature and Copyright Clearance Center.

License Number	4653670477272
License date	Aug 21, 2019
Licensed Content Publisher	Springer Nature
Licensed Content Publication	Laboratory Investigation
Licensed Content Title	Wnt signaling in cartilage development and diseases: lessons from animal studies
Licensed Content Author	Yu Usami, Aruni T Gunawardena, Masahiro Iwamoto, Motomi Enomoto-Iwamoto
Licensed Content Date	Dec 7, 2015
Licensed Content Volume	96
Licensed Content Issue	2
Type of Use	Thesis/Dissertation
Requestor type	academic/university or research institute
Format	print and electronic
Portion	figures/tables/illustrations
Number of figures/tables/illustrations	2
High-res required	no
Will you be translating?	no
Circulation/distribution	>50,000
Author of this Springer Nature content	no
Title	Force-based Engineering of Gradients
Institution name	n/a
Expected presentation date	Nov 2019
Portions	Figure 1, 2
Requestor Location	Imperial College London South Kensington Campus London, SW7 2AZ, UK United Kingdom Attn: Imperial College London
Total	0.00 USD
Terms and Conditions	

Springer Nature Customer Service Centre GmbH Terms and Conditions

This agreement sets out the terms and conditions of the licence (the **Licence**) between you and **Springer Nature Customer Service Centre GmbH** (the **Licensor**). By clicking 'accept' and completing the transaction for the material (**Licensed Material**), you also confirm your acceptance of these terms and conditions.

1. Grant of License

1. 1. The Licensor grants you a personal, non-exclusive, non-transferable, world-wide licence to reproduce the Licensed Material for the purpose specified in your order only. Licences are granted for the specific use requested in the order and for no other use, subject to the conditions below.

1. 2. The Licensor warrants that it has, to the best of its knowledge, the rights to license reuse of the Licensed Material. However, you should ensure that the material you are requesting is original to the Licensor and does not carry the copyright of another entity (as credited in the published version).

1. 3. If the credit line on any part of the material you have requested indicates that it was reprinted or adapted with permission from another source, then you should also seek permission from that source to reuse the material.

2. Scope of Licence

2. 1. You may only use the Licensed Content in the manner and to the extent permitted by these Ts&Cs and any applicable laws.

2. 2. A separate licence may be required for any additional use of the Licensed Material, e.g. where a licence has been purchased for print only use, separate permission must be obtained for electronic re-use. Similarly, a licence is only valid in the language selected and does not apply for editions in other languages unless additional translation rights have been granted separately in the licence. Any content owned by third parties are expressly excluded from the licence.

2. 3. Similarly, rights for additional components such as custom editions and derivatives require additional permission and may be subject to an additional fee. Please apply to Journalpermissions@springernature.com/bookpermissions@springernature.com for these rights.

2. 4. Where permission has been granted **free of charge** for material in print, permission may also be granted for any electronic version of that work, provided that the material is incidental to your work as a whole and that the electronic version is essentially equivalent to, or substitutes for, the print version.

2. 5. An alternative scope of licence may apply to signatories of the STM Permissions Guidelines, as amended from time to time.

3. Duration of Licence

3. 1. A licence for is valid from the date of purchase ('Licence Date') at the end of the relevant period in the below table:

Scope of Licence	Duration of Licence
Post on a website	12 months
Presentations	12 months
Books and journals	Lifetime of the edition in the language purchased

4. Acknowledgement

4. 1. The Licensor's permission must be acknowledged next to the Licenced Material in print. In electronic form, this acknowledgement must be visible at the same time as the figures/tables/illustrations or abstract, and must be hyperlinked to the journal/book's homepage. Our required acknowledgement format is in the Appendix below.

5. Restrictions on use

5. 1. Use of the Licensed Material may be permitted for incidental promotional use and minor editing privileges e.g. minor adaptations of single figures, changes of format, colour and/or style where the adaptation is credited as set out in Appendix 1 below. Any other changes including but not limited to, cropping, adapting, omitting material that affect the meaning, intention or moral rights of the author are strictly prohibited.

5. 2. You must not use any Licensed Material as part of any design or trademark.

5. 3. Licensed Material may be used in Open Access Publications (OAP) before publication by Springer Nature, but any Licensed Material must be removed from OAP sites prior to final publication.

6. Ownership of Rights

6. 1. Licensed Material remains the property of either Licensor or the relevant third party and any rights not explicitly granted herein are expressly reserved.

7. Warranty

IN NO EVENT SHALL LICENSOR BE LIABLE TO YOU OR ANY OTHER PARTY OR ANY OTHER PERSON OR FOR ANY SPECIAL, CONSEQUENTIAL, INCIDENTAL OR INDIRECT DAMAGES, HOWEVER CAUSED, ARISING OUT OF OR IN CONNECTION WITH THE DOWNLOADING, VIEWING OR USE OF THE MATERIALS REGARDLESS OF THE FORM OF ACTION, WHETHER FOR BREACH OF CONTRACT, BREACH OF WARRANTY, TORT, NEGLIGENCE, INFRINGEMENT OR OTHERWISE (INCLUDING, WITHOUT LIMITATION, DAMAGES BASED ON LOSS OF PROFITS, DATA, FILES, USE, BUSINESS OPPORTUNITY OR CLAIMS OF THIRD PARTIES), AND
WHETHER OR NOT THE PARTY HAS BEEN ADVISED OF THE POSSIBILITY OF SUCH DAMAGES. THIS LIMITATION SHALL APPLY NOTWITHSTANDING ANY FAILURE OF ESSENTIAL PURPOSE OF ANY LIMITED REMEDY PROVIDED HEREIN.

8. Limitations

8. 1. ***BOOKS ONLY:***Where **'reuse in a dissertation/thesis'** has been selected the following terms apply: Print rights of the final author's accepted manuscript (for clarity, NOT the published version) for up to 100 copies, electronic rights for use only on a personal website or institutional repository as defined by the Sherpa guideline (www.sherpa.ac.uk/romeo/).

9. Termination and Cancellation

9. 1. Licences will expire after the period shown in Clause 3 (above).

9. 2. Licensee reserves the right to terminate the Licence in the event that payment is not received in full or if there has been a breach of this agreement by you.

Appendix 1 — Acknowledgements:

For Journal Content:
Reprinted by permission from [**the Licensor**]: [**Journal Publisher** (e.g. Nature/Springer/Palgrave)] [**JOURNAL NAME**] [**REFERENCE CITATION** (Article name, Author(s) Name), [**COPYRIGHT**] (year of publication)

For **Advance Online Publication papers:**
Reprinted by permission from [**the Licensor**]: [**Journal Publisher** (e.g. Nature/Springer/Palgrave)] [**JOURNAL NAME**] [**REFERENCE CITATION** (Article name, Author(s) Name), [**COPYRIGHT**] (year of publication), advance online publication, day month year (doi: 10.1038/sj.[JOURNAL ACRONYM].)

For Adaptations/Translations:
Adapted/Translated by permission from [**the Licensor**]: [**Journal Publisher** (e.g. Nature/Springer/Palgrave)] [**JOURNAL NAME**] [**REFERENCE CITATION** (Article name, Author(s) Name), [**COPYRIGHT**] (year of publication)

Note: For any republication from the British Journal of Cancer, the following credit line style applies:

Reprinted/adapted/translated by permission from [**the Licensor**]: on behalf of Cancer Research UK: : [**Journal Publisher** (e.g. Nature/Springer/Palgrave)] [**JOURNAL NAME**] [**REFERENCE CITATION** (Article name, Author(s) Name), [**COPYRIGHT]** (year of publication)

For **Advance Online Publication** papers:
Reprinted by permission from The [**the Licensor**]: on behalf of Cancer Research UK: [**Journal Publisher** (e.g. Nature/Springer/Palgrave)] [**JOURNAL NAME**] [**REFERENCE CITATION** (Article name, Author(s) Name), [**COPYRIGHT**] (year of publication), advance online publication, day month year (doi: 10.1038/sj. [JOURNAL ACRONYM])

For Book content:
Reprinted/adapted by permission from [**the Licensor**]: [**Book Publisher** (e.g. Palgrave Macmillan, Springer etc) [**Book Title**] by [**Book author**(s)] [**COPYRIGHT**] (year of publication)

Other Conditions:

Version 1.2

Questions? customercare@copyright.com or +1-855-239-3415 (toll free in the US) or +1-978-646-2777.

ELSEVIER LICENSE
TERMS AND CONDITIONS

Aug 21, 2019

This Agreement between Imperial College London -- Chunching Li ("You") and Elsevier ("Elsevier") consists of your license details and the terms and conditions provided by Elsevier and Copyright Clearance Center.

License Number	4653670665270
License date	Aug 21, 2019
Licensed Content Publisher	Elsevier
Licensed Content Publication	Biochimica et Biophysica Acta (BBA) - General Subjects
Licensed Content Title	Cartilage tissue engineering: Molecular control of chondrocyte differentiation for proper cartilage matrix reconstruction
Licensed Content Author	Magali Demoor,David Ollitrault,Tangni Gomez-Leduc,Mouloud Bouyoucef,Magalie Hervieu,Hugo Fabre,Jérôme Lafont,Jean-Marie Denoix,Fabrice Audigié,Frédéric Mallein-Gerin,Florence Legendre,Philippe Galera
Licensed Content Date	Aug 1, 2014
Licensed Content Volume	1840
Licensed Content Issue	8
Licensed Content Pages	27
Start Page	2414
End Page	2440
Type of Use	reuse in a thesis/dissertation
Intended publisher of new work	other
Portion	figures/tables/illustrations
Number of figures/tables/illustrations	1
Format	both print and electronic
Are you the author of this Elsevier article?	No
Will you be translating?	No
Original figure numbers	Figure 3
Title of your thesis/dissertation	Force-based Engineering of Gradients
Expected completion date	Nov 2019
Estimated size (number of pages)	200
Requestor Location	Imperial College London South Kensington Campus London, SW7 2AZ, UK United Kingdom Attn: Imperial College London
Publisher Tax ID	GB 494 6272 12
Total	0.00 USD

Terms and Conditions

INTRODUCTION

1. The publisher for this copyrighted material is Elsevier. By clicking "accept" in connection with completing this licensing transaction, you agree that the following terms and conditions apply to this transaction (along with the Billing and Payment terms and conditions established by Copyright Clearance Center, Inc. ("CCC"), at the time that you opened your Rightslink account and that are available at any time at http://myaccount.copyright.com).

GENERAL TERMS

2. Elsevier hereby grants you permission to reproduce the aforementioned material subject to the terms and conditions indicated.
3. Acknowledgement: If any part of the material to be used (for example, figures) has appeared in our publication with credit or acknowledgement to another source, permission must also be sought from that source. If such permission is not obtained then that material may not be included in your publication/copies. Suitable acknowledgement to the source must be made, either as a footnote or in a reference list at the end of your publication, as follows:
"Reprinted from Publication title, Vol /edition number, Author(s), Title of article / title of chapter, Pages No., Copyright (Year), with permission from Elsevier [OR APPLICABLE SOCIETY COPYRIGHT OWNER]." Also Lancet special credit - "Reprinted from The Lancet, Vol. number, Author(s), Title of article, Pages No., Copyright (Year), with permission from Elsevier."
4. Reproduction of this material is confined to the purpose and/or media for which permission is hereby given.
5. Altering/Modifying Material: Not Permitted. However figures and illustrations may be altered/adapted minimally to serve your work. Any other abbreviations, additions, deletions and/or any other alterations shall be made only with prior written authorization of Elsevier Ltd. (Please contact Elsevier at permissions@elsevier.com). No modifications can be made to any Lancet figures/tables and they must be reproduced in full.
6. If the permission fee for the requested use of our material is waived in this instance, please be advised that your future requests for Elsevier materials may attract a fee.
7. Reservation of Rights: Publisher reserves all rights not specifically granted in the combination of (i) the license details provided by you and accepted in the course of this licensing transaction, (ii) these terms and conditions and (iii) CCC's Billing and Payment terms and conditions.
8. License Contingent Upon Payment: While you may exercise the rights licensed immediately upon issuance of the license at the end of the licensing process for the transaction, provided that you have disclosed complete and accurate details of your proposed use, no license is finally effective unless and until full payment is received from you (either by publisher or by CCC) as provided in CCC's Billing and Payment terms and conditions. If full payment is not received on a timely basis, then any license preliminarily granted shall be deemed automatically revoked and shall be void as if never granted. Further, in the event that you breach any of these terms and conditions or any of CCC's Billing and Payment terms and conditions, the license is automatically revoked and shall be void as if never granted. Use of materials as described in a revoked license, as well as any use of the materials beyond the scope of an unrevoked license, may constitute copyright infringement and publisher reserves the right to take any and all action to protect its copyright in the materials.
9. Warranties: Publisher makes no representations or warranties with respect to the licensed material.
10. Indemnity: You hereby indemnify and agree to hold harmless publisher and CCC, and their respective officers, directors, employees and agents, from and against any and all claims arising out of your use of the licensed material other than as specifically authorized pursuant to this license.
11. No Transfer of License: This license is personal to you and may not be sublicensed, assigned, or transferred by you to any other person without publisher's written permission.
12. No Amendment Except in Writing: This license may not be amended except in a writing signed by both parties (or, in the case of publisher, by CCC on publisher's behalf).

13. Objection to Contrary Terms: Publisher hereby objects to any terms contained in any purchase order, acknowledgment, check endorsement or other writing prepared by you, which terms are inconsistent with these terms and conditions or CCC's Billing and Payment terms and conditions. These terms and conditions, together with CCC's Billing and Payment terms and conditions (which are incorporated herein), comprise the entire agreement between you and publisher (and CCC) concerning this licensing transaction. In the event of any conflict between your obligations established by these terms and conditions and those established by CCC's Billing and Payment terms and conditions, these terms and conditions shall control.
14. Revocation: Elsevier or Copyright Clearance Center may deny the permissions described in this License at their sole discretion, for any reason or no reason, with a full refund payable to you. Notice of such denial will be made using the contact information provided by you. Failure to receive such notice will not alter or invalidate the denial. In no event will Elsevier or Copyright Clearance Center be responsible or liable for any costs, expenses or damage incurred by you as a result of a denial of your permission request, other than a refund of the amount(s) paid by you to Elsevier and/or Copyright Clearance Center for denied permissions.

LIMITED LICENSE

The following terms and conditions apply only to specific license types:
15. **Translation**: This permission is granted for non-exclusive world **English** rights only unless your license was granted for translation rights. If you licensed translation rights you may only translate this content into the languages you requested. A professional translator must perform all translations and reproduce the content word for word preserving the integrity of the article.
16. **Posting licensed content on any Website**: The following terms and conditions apply as follows: Licensing material from an Elsevier journal: All content posted to the web site must maintain the copyright information line on the bottom of each image; A hyper-text must be included to the Homepage of the journal from which you are licensing at http://www.sciencedirect.com/science/journal/xxxxx or the Elsevier homepage for books at http://www.elsevier.com; Central Storage: This license does not include permission for a scanned version of the material to be stored in a central repository such as that provided by Heron/XanEdu.
Licensing material from an Elsevier book: A hyper-text link must be included to the Elsevier homepage at http://www.elsevier.com . All content posted to the web site must maintain the copyright information line on the bottom of each image.

Posting licensed content on Electronic reserve: In addition to the above the following clauses are applicable: The web site must be password-protected and made available only to bona fide students registered on a relevant course. This permission is granted for 1 year only. You may obtain a new license for future website posting.
17. **For journal authors:** the following clauses are applicable in addition to the above:
Preprints:
A preprint is an author's own write-up of research results and analysis, it has not been peer-reviewed, nor has it had any other value added to it by a publisher (such as formatting, copyright, technical enhancement etc.).
Authors can share their preprints anywhere at any time. Preprints should not be added to or enhanced in any way in order to appear more like, or to substitute for, the final versions of articles however authors can update their preprints on arXiv or RePEc with their Accepted Author Manuscript (see below).
If accepted for publication, we encourage authors to link from the preprint to their formal publication via its DOI. Millions of researchers have access to the formal publications on ScienceDirect, and so links will help users to find, access, cite and use the best available version. Please note that Cell Press, The Lancet and some society-owned have different preprint policies. Information on these policies is available on the journal homepage.
Accepted Author Manuscripts: An accepted author manuscript is the manuscript of an article that has been accepted for publication and which typically includes author-incorporated changes suggested during submission, peer review and editor-author communications.

Authors can share their accepted author manuscript:

- immediately
  - via their non-commercial person homepage or blog
  - by updating a preprint in arXiv or RePEc with the accepted manuscript
  - via their research institute or institutional repository for internal institutional uses or as part of an invitation-only research collaboration work-group
  - directly by providing copies to their students or to research collaborators for their personal use
  - for private scholarly sharing as part of an invitation-only work group on commercial sites with which Elsevier has an agreement
- After the embargo period
  - via non-commercial hosting platforms such as their institutional repository
  - via commercial sites with which Elsevier has an agreement

In all cases accepted manuscripts should:

- link to the formal publication via its DOI
- bear a CC-BY-NC-ND license - this is easy to do
- if aggregated with other manuscripts, for example in a repository or other site, be shared in alignment with our hosting policy not be added to or enhanced in any way to appear more like, or to substitute for, the published journal article.

Published journal article (JPA): A published journal article (PJA) is the definitive final record of published research that appears or will appear in the journal and embodies all value-adding publishing activities including peer review co-ordination, copy-editing, formatting, (if relevant) pagination and online enrichment.
Policies for sharing publishing journal articles differ for subscription and gold open access articles:
Subscription Articles: If you are an author, please share a link to your article rather than the full-text. Millions of researchers have access to the formal publications on ScienceDirect, and so links will help your users to find, access, cite, and use the best available version.
Theses and dissertations which contain embedded PJAs as part of the formal submission can be posted publicly by the awarding institution with DOI links back to the formal publications on ScienceDirect.
If you are affiliated with a library that subscribes to ScienceDirect you have additional private sharing rights for others' research accessed under that agreement. This includes use for classroom teaching and internal training at the institution (including use in course packs and courseware programs), and inclusion of the article for grant funding purposes.
Gold Open Access Articles: May be shared according to the author-selected end-user license and should contain a CrossMark logo, the end user license, and a DOI link to the formal publication on ScienceDirect.
Please refer to Elsevier's posting policy for further information.
18. **For book authors** the following clauses are applicable in addition to the above: Authors are permitted to place a brief summary of their work online only. You are not allowed to download and post the published electronic version of your chapter, nor may you scan the printed edition to create an electronic version. **Posting to a repository:** Authors are permitted to post a summary of their chapter only in their institution's repository.
19. **Thesis/Dissertation**: If your license is for use in a thesis/dissertation your thesis may be submitted to your institution in either print or electronic form. Should your thesis be published commercially, please reapply for permission. These requirements include permission for the Library and Archives of Canada to supply single copies, on demand, of the complete thesis and include permission for Proquest/UMI to supply single copies, on demand, of the complete thesis. Should your thesis be published commercially, please reapply for permission. Theses and dissertations which contain embedded PJAs as part of the formal submission can be posted publicly by the awarding institution with DOI links back to the formal publications on ScienceDirect.

Elsevier Open Access Terms and Conditions

You can publish open access with Elsevier in hundreds of open access journals or in nearly 2000 established subscription journals that support open access publishing. Permitted third party re-use of these open access articles is defined by the author's choice of Creative Commons user license. See our open access license policy for more information.

Terms & Conditions applicable to all Open Access articles published with Elsevier:

Any reuse of the article must not represent the author as endorsing the adaptation of the article nor should the article be modified in such a way as to damage the author's honour or reputation. If any changes have been made, such changes must be clearly indicated.

The author(s) must be appropriately credited and we ask that you include the end user license and a DOI link to the formal publication on ScienceDirect.

If any part of the material to be used (for example, figures) has appeared in our publication with credit or acknowledgement to another source it is the responsibility of the user to ensure their reuse complies with the terms and conditions determined by the rights holder.

Additional Terms & Conditions applicable to each Creative Commons user license:

CC BY: The CC-BY license allows users to copy, to create extracts, abstracts and new works from the Article, to alter and revise the Article and to make commercial use of the Article (including reuse and/or resale of the Article by commercial entities), provided the user gives appropriate credit (with a link to the formal publication through the relevant DOI), provides a link to the license, indicates if changes were made and the licensor is not represented as endorsing the use made of the work. The full details of the license are available at http://creativecommons.org/licenses/by/4.0.

CC BY NC SA: The CC BY-NC-SA license allows users to copy, to create extracts, abstracts and new works from the Article, to alter and revise the Article, provided this is not done for commercial purposes, and that the user gives appropriate credit (with a link to the formal publication through the relevant DOI), provides a link to the license, indicates if changes were made and the licensor is not represented as endorsing the use made of the work. Further, any new works must be made available on the same conditions. The full details of the license are available at http://creativecommons.org/licenses/by-nc-sa/4.0.

CC BY NC ND: The CC BY-NC-ND license allows users to copy and distribute the Article, provided this is not done for commercial purposes and further does not permit distribution of the Article if it is changed or edited in any way, and provided the user gives appropriate credit (with a link to the formal publication through the relevant DOI), provides a link to the license, and that the licensor is not represented as endorsing the use made of the work. The full details of the license are available at http://creativecommons.org/licenses/by-nc-nd/4.0. Any commercial reuse of Open Access articles published with a CC BY NC SA or CC BY NC ND license requires permission from Elsevier and will be subject to a fee.

Commercial reuse includes:

- Associating advertising with the full text of the Article
- Charging fees for document delivery or access
- Article aggregation
- Systematic distribution via e-mail lists or share buttons

Posting or linking by commercial companies for use by customers of those companies.

20. **Other Conditions**:

v1.9

Questions? customercare@copyright.com or +1-855-239-3415 (toll free in the US) or +1-978-646-2777.

JOHN WILEY AND SONS LICENSE
TERMS AND CONDITIONS

Aug 21, 2019

This Agreement between Imperial College London -- Chunching Li ("You") and John Wiley and Sons ("John Wiley and Sons") consists of your license details and the terms and conditions provided by John Wiley and Sons and Copyright Clearance Center.

License Number	4653670797321
License date	Aug 21, 2019
Licensed Content Publisher	John Wiley and Sons
Licensed Content Publication	Birth Defects Research Part C: Embryo Today: Reviews
Licensed Content Title	The osteochondral interface as a gradient tissue: From development to the fabrication of gradient scaffolds for regenerative medicine
Licensed Content Author	Lorenzo Moroni, Clemens Van Blitterswijk, Andrea Di Luca
Licensed Content Date	Mar 16, 2015
Licensed Content Volume	105
Licensed Content Issue	1
Licensed Content Pages	19
Type of use	Dissertation/Thesis
Requestor type	University/Academic
Format	Print and electronic
Portion	Figure/table
Number of figures/tables	1
Original Wiley figure/table number(s)	Figure 2
Will you be translating?	No
Title of your thesis / dissertation	Force-based Engineering of Gradients
Expected completion date	Nov 2019
Expected size (number of pages)	200
Requestor Location	Imperial College London South Kensington Campus London, SW7 2AZ, UK United Kingdom Attn: Imperial College London
Publisher Tax ID	EU826007151
Total	0.00 USD
Terms and Conditions	

TERMS AND CONDITIONS

This copyrighted material is owned by or exclusively licensed to John Wiley & Sons, Inc. or one of its group companies (each a"Wiley Company") or handled on behalf of a society with which a Wiley Company has exclusive publishing rights in relation to a particular work (collectively "WILEY"). By clicking "accept" in connection with completing this licensing transaction, you agree that the following terms and conditions apply to this transaction (along with the billing and payment terms and conditions established by the Copyright

Clearance Center Inc., ("CCC's Billing and Payment terms and conditions"), at the time that you opened your RightsLink account (these are available at any time at http://myaccount.copyright.com).

Terms and Conditions

- The materials you have requested permission to reproduce or reuse (the "Wiley Materials") are protected by copyright.

- You are hereby granted a personal, non-exclusive, non-sub licensable (on a stand-alone basis), non-transferable, worldwide, limited license to reproduce the Wiley Materials for the purpose specified in the licensing process. This license, **and any CONTENT (PDF or image file) purchased as part of your order,** is for a one-time use only and limited to any maximum distribution number specified in the license. The first instance of republication or reuse granted by this license must be completed within two years of the date of the grant of this license (although copies prepared before the end date may be distributed thereafter). The Wiley Materials shall not be used in any other manner or for any other purpose, beyond what is granted in the license. Permission is granted subject to an appropriate acknowledgement given to the author, title of the material/book/journal and the publisher. You shall also duplicate the copyright notice that appears in the Wiley publication in your use of the Wiley Material. Permission is also granted on the understanding that nowhere in the text is a previously published source acknowledged for all or part of this Wiley Material. Any third party content is expressly excluded from this permission.

- With respect to the Wiley Materials, all rights are reserved. Except as expressly granted by the terms of the license, no part of the Wiley Materials may be copied, modified, adapted (except for minor reformatting required by the new Publication), translated, reproduced, transferred or distributed, in any form or by any means, and no derivative works may be made based on the Wiley Materials without the prior permission of the respective copyright owner.**For STM Signatory Publishers clearing permission under the terms of the STM Permissions Guidelines only, the terms of the license are extended to include subsequent editions and for editions in other languages, provided such editions are for the work as a whole in situ and does not involve the separate exploitation of the permitted figures or extracts,** You may not alter, remove or suppress in any manner any copyright, trademark or other notices displayed by the Wiley Materials. You may not license, rent, sell, loan, lease, pledge, offer as security, transfer or assign the Wiley Materials on a stand-alone basis, or any of the rights granted to you hereunder to any other person.

- The Wiley Materials and all of the intellectual property rights therein shall at all times remain the exclusive property of John Wiley & Sons Inc, the Wiley Companies, or their respective licensors, and your interest therein is only that of having possession of and the right to reproduce the Wiley Materials pursuant to Section 2 herein during the continuance of this Agreement. You agree that you own no right, title or interest in or to the Wiley Materials or any of the intellectual property rights therein. You shall have no rights hereunder other than the license as provided for above in Section 2. No right, license or interest to any trademark, trade name, service mark or other branding ("Marks") of WILEY or its licensors is granted hereunder, and you agree that you shall not assert any such right, license or interest with respect thereto

- NEITHER WILEY NOR ITS LICENSORS MAKES ANY WARRANTY OR REPRESENTATION OF ANY KIND TO YOU OR ANY THIRD PARTY, EXPRESS, IMPLIED OR STATUTORY, WITH RESPECT TO THE MATERIALS OR THE ACCURACY OF ANY INFORMATION CONTAINED IN THE MATERIALS, INCLUDING, WITHOUT LIMITATION, ANY IMPLIED WARRANTY OF MERCHANTABILITY, ACCURACY, SATISFACTORY QUALITY, FITNESS FOR A PARTICULAR PURPOSE, USABILITY,

INTEGRATION OR NON-INFRINGEMENT AND ALL SUCH WARRANTIES ARE HEREBY EXCLUDED BY WILEY AND ITS LICENSORS AND WAIVED BY YOU.

- WILEY shall have the right to terminate this Agreement immediately upon breach of this Agreement by you.

- You shall indemnify, defend and hold harmless WILEY, its Licensors and their respective directors, officers, agents and employees, from and against any actual or threatened claims, demands, causes of action or proceedings arising from any breach of this Agreement by you.

- IN NO EVENT SHALL WILEY OR ITS LICENSORS BE LIABLE TO YOU OR ANY OTHER PARTY OR ANY OTHER PERSON OR ENTITY FOR ANY SPECIAL, CONSEQUENTIAL, INCIDENTAL, INDIRECT, EXEMPLARY OR PUNITIVE DAMAGES, HOWEVER CAUSED, ARISING OUT OF OR IN CONNECTION WITH THE DOWNLOADING, PROVISIONING, VIEWING OR USE OF THE MATERIALS REGARDLESS OF THE FORM OF ACTION, WHETHER FOR BREACH OF CONTRACT, BREACH OF WARRANTY, TORT, NEGLIGENCE, INFRINGEMENT OR OTHERWISE (INCLUDING, WITHOUT LIMITATION, DAMAGES BASED ON LOSS OF PROFITS, DATA, FILES, USE, BUSINESS OPPORTUNITY OR CLAIMS OF THIRD PARTIES), AND WHETHER OR NOT THE PARTY HAS BEEN ADVISED OF THE POSSIBILITY OF SUCH DAMAGES. THIS LIMITATION SHALL APPLY NOTWITHSTANDING ANY FAILURE OF ESSENTIAL PURPOSE OF ANY LIMITED REMEDY PROVIDED HEREIN.

- Should any provision of this Agreement be held by a court of competent jurisdiction to be illegal, invalid, or unenforceable, that provision shall be deemed amended to achieve as nearly as possible the same economic effect as the original provision, and the legality, validity and enforceability of the remaining provisions of this Agreement shall not be affected or impaired thereby.

- The failure of either party to enforce any term or condition of this Agreement shall not constitute a waiver of either party's right to enforce each and every term and condition of this Agreement. No breach under this agreement shall be deemed waived or excused by either party unless such waiver or consent is in writing signed by the party granting such waiver or consent. The waiver by or consent of a party to a breach of any provision of this Agreement shall not operate or be construed as a waiver of or consent to any other or subsequent breach by such other party.

- This Agreement may not be assigned (including by operation of law or otherwise) by you without WILEY's prior written consent.

- Any fee required for this permission shall be non-refundable after thirty (30) days from receipt by the CCC.

- These terms and conditions together with CCC's Billing and Payment terms and conditions (which are incorporated herein) form the entire agreement between you and WILEY concerning this licensing transaction and (in the absence of fraud) supersedes all prior agreements and representations of the parties, oral or written. This Agreement may not be amended except in writing signed by both parties. This Agreement shall be binding upon and inure to the benefit of the parties' successors, legal representatives, and authorized assigns.

- In the event of any conflict between your obligations established by these terms and conditions and those established by CCC's Billing and Payment terms and conditions, these terms and conditions shall prevail.

- WILEY expressly reserves all rights not specifically granted in the combination of (i) the license details provided by you and accepted in the course of this licensing transaction, (ii) these terms and conditions and (iii) CCC's Billing and Payment terms and conditions.
- This Agreement will be void if the Type of Use, Format, Circulation, or Requestor Type was misrepresented during the licensing process.
- This Agreement shall be governed by and construed in accordance with the laws of the State of New York, USA, without regards to such state's conflict of law rules. Any legal action, suit or proceeding arising out of or relating to these Terms and Conditions or the breach thereof shall be instituted in a court of competent jurisdiction in New York County in the State of New York in the United States of America and each party hereby consents and submits to the personal jurisdiction of such court, waives any objection to venue in such court and consents to service of process by registered or certified mail, return receipt requested, at the last known address of such party.

WILEY OPEN ACCESS TERMS AND CONDITIONS
Wiley Publishes Open Access Articles in fully Open Access Journals and in Subscription journals offering Online Open. Although most of the fully Open Access journals publish open access articles under the terms of the Creative Commons Attribution (CC BY) License only, the subscription journals and a few of the Open Access Journals offer a choice of Creative Commons Licenses. The license type is clearly identified on the article.
The Creative Commons Attribution License
The Creative Commons Attribution License (CC-BY) allows users to copy, distribute and transmit an article, adapt the article and make commercial use of the article. The CC-BY license permits commercial and non-
Creative Commons Attribution Non-Commercial License
The Creative Commons Attribution Non-Commercial (CC-BY-NC)License permits use, distribution and reproduction in any medium, provided the original work is properly cited and is not used for commercial purposes.(see below)

Creative Commons Attribution-Non-Commercial-NoDerivs License
The Creative Commons Attribution Non-Commercial-NoDerivs License (CC-BY-NC-ND) permits use, distribution and reproduction in any medium, provided the original work is properly cited, is not used for commercial purposes and no modifications or adaptations are made. (see below)
Use by commercial "for-profit" organizations
Use of Wiley Open Access articles for commercial, promotional, or marketing purposes requires further explicit permission from Wiley and will be subject to a fee.
Further details can be found on Wiley Online Library
http://olabout.wiley.com/WileyCDA/Section/id-410895.html

Other Terms and Conditions:

v1.10 Last updated September 2015

Questions? customercare@copyright.com or +1-855-239-3415 (toll free in the US) or +1-978-646-2777.

SPRINGER NATURE LICENSE TERMS AND CONDITIONS

Aug 21, 2019

This Agreement between Imperial College London -- Chunching Li ("You") and Springer Nature ("Springer Nature") consists of your license details and the terms and conditions provided by Springer Nature and Copyright Clearance Center.

License Number	4653670919830
License date	Aug 21, 2019
Licensed Content Publisher	Springer Nature
Licensed Content Publication	Nature
Licensed Content Title	Developmental regulation of the growth plate
Licensed Content Author	Henry M. Kronenberg
Licensed Content Date	May 15, 2003
Type of Use	Thesis/Dissertation
Requestor type	academic/university or research institute
Format	print and electronic
Portion	figures/tables/illustrations
Number of figures/tables/illustrations	1
High-res required	no
Will you be translating?	no
Circulation/distribution	>50,000
Author of this Springer Nature content	no
Title	Force-based Engineering of Gradients
Institution name	n/a
Expected presentation date	Nov 2019
Portions	Figure 2
Requestor Location	Imperial College London South Kensington Campus London, SW7 2AZ, UK United Kingdom Attn: Imperial College London
Total	0.00 USD
Terms and Conditions	

Springer Nature Customer Service Centre GmbH Terms and Conditions

This agreement sets out the terms and conditions of the licence (the **Licence**) between you and **Springer Nature Customer Service Centre GmbH** (the **Licensor**). By clicking 'accept' and completing the transaction for the material (**Licensed Material**), you also confirm your acceptance of these terms and conditions.

1. Grant of License

1. 1. The Licensor grants you a personal, non-exclusive, non-transferable, world-wide licence to reproduce the Licensed Material for the purpose specified in your order only.

Licences are granted for the specific use requested in the order and for no other use, subject to the conditions below.

1. 2. The Licensor warrants that it has, to the best of its knowledge, the rights to license reuse of the Licensed Material. However, you should ensure that the material you are requesting is original to the Licensor and does not carry the copyright of another entity (as credited in the published version).

1. 3. If the credit line on any part of the material you have requested indicates that it was reprinted or adapted with permission from another source, then you should also seek permission from that source to reuse the material.

2. Scope of Licence

2. 1. You may only use the Licensed Content in the manner and to the extent permitted by these Ts&Cs and any applicable laws.

2. 2. A separate licence may be required for any additional use of the Licensed Material, e.g. where a licence has been purchased for print only use, separate permission must be obtained for electronic re-use. Similarly, a licence is only valid in the language selected and does not apply for editions in other languages unless additional translation rights have been granted separately in the licence. Any content owned by third parties are expressly excluded from the licence.

2. 3. Similarly, rights for additional components such as custom editions and derivatives require additional permission and may be subject to an additional fee. Please apply to Journalpermissions@springernature.com/bookpermissions@springernature.com for these rights.

2. 4. Where permission has been granted **free of charge** for material in print, permission may also be granted for any electronic version of that work, provided that the material is incidental to your work as a whole and that the electronic version is essentially equivalent to, or substitutes for, the print version.

2. 5. An alternative scope of licence may apply to signatories of the STM Permissions Guidelines, as amended from time to time.

3. Duration of Licence

3. 1. A licence for is valid from the date of purchase ('Licence Date') at the end of the relevant period in the below table:

Scope of Licence	Duration of Licence
Post on a website	12 months
Presentations	12 months
Books and journals	Lifetime of the edition in the language purchased

4. Acknowledgement

4. 1. The Licensor's permission must be acknowledged next to the Licenced Material in print. In electronic form, this acknowledgement must be visible at the same time as the figures/tables/illustrations or abstract, and must be hyperlinked to the journal/book's homepage. Our required acknowledgement format is in the Appendix below.

5. Restrictions on use

5. 1. Use of the Licensed Material may be permitted for incidental promotional use and minor editing privileges e.g. minor adaptations of single figures, changes of format, colour and/or style where the adaptation is credited as set out in Appendix 1 below. Any other changes including but not limited to, cropping, adapting, omitting material that affect the meaning, intention or moral rights of the author are strictly prohibited.

5. 2. You must not use any Licensed Material as part of any design or trademark.

5. 3. Licensed Material may be used in Open Access Publications (OAP) before publication by Springer Nature, but any Licensed Material must be removed from OAP sites prior to final publication.

6. Ownership of Rights

6. 1. Licensed Material remains the property of either Licensor or the relevant third party and any rights not explicitly granted herein are expressly reserved.

7. Warranty

IN NO EVENT SHALL LICENSOR BE LIABLE TO YOU OR ANY OTHER PARTY OR ANY OTHER PERSON OR FOR ANY SPECIAL, CONSEQUENTIAL, INCIDENTAL OR INDIRECT DAMAGES, HOWEVER CAUSED, ARISING OUT OF OR IN CONNECTION WITH THE DOWNLOADING, VIEWING OR USE OF THE MATERIALS REGARDLESS OF THE FORM OF ACTION, WHETHER FOR BREACH OF CONTRACT, BREACH OF WARRANTY, TORT, NEGLIGENCE, INFRINGEMENT OR OTHERWISE (INCLUDING, WITHOUT LIMITATION, DAMAGES BASED ON LOSS OF PROFITS, DATA, FILES, USE, BUSINESS OPPORTUNITY OR CLAIMS OF THIRD PARTIES), AND
WHETHER OR NOT THE PARTY HAS BEEN ADVISED OF THE POSSIBILITY OF SUCH DAMAGES. THIS LIMITATION SHALL APPLY NOTWITHSTANDING ANY FAILURE OF ESSENTIAL PURPOSE OF ANY LIMITED REMEDY PROVIDED HEREIN.

8. Limitations

8. 1. ***BOOKS ONLY:***Where **'reuse in a dissertation/thesis'** has been selected the following terms apply: Print rights of the final author's accepted manuscript (for clarity, NOT the published version) for up to 100 copies, electronic rights for use only on a personal website or institutional repository as defined by the Sherpa guideline (www.sherpa.ac.uk/romeo/).

9. Termination and Cancellation

9. 1. Licences will expire after the period shown in Clause 3 (above).

9. 2. Licensee reserves the right to terminate the Licence in the event that payment is not received in full or if there has been a breach of this agreement by you.

Appendix 1 — Acknowledgements:

For Journal Content:
Reprinted by permission from [**the Licensor**]: [**Journal Publisher** (e.g. Nature/Springer/Palgrave)] [**JOURNAL NAME**] [**REFERENCE CITATION** (Article name, Author(s) Name), [**COPYRIGHT**] (year of publication)

For **Advance Online Publication papers:**
Reprinted by permission from [**the Licensor**]: [**Journal Publisher** (e.g. Nature/Springer/Palgrave)] [**JOURNAL NAME**] [**REFERENCE CITATION**

(Article name, Author(s) Name), [**COPYRIGHT**] (year of publication), advance online publication, day month year (doi: 10.1038/sj.[JOURNAL ACRONYM].)

For Adaptations/Translations:
Adapted/Translated by permission from [**the Licensor**]: [**Journal Publisher** (e.g. Nature/Springer/Palgrave)] [**JOURNAL NAME**] [**REFERENCE CITATION** (Article name, Author(s) Name), [**COPYRIGHT**] (year of publication)

Note: For any republication from the British Journal of Cancer, the following credit line style applies:

Reprinted/adapted/translated by permission from [**the Licensor**]: on behalf of Cancer Research UK: : [**Journal Publisher** (e.g. Nature/Springer/Palgrave)] [**JOURNAL NAME**] [**REFERENCE CITATION** (Article name, Author(s) Name), [**COPYRIGHT**] (year of publication)

For **Advance Online Publication** papers:
Reprinted by permission from The [**the Licensor**]: on behalf of Cancer Research UK: [**Journal Publisher** (e.g. Nature/Springer/Palgrave)] [**JOURNAL NAME**] [**REFERENCE CITATION** (Article name, Author(s) Name), [**COPYRIGHT**] (year of publication), advance online publication, day month year (doi: 10.1038/sj. [JOURNAL ACRONYM])

For Book content:
Reprinted/adapted by permission from [**the Licensor**]: [**Book Publisher** (e.g. Palgrave Macmillan, Springer etc) [**Book Title**] by [**Book author**(s)] [**COPYRIGHT**] (year of publication)

Other Conditions:

Version 1.2

Questions? customercare@copyright.com or +1-855-239-3415 (toll free in the US) or +1-978-646-2777.

JOHN WILEY AND SONS LICENSE
TERMS AND CONDITIONS

Aug 21, 2019

This Agreement between Imperial College London -- Chunching Li ("You") and John Wiley and Sons ("John Wiley and Sons") consists of your license details and the terms and conditions provided by John Wiley and Sons and Copyright Clearance Center.

License Number	4653671175731
License date	Aug 21, 2019
Licensed Content Publisher	John Wiley and Sons
Licensed Content Publication	Journal of Tissue Engineering and Regenerative Medicine
Licensed Content Title	FGF, TGFβ and Wnt crosstalk: embryonic to in vitro cartilage development from mesenchymal stem cells
Licensed Content Author	Roberto Narcisi, Catharine A. Hellingman, Pieter A. Brama, et al
Licensed Content Date	Apr 11, 2013
Licensed Content Volume	9
Licensed Content Issue	4
Licensed Content Pages	11
Type of use	Dissertation/Thesis
Requestor type	University/Academic
Format	Print and electronic
Portion	Figure/table
Number of figures/tables	1
Original Wiley figure/table number(s)	Figure 2
Will you be translating?	No
Title of your thesis / dissertation	Force-based Engineering of Gradients
Expected completion date	Nov 2019
Expected size (number of pages)	200
Requestor Location	Imperial College London South Kensington Campus London, SW7 2AZ, UK United Kingdom Attn: Imperial College London
Publisher Tax ID	EU826007151
Total	0.00 USD
Terms and Conditions	

TERMS AND CONDITIONS

This copyrighted material is owned by or exclusively licensed to John Wiley & Sons, Inc. or one of its group companies (each a"Wiley Company") or handled on behalf of a society with which a Wiley Company has exclusive publishing rights in relation to a particular work (collectively "WILEY"). By clicking "accept" in connection with completing this licensing transaction, you agree that the following terms and conditions apply to this transaction (along with the billing and payment terms and conditions established by the Copyright

Clearance Center Inc., ("CCC's Billing and Payment terms and conditions"), at the time that you opened your RightsLink account (these are available at any time at http://myaccount.copyright.com).

Terms and Conditions

- The materials you have requested permission to reproduce or reuse (the "Wiley Materials") are protected by copyright.

- You are hereby granted a personal, non-exclusive, non-sub licensable (on a stand-alone basis), non-transferable, worldwide, limited license to reproduce the Wiley Materials for the purpose specified in the licensing process. This license, **and any CONTENT (PDF or image file) purchased as part of your order,** is for a one-time use only and limited to any maximum distribution number specified in the license. The first instance of republication or reuse granted by this license must be completed within two years of the date of the grant of this license (although copies prepared before the end date may be distributed thereafter). The Wiley Materials shall not be used in any other manner or for any other purpose, beyond what is granted in the license. Permission is granted subject to an appropriate acknowledgement given to the author, title of the material/book/journal and the publisher. You shall also duplicate the copyright notice that appears in the Wiley publication in your use of the Wiley Material. Permission is also granted on the understanding that nowhere in the text is a previously published source acknowledged for all or part of this Wiley Material. Any third party content is expressly excluded from this permission.

- With respect to the Wiley Materials, all rights are reserved. Except as expressly granted by the terms of the license, no part of the Wiley Materials may be copied, modified, adapted (except for minor reformatting required by the new Publication), translated, reproduced, transferred or distributed, in any form or by any means, and no derivative works may be made based on the Wiley Materials without the prior permission of the respective copyright owner.**For STM Signatory Publishers clearing permission under the terms of the STM Permissions Guidelines only, the terms of the license are extended to include subsequent editions and for editions in other languages, provided such editions are for the work as a whole in situ and does not involve the separate exploitation of the permitted figures or extracts,** You may not alter, remove or suppress in any manner any copyright, trademark or other notices displayed by the Wiley Materials. You may not license, rent, sell, loan, lease, pledge, offer as security, transfer or assign the Wiley Materials on a stand-alone basis, or any of the rights granted to you hereunder to any other person.

- The Wiley Materials and all of the intellectual property rights therein shall at all times remain the exclusive property of John Wiley & Sons Inc, the Wiley Companies, or their respective licensors, and your interest therein is only that of having possession of and the right to reproduce the Wiley Materials pursuant to Section 2 herein during the continuance of this Agreement. You agree that you own no right, title or interest in or to the Wiley Materials or any of the intellectual property rights therein. You shall have no rights hereunder other than the license as provided for above in Section 2. No right, license or interest to any trademark, trade name, service mark or other branding ("Marks") of WILEY or its licensors is granted hereunder, and you agree that you shall not assert any such right, license or interest with respect thereto

- NEITHER WILEY NOR ITS LICENSORS MAKES ANY WARRANTY OR REPRESENTATION OF ANY KIND TO YOU OR ANY THIRD PARTY, EXPRESS, IMPLIED OR STATUTORY, WITH RESPECT TO THE MATERIALS OR THE ACCURACY OF ANY INFORMATION CONTAINED IN THE MATERIALS, INCLUDING, WITHOUT LIMITATION, ANY IMPLIED WARRANTY OF MERCHANTABILITY, ACCURACY, SATISFACTORY QUALITY, FITNESS FOR A PARTICULAR PURPOSE, USABILITY,

INTEGRATION OR NON-INFRINGEMENT AND ALL SUCH WARRANTIES ARE HEREBY EXCLUDED BY WILEY AND ITS LICENSORS AND WAIVED BY YOU.

- WILEY shall have the right to terminate this Agreement immediately upon breach of this Agreement by you.
- You shall indemnify, defend and hold harmless WILEY, its Licensors and their respective directors, officers, agents and employees, from and against any actual or threatened claims, demands, causes of action or proceedings arising from any breach of this Agreement by you.
- IN NO EVENT SHALL WILEY OR ITS LICENSORS BE LIABLE TO YOU OR ANY OTHER PARTY OR ANY OTHER PERSON OR ENTITY FOR ANY SPECIAL, CONSEQUENTIAL, INCIDENTAL, INDIRECT, EXEMPLARY OR PUNITIVE DAMAGES, HOWEVER CAUSED, ARISING OUT OF OR IN CONNECTION WITH THE DOWNLOADING, PROVISIONING, VIEWING OR USE OF THE MATERIALS REGARDLESS OF THE FORM OF ACTION, WHETHER FOR BREACH OF CONTRACT, BREACH OF WARRANTY, TORT, NEGLIGENCE, INFRINGEMENT OR OTHERWISE (INCLUDING, WITHOUT LIMITATION, DAMAGES BASED ON LOSS OF PROFITS, DATA, FILES, USE, BUSINESS OPPORTUNITY OR CLAIMS OF THIRD PARTIES), AND WHETHER OR NOT THE PARTY HAS BEEN ADVISED OF THE POSSIBILITY OF SUCH DAMAGES. THIS LIMITATION SHALL APPLY NOTWITHSTANDING ANY FAILURE OF ESSENTIAL PURPOSE OF ANY LIMITED REMEDY PROVIDED HEREIN.
- Should any provision of this Agreement be held by a court of competent jurisdiction to be illegal, invalid, or unenforceable, that provision shall be deemed amended to achieve as nearly as possible the same economic effect as the original provision, and the legality, validity and enforceability of the remaining provisions of this Agreement shall not be affected or impaired thereby.
- The failure of either party to enforce any term or condition of this Agreement shall not constitute a waiver of either party's right to enforce each and every term and condition of this Agreement. No breach under this agreement shall be deemed waived or excused by either party unless such waiver or consent is in writing signed by the party granting such waiver or consent. The waiver by or consent of a party to a breach of any provision of this Agreement shall not operate or be construed as a waiver of or consent to any other or subsequent breach by such other party.
- This Agreement may not be assigned (including by operation of law or otherwise) by you without WILEY's prior written consent.
- Any fee required for this permission shall be non-refundable after thirty (30) days from receipt by the CCC.
- These terms and conditions together with CCC's Billing and Payment terms and conditions (which are incorporated herein) form the entire agreement between you and WILEY concerning this licensing transaction and (in the absence of fraud) supersedes all prior agreements and representations of the parties, oral or written. This Agreement may not be amended except in writing signed by both parties. This Agreement shall be binding upon and inure to the benefit of the parties' successors, legal representatives, and authorized assigns.
- In the event of any conflict between your obligations established by these terms and conditions and those established by CCC's Billing and Payment terms and conditions, these terms and conditions shall prevail.

- WILEY expressly reserves all rights not specifically granted in the combination of (i) the license details provided by you and accepted in the course of this licensing transaction, (ii) these terms and conditions and (iii) CCC's Billing and Payment terms and conditions.
- This Agreement will be void if the Type of Use, Format, Circulation, or Requestor Type was misrepresented during the licensing process.
- This Agreement shall be governed by and construed in accordance with the laws of the State of New York, USA, without regards to such state's conflict of law rules. Any legal action, suit or proceeding arising out of or relating to these Terms and Conditions or the breach thereof shall be instituted in a court of competent jurisdiction in New York County in the State of New York in the United States of America and each party hereby consents and submits to the personal jurisdiction of such court, waives any objection to venue in such court and consents to service of process by registered or certified mail, return receipt requested, at the last known address of such party.

WILEY OPEN ACCESS TERMS AND CONDITIONS
Wiley Publishes Open Access Articles in fully Open Access Journals and in Subscription journals offering Online Open. Although most of the fully Open Access journals publish open access articles under the terms of the Creative Commons Attribution (CC BY) License only, the subscription journals and a few of the Open Access Journals offer a choice of Creative Commons Licenses. The license type is clearly identified on the article.
The Creative Commons Attribution License
The Creative Commons Attribution License (CC-BY) allows users to copy, distribute and transmit an article, adapt the article and make commercial use of the article. The CC-BY license permits commercial and non-
Creative Commons Attribution Non-Commercial License
The Creative Commons Attribution Non-Commercial (CC-BY-NC)License permits use, distribution and reproduction in any medium, provided the original work is properly cited and is not used for commercial purposes.(see below)

Creative Commons Attribution-Non-Commercial-NoDerivs License
The Creative Commons Attribution Non-Commercial-NoDerivs License (CC-BY-NC-ND) permits use, distribution and reproduction in any medium, provided the original work is properly cited, is not used for commercial purposes and no modifications or adaptations are made. (see below)
Use by commercial "for-profit" organizations
Use of Wiley Open Access articles for commercial, promotional, or marketing purposes requires further explicit permission from Wiley and will be subject to a fee.
Further details can be found on Wiley Online Library
http://olabout.wiley.com/WileyCDA/Section/id-410895.html

Other Terms and Conditions:

v1.10 Last updated September 2015

Questions? customercare@copyright.com or +1-855-239-3415 (toll free in the US) or +1-978-646-2777.

ELSEVIER LICENSE
TERMS AND CONDITIONS

Aug 21, 2019

This Agreement between Imperial College London -- Chunching Li ("You") and Elsevier ("Elsevier") consists of your license details and the terms and conditions provided by Elsevier and Copyright Clearance Center.

License Number	4653671264381
License date	Aug 21, 2019
Licensed Content Publisher	Elsevier
Licensed Content Publication	Osteoarthritis and Cartilage
Licensed Content Title	The structural architecture of adult mammalian articular cartilage evolves by a synchronized process of tissue resorption and neoformation during postnatal development
Licensed Content Author	E.B. Hunziker,E. Kapfinger,J. Geiss
Licensed Content Date	Apr 1, 2007
Licensed Content Volume	15
Licensed Content Issue	4
Licensed Content Pages	11
Start Page	403
End Page	413
Type of Use	reuse in a thesis/dissertation
Intended publisher of new work	other
Portion	figures/tables/illustrations
Number of figures/tables/illustrations	1
Format	both print and electronic
Are you the author of this Elsevier article?	No
Will you be translating?	No
Original figure numbers	Figure 3
Title of your thesis/dissertation	Force-based Engineering of Gradients
Expected completion date	Nov 2019
Estimated size (number of pages)	200
Requestor Location	Imperial College London South Kensington Campus London, SW7 2AZ, UK United Kingdom Attn: Imperial College London
Publisher Tax ID	GB 494 6272 12
Total	0.00 USD
Terms and Conditions	

INTRODUCTION

1. The publisher for this copyrighted material is Elsevier. By clicking "accept" in connection with completing this licensing transaction, you agree that the following terms and conditions apply to this transaction (along with the Billing and Payment terms and conditions established by Copyright Clearance Center, Inc. ("CCC"), at the time that you opened your Rightslink account and that are available at any time at http://myaccount.copyright.com).

GENERAL TERMS

2. Elsevier hereby grants you permission to reproduce the aforementioned material subject to the terms and conditions indicated.

3. Acknowledgement: If any part of the material to be used (for example, figures) has appeared in our publication with credit or acknowledgement to another source, permission must also be sought from that source. If such permission is not obtained then that material may not be included in your publication/copies. Suitable acknowledgement to the source must be made, either as a footnote or in a reference list at the end of your publication, as follows:

"Reprinted from Publication title, Vol /edition number, Author(s), Title of article / title of chapter, Pages No., Copyright (Year), with permission from Elsevier [OR APPLICABLE SOCIETY COPYRIGHT OWNER]." Also Lancet special credit - "Reprinted from The Lancet, Vol. number, Author(s), Title of article, Pages No., Copyright (Year), with permission from Elsevier."

4. Reproduction of this material is confined to the purpose and/or media for which permission is hereby given.

5. Altering/Modifying Material: Not Permitted. However figures and illustrations may be altered/adapted minimally to serve your work. Any other abbreviations, additions, deletions and/or any other alterations shall be made only with prior written authorization of Elsevier Ltd. (Please contact Elsevier at permissions@elsevier.com). No modifications can be made to any Lancet figures/tables and they must be reproduced in full.

6. If the permission fee for the requested use of our material is waived in this instance, please be advised that your future requests for Elsevier materials may attract a fee.

7. Reservation of Rights: Publisher reserves all rights not specifically granted in the combination of (i) the license details provided by you and accepted in the course of this licensing transaction, (ii) these terms and conditions and (iii) CCC's Billing and Payment terms and conditions.

8. License Contingent Upon Payment: While you may exercise the rights licensed immediately upon issuance of the license at the end of the licensing process for the transaction, provided that you have disclosed complete and accurate details of your proposed use, no license is finally effective unless and until full payment is received from you (either by publisher or by CCC) as provided in CCC's Billing and Payment terms and conditions. If full payment is not received on a timely basis, then any license preliminarily granted shall be deemed automatically revoked and shall be void as if never granted. Further, in the event that you breach any of these terms and conditions or any of CCC's Billing and Payment terms and conditions, the license is automatically revoked and shall be void as if never granted. Use of materials as described in a revoked license, as well as any use of the materials beyond the scope of an unrevoked license, may constitute copyright infringement and publisher reserves the right to take any and all action to protect its copyright in the materials.

9. Warranties: Publisher makes no representations or warranties with respect to the licensed material.

10. Indemnity: You hereby indemnify and agree to hold harmless publisher and CCC, and their respective officers, directors, employees and agents, from and against any and all claims arising out of your use of the licensed material other than as specifically authorized pursuant to this license.

11. No Transfer of License: This license is personal to you and may not be sublicensed, assigned, or transferred by you to any other person without publisher's written permission.

12. No Amendment Except in Writing: This license may not be amended except in a writing signed by both parties (or, in the case of publisher, by CCC on publisher's behalf).

13. Objection to Contrary Terms: Publisher hereby objects to any terms contained in any purchase order, acknowledgment, check endorsement or other writing prepared by you, which terms are inconsistent with these terms and conditions or CCC's Billing and Payment terms and conditions. These terms and conditions, together with CCC's Billing and Payment terms and conditions (which are incorporated herein), comprise the entire agreement between you and publisher (and CCC) concerning this licensing transaction. In the event of any conflict between your obligations established by these terms and conditions and those established by CCC's Billing and Payment terms and conditions, these terms and conditions shall control.

14. Revocation: Elsevier or Copyright Clearance Center may deny the permissions described in this License at their sole discretion, for any reason or no reason, with a full refund payable to you. Notice of such denial will be made using the contact information provided by you. Failure to receive such notice will not alter or invalidate the denial. In no event will Elsevier or Copyright Clearance Center be responsible or liable for any costs, expenses or damage incurred by you as a result of a denial of your permission request, other than a refund of the amount(s) paid by you to Elsevier and/or Copyright Clearance Center for denied permissions.

LIMITED LICENSE

The following terms and conditions apply only to specific license types:

15. **Translation**: This permission is granted for non-exclusive world **English** rights only unless your license was granted for translation rights. If you licensed translation rights you may only translate this content into the languages you requested. A professional translator must perform all translations and reproduce the content word for word preserving the integrity of the article.

16. **Posting licensed content on any Website**: The following terms and conditions apply as follows: Licensing material from an Elsevier journal: All content posted to the web site must maintain the copyright information line on the bottom of each image; A hyper-text must be included to the Homepage of the journal from which you are licensing at http://www.sciencedirect.com/science/journal/xxxxx or the Elsevier homepage for books at http://www.elsevier.com; Central Storage: This license does not include permission for a scanned version of the material to be stored in a central repository such as that provided by Heron/XanEdu.

Licensing material from an Elsevier book: A hyper-text link must be included to the Elsevier homepage at http://www.elsevier.com . All content posted to the web site must maintain the copyright information line on the bottom of each image.

Posting licensed content on Electronic reserve: In addition to the above the following clauses are applicable: The web site must be password-protected and made available only to bona fide students registered on a relevant course. This permission is granted for 1 year only. You may obtain a new license for future website posting.

17. **For journal authors:** the following clauses are applicable in addition to the above:

Preprints:

A preprint is an author's own write-up of research results and analysis, it has not been peer-reviewed, nor has it had any other value added to it by a publisher (such as formatting, copyright, technical enhancement etc.).

Authors can share their preprints anywhere at any time. Preprints should not be added to or enhanced in any way in order to appear more like, or to substitute for, the final versions of articles however authors can update their preprints on arXiv or RePEc with their Accepted Author Manuscript (see below).

If accepted for publication, we encourage authors to link from the preprint to their formal publication via its DOI. Millions of researchers have access to the formal publications on ScienceDirect, and so links will help users to find, access, cite and use the best available version. Please note that Cell Press, The Lancet and some society-owned have different preprint policies. Information on these policies is available on the journal homepage.

Accepted Author Manuscripts: An accepted author manuscript is the manuscript of an article that has been accepted for publication and which typically includes author-incorporated changes suggested during submission, peer review and editor-author communications.

Authors can share their accepted author manuscript:

- immediately
  - via their non-commercial person homepage or blog
  - by updating a preprint in arXiv or RePEc with the accepted manuscript
  - via their research institute or institutional repository for internal institutional uses or as part of an invitation-only research collaboration work-group
  - directly by providing copies to their students or to research collaborators for their personal use
  - for private scholarly sharing as part of an invitation-only work group on commercial sites with which Elsevier has an agreement
- After the embargo period
  - via non-commercial hosting platforms such as their institutional repository
  - via commercial sites with which Elsevier has an agreement

In all cases accepted manuscripts should:

- link to the formal publication via its DOI
- bear a CC-BY-NC-ND license - this is easy to do
- if aggregated with other manuscripts, for example in a repository or other site, be shared in alignment with our hosting policy not be added to or enhanced in any way to appear more like, or to substitute for, the published journal article.

Published journal article (JPA): A published journal article (PJA) is the definitive final record of published research that appears or will appear in the journal and embodies all value-adding publishing activities including peer review co-ordination, copy-editing, formatting, (if relevant) pagination and online enrichment.

Policies for sharing publishing journal articles differ for subscription and gold open access articles:

Subscription Articles: If you are an author, please share a link to your article rather than the full-text. Millions of researchers have access to the formal publications on ScienceDirect, and so links will help your users to find, access, cite, and use the best available version. Theses and dissertations which contain embedded PJAs as part of the formal submission can be posted publicly by the awarding institution with DOI links back to the formal publications on ScienceDirect.

If you are affiliated with a library that subscribes to ScienceDirect you have additional private sharing rights for others' research accessed under that agreement. This includes use for classroom teaching and internal training at the institution (including use in course packs and courseware programs), and inclusion of the article for grant funding purposes.

Gold Open Access Articles: May be shared according to the author-selected end-user license and should contain a CrossMark logo, the end user license, and a DOI link to the formal publication on ScienceDirect.

Please refer to Elsevier's posting policy for further information.

18. **For book authors** the following clauses are applicable in addition to the above: Authors are permitted to place a brief summary of their work online only. You are not allowed to download and post the published electronic version of your chapter, nor may you scan the printed edition to create an electronic version. **Posting to a repository:** Authors are permitted to post a summary of their chapter only in their institution's repository.

19. **Thesis/Dissertation**: If your license is for use in a thesis/dissertation your thesis may be submitted to your institution in either print or electronic form. Should your thesis be published commercially, please reapply for permission. These requirements include permission for the Library and Archives of Canada to supply single copies, on demand, of the complete thesis and include permission for Proquest/UMI to supply single copies, on demand, of the complete thesis. Should your thesis be published commercially, please reapply for permission. Theses and dissertations which contain embedded PJAs as part of the formal submission can be posted publicly by the awarding institution with DOI links back to the formal publications on ScienceDirect.

Elsevier Open Access Terms and Conditions

You can publish open access with Elsevier in hundreds of open access journals or in nearly 2000 established subscription journals that support open access publishing. Permitted third party re-use of these open access articles is defined by the author's choice of Creative Commons user license. See our open access license policy for more information.

Terms & Conditions applicable to all Open Access articles published with Elsevier:

Any reuse of the article must not represent the author as endorsing the adaptation of the article nor should the article be modified in such a way as to damage the author's honour or reputation. If any changes have been made, such changes must be clearly indicated.

The author(s) must be appropriately credited and we ask that you include the end user license and a DOI link to the formal publication on ScienceDirect.

If any part of the material to be used (for example, figures) has appeared in our publication with credit or acknowledgement to another source it is the responsibility of the user to ensure their reuse complies with the terms and conditions determined by the rights holder.

Additional Terms & Conditions applicable to each Creative Commons user license:

CC BY: The CC-BY license allows users to copy, to create extracts, abstracts and new works from the Article, to alter and revise the Article and to make commercial use of the Article (including reuse and/or resale of the Article by commercial entities), provided the user gives appropriate credit (with a link to the formal publication through the relevant DOI), provides a link to the license, indicates if changes were made and the licensor is not represented as endorsing the use made of the work. The full details of the license are available at http://creativecommons.org/licenses/by/4.0.

CC BY NC SA: The CC BY-NC-SA license allows users to copy, to create extracts, abstracts and new works from the Article, to alter and revise the Article, provided this is not done for commercial purposes, and that the user gives appropriate credit (with a link to the formal publication through the relevant DOI), provides a link to the license, indicates if changes were made and the licensor is not represented as endorsing the use made of the work. Further, any new works must be made available on the same conditions. The full details of the license are available at http://creativecommons.org/licenses/by-nc-sa/4.0.

CC BY NC ND: The CC BY-NC-ND license allows users to copy and distribute the Article, provided this is not done for commercial purposes and further does not permit distribution of the Article if it is changed or edited in any way, and provided the user gives appropriate credit (with a link to the formal publication through the relevant DOI), provides a link to the license, and that the licensor is not represented as endorsing the use made of the work. The full details of the license are available at http://creativecommons.org/licenses/by-nc-nd/4.0.

Any commercial reuse of Open Access articles published with a CC BY NC SA or CC BY NC ND license requires permission from Elsevier and will be subject to a fee.

Commercial reuse includes:

- Associating advertising with the full text of the Article
- Charging fees for document delivery or access
- Article aggregation
- Systematic distribution via e-mail lists or share buttons

Posting or linking by commercial companies for use by customers of those companies.

20. **Other Conditions**:

v1.9

Questions? customercare@copyright.com or +1-855-239-3415 (toll free in the US) or +1-978-646-2777.

E-theses letter template: request to reproduce an extract from a third party's published work

Dear IOS Press,

I am completing my PhD thesis at Imperial College London entitled 'Force-based Engineering of Gradients'.

I seek your permission to reprint, in my thesis an extract from: **Mechano-acoustic determination of Young's modulus of articular cartilage**. The extract to be reproduced is: **Figure 2**

I would like to include the extract in my thesis which will be added to Spiral, Imperial's institutional repository http://spiral.imperial.ac.uk/ and made available to the public under a Attribution-Non Commercial 4.0 International Licence (CC BY-NC)

If you are happy to grant me all the permissions requested, please return a signed copy of this letter. If you wish to grant only some of the permissions requested, please list these and then sign.

Yours sincerely,

Chunching Li

Permission granted for the use requested above:

I confirm that I am the copyright holder of the extract above and hereby give permission to include it in your thesis which will be made available, via the internet, for non-commercial purposes under the terms of the user licence.

Name: C. Koolbergen

Organisation: IOS Press

Job title: Rights & Permissions Coordinator.

Nieuwe Hemweg 6B
1013 BG AMSTERDAM
Netherlands
Fax: +31 20 6870019

Please note the attached email message.

Carry Koolbergen

Onderwerp: Chunching Li Permission for data reuse in PhD Thesis
Bijlagen: scan.pdf

Van: Carry Koolbergen
Aan: 'c.li15@imperial.ac.uk' <c.li15@imperial.ac.uk>
Onderwerp: Chunching Li Permission for data reuse in PhD Thesis

Citation: Biorheology, vol. 41, no. 3-4, pp. 167-179, 2004
https://content.iospress.com/articles/biorheology/bir296

Dear Chunching Li,

We hereby grant you permission to reproduce the below mentioned material in **print and electronic format** at no charge subject to the following conditions:

1. Permission should also be granted by the original authors of the article in question.
2. If any part of the material to be used (for example, figures) has appeared in our publication with credit or acknowledgement to another source, permission must also be sought from that source. If such permission is not obtained then that material may not be included in your publication/copies.
3. Suitable acknowledgement to the source must be made, either as a footnote or in a reference list at the end of your publication, as follows:

   "Reprinted from Publication title, Vol number, Author(s), Title of article, Pages No., Copyright (Year), with permission from IOS Press".
   The publication is available at IOS Press through https://content.iospress.com/articles/biorheology/bir296
4. This permission is granted for non-exclusive world **English** rights only. For other languages please reapply separately for each one required.
5. Reproduction of this material is confined to the purpose for which permission is hereby given.

Yours sincerelv
Carry Koolbergen (Mrs.)
Contracts, Rights & Permissions Coordinator
Not in the office on Wednesdays

IOS Press BV
Nieuwe Hemweg 6B
1013 BG Amsterdam
The Netherlands
Tel.: +31 (0)20 687 0022
Fax: +31 (0)20 687 0019
Email: c.koolbergen@iospress.nl / publisher@iospress.nl
URL: www.iospress.nl

IOS PRESS BV
Nieuwe Hemweg 6B
1013 BG AMSTERDAM
Netherlands
Fax: +31 20 6870019

Please consider the environment before printing this email.

From: Li, Chunching [mailto:c.li15@imperial.ac.uk]
Sent: woensdag 21 augustus 2019 17:01
To: IOS Press Info <Info@iospress.nl>
Subject: URGENT - Permission for data reuse in PhD Thesis

Dear IOS Press,

I am Chunching, now completing my PhD thesis at Imperial College London entitled 'Force-based Engineering of Gradients'.

I seek your permission to reprint, in my thesis an extract from: **Mechano-acoustic determination of Young's modulus of articular cartilage**. The extract to be reproduced is: **Figure 2** of the paper**.**

I would like to include the extract in my thesis which will be added to Spiral, Imperial's institutional repository http://spiral.imperial.ac.uk/ and made available to the public under a Attribution-Non Commercial 4.0 International Licence (CC BY-NC)

If you are happy to grant me all the permissions requested, please return a signed copy of **the attached letter**. If you wish to grant only some of the permissions requested, please list these and then sign.

Thank you very much for your assistance.

Yours sincerely,

Chunching Li